Soil-lubricant-structure interface mechanics for microtunnelling



Bryn Phillips
Harris Manchester College
University of Oxford

A thesis submitted for the degree of
Doctor of Philosophy

Hilary 2023

Abstract

Soil-lubricant-structure interface mechanics for microtunnelling

Bryn M. Phillips
Harris Manchester College, University of Oxford
A thesis submitted for the degree of *Doctor of Philosophy*
Hilary 2023

Pipe-jacking is a trenchless underground construction technique commonly used to create conduits for conveying services such as electrical cables, gas, sewerage, or water pipes whilst keeping surface disruption to a minimum. The installation process consists of a tunnel boring machine (TBM) undertaking controlled excavation at the front of a string of pipes, whilst thrust is applied from a jacking frame located at the rear of the string. As the jacking frame advances the machine and pipe string, lubricant (typically comprising Bentonite clay) is simultaneously injected into an overcut between the pipes and soil formed by the TBM . This process is periodically paused whilst pipes are added and for planned or unplanned stoppages. Currently, there is no commonly accepted model for the behaviour of the soil-lubricant-structure (SLS) interface around these tunnel pipes during advances and stoppages, which results in excessive conservatism in the design stage.

This thesis explores the behaviour of the SLS interface using a combination of field and laboratory study. Two custom instrumented jacking pipes have been developed and deployed during two instrumented tunnel drives. Strain gauges, pore pressure sensors and contact stress sensors were used to identify the location and magnitude of stresses at the interface. These field studies are supplemented by analysis of 12 industry case histories, which provide insight into the SLS interface response in different ground conditions.

The field study program is complemented by a suite of laboratory scale testing of tunnelling lubricants and SLS interface behaviour. To facilitate this, a novel scale interface test apparatus has been developed. The plane strain apparatus has been designed to faithfully recreate the conditions at the SLS interface during tunnelling by incorporating such key features as: discrete lubricant injection, large uni-directional shear strains, variable normal stress, and the creation of an overcut at the interface. The apparatus has been used to complete a test program examining the influence of these factors on the SLS interface conditions during tunnelling in sand. To guide this experimentation, an elemental study has been completed to examine the salient properties of common tunnelling lubricants and explore their interaction with sand in isolation.

The findings from the laboratory experimentation and SLS interface behaviours observed during field monitoring are then applied in the development of a new conceptual model of the SLS interface during tunnelling, from which an empirical model of friction prediction is derived that predicts interface friction in different ground conditions during tunnelling. Using this new understanding of the mechanics of the SLS interface, methods to minimise interface friction are also proposed.

Acknowledgements

First and foremost, I would like to thank my supervisors Brian Sheil and Byron Byrne. Their patient supervision, guidance, and encouragement have been indispensable throughout this project. I must also thank them both for setting me on this path from during my undergraduate studies, for they offered me the opportunity of a summer placement with Ward and Burke sinking shafts in Blackpool in 2015.

I must thank the multiple individuals within Ward and Burke in the UK, Ireland and Canada who have tolerated my persistent emails and requests for information. Particular thanks must go to those involved in the field monitoring projects, as they were particularly accommodating of my presence on active tunnelling sites. Finally to Michael Ward, for offering this research opportunity to me, and providing boundless energy and stimulating conversation to drive it forward.

Within the University engineering department I must thank Clive Baker for providing practical advice, high quality fabrications, and cheery conversation during long days in the laboratory. A special mention must also be made to Alison May and the Stores team, who have negotiated a barrage of orders and deliveries from suppliers outside of the normal university systems. To those in Room 11 and the FOCUS research group, I must thank you all for your friendship during the course of my time in Oxford.

I wish to thank my friends and family for their unbridled support and encouragement over the years. Finally, I must thank my partner Lulu, for your unbreakable tolerance has kept me on an even keel throughout.

Contents

1 Research introduction and objectives **1**
- 1.1 Introduction . . . 1
- 1.2 Current practice . . . 4
  - 1.2.1 Design of jacking pipes . . . 4
  - 1.2.2 Soil-lubricant-structure interface friction . . . 5
- 1.3 Research objectives and structure . . . 8
- 1.4 Industry collaboration . . . 12

2 Literature review **14**
- 2.1 Introduction . . . 14
- 2.2 Soil-structure friction . . . 14
- 2.3 Normal stress calculation and overcut pore pressure . . . 15
- 2.4 Interface friction in stable bore conditions . . . 17
- 2.5 Bentonite lubricants . . . 18
  - 2.5.1 Bentonite structure . . . 18
  - 2.5.2 Shear behaviour and thixotropy . . . 19
  - 2.5.3 Temperature . . . 21
  - 2.5.4 Additives . . . 21
- 2.6 1989 - 2006 research program . . . 22
  - 2.6.1 Introduction . . . 22
  - 2.6.2 PJA Phase 1 . . . 22
  - 2.6.3 PJA Phase 2 . . . 22
  - 2.6.4 Loughborough study . . . 24
  - 2.6.5 PJA Phase 3 . . . 25
  - 2.6.6 PJA Phase 4 and further PJA research . . . 25
- 2.7 Filter cake formation . . . 26
- 2.8 Analogies to diaphragm wall excavation . . . 29
- 2.9 Influence of lubrication on sliding friction . . . 32
- 2.10 Field studies . . . 33
- 2.11 Summary of gaps in current literature . . . 38

3 Experimental methods **40**
- 3.1 Overview of field studies . . . 40
  - 3.1.1 Introduction . . . 40
  - 3.1.2 Castlerigg tunnel drive . . . 40
  - 3.1.3 Castlerigg instrumented tunnel pipe . . . 42
  - 3.1.4 Putney tunnel drive . . . 45
  - 3.1.5 Putney instrumented tunnel pipe . . . 46
  - 3.1.6 Historical drive database . . . 49
- 3.2 Laboratory elemental lubricant testing . . . 52
  - 3.2.1 Scope of parametric study . . . 52
  - 3.2.2 Sand selection . . . 52
  - 3.2.3 Selected lubricants and additives . . . 53
  - 3.2.4 Sample preparation . . . 54
  - 3.2.5 Test methodologies . . . 55
- 3.3 Shear box apparatus . . . 59
  - 3.3.1 Apparatus overview . . . 59
  - 3.3.2 Test procedure . . . 60

3.4 Permeameter apparatus . . . 61
3.4.1 Apparatus overview . . . 61
3.4.2 Sample preparation . . . 63
3.4.3 Test procedure . . . 67

4 Field study results **69**
4.1 Analysed tunnel drives . . . 69
4.2 Tunnel advance rates . . . 70
4.3 Axial force measurement . . . 73
4.4 Interface friction . . . 79
4.5 Local interface stress sensors . . . 87
4.6 Local overcut pressure monitoring . . . 89
4.7 Distributed overcut pressure monitoring . . . 94
4.8 Local overcut stability . . . 96
4.9 Temperature . . . 98
4.10 Summary of field studies . . . 100

5 Lubricant testing results **103**
5.1 Testing overview . . . 103
5.2 Viscosity and filtration testing . . . 104
5.2.1 Exemplar baseline mix results . . . 104
5.2.2 Compensation of temperature effects . . . 105
5.2.3 Effect of lubricant type . . . 107
5.2.4 Effect of pressure . . . 108
5.2.5 Effect of mix ratio . . . 109
5.2.6 Effect of additives . . . 110
5.3 Consolidation shear box testing . . . 113
5.3.1 Exemplar calculations . . . 113
5.3.2 Effect of consolidation pressure . . . 115
5.3.3 Effect of mix ratio . . . 117
5.3.4 Water content - shear strength relationship . . . 118
5.4 Permeameter testing . . . 119
5.4.1 Exemplar calculations . . . 119
5.4.2 Typical results . . . 121
5.4.3 Effect of lubricant type . . . 127
5.4.4 Effect of pressure . . . 128
5.4.5 Effect of mix ratio . . . 131
5.4.6 Effect of additives . . . 132
5.4.7 Filter cake water content . . . 134
5.4.8 Filter cake penetration resistance . . . 136
5.5 Summary of lubricant testing . . . 137

6 Soil-lubricant-structure interface apparatus development **140**
6.1 Introduction . . . 140
6.2 Apparatus design . . . 140
6.2.1 Chamber construction . . . 140
6.2.2 Test piece construction . . . 144
6.2.3 Test piece interface . . . 146
6.2.4 Actuation system . . . 148
6.3 Data acquisition and control system . . . 150
6.4 Lubrication system . . . 153

6.5 Lubrication rate calculation . . . 154
6.6 Total stress control . . . 155
6.7 Contact stress sensors . . . 156
6.8 Sand sample preparation . . . 158
6.9 Summary . . . 160

7 Soil-lubricant-structure interface apparatus results 162
7.1 Introduction . . . 162
7.1.1 Testing objectives . . . 162
7.1.2 Test structure . . . 164
7.1.3 Chapter structure . . . 169
7.2 Commissioning results . . . 169
7.2.1 Chamber deformations . . . 169
7.2.2 Chamber wall friction . . . 170
7.2.3 Concrete interface friction . . . 171
7.2.4 Apparatus axial friction . . . 172
7.3 Sources of uncertainty . . . 173
7.4 Unlubricated interface friction . . . 176
7.5 Influence of initial lubricant injection . . . 178
7.5.1 Effect on local stress . . . 178
7.5.2 Effect on global friction . . . 180
7.6 Influence of intermittent lubricant injection . . . 183
7.7 Influence of overcut . . . 186
7.8 Influence of stoppages . . . 190
7.8.1 Stoppage testing objectives . . . 190
7.8.2 Intra-stoppage visual observations . . . 191
7.8.3 Intra-stoppage stress measurements . . . 195
7.8.4 Effect on post stoppage global friction . . . 196
7.8.5 Effect on post stoppage local friction . . . 200
7.9 Post-test observations . . . 202
7.9.1 Vertical Bentonite penetration . . . 202
7.9.2 Infiltration zone water content . . . 204
7.9.3 Interface condition . . . 205
7.10 SLS interface testing summary . . . 206

8 Results discussion and soil-lubricant-structure interface friction model development 210
8.1 Introduction . . . 210
8.2 Results discussion . . . 210
8.3 SLS interface model . . . 214
8.3.1 Form of model . . . 214
8.3.2 Interface friction calculation . . . 215
8.3.3 Stoppage induced variations . . . 218
8.3.4 Model application procedure . . . 219
8.3.5 Model and procedure validation . . . 222
8.4 Friction increase mitigation methods . . . 226
8.5 Summary . . . 227

9 Conclusions 229
9.1 Introduction . . . 229
9.2 Key contributions . . . 229

9.3 Key recommendations for industry practice 233
9.4 Recommendations for future research 234
9.5 Concluding remarks 236

Bibliography **237**

Appendix A Castlerigg tunnel drawings **245**

Appendix B Putney tunnel drawings **248**

Nomenclature

Abbreviations of common names, components and sensors

LM	Linear model
API	American Petroleum Institute
BSI	British Standards Institution
BTF	Ball transfer unit
CSOs	Combined sewer overflows
DC	Direct current
E	East
EPB	Earth pressure balance
FBG	Fibre Bragg grating
FE	Finite element
FRC	Fibre reinforced concrete
FRP	Fibre reinforced polymer
HK	Herrenknecht
HZ	Hydraul-Ez
ID	Internal diameter
IJS	Intermediate jacking stations, or inter-jacks
IP	Instrumented pipe section
ISO	International standards organisation
LC	Load cell
LPM	Litres per minute
N	North
NBR	Nitrile Rubber
NE	North east
NI	National Instruments
Nr	Number
NW	North west
PJA	Pipe Jacking Association
PT	Pressure transducer
PUTEF	Putney embankment foreshore
RC	Steel bar reinforced concrete
rpm	Revolutions per minute
S	South

SE	South east
SLS	Soil Lubricant Structure
SW	South west
TBM	Tunnel boring machine
TG	Tunnel Gel Plus
TP	Test piece
UPS	Uninterruptable power supply
VC	Vitrified clay
VWS	Vibrating wire strain gauges
W	West
WB	Ward and Burke Construction LTD.
WC	Water content

Abbreviations of test stages and conditions

C	Changeover stage
CI	Confidence interval
Cl	Class of test stage
FC	Filter cake type
FP	Filter cake - pipe contact
L_c	Continuously lubricated advance
L_i	Intermittently lubricated advance
L_u	Unlubricated advance
LP	Lubricant - Pipe contact
S	Setup phase
SI	Slurry infiltration type
SP	Soil - pipe contact
ST	Stoppage stage

Material parameters, factors and constants

α	Adhesion coefficient
α_f	Coefficient thermal expansion fibre (fibre optic sensing)
α_s	Coefficient thermal expansion substrate (fibre optic sensing)
δ_0	Apparent displacement for zero consolidation
γ	Soil bulk unit weight
γ'	Effective soil unit weight
γ_L	Lubricant unit weight
γ_w	Water unit weight

γ_{ck}	Partial factor for concrete strength
κ	Flow consistency index
ν	Flow behavioural index
ν_a	Apparent viscosity
ν_p	Plastic viscosity
ν_s	Poisson's ratio of soil
ν_v	Dynamic viscosity
ϕ	Soil friction angle
ψ	Soil dilation angle
ρ	Density
C	Rotor - bob factor (viscometer testing)
c'	Effective soil cohesion
C_a	Additive Concentration
C_U	Coefficient of Uniformity
c_v	Consolidation coefficient
C_Z	Coefficient of curvature
D_r	Relative density
D_{10}, D_{50}, D_{90}	Soil particle size
e	Void ratio
E_p	Elastic modulus of tunnel pipe
E_s	Elastic modulus of soil
f	Filtration rate gradient
f	Spring factor
F_{ck}	Concrete compressive strength
g	Gravitational constant
G_s	Particle specific gravity
h	Empirical factor
K	Permittivity
k	Permeability
k	Sensitivity to mechanical strain (fibre optic testing)
K_0	Coefficient of lateral earth pressure at rest
k_1, k_2, k_3	Viscometer apparatus constants
K_P	Coefficient of passive lateral earth pressure
M	Mix ratio (water/Bentonite by weight)
R_a	Roughness of surface
S	Speed factor
S_1	Sensitivity to temperature coefficient (fibre optic testing)
S_2	Sensitivity to temperature coefficient (fibre optic testing)

t_{90}	Time to 90% consolidation
u	Pore water pressure
W	Weight
w_p	Pipe of tunnel pipe per linear metre
Y_p	Plastic yield point

Geometric parameters

Å	Angstrom
δ_h	Horizontal displacement
δ_v	Vertical displacement
λ	Wavelength
Φ	Pipe contact angle
A_c	Column Area
A_p	Area of packers between pipes
A_w	Wall cross sectional area
B	Width, or 1/2 Terzaghi soil width
b	Contact width
C_e	Elastic analysis parameter
D_I	Internal pipe diameter
D_O	External pipe diameter
D_{TBM}	TBM diameter
H	Cover to pipe crown, sample height
H_{DR}	Drainage length
k_d	Elastic analysis parameter
L	Length
n	Number
N_i	Stoppages per i m advanced
R_n	Normalised roughness parameter
t_w	Pipe wall thickness
V	Volume
X	Depth below soil surface
x	Distance or position
x_s	Chainage at stoppage
x_{ch}	Axial position within test chamber
y_{ch}	Lateral position within test chamber

Force, stress and general parameters

ΔP	Difference in total jacking force
δ	Interface friction angle
δ_w	Wall friction angle
δ_G	Global (average) interface friction angle
ϵ	Strain
ϵ_m	Mechanical strain
γ_r	Shear rate
μ	Interface friction coefficient
μ_2	Rolling resistance coefficient
ϕ	Dial reading (viscometer testing)
σ_N	Normal stress
σ'_N	Effective normal stress
σ'_v	Vertical effective stress
τ	Shear stress
τ_0	Yield stress
a, b, c, d	Equation fitting parameters
F	Interface friction force
F_a	Actuation force
F_{e1}	Entry seal resistance
F_{e2}	Exit seal resistance
N	Normal force
n'	Effective normal contact stress
P	Total jacking force
p	Axial stress across an interface
p	Pressure
P_a	Overcut pressure
P_r	Penetration rate
Q	Flow rate
q_c	Tip resistance (CPT testing)
R	General reading value
R	Tunnel boring machine face resistance
s	Second
T	Temperature
T	Traction force
t	Time
X_c	Normalised tip resistance

Common subscripts, superscripts, prefixes and diacritics

$\overline{X}$	Mean average value of X
X_{10m}	Value of X after 10 minutes
X_{10s}	Value of X after 10 seconds
$X_1, X_2, etc.$	Relating to location 1, 2, etc. of X
X_ν	Relating to viscosity
X_{cs}	Critical state value of X
X_c	Corrected value of X (to reference conditions)
X_F	Relating to filter cake - pipe contact properties
X_{inf}	X at infinity
X_{IP}	X at the instrumented pipe location
X_i	X at value 'i', typically location or rate
X_L	Relating to lubricant - pipe contact properties
X_{max}	Maximum value of X
X_{min}	Minimum value of X
X_{Peak}	Peak Value of X
X_p	Relating to pressure of X
X_{ref}	Reference value of X
X_S	Relating to soil - pipe contact properties
X_s	Stoppage related value of X
X_{TP1}, X_{TP2}	Relating to Test Piece 1, 2, etc.
X_t	X at time 't'

1 | Research introduction and objectives

1.1 Introduction

Continuing global trends towards urbanisation, exacerbated by more variable weather patterns, are increasing the demands on municipal services throughout the world. For example, the 2020 UK census showed an increase in urban populations of 6.6% in the preceding nine years (Dept. for Environment Food and Rural Affairs (2021)), whilst rainfall in the decade to 2020 was 4% higher than the 1981-2010 average (Kendon et al. (2021)). This increased stress on urban infrastructure systems, coupled with increasing environmental awareness of issues such as river pollution, is driving unprecedented demand for upgrade or replacement of existing assets. The installation of additional services through densely populated subterranean landscapes poses significant challenges to designers who aspire to balance the substantial environmental and financial costs for the bodies responsible.

Projects routinely require small diameter conduits to convey cables, water, sewerage, and other services along difficult trajectories whilst minimising surface disruption. Trenchless installation techniques provide significant benefits compared to traditional (open cut) methods, namely: a reduced above ground footprint, fixed site locations, and an ability to cross beneath railways, roads, rivers, and other obstacles without disruption. The importance of the tunnelling industry to the global economy is evidenced by its value of €86 billion in 2016, with growth of around 7% per year forecast, the International Tunnelling and Underground Space Association (2016).

Microtunnelling is an increasingly popular means of trenchless installation for tunnels of between 600 mm and 3500 mm internal diameter (ID) (Dean and Goodwin (2021)) and drive lengths of less than 1500 m (typically). Pipe-jacking is a specific form of microtunnelling, shown in Figure 1.1, where a pipeline is driven between a launch and reception excavation. A jacking

frame and guide rails are installed between a 'head wall' and a heavily reinforced 'thrust wall'. To create the tunnel, controlled excavation is conducted by a tunnel boring machine (TBM) whilst the jacking frame applies an axial load to the pipe string behind the TBM to push the TBM and pipes through the ground. Various methods of excavation exist, such as the use of an open face and back actor in dry and stable ground types or slurry shield tunnelling in more difficult ground, as depicted in Figure 1.1. The TBM excavation diameter is slightly greater than that of the pipes so that an overcut is formed around the pipe string. This is filled with a lubricant, typically consisting of a Bentonite clay, which is intended to reduce interface friction between the pipe string and surrounding soil.

Once the TBM has been jacked forward (i.e., the jacking rams are fully-extended) the rams are retracted and a new pipe is lowered into position on the guide rails in the launch excavation. This cycle is termed an 'advance' and is repeated as the tunnel length increases until the TBM excavates into a reception excavation. The TBM is then extracted, and all services are stripped from the inside of the tunnel for reuse. Finally, the tunnel is thoroughly cleaned, and any ancillary works are completed prior to service use.

A key consideration for the design and construction of a pipe-jack is the total force P required to advance the tunnel. This is composed of the TBM face resistance R and the frictional force acting on the exterior surface of the pipe string F. The limits of the allowable thrust determine the maximum length of drive that can be completed before intermediate

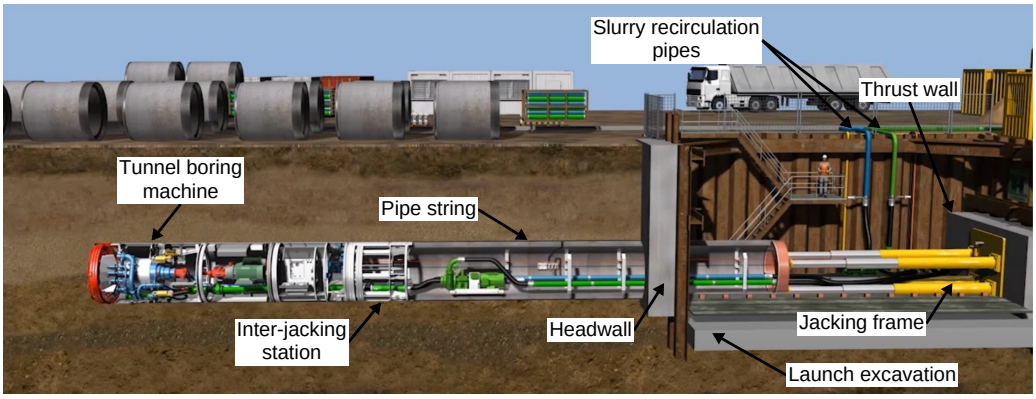


Figure 1.1: Slurry shield pipe-jacking overview schematic highlighting key features, after Herrenknecht AG (2019).

jacking stations (IJS) are required. This limit is defined by the minimum capacity of: (a) the thrust wall, (b) the jacking frame, or (c) the jacking pipes. IJSs, as shown in Figure 1.2, provide additional thrust from within the pipe-string. These allow the maximum thrust to be increased by using the interface friction behind the IJS to provide the reaction to the advancing section in-front. A key challenge associated with the use of IJS is that the tunnel designer needs to estimate (in advance of tunnel construction) how many stations might be required within the drive in a reasonable worst-case scenario.

For long drives, the total jacking force required to construct the tunnel is dominated by F as the surface area of the interface is orders of magnitude larger than the face area. Quantifying the frictional resistance at the interface is therefore essential for the prediction of pipe-jacking jacking force. However, accurate prediction of jacking forces is difficult given that significant fluctuations are possible, often by an order of magnitude, within a short time period. The forces are dependent on a large number of lubricant parameters, including: pressure, make-up, volume delivered, coverage, as well as tunnel parameters, such as: alignment curves, steering deviations, advance speed, and the ground type being tunnelling through. Transient factors, such as stoppages, have also been shown to have a large effect. For example, Pellet-Beaucour et al. (2002) report increases in friction of up to 22 kPa after a single overnight stoppage. As a result of this variability, tunnel design is often overly-conservative resulting in redundant inter-jack stations, or shorter drive lengths.

These risk mitigations increase both the financial and environmental costs of the pipe-jacking method, as additional excavations increase the above ground footprint and embodied carbon of the tunnelling schemes. The installation and decommissioning of IJS also increase the duration of tunnel drives and introduce hazardous confined space working when removing the rams from within the tunnel. These factors reduce the appeal of the pipe-jacking method to clients, despite its potential benefits.

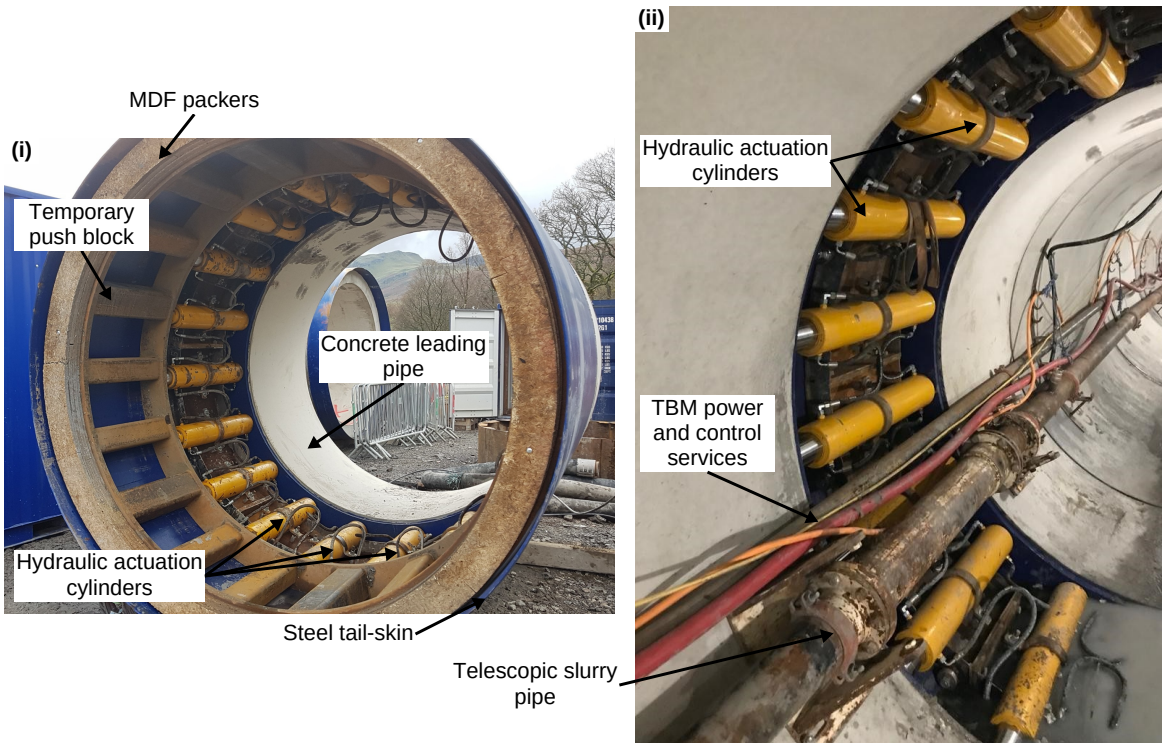


Figure 1.2: Example intermediate jacking station: (i) leading pipe before installation and (ii) as installed within the pipe string.

1.2 Current practice

1.2.1 Design of jacking pipes

There are many types of jacking pipe, such as: steel bar reinforced concrete (RC), fibre reinforced concrete (FRC), fibre reinforced polymer (FRP), or vitrified clay (VC). The design of RC pipes is considered here as these are the pipes predominantly used in pipe-jacking. In the authors experience this is due primarily to industry momentum and risk aversion, as supply frameworks are already established for RC tunnel pipes and tunnelling contractors have experience in their use and limitations.

Within the scope of this research, the salient output of pipe design process is the axial capacity, as this dictates the maximum jacking force the pipe may be subjected to. Commercial design of pipes in the UK is governed by *BS EN 640* and *BS EN 641* British Standards Institution (1995a,b), the British Tunnelling Society: *Specification for tunnelling* (British Tunnelling Society (2010)), and the UK Pipe-Jacking Association's: *Guide to best practice* (Pipe Jacking Association (1995)). The latter adopts the "linear stress approach" updated more recently in

the Concrete Pipe Association of Australasia *Design Manual* (Concrete Pipe Association of Australasia (2013)) for the calculation of the axial capacity of the pipe and shown in Figure 1.3.

The design calculations use a closed-form expression to calculate the maximum allowable force P_{max} in a pipe joint. The contact stress between the pipes varies from zero at one side linearly to a maximum of p at the other. This profile allows for small deviations in the alignment of the drive, caused by steering deviations of the TBM, to be accounted for without direct calculation. To reduce the stiffness of the joint, and therefore facilitate small angular deflections accommodated by the stress profile, 'packers' are fixed between the pipes to enable load transfer without a direct concrete-concrete connection. These are made from compressible material, typically 25 mm thick medium density fibreboard (MDF), and their low modulus allows the load to be distributed across the joint. P_{max} is calculated as:

$$P_{max} = 0.5 A_p . p \tag{1.1}$$

where A_p is the cross-sectional area of the packers between pipes and p is determined from the concrete strength, F_{ck}, reduced by a partial factor γ_{ck} as follows:

$$p = \frac{F_{ck}}{\gamma_{ck}} \tag{1.2}$$

For curved drives, additional reductions are made to account for the increased angle at pipe joints, as this leads to smaller load transfer areas. Standard tables are provided in Pipe Jacking Association (1995) and Concrete Pipe Association of Australasia (2013) which detail the reduction in axial capacity for a given pipe diameter and joint angle caused by the curve, as well as the closed-form calculations from which they are derived.

1.2.2 Soil-lubricant-structure interface friction

Although a number of different theories have been proposed in the literature, there is currently no universally accepted theory for the calculation of interface friction forces at the soil-lubricant-structure (SLS) interface during a tunnel drive. An example of current practice

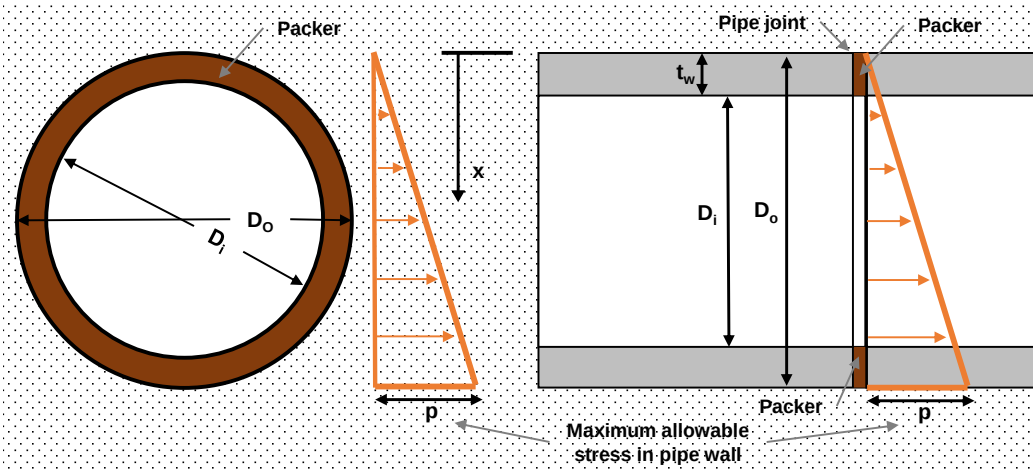


Figure 1.3: Key parameters of the "linear stress approach" used to calculate the axial capacity of pipe-jacked tunnel drives, adapted from Concrete Pipe Association of Australasia (2013). The stress across the pipe joint linearly increases with the distance x, from zero at one edge of the pipe to a maximum of p at the opposing side.

is provided by the French Society for Trenchless Technology (Comité Français des Travaux sans Tranchée (2006)) which presents a comparison between pipe-soil frictional stresses monitored from drives in various ground conditions. These are then compared to predictions determined using two different approaches: (i) Terzaghi's 'trap-door' model (Terzaghi (1943)) to calculate stresses around the pipe and (ii) frictional sliding of the pipe under its own weight only. These approaches represent the two extremes of tunnel stability: (i) a fully-collapsed bore where full pipe-soil contact is achieved, and (ii) a fully-stable bore where the only contact is due to the self-weight of the pipe. These methods provide significantly different friction values (up to an order of magnitude) and the values to be adopted are left to the tunnel designer to decide.

Different tunnelling contractors have, therefore, adopted different approaches to design, based on their accumulated site experience. Some guidance has been provided by the PJA and the Health and Safety Executive (Health and Safety Executive et al. (2006)) which provides achievable, "safe", drive lengths for different diameters and pipe-jacking methods. Contractors tend to rely heavily on previous experience to estimate friction; for example, some contractors compare basic data from drives of similar diameters in similar ground conditions, whilst engineering judgement still plays a pivotal role. There is, therefore, a requirement for a unified

design approach to be adopted across the industry.

Effective lubrication of the SLS interface is recognised as the key factor to reduce friction during pipe-jacking. This technology was in its infancy during previous research programs, particularly those undertaken by the PJA, and as such practice has moved on significantly. Some industry guidance is provided by different equipment manufacturers for their specific systems of lubrication. This research focusses on the systems supplied by Herrenknecht (HK) as (anecdotally) these appear to be the most commonly used system in western tunnelling. Equipment from other providers typically works in a similar way and are likely comparable, although they will not be discussed explicitly herein.

Figure 1.4 presents an overview of the Herrenknecht lubrication system with key components identified. The system is controlled from the TBM control container which sends signals to the different lubrication stations distributed along the pipe string. Each of these lubrication stations connects to 3 ports which pass through the pipe to convey the lubricant into the overcut. In some instances, an addition lubrication ring is built into the rear of the TBM and used to complete the initial filling of the overcut, with the intention of preventing initial collapse before filling. Bentonite is mixed and stored in tanks at the launch site, which allow for hydration of the clay to occur before it is pumped into the tunnel overcut.

The lubrication system is controlled in one of two modes:

1. **Time** - in this mode each port in the pipe string is opened in turn for a specific duration.
2. **Volume** - in this mode the system calculates a theoretical volume of lubricant that should be delivered to each 1 m section of tunnel based on the ground type (sand, gravel, rock, etc.) and the total lubricant volume pumped into that section. It then deduces the lubrication station with the smallest proportion of this value and lubricates this section until the theoretical value is reached. This process is then repeated for the duration of the tunnel drive.

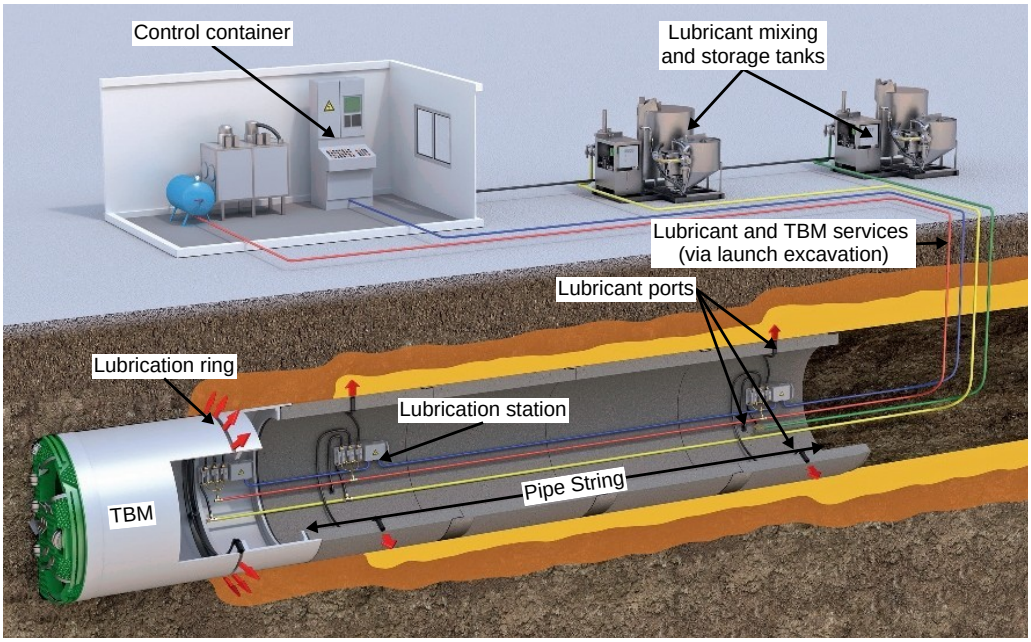


Figure 1.4: Components of the Herrenknecht tunnel lubrication system, after Praetorius and Schößer (2017). Note that the launch excavation is omitted and services are shown indicatively.

Tunnels are typically lubricated with Bentonite clays, although sometimes drives are lubricated with other polymer-based solutions or water alone. Bentonite clays have important properties desirable for a lubricant. Therefore, a detailed understanding of the properties of these clays, and their interactions with the surrounding ground, is essential in predicting the SLS interface friction during pipe-jacking and improving this understanding is a main objective of this research.

1.3 Research objectives and structure

The primary objective of this research is to reduce the uncertainty surrounding SLS interface mechanics during pipe-jacking. Insights into the sources of friction and their development during tunnel drives will reduce over-conservatism during design, enabling longer drive lengths with fewer inter-jacks, thereby reducing the associated disruption and environmental impact. This research will focus on granular soils (primarily sands), as these are the most problematic in practice, using a combination of field studies, elemental laboratory testing of the Bentonite slurry and elements of the SLS interface, and scale testing of the SLS interface under field conditions in the laboratory. A summary of the key objectives and research areas are shown in

Figure 1.5.

To achieve these objectives, the research is presented in the following order:

Chapter 2 - Literature review

Literature pertinent to this research is reviewed in this chapter. Firstly, theories of circular tunnel overcut stability are examined, providing detail on the support function of lubricants used in tunnelling. Secondly, previous research around the SLS interface is presented, using research conducted by various groups as the pipe-jacking method began to gain popularity between 1990 and 2010. This will focus on Bentonite based proprietary products, as these are the focus of this research. More modern lubrication methods and research examining their effectiveness are then introduced. Papers pertaining to friction changes during stoppages are also reviewed, to consolidate the available literature into a suitable base for this project. Finally, a review is also conducted concerning additives and their time-dependent properties. Polymers are considered here as additives to the Bentonite base lubricant, and their effects on the salient properties are reviewed.

Chapter 3 - Experimental methods

This chapter outlines the methodology used to collect and interpret data from field and laboratory sources. The two instrumented tunnel drives completed as part of this research are introduced, as well as the methods developed to record the interface conditions around them during installation. Sources of commercially available data are then explored, before the available information is collated into a database for further analysis.

The chapter then presents the methods used to assess the lubricants within the laboratory, first introducing the sand, Bentonites, and additives used for the study, before introducing the industry standard testing methodologies used to quantify the basic lubricant properties. A consolidation shear box and permeameter apparatus are then introduced and the research objectives of each piece of apparatus discussed. Finally, calculations used for determining key

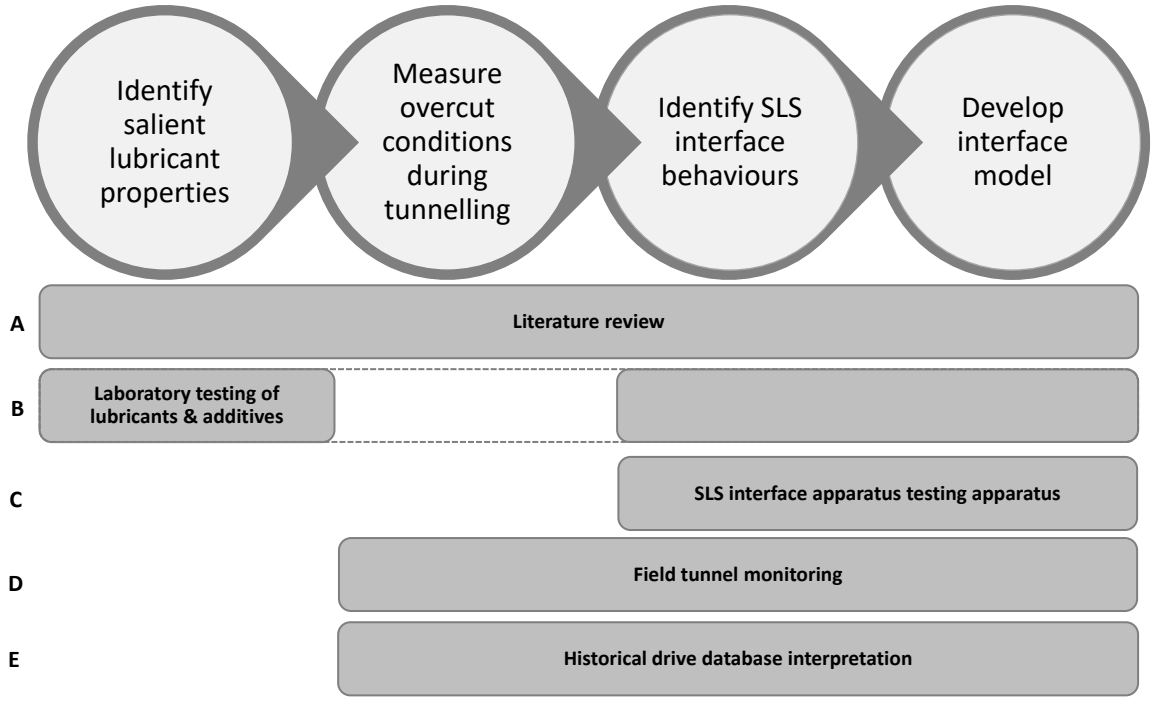


Figure 1.5: Summary of the research objectives and five key research areas (A-E). Research areas are aligned vertically with the objectives they contribute towards.

lubricant parameters are presented for use in the subsequent chapters.

Chapter 4 - Field results

This chapter details the observations from the instrumented tunnel drives and industry case histories. Initially, the tunnel drives selected from the database for analysis are introduced. The salient parameters for these drives, such as: advance rates, total jacking force, and interface friction are compared between the different drives and ground conditions. Additional data from the instrumented tunnel drives is then introducd, to provide insight into SLS interface conditions and industry practice above that available in the historical drive data.

Chapter 5 - Elemental lubricant testing results

The results from the laboratory testing of the lubricants and additives are presented in this chapter. Initially, the influence of temperature, concentration, and additive inclusion on yield stress, thixotropy, viscosity, and filtration rate of lubricants are presented from the filter press and viscometer apparatus. The results from the consolidation shear box are then presented, with the effects of consolidation pressure and lubricant mix ratio on the resulting shear strength

of the consolidated filter cakes identified. The permeameter testing exploring the influence of: mix ratio, pressure, additive inclusion, and lubricant type on the infiltration distance, filtration rate, pressure distribution, permeability, and resulting sample water contents are explored. The key findings of this study are then summarised and the implications for the SLS interface are discussed.

Chapter 6 - Soil-lubricant-structure interface apparatus development

This chapter details the development of a novel apparatus used to examine SLS interface in this research. Initially, the apparatus objectives and key constraints for the design are detailed. The apparatus systems are then discussed in detail, including the methods of boundary stress control, actuation, and sealing. The data acquisition and instrumentation systems used are also presented. These include the novel fibre optic contact stress sensors used in the apparatus and an overview of how the sensors function is provided. Finally, the sample preparation method is introduced and testing to demonstrate the consistency of the samples produced is discussed.

Chapter 7 - Soil-lubricant-structure interface apparatus results

The results from the SLS interface apparatus are presented in Chapter 7. First, the testing objectives and structure are described, followed by results from commissioning tests. The unlubricated interface conditions are established to provide baseline conditions for comparison to subsequent tests. The effects of lubricant injection, overcut inclusion, and stoppages of up to 60 hour duration on the SLS interface are then presented in detail. These are used to identify the mechanisms of friction generation at the SLS interface during tunnelling, and their magnitude, to provide input into the SLS interface model and friction mitigation strategies developed in Chapter 8.

Chapter 8 - Results discussion

This chapter discusses the results from the field monitoring in Chapters 4 and experimentation in Chapters 5 and 7. These data are used to develop a new model of the SLS interface

around tunnel during pipe jacking, which will capture the observed field behaviours and predict interface friction using simple input parameters. The method will also enable friction increases observed during stoppages in tunnelling to be predicted. Using the findings of the research methods for mitigating friction increases during tunnelling will also be proposed, for adoption by industry.

Chapter 9 - Conclusions

The final chapter of this thesis provides a summary of the key contributions of the work. It will also provide recommendations for changes to industry practice and highlight beneficial areas for future work.

1.4 Industry collaboration

This research has been sponsored by Ward and Burke Construction Ltd. (WB). Industry collaboration is essential for researching pipe-jacking operations. Monitoring of live tunnelling drives requires industry investment of both time and resources as the additional work required to create and install instrumented tunnel pipes is significant. The field studies conducted as part of this research were completed on WB tunnel drives and they have provided data from historical drives to form the drive database.

Their guidance has also been sought on key parameters are believed to influence the SLS interface as the parameters which can affect the SLS interface during tunnelling are too numerous to study in one research project. The output of these early consultations is summarised below:

- **Lubricants** - two of the most common lubricants used in industry, 'Tunnel Gel Plus' (TG) manufactured by Cebo Holland BV and 'Hydraul-ez' (HZ) produced by Cetco Minerals Technologies, will be the focus of the study in order to maximise the applicability of the results.
- **Lubricant additives** - again, two of the most common additives used in lubrication will

be examined, 'PAC-L' and 'TK60' produced by Halliburton and Mudtech Ltd. respectively. These are described as a filtrate reducer and viscosifier respectively and are added to Bentonite lubricants or can be mixed with water alone.

- **Mix design** - different lubricant mix designs are used in different ground conditions. WB recommended ratios (M) of between 14:1 and 24:1 (water/Bentonite by weight) are used in industry.

2 | Literature review

2.1 Introduction

In this chapter literature relevant to this research project is described. Basic friction theory is reflected on, before methods of assessing tunnel overcut stability are introduced. Previous research into pipe-jacking friction is then summarised, including the 1980 - 2006 PJA funded research program on which much of modern pipe jacking theory is based. Lubricants, typically Bentonite clays, used to reduce the friction and provide overcut stability during tunnelling are then introduced. Key properties and characteristics of Bentonite are reviewed, before the process of ground support through filter cake formation is explored. Recent studies of pipe-jacked tunnel drives from the UK, Ireland, China, and Japan are discussed. Relevant research from similar fields, such as oil well drilling and diaphragm walling, is also examined. Finally, a summary of gaps identified in current literature is presented, which this research aims to resolve.

2.2 Soil-structure friction

A simplified description of friction at the soil-pipe interface can be achieved using a sliding block analogy. An object exerting a normal force N (or contact stress σ_N) on a rough surface requires traction force T (or shear stress τ) to induce movement:

$$T = N\tan(\delta). \quad or \quad \tau = \sigma_N.\tan(\delta) \tag{2.1}$$

where δ is the interface friction angle. For a given total normal stress any pore water pressure u will reduce the effective stress on the interface as follows:

$$\sigma'_N = \sigma_N - u \tag{2.2}$$

If $\delta < \phi_{cs}$ (the critical state soil internal friction angle) shearing will occur at the interface, otherwise the shearing may occur in the soil. Noting that δ is dependent on the soil particle

size, Reilly and Orr (2017) characterise the δ - roughness relationship using the 'normalised roughness parameter' R_n, defined through:

$$R_n = \frac{R_{max}}{D_{50}} \tag{2.3}$$

where D_{50} is the mean particle size of the soil and R_{max} is the maximum variation in the height of the solid surface over a profile with length equal to D_{50}. Those authors demonstrated a linear relationship between the friction angle ratio ($\frac{\delta}{\phi_{cs}}$) and R_n. As ϕ_{cs} is constant for a given soil, density, and stress state, increasing the normalised roughness will increase the interface friction angle.

Staheli et al. (2006) also examined the effects of surface roughness on the interface friction. Five different pipe materials were examined: wet and dry cast RC, VC, polycrete, and FRP. The surface roughness of each was determined before being tested in a shear apparatus against two different sand types at normal stresses of 40 kPa to 120 kPa. Peak and residual interface friction angles were found to increase with surface roughness. Increasing normal stress or decreasing relative density decreased the peak interface friction angle δ_p, but had little effect on δ_{cs}.

2.3 Normal stress calculation and overcut pore pressure

The most common method for calculating the normal stresses acting on buried pipes is based on the trapdoor model (Terzaghi (1943)). The vertical effective stress at the pipe crown σ'_v is defined as:

$$\sigma'_v = H\frac{(\gamma' - \frac{c'}{B})(1 - e^{-K_0.\tan(\phi)\frac{H}{B}})}{K_0.\tan(\phi)} \tag{2.4}$$

where γ' is the effective soil unit weight, c' the effective soil cohesion, and K_0 coefficient of lateral earth pressure for the soil, and H the cover to the pipe crown. Finally, B is one half the 'silo' width for a given TBM diameter (D_{TBM}), as shown in Figure 2.1, and defined as:

$$B = D_{TBM}(\frac{1}{2} + \tan(\frac{\pi}{4} - \frac{\phi_{cs}}{2})) \tag{2.5}$$

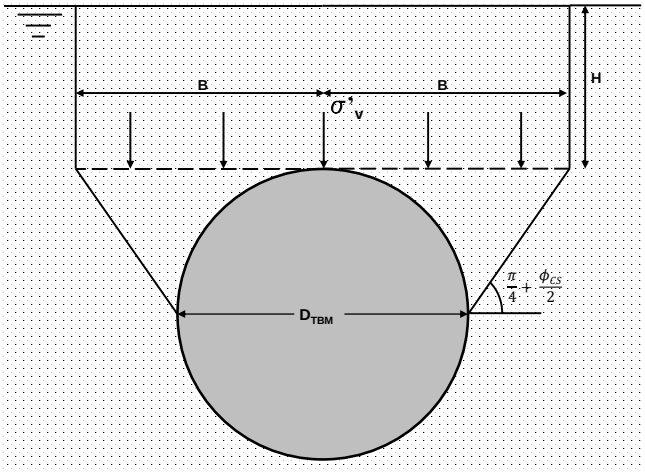


Figure 2.1: Terzaghi silo model, defining the vertical effective stress at the pipe crown σ'_v and silo width $2B$, for a soil of friction angle ϕ_{cs}, TBM diameter D_{TBM}, and cover H.

Atkinson and Potts (1977) developed closed-form upper and lower bound equations for the stability pressure (i.e., lubricant pressure) of shallow tunnels in dry granular soils based on plane strain centrifuge modelling of tunnel sections. During the tests, a 60 mm diameter tunnel surrounded with a fluid filled rubber membrane was accelerated to 75g to replicate the behaviour of a 4.5 m diameter tunnel in Earth's gravitational field. The fluid pressure within the rubber was reduced during the tests until a collapse of the tunnel bore was observed and the corresponding required support pressure was recorded.

Using this experimental data, a lower bound set of equations is defined to satisfy the soil stress state around the tunnel. Additional inputs for the equations are: D_O - the diameter of the tunnel pipe extrados, and K_p - the passive earth pressure constant. The equations then follow:

$$\frac{P_A}{\gamma.D_{TBM}} = \frac{1}{2(K_p-2)}\left(\left(\frac{D_{TBM}}{2(H+D_O)}\right)^{K_p-2}\left(3-\frac{4}{K_p}\right)-1\right) \tag{2.6}$$

and

$$\frac{P_A}{\gamma.D_{TBM}} = \frac{K_p}{(K_p^2-1)} \tag{2.7}$$

The upper bound mechanism is defined as a wedge of soil translating downward from the pipe crown, as shown in Figure 2.2. The wedge is formed of two tangents from the bore extrados

at an angle 2ψ, where ψ is the dilation angle of the soil. If the associated flow rule $\psi = \phi$ is assumed and the limit $\frac{2H}{D_{TBM}} \geq (\frac{1}{\sin(\phi)}) - 1$ is satisfied the peak of the failure wedge is below the ground and the P_a is calculated as:

$$\frac{P_A}{\gamma.D_{TBM}} = \frac{1}{4\cos(\phi)}\left(\frac{1}{\tan(\phi)} + \phi - \frac{\pi}{2}\right) \tag{2.8}$$

2.4 Interface friction in stable bore conditions

In cohesive or cemented soils, the tunnel bore can be considered intrinsically stable, i.e., no lubricant pressure is required to maintain stability. In this instance two general methods for calculating the contact stress have been reported. The first approach assumes that the tunnel-bore is filled with lubricant and the N is reduced by the buoyancy of the pipe (Sheil et al. (2016)). The effective normal contact force N' is calculated as:

$$N' = w_p - \rho_L.\pi\left(\frac{D_O}{2}\right)^2 \tag{2.9}$$

where ρ_L is the density of the lubricant and w_p is the weight of the pipe section per metre length.

The second approach assumes that the interface can be modelled as two concentric cylinders of different size. This approach was adopted by Milligan and Norris (1996), using elastic analysis from Young et al. (1976). First, the contact width b is given empirically by:

$$b = 1.6\left(N.k_d.C_e\right)^{\frac{1}{2}} \tag{2.10}$$

where $k_d = \frac{D_{TBM}D_O}{(D_{TBM}-D_O)}$, and $C_e = \frac{(1-\nu_s^2)}{E_s} + \frac{(1-\nu_P^2)}{E_P}$ in which E_s and E_p are the elastic moduli of the soil and pipe respectively, and ν_s and ν_p are the Poisson's ratios of the soil and pipe respectively. The normal contact stress is then calculated as:

$$\sigma_N = \frac{2N}{\pi.a}\left(1 - \frac{x^2}{a^2}\right)^{\frac{1}{2}} \tag{2.11}$$

where $a = b/2$ and x is the tangential distance from the centre of contact to the position of analysis, as defined in Figure 2.3. These equations are then used to calculate peak and average contact stress, from which the friction is determined using the sliding block analogy.

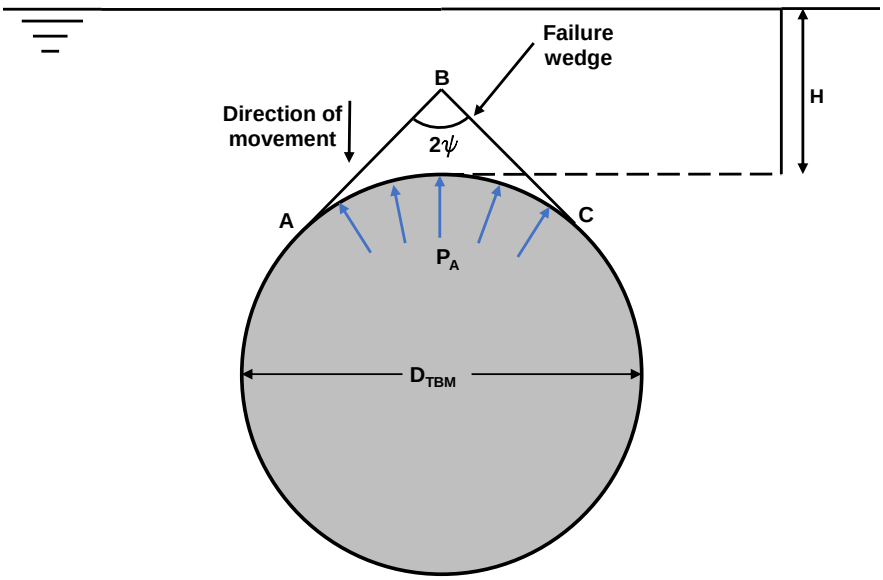


Figure 2.2: Upper bound collapse mechanism proposed in Atkinson and Potts (1977). The soil wedge A-B-C translates downwards against the overcut pressure P_A. A-B-C is defined by tangents to the bore diameter D_{TBM} at the angle 2ψ where ψ is the dilation angle of the soil.

2.5 Bentonite lubricants

2.5.1 Bentonite structure

Praetorius and Schößer (2017) identified the chemical stability of Bentonite clay mixtures, wide availability, low cost, and variable mechanical properties as the main reasons for adoption as lubricants in tunnelling. Inglethorpe et al. (1993) also discusses the sources and structure of Bentonite clays in detail. The clays are formed of minerals from the smectite group, predominantly montmorillonite. These minerals form microscopic plates which have a negative electrical charge on the face and positive charge on the edge. Figure 2.4 (i) shows a schematic of a single plate. The negative charge across the face of the plates is neutralised by *loosely-held* exchange ions, Figure 2.4 (ii). These are typically either Sodium (Na^{2+}) or Calcium (Ca^{2+}). Depending on which of these ions is dominant in the clay, it is commonly referred to as either a Sodium or Calcium Bentonite.

The process of dispersing the clay plates in water is called 'swelling'. When Bentonite undergoes swelling, the spacing between the crystalline layers (Figure 2.4 (ii)) can increase to

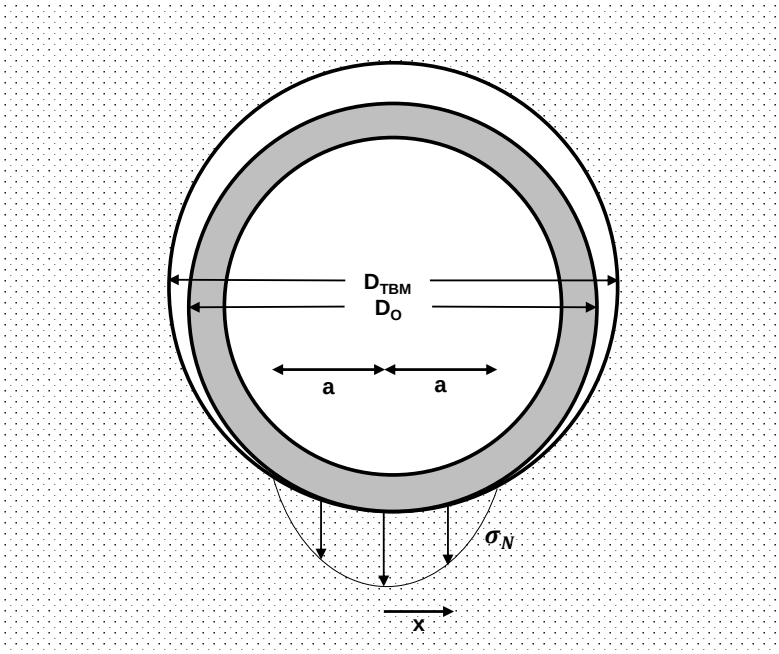


Figure 2.3: Contact stress distribution within a stable overcut, after Milligan and Norris (1996). The contact width $2a$, normal stress σ_N, distance from centre of contact x, and TBM and pipe diameter D_{TBM} and D_O are shown.

over 160 Å (Praetorius and Schößer (2017)). This causes the crystalline bonds between the clay plates to break down and the crystal decomposes to individual plates as the water/clay ratio increases. The plates reform into a loosely organised 'house of cards' arrangement after dispersal, as shown in Figure 2.4 (iii), which exhibits different properties to the mixture of plates and water alone.

The swelling potential is defined by Praetorius and Schößer (2017) as the ratio of water/clay which the clay can incorporate into its matrix. Those authors quote swelling potentials of up to 700% for Sodium Bentonites and 300% for Calcium. The ability of the clay to incorporate a greater degree of water into its structure enables properties such as yield point and viscosity to be tailored to suit user requirements. Therefore, the higher swelling potential of Sodium clays makes their use more common in tunnelling applications.

2.5.2 Shear behaviour and thixotropy

Bentonite clays exhibit shear thinning behaviour, i.e., their yield stress and viscosity are shear strain rate dependent, as well as thixotropy, where the characteristics of the Bentonite change with time after shearing ceases. Li et al. (2016) explored several rheological models to

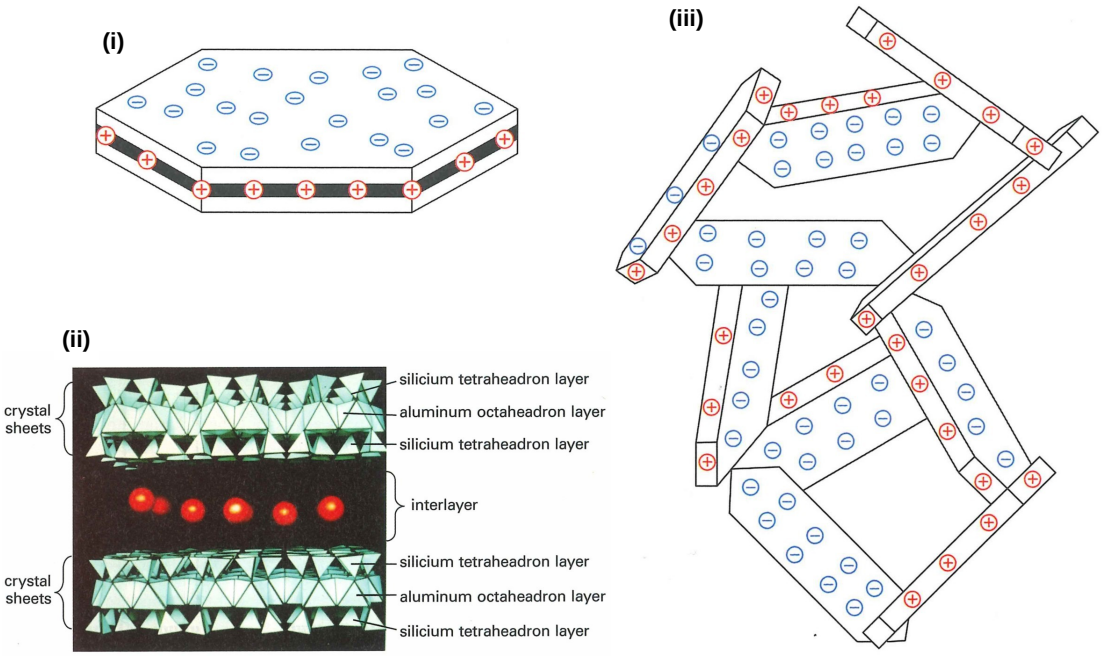


Figure 2.4: The structure of montmorillonite clay: (i) charge on clay plates, (ii) structure of plates and interlayer exchange ions and, (iii) 'house of cards' type plate arrangement, after Praetorius and Schößer (2017).

identify which best represented Bentonite behaviour. The Bingham model (Bingham (1916)) is commonly used, whereby τ increases linearly with shear rate and is defined as:

$$\tau = \tau_0 + \mu_p.\dot{\gamma} \tag{2.12}$$

where τ_0 is the yield stress, μ_p is the plastic viscosity, and $\dot{\gamma}$ is the shear rate. This equation assumes a linear relationship between shear rate and stress, whilst in practice the relationship is non-linear for Bentonite lubricants. Li et al. (2016) concluded, through comparison of the models to laboratory data, the Sisko (1958) model was the more accurate. This is a non-linear model of the form:

$$\tau = \mu_{\text{inf}}.\dot{\gamma} + \kappa.\dot{\gamma}^{\eta} \tag{2.13}$$

where μ_{inf} is the viscosity at an infinite shear rate, κ is the flow consistency coefficient, and η is the flow behavioural index, both of which are constants.

These models do not account for the transient change Bentonite properties which occur after a change in $\dot{\gamma}$. This transient behaviour is due to Bentonites reforming the 'house of cards' structure shown in Figure 2.4 (iii) once shearing ceases (Praetorius and Schößer (2017)).

The inter-plate bonds formed increase the yield stress of the Bentonite. When an applied shear stress exceeds the yield stress, the Bentonite yields at an elevated stress before reducing to a steady state value (such as those predicted by the Sisko or Bingham models).

2.5.3 Temperature

Studies on deep well drilling have explored influence of temperature variation on Bentonite behaviour. The trends identified are relevant to this research as they can be used to correct for temperature variations to standardise results. Studies, such as Mostafa et al. (2007), Vryzas et al. (2017), and Ahmad et al. (2018), have demonstrated temperature effects on different Bentonite mixtures between 24:1 (4 %) and 11.5:1 (8 %) concentration. Those authors found increasing temperature increases the apparent viscosity and filtration rate of the Bentonite. The plastic viscosity, yield point, and flow consistency index were found to reduce with increasing temperature. Vryzas et al. (2017) states that the relationship between viscosity and temperature is linear but dependent on shear rate, as at high shear rates the effect of temperature on viscosity is less than at low rates. Qualitatively, the relationships identified by those authors are anticipated to be true for all Bentonites, however, due to the proprietary nature of Bentonite products, the relationships will require quantification for the Bentonites used in this research.

2.5.4 Additives

Two common additives will be considered in this study following consultation with industry collaborators, PAC-L and TK60. PAC-L is defined by Heinz et al. (2004) as a "natural long chain cellulose polymer", whereas TK60 is defined by Al-Maamori et al. (2016) as an "anionic polyacrylamide suspension in a water-in-oil emulsion". Both Mostafa et al. (2007) and Li et al. (2016) discuss the relative effects of the two additives. The papers demonstrate that both additives increase lubricant viscosity whilst reducing the water filtration rate. The filtrate reducing effect of PAC-L is more pronounced than TK60, such that when used in combination the effect on filtrate reduction of TK60 is not observed. The opposite is true for the influence on viscosity. For example, Figure 2.5 shows the increase in viscosity, shear stress, and reduction in

filtration rate with increasing PAC concentration found by Li et al. (2016). Al-Maamori et al. (2016) also notes TK60's ability to inhibit the swelling of clay formations; noting a reduction in swelling of 90% using a TK-60-water mixture compared to water alone.

2.6 1989 - 2006 research program

2.6.1 Introduction

The UK Pipe-Jacking Association (PJA; Pipe Jacking Association (2022)) conducted an extensive research program into pipe-jacking between 1989 and 2006 primarily at the University of Oxford, which was complemented by an additional study at Loughborough University. More recently, the PJA has sponsored research into the optimisation of slurry separation techniques, although these will not be discussed further herein. The PJA research program was split into four phases: phase one focussed on simulating tunnel pipe loading during jacking; phases two and three explored frictional effects on the pipe string (including field studies); whilst phase four involved laboratory testing to explore the effects of polymer lubricants on friction in clay soils. Salient findings from the program are summarised in the following sections.

2.6.2 PJA Phase 1

The first phase of the research program is reported in Ripley (1989). This phase was laboratory based, focussing on the structural performance of the jacking pipes and their axial capacity under different load conditions. Whilst not directly related to this research, it was noted that during laboratory scale testing of unlubricated pipes in granular soils, the interface friction angle, and therefore the interface friction, depended on the normal stress across the soil-structure interface, as discussed in Section 2.2.

2.6.3 PJA Phase 2

Norris (1992) conducted an extensive field monitoring program, which included the development of instrumented pipe sections (IPs). The monitoring identified large normal contact stresses, and large shear stresses, during tunnelling in over-consolidated clay soils. It was concluded that the elastic unloading of the soil post excavation caused the soil to close onto the

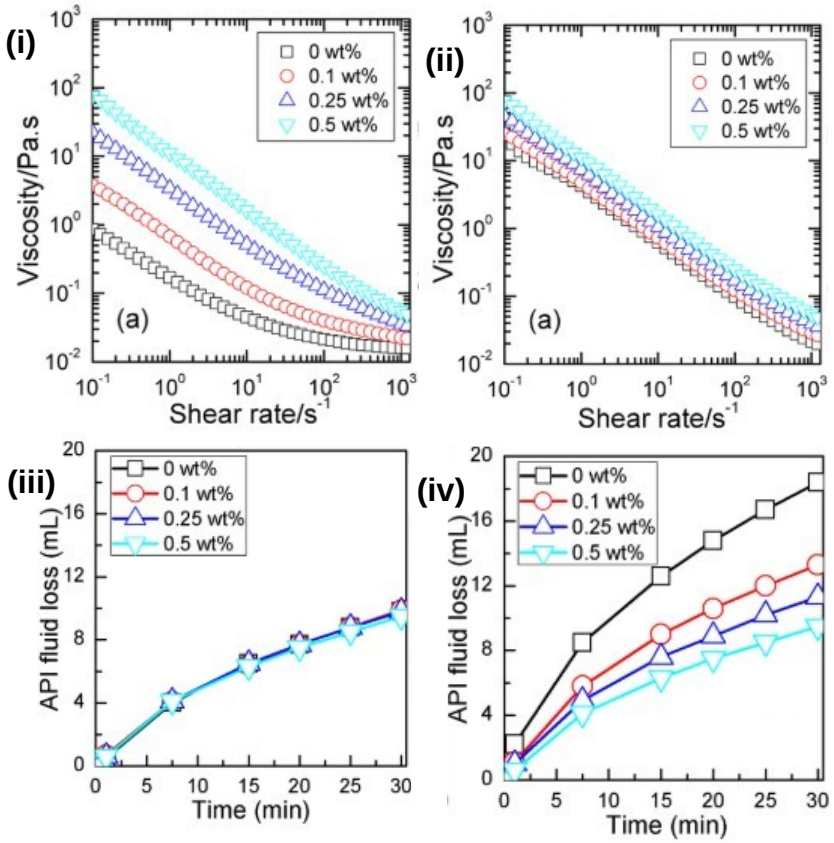


Figure 2.5: Comparison of viscosity and fluid loss tests for varying TK60 and PAC-L concentrations. (i) show the large reduction in viscosity between 0% and 0.5% TK60, whereas (iii) shows little influence of TK60 concentration in the fluid loss. (ii) and (iv) show the smaller influence PAC-L on viscosity when compared to TK60, but a greater influence on fluid loss, after Li et al. (2016).

pipes. On another drive, in silty sand, large contact stresses were observed to act on the pipe crown only, implying that the overcut collapsed. A drive in loose sandy soil was monitored. During the drive the overcut was continuously filled with Bentonite - deviating from standard practice at the time (which was to only inject lubrication periodically). Three benefits were noted: (i) the lubricant stabilised the soil around the pipe, (ii) a layer of low shear strength "Bentonite gel" formed around the pipes, and (iii) the pipes were buoyant - reducing friction.

Some of the research conclusions are not applicable to modern pipe jacking techniques, as all pipe jacks were not continuously lubricated. As an example of this, peaks in jacking force observed after $<$ 10 minute stoppages were attributed to excess pore water pressure dissipation within the clay adjacent to the pipe string. The smooth wall of the cast jacking pipe resulted in drainage paths as short as 0.1 mm, which facilitated the rapid changes in pore pressure

observed as the pipe acted as a drain to the surrounding clay.

The jacking forces from a drive exhibiting this behaviour are presented in Figure 2.6 (i), with the durations of stoppages highlighted. Figure 2.6 (ii) also shows the increase in effective radial stresses on the IP during stoppages. These results show that the effective radial interface stress increases during the stoppages in most cases, resulting in an increase in the total jacking load.

2.6.4 Loughborough study

Yonan (1993) conducted research at Loughborough University on pipe jacking forces in sand at a similar time to phase 2 and 3 of the PJA research program. The research involved laboratory experiments, coupled with field results, to assess the dependence of unlubricated pipe jacking forces on parameters such as: overburden depth, over-cut ratio, pipe soil, soil type, and pipe diameter. The experimental setup consisted of a chamber 1.8 m long, 1.5 m wide, and 1.5 m deep, through which 200 mm diameter pipe sections were jacked. Sand samples were rained into the chamber to a density of 16.5 kN/m^3 with a surcharge pressure applied using a 6 mm thick 'soft white' rubber pressure bag clamped around the top of the chamber.

A 50 tonne hydraulic jack was used to advance the test pipes through the chamber. As the pipes were installed, excavation was undertaken at the cutting face using a steel cutter with an adjustable overcut width. Advances were completed in short stages to minimise any face loss which occurred during the process. The study resulted in the empirical "Loughborough method" of calculating pipe jacking friction:

$$F = h.\pi.D_O.L \tag{2.14}$$

where h is an empirical factor derived from the laboratory testing.

The results obtained pipe frictions in excess of 25 kPa from the experiments and field studies. These are an order of magnitude larger than those observed in current practice. The paper notes that if sufficient lubrication is supplied the pipes within the drive can be made to

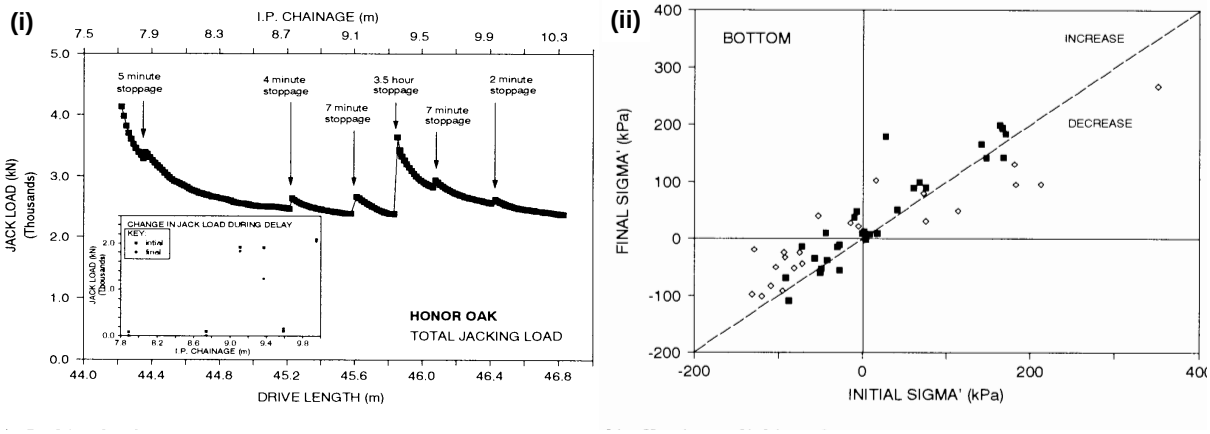


Figure 2.6: Time-dependent effects on tunnel drives: (i) increases in jacking force after stoppages in monitored drive 3 and, (ii) increase in effective radial stresses around the instrumented pipe in monitored drive 1, after Norris (1992).

float - which reduced the friction dramatically.

2.6.5 PJA Phase 3

Marshall (1998) extended the work of Norris (1992) through further field and experimental testing in phase 3 of the PJA research program. The focus of the work was pipe loading during jacking, and on primarily unlubricated (or partially lubricated) tunnel drives. Two drives were completed with full annular lubrication and it was found that during weekend stoppages the overcut lubricant dissipated. This resulted in the pipe string losing buoyancy and an associated increase in jacking force upon restarting of tunnelling operations. During one weekend stoppage it was noted the overcut converged onto the pipe wall, generating substantial normal stresses and friction.

A linear relationship between effective radial stress and shear stress was noted in field studies, with an overall reduction in interface friction of 45% observed. As well as the reduction in effective stress, the assumed low shear strength of the Bentonite around the pipes was also credited with causing this reduction.

2.6.6 PJA Phase 4 and further PJA research

Phase four focussed on the use of foams for soil stabilisation around the face of earth pressure balance (EPB) TBMs (Psomas (2001)) which is of little relevance to these research activities. Borghi (2006) continued work on friction during pipe-jacking by simulating the installation of

a pipe string under saturated and pressurised conditions in over consolidated clay to assess the changes in the overcut during, and after, installation. The chamber was similar to Yonan (1993) with an additional cylinder on the soil surface to consolidate the Kaolin clay sample, which also applied vertical stress during testing. During a test: pipe installation, clay excavation, and lubricant injection occurred simultaneously until the pipe had passed through the chamber. At this stage movement ceased and the overcut conditions were monitored. Instrumentation consisted of earth and pore pressure cells within the pipe and a load-cell mounted at the connection between the hydraulic actuator and the pipe assembly to measure total actuation force. The load-cells deployed were of the null type described by Talesnick et al. (2014), though they were not used in this mode due to the additional complexity of the installation.

The experiments explored the effect of different over-cut lubricants on installation forces, as well as subsequent clay swelling. Borghi (2006) noted continuous field monitoring of annular pressures during tunnelling operations was required to validate the experimental results. This recommendation aligns with the objectives of this research.

2.7 Filter cake formation

Bentonite clay lubricants support the tunnel overcut by applying a hydraulic stress to the soil structure. In soils where the 10% particle size fraction (D_{10}) is less than 6 mm, normal stress is transferred to the soil structure by a low permeability filter cake which forms at the lubricant-soil boundary (Praetorius and Schößer (2017); Xu and Bezuijen (2019)). Two types are defined: External, where the cake forms in the tunnel overcut; and internal, where the cake forms in the soil structure. Those authors define internal filter cakes as forming at high Bentonite concentrations or when pore sizes are large (1 mm $< D_{10} <$ 6 mm), whereas external filter cakes form at lower concentrations or smaller pore sizes ($D_{10} <$ 1 mm).

Min et al. (2010) and Min et al. (2013) recreated conditions at the TBM head using a permeameter apparatus. The studies assessed the effects of sand inclusion within the slurry

and grain size of soil on penetration and filtration rate. Three types of filter cake were defined: (A) an external filter cake, (B) a thinner external filter cake and internal filter cake, (C) infiltration only, where a filter cake did not form. These three conditions are shown in Figure 2.7.

Min et al. (2013) did not define the filtration rate as a means of comparing the filter cake permittivity directly. Instead, the variable Q_{max} is defined, corresponding to the cumulative quantity of discharged water from the experiment. 45 experiments were completed with nine slurry concentrations and five soil types. An un-named Sodium Bentonite with additions of silts and sands was used, with Table 2.1 showing three compositions' properties. Similarly, three soils mixtures are summarised in Table 2.2 for comparison.

Table 2.1: Select slurry properties from Min et al. (2013).

Slurry Name (-)	**Bentonite content (%)**	**Filler (content) (%)**	ρ **(g/cm^3)**	τ_0 **(Pa)**	**Dynamic yield (Pa)**	μ_p **(PaS)**	**Marsh time (s)**
SL1	8.55	Silt[1] (8.06)	1.1	1.79	2.18	1.45 x10^{-2}	33
SL5	7.34	Silt[2] (42.7)	1.2	2.85	3.45	1.68 x10^{-2}	33
SL8	7.34	Silty sand[3] (51.04)	1.2	3.96	4.59	1.75 x10^{-2}	34

[1] Silt with $d_{50} < 75\mu m$.
[2] Silt with $d_{50} < 100\mu m$.
[3] Silty sand with $d_{50} < 250\mu m$.

Table 2.2: Select soil properties from Min et al. (2013). k is the permeability of the soil, whilst $\overline{D_0}$ is the mean particle size.

Soil (-)	D_0**,** D_{10}**,** D_{50}**,** D_{100} **(mm)**	**k (m/s)**	$\overline{D_0}$ (μm)
S1	0.1, 0.115, 0.175, 0.25	9.2 x10^{-5}	21.5
S3	0.5, 0.55, 0.75, 1	2.8 x10^{-3}	214
S5	2, 2.3, 3.5, 5	4.2 x10^{-2}	459

The slurry infiltration (SI) types were defined as: A) $< 0.01\ m^3m^{-2}$ filtrate volume at 300 kPa applied pressure, B) an observable increase in filtrate with each loading step but $Q_{max} < 0.1\ m^3m^{-2}$ at 300 kPa, and C) rapid filtration occurring under the first (50 kPa) loading step,

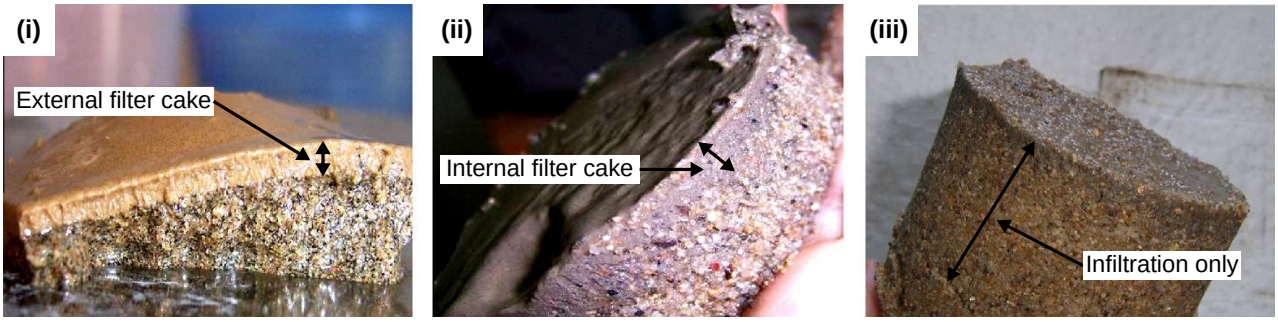


Figure 2.7: Photographs showing the three filter cake types identified by Min et al. (2013). Filter cakes are identified in red: (i) an external cake, (ii) an thinner external and internal filter cake, (iii) no identifiable cake, instead a deep infiltration zone.

and the test not achieving 300 kPa. Table 2.3 highlights the correlation between the infiltration type, filter cake type, and Q_{max} present in the data.

Increasing the soil percentage, as well as increasing the particle size, reduced the filtration volume. For example, SL9 produced a Q_{max} of 12 10^{-3} m^3/m^2 in the largest soil (S5), whereas SL1 (with a lower percentage of solids) produced a type C response, yielding 179 10^{-3} m^3/m^2 at 50 kPa. The research did not assess the properties of the filter cakes further than the categorisation presented here.

Table 2.3: Select results from Min et al. (2013). SI is the slurry infiltration curve type, FC is the filter cake type, and Q_{max} is the filtrate volume with units of 10^{-3} m^3/m^2.

Soil/	**S1**			**S3**			**S5**		
Slurry	**SI**	**FC**	Q_{max}	**SI**	**FC**	Q_{max}	**SI**	**FC**	Q_{max}
SL1	A	I	3.9	B	III	101.2	C	III	179
SL5	A	I	3.8	A	II	10.7	C	III	177
SL8	A	I	3.5	A	I	3.5	B	III	12

Praetorius and Schößer (2017) also note the condition of "pure penetration" (similar to SI type C) which occurs at larger pore sizes ($D_{10} > 6$ mm). In this instance the viscosity of the lubricant is said to support the soil by transferring shear stresses gradually to the soil structure during permeation. In this state, local instability may occur if the shear stress transferred to a single soil grain is less than the forces acting to dislodge it (such as its weight).

Xu and Bezuijen (2019) also explores the behaviour of lubricants at the cutting face of TBMs using a permeameter apparatus. The Bentonite was pressurised above a sand layer to

simulate the injection and subsequent infiltration into the soil in a tunnel overcut. The initial rapid infiltration was termed the "mud spurt" phase. Figure 2.8 summarises the model for filter cake formation those authors developed. Differential pore pressures across the filter cake were noted, confirming the transfer of stress to the soil structure.

2.8 Analogies to diaphragm wall excavation

Analogies can be made between pipe-jacking and bored pile or diaphragm wall construction. In bored pile or diaphragm wall construction, Bentonite supports an excavation by exerting a hydrostatic pressure on the excavation walls to establish stability by either: (i) the phreatic surface in the excavation being higher than the surrounding soil or, (ii) the density of the slurry being greater than that of the surrounding pore-water. This action creates a hydraulic gradient (analogous to the pressure in an overcut) that drives the support fluid through the surrounding soil, creating a filter cake at the interface (Calçada et al. (2011); Lam et al. (2014)).

Lam et al. (2014) conducts a detailed literature review of previous studies and notes the friction resistance of the pile - filter cake - soil boundary is dependent on the amount of concrete aggregates that penetrate the filter cake during construction. The interface shear capacity varies between the filter cake shear strength (at 0% concrete penetration) to the shear strength of the soil (at $\sim$ 50% penetration). As such, the results from tests with little penetration provide insight into the shear strength of filter cakes. Similarly, studies where 'micro-concretes' (meaning concretes with no aggregates $>$ 5 mm diameter) were used and studies with smooth concrete interface are also of interest.

Lam et al. (2014) reported a Bentonite filter cake build-up of 3.376 mm per hour$^{1/2}$ under a 230 kPa driving head for periods of between 15 minutes and 25 hours. This pressure is in excess of those typically experienced in pipe jacking but demonstrates the build-up of filter cake for the 24:1 water/Berkbent 163 mixture tested. These conditions were repeated in a modified shear box (described in Lam (2011)) and the shear stresses achieved by the filter cake

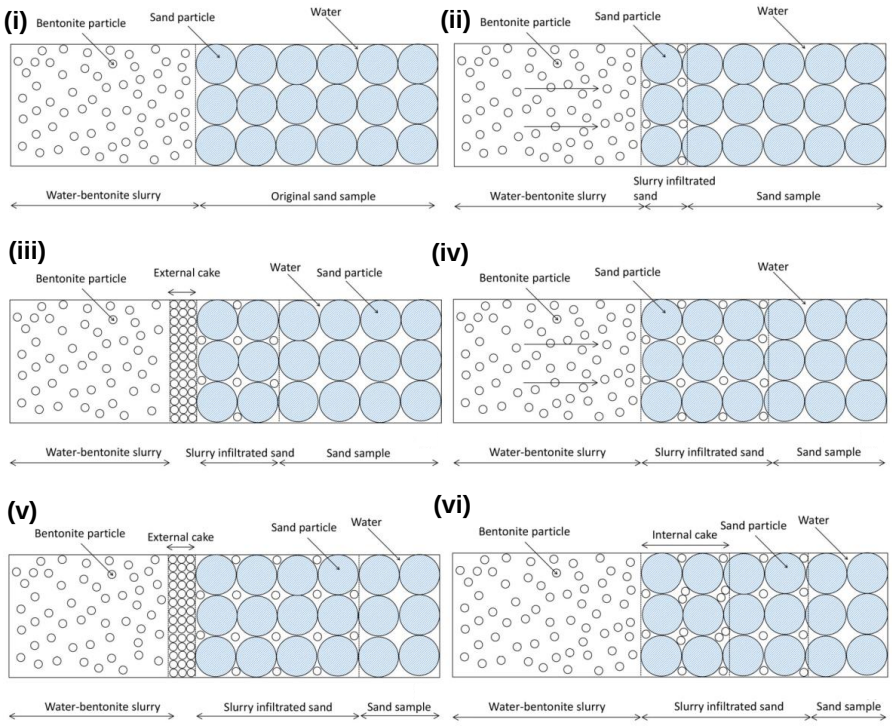


Figure 2.8: Filter cake formation stages, after Xu and Bezuijen (2019): (i) initial conditions, (ii) infiltration of Bentonite during the mud spurt phase, (iii) an external filter cake forms, (iv) filter cake removed by TBM cutting tools, (v) filter cake reforms, (vi) external cake removed by TBM cutting tools and an internal filter cake forms.

and a micro concrete were recorded. The filter cake shearing exhibited a peak of 40 kPa after < 1 mm sheared before it reduced to a stress of 30 kPa. The filter cake in contact with the micro-concrete exhibited a larger peak of 50 kPa after < 1 mm sheared, before reducing to a critical state value of 40 kPa.

Verst et al. (2022) conducts a study of micro-concrete - filter cake - soil friction using "Ibeco B1" and "Ibeco S" type Bentonites and an apparatus similar to Lam et al. (2014). Mixtures filtered through sand for periods of between 23 and 72 hours before tests were conducted at between 40 kPa and 160 kPa normal stress. The effect of sand inclusion in the filter cake was also examined, as shown in Table 2.4. Tests -08 and -09, included "fine sand" and quartz powder with $d_{85} < 0.1$ mm.

The results presented demonstrate the increase in shear strength caused by: sand contamination of the filter cake, increased ΔT, and increased filtration pressure. Figure 2.9 shows the thickness of the filter cake formed after 48 hours filtering at 80 kPa. The filter cake had

Table 2.4: Lubricant mixes, filtration time, vertical stresses, and peak friction angles from Bentonite tests documented in Verst et al. (2022).

Test (-)	**Bentonite type** (g/l)	**Sand (s) / quartz (qz) inclusion** (g/l)	**Filtration time** ΔT **(h)**	**Vertical Stress** (kPa)	**Cake Thickness** (mm)	**Friction angle** (^{o})
V-B-01	B1 (55)	-	48	80	3	27.9
V-B-02	B1 (55)	-	48	80	4-10	27.0
V-B-03	B1 (55)	-	48	160	3-5	28.0
V-B-04	B1 (55)	-	72	40	10-12	27.6
V-B-06	S (55)	-	44	80	8-10	24.2
V-B-08	S (45)	s (322)	23	80	8-9	32.3
V-B-09	S (45)	s (81), qz (81)	26	80	5-6	29.5

sufficient thickness to allow shearing at the cake-concrete interface, without being influenced by the sand.

Sims (2020) examined the properties of "Berkbent 100" and "SlurryPro CDP PHPA" polymer support fluids. The effect of soil pore size variation was compared using samples of freshly mixed and used support fluid, with the used fluid coming from a piling site after it had been deemed ready for re-use. The properties of the two fluids were similar although the used sample was slightly more dense and viscous, with pH, relative density, and Marsh funnel times of: 9.02/9.33, 1.01/1.07, and 28.9/37.2 for the clean/used, respectively. Viscosities and yield stresses of the fluids were not presented.

The used fluid was shown to have a smaller mud-spurt distance than the clean on a 25 μm porous plastic disc. This was attributed to the inclusion of larger particles of excavated material within the Bentonite clogging the pores more easily than the fresh sample. Once a filter cake had formed, the filtration rates (at 1 bar pressure) for the clean/used samples were 0.55 ml $s^{-1/2}$ / 0.29 ml $s^{-1/2}$ respectively, demonstrating a lower permeability filter cake was formed by the used Bentonite. Pore sizes of 2.7 μm, 10 μm, and 25 μm were also tested at 2 bar pressure. Filtration rates of 0.58 ml $s^{-1/2}$, 0.58 ml $s^{-1/2}$, and 0.63 ml $s^{-1/2}$ were recorded demonstrating that, once a filter cake forms, the permeability is similar in this pore size range.

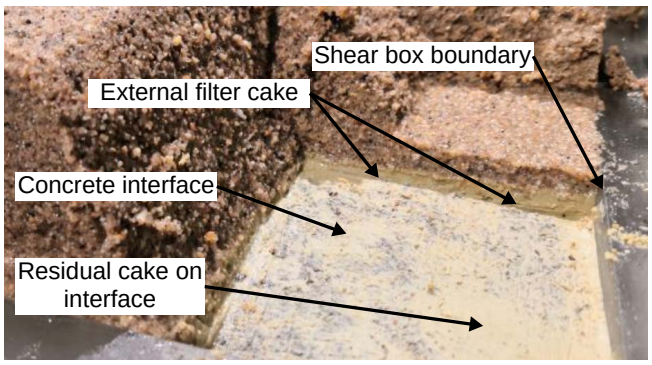


Figure 2.9: Photograph showing the interface from the V-B-02 test, after Verst et al. (2022). The thickness of the filter cake is highlighted in red.

2.9 Influence of lubrication on sliding friction

Shou et al. (2010) used a simple shear apparatus to record the frictional force between a concrete block and sand sample. Reductions in friction of up to 75% were recorded when a 45 mm layer of lubricant was placed between the block and soil compared to the soil-concrete contact alone. However, the apparatus generated normal contact stresses of 1.75 kPa, which is lower than would be expected in practice.

Reilly (2014) and Reilly and Orr (2017) used a novel triaxial apparatus to demonstrate that the reduction in σ'_N is the predominant factor in reducing interface friction. The apparatus had a concrete-sand interface inclined to coincide with the sand failure surface. Injections of lubricant prior to shearing had a negligible effect in reducing steady state friction but did eliminate the peak resistance. During shearing, a single injection at 4% strain was shown to reduce friction, but the effect was transient, as can be observed in Figure 2.10 (i). Constant pressure injection, as shown in Figure 2.10 (ii) reduced the steady-state deviator stress significantly when both water and Bentonite (Hydraul-Ez) were used.

Namli and Guler (2017) hypothesised the reduction in friction was caused by Bentonite reducing μ instead of σ'_N. Others, such as Staheli (2006), have also adopted this approach. Namli and Guler (2017) conducted experiments where a cylindrical concrete tube with a lubricated interface was removed from a sand sample. An excess head was maintained in the overcut of approximately 50 mm during the test. The Bentonite used was described by Namli (2011)

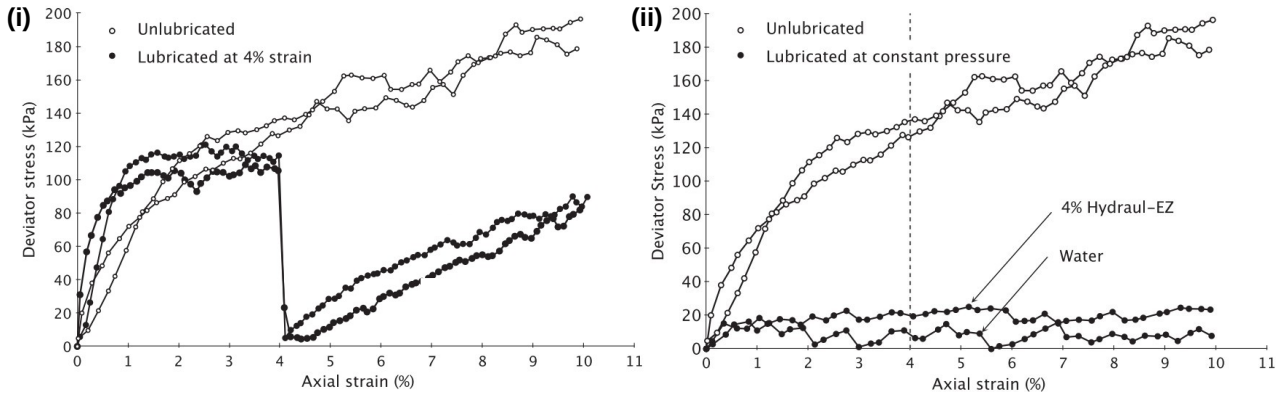


Figure 2.10: Axial strain - deviator stress relationship from six tests where: (i) a single lubricant injection was completed at 4% axial strain, and (ii) where lubricant was injected at constant pressure throughout the test, after Reilly and Orr (2017).

as having a plastic viscosity of 4 cP at 15.7:1 (6 %) concentration. The results, and a case study beneath the Tuzla river, demonstrated that minimal Bentonite pressures are required to "provide the full lubricant effect".

Reilly et al. (2019) responded to the paper suggesting the authors had not considered the effective stress reduction. Namli and Guler (2019) presented additional tests where samples were prepared using a method similar to Verst et al. (2022). The prepared samples were then transferred to a shear box and sheared against a concrete interface. The interface friction coefficient μ_{int} was reduced from 0.9 to 0.46 without additional Bentonite injection. Similar results were reported from two field tunnel drives. It suggested that the precise, triaxial, experiments of Reilly and Orr (2017) do not accurately recreate the field conditions. Instead, injections from discrete lubricant ports, coupled with pauses between injections, cause partial overcut collapse and flow of the Bentonite perpendicular to the tunnel pipe. If this is case, the Bentonite film reducing μ_{int} alone lubricates the pipes.

2.10 Field studies

Several studies have back-analysed the friction forces from Pipe-jacked tunnel drives e.g Pellet-Beaucour et al. (2002); Comité Français des Travaux sans Tranchée (2006); Curran and McCabe (2011); Reilly et al. (2012); Sheil et al. (2016); Cheng et al. (2018); Shi et al. (2018);

O'Dwyer et al. (2019); Chesterton (2019). Pellet-Beaucour et al. (2002) proposed a method for inferring the interface friction on a pipe string using the total jacking force data alone. Those authors theorised that variations in jacking force were created by variation in forces acting on the head of the TBM. By connecting the minima of the jacking forces for a given advance distance (or 'bin') the interface friction could be determined as the head forces are assumed minimal at these locations. Chesterton (2019) compared two further methods: (i) the average jacking force over the first 3 m is adopted as the head force for the entire drive, and (ii) the jacking force once the TBM has broken through is assumed to be from interface friction alone. Both of these methods were shown to be less accurate than the Pellet-Beaucour et al. (2002) method.

The literature has shown that friction varies between different ground types, with sands and gravels being highest. Pellet-Beaucour et al. (2002) show that at the start of lubrication in these ground conditions the friction forces can reduce by up to 90%. Those authors documented nine tunnel drives in France for which the increase in jacking force after stoppages were recorded. Example increases in friction from a drive are shown in Figure 2.11. These data showed that the increase in interface friction during a stoppage was proportional to the logarithm of the stoppage duration as follows:

$$\frac{\Delta P}{P_{start}}\% \;=\; a.ln(t_s) + b \tag{2.15}$$

where P_{start} is the total jacking force before the stoppage, ΔP is the force increase, t_s is the time stopped (in hours), and a and b are constants. The model constants were reported to vary according to: lubrication effectiveness, ground condition, restart procedure, and overcut size. A range of $4.8 < a < 8.2$ and $2 < b < 11$ was observed. This variation is significant considering that the drives were conducted in similar ground conditions. Potential reasons for the differences were identified as: (a) loss of lubricant pressure (leading to increased effective stresses), (b) the thixotropic nature of Bentonite, and (c) consolidation.

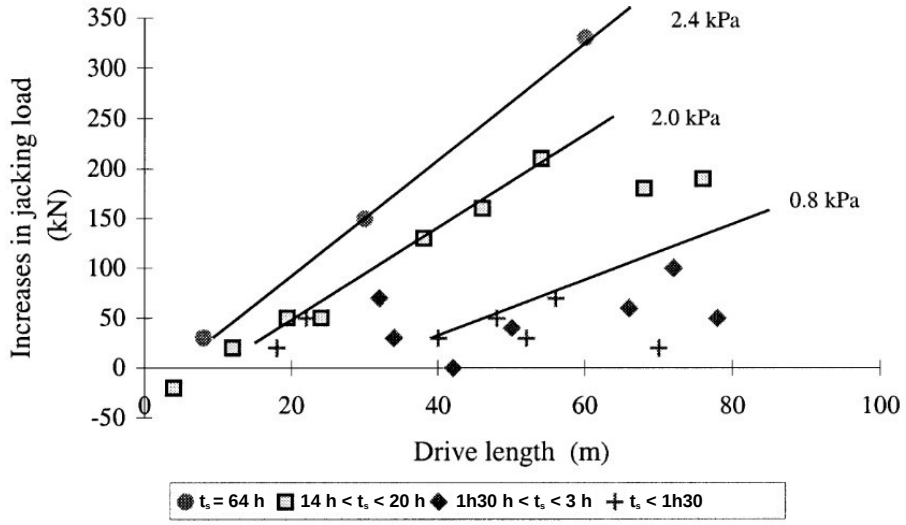


Figure 2.11: Jacking load increases after stoppages of various lengths during a tunnel drive, after Pellet-Beaucour et al. (2002), t_s denotes the duration of the stoppage.

Khazaei et al. (2006) used ground penetrating radar (GPR) and down borehole cameras to demonstrate overcut presence around pipes in sandy soil during a drive in Fujisawa Japan. The measurements revealed a variable void thickness surrounding the tunnel pipe. However, neither the camera nor the GPR was able to distinguish between air and lubricant in the void. Nevertheless, a correlation (albeit weak) between void thickness and reduced interface friction was observed.

Curran and McCabe (2011) found that for eleven drives in clay, gravel, and sands there was a linear relationship between tunnelled distance and ΔP for a given stoppage duration. The values recorded were significantly lower than those in Pellet-Beaucour et al. (2002) (for example 0.7 kPa compared to 2 kPa for a 12 hour stoppage). This was likely due to the increased effectiveness of lubrication in the period between the two studies. O'Dwyer et al. (2019) confirmed a relationship between stoppage duration and ΔP using data from two drives through silty sands and silts in Lennox Gate, UK. It is of note that ΔP measured during a stoppage was larger than P before the stoppage in some cases.

Friction development in rock-tunnel drives and the effect of over-cut clogging due to fines build-up has been studied by Deng et al. (2021, 2022a,b). These studies detail three tunnel

drives through mudstone and sandstone in Chongqing, China. Jacking forces were shown to increase dramatically when deviations from the desired line of the tunnel occurred, or when sediment collected around the tunnel pipes. The sediment clogging phenomenon was quantified in Deng et al. (2022a) using total stress earth pressure sensors mounted externally on the tunnel pipes. These sensors measured significantly higher contact stresses at the pipe invert compared to the crown, typically 60 kPa - 70 kPa compared to under 10 kPa at the crown, demonstrating the clogging in the lower part of the overcut.

Additionally, four vibrating wire strain gauges were cast into the pipes at the N,E,S,W compass points. These measured the axial strains at the mid-section of the wall to give an indication of the jacking force transfer through the pipe section. Results from these sensors, such as those in Figure 2.12, showed that typically the jacking force was transferred through the bottom of the pipe section - suggesting the friction was concentrated in that region.

Direct shear tests examining a concrete - lubricant - rock interface were also conducted under a 666 kPa normal stress. μ was shown to decrease with increasing lubrication concentration, verifying similar results reported by Shou et al. (2010) and Zhong et al. (2021). Tests were also conducted on slurry-sediment mixtures at ratios of between 0.5 and 1.5 by weight. The results, shown in Table 2.5, identified that increasing sediment concentration increased the friction coefficient - a similar response to that observed by Verst et al. (2022).

Pan et al. (2021) presented scale testing of a lubricated rectangular pipe-jack installation through a large, rectangular, soil chamber at 1 g. The test piece designed to achieve a 2 mm overcut, whilst lubricant was injected through a port on each of the four faces. Earth pressure gauges were installed to record total normal stress and a load-cell between the test pieces to log the friction force. Two tests, where the total volume of lubricant injected was 200 % of the over-cut volume, were reported with varying lubricant distributions, as shown in Table 2.6.

Only pore pressure results were discussed in the paper, but the distributions showed that

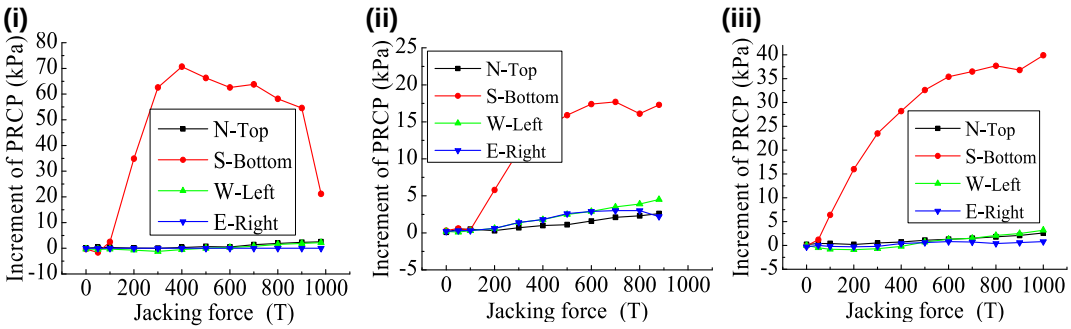


Figure 2.12: Incremental value of pipe-rock contact pressure (PRCP) under different jacking force and different jacking distances: (a) 20 m, (b) 40 m, (c) 47.5 m, after Deng et al. (2022a).

Table 2.5: Summary of friction test results from Deng et al. (2022b).

Interface Media concentration (%)	**Slurry:Sediment ratio** (-)	μ (-)	**Difference to 4.5 % clean slurry** (%)
1	0	0.429	29.2
2	0	0.398	19.9
4.5	0	0.332	0.00
6	0	0.328	-1.20
7.5	0	0.338	1.81
4.5	0.5	0.409	23.2
4.5	1	0.439	32.2
4.5	1.5	0.501	50.9

after an initial peak around the injecting ports, the pressures at different ports converged, suggesting an over-cut had been successfully formed and hydraulic connectivity had been established.

Lehmann et al. (2022) presented a case study of a long pipe-jacked tunnel drive in strong metamorphic rocks in Brittany, France. The drive used the same HK TBMs and lubrication systems as the drives in this study, with the lubrication system operating in volume control mode. The paper focussed on the production and power utilisation of the drive but noted τ averaged 1.2 kPa during the drive. The evolution of τ is discussed, with the high values calculated for the first 100 m of the tunnel drive explained as the influence of the high friction on the TBM having a larger effect on the average when the overall drive length is short. This effect dissipates as the drive progresses, and the friction value tends to reflect the average

Table 2.6: Fractions of the total lubricant injection volume sent to different ports during two tests in Pan et al. (2021).

Condition	Upper left	Upper right	Left side	Right side	Bottom
i	0.4	0.4	0.1	0.1	0
ii	0.3	0.3	0.15	0.15	0.1

friction on the rest of the pipe string.

2.11 Summary of gaps in current literature

The literature reviewed herein demonstrates that significant research has been completed on the subject of the SLS interface during pipe-jacking and the frictional forces which develop. Studies have examined data from tunnel drives to give indications of the friction changes which occur during a drive, and during stoppages. Experimentation has been completed into filter cake formation and the changes in permeability which occur during clay build-up on the inside of tunnel (or oil well) bores. The research into the SLS mechanics can be broadly categorised as:

1. Small scale testing examining the effects of lubricant injection on the effective stresses at the interface, or
2. Larger scale (shear box type) testing at low normal stress, with a layer lubricant manually installed at the interface prior to shearing.

These methods have yielded contradicting results. The small scale testing has demonstrated that effective stress reduction is the method by which lubricants reduce τ. In contrast, the larger shear-box tests have largely demonstrated that effective lubrication causes a reduction in μ at the interface, hence reducing τ. These differences are evidenced by recent discussion papers.

However, little work has been conducted into understanding what mechanisms cause the friction increases observed during tunnel drives, especially following stoppages. Previous experimental work has been short duration and lacked the ability to faithfully recreate the overcut

conditions expected in field tunnel sites. Alternative research has focussed on the soil-lubricant-structure interface around diaphragm wall construction, which (although analogous) does not model seepages during stoppages interspersed with periods of large-strain shearing.

This research therefore aims to advance current knowledge how Bentonite lubricants behave at the SLS interface during these periods and how this contributes to friction increases observed during pipe-jacking operations. Long duration experiments will be used identify processes which occur at the time scales experienced in pipe-jacking and a new SLS interface apparatus will faithfully recreate overcut conditions, including large interface strains and intermittent lubricant injection from discrete locations.

3 | Experimental methods

3.1 Overview of field studies

3.1.1 Introduction

Monitoring projects have been undertaken to analyse SLS conditions in modern, automatically lubricated, pipe-jacked tunnels in the field. These will quantify changes which occur during tunnelling and establish accurate parameters to maximise the fidelity of the laboratory testing. This monitoring had two distinct focuses. First, bespoke instrumented pipe sections (IPs) were produced to measure and record overcut conditions and pipe behaviour during two tunnel drives in the UK. To complement this data, a database was developed to compile drive data from recent Ward and Burke Construction tunnel drives. These data provided insight into: tunnel lubrication practice, stoppage frequency and duration, frictional changes during stoppages and total jacking forces. The following sections introduce the two monitored tunnel drives and their monitoring regimes, before highlighting the measurements available from historical drive data for comparison.

3.1.2 Castlerigg tunnel drive

The first field monitoring project was conducted near Keswick, Cumbria, in 2018 and a schematic of the alignment is shown in Figure 3.1 and the detailed plan and long section drawings are included in A. The drive formed one of four tunnelled sections in a new 30 km pipeline with the United Utilities (UU) West Cumbria Water Supplies Project (United Utilities LTD. (2021)). The four inaccessible sections, crossing beneath roads or rivers were pipe-jacked to reduce disruption and cost, with the remainder utilising open cut construction. The Castlerigg drive reduced the overall length of the pipeline by tunnelling through a Mudstone ridge to the East of Keswick.

The tunnel drive consisted of a 2.76 m outside diameter (D_O), 1237 m long (L) tunnel,



Figure 3.1: Location of the Castlerigg tunnel drive.

which is the longest pipe-jacked drive to be completed in the UK, to the author's knowledge. The drive commenced on the 5th of September 2018 and was completed on the 5th of December 2018. During the first 35 days of the works, operations were completed by a single 12 hour day shift, working 5 days per week. For the remaining 56 days of the drive, work was completed by two 12 hour shifts working 24/7. The TBM was a Herrenknecht (HK) AVN 2200.

Pipe-jacking was conducted in the downstream direction of the pipeline (from E-SE to W-NW) at a positive grade of 1%. Lubrication utilised an 18:1 water/Tunnel Gel (by weight) mix, with 1 kg/m3 TK60 polymer. This was delivered to the overcut by 3-port lubrication pipes distributed along the length of the drive at spacings of 3 m (behind the TBM and either side of an IJS) and 15 m at all other locations. The lubricant was batched at ground level and delivered to the lubricant ports by three 2" pressurised slurry lines, each serving a different section of the tunnel.

The drive predominantly passed through extremely weak to medium strong mudstone of low abrasivity and permeability. The first 50 m and final 200 m of the drive were in superficial glacial till soils as the tunnel passed through the overlaying strata (sand and gravel lenses with

cobbles and boulders in a matrix of clay). Key parameters of the mudstone are shown in Table 3.1.

Table 3.1: Summary mudstone properties encountered during the Castlerigg tunnel drive.

Parameter	Unit	Value
Compressive strength[1]	MPa	1 - 50
Tensile strength[1]	MPa	< 1
Abrasivity[2]	-	Low
Permeability[3]	m/s	1×10^{-8} - 1×10^{-5}
Maximum depth of cover	m	57.8
Maximum pressure head	m	25

[1] Rock strength from laboratory testing and qualitative borehole recovery reporting to BS EN ISO 14689-1:2018 (British Standards Institution (2003)).
[2] Abrasivity measured using Cherchar test (Ulusay (2014)).
[3] Permeability testing to BS EN ISO 22282-3:2012 (British Standards Institution (2012)).

3.1.3 Castlerigg instrumented tunnel pipe

The IP produced for the drive collected measurements of: (i) local normal and shear contact stresses, (ii) pore water pressures, and (iii) pipe wall strains. The IP was 'wet cast' using self-compacting concrete which reduced the risk of the sensors moving from their installed positions during casting. Table 3.2 provides a summary of the salient physical pipe parameters.

The fabrication process for the instrumented pipe was as follows: (i) installation of outside mould, (ii) placement of prefabricated reinforcement cages, (iii) placement of sensors on outside reinforcement cage, (iv) installation of inside mould, (v) placement of the concrete, (vi) curing for 28 days, and (vii) transport to site. Key stages of this process are shown in Figure 3.2. All sensor cables were routed to the interior face of the pipe and wrapped in foam to protect them during casting and allow access once on site.

The external soil contact stresses were monitored using four three-axis Interface Force Measure Solutions 3A series load cells with a 5 kN capacity for each axis. The four load cells were fitted within bespoke aluminium housings and installed flush with the exterior surface of the pipe at locations N, W, S and E, as shown in Figure 3.3. Each housing was fitted with a

Table 3.2: Summary salient tunnel pipe parameters from the Castlerigg tunnel drive.

Parameter	Symbol	Unit	Value
Length	L	m	3
Internal diameter	D_I	m	2.286
External diameter	D_O	m	2.756
Wall thickness	t_w	m	0.235
Wall section area	A_w	m^2	1.861
Concrete UCS	F_{ck}	MPa	50
Concrete Young's modulus[1]	E_c	GPa	37
Pipe weight per m	w_p	kN/m	46.5

[1] Calculated using methodology in BS EN 1992-1.

125 mm × 125 mm aluminium sensing plate, with the joint between the faceplate and housing sealed using flexible silicone sealant to ensure full load transfer to the load cell. This approach had been found to be successful in previous monitoring, Royston (2018).

An Omega PX309-200GV electrical pressure transducer, fitted with a filter cap, was installed beside each load cell to monitor the pore water pressure in the tunnel overcut. Glycerine was used to saturate the tube between the pressure transducer diaphragm and filter cap. An additional rubber membrane was placed over the filter cap prior to installation to prevent issues arising from a loss of saturation (such as those reported in Borghi (2006)). This was only removed immediately prior to the pipe being lifted into the launch excavation.

A total of 16 Soil Instruments ST4 vibrating wire strain gauges (VWS) were cast into the pipe wall on the outside reinforcement layer, 60 mm from the exterior face and 1.5 m from the spigot end of the pipe. At four locations (N, W, S, E in Figure 3.3) the strain gauges were placed in rosette formation to measure axial, hoop, and 45° in-plane strain. An additional four strain gauges were deployed to measure hoop strains only, one each at locations NW, SW, SE, and NE. The monitoring was designed to capture both short term changes, such as those caused by lubricant injection, and long term trends, such as gradual changes in friction, or overcut pressure. To identify the short term trends a logging period of 60 s was selected for the strain gauge data, and 1 s for the pressure transducers and three-axis load cells.

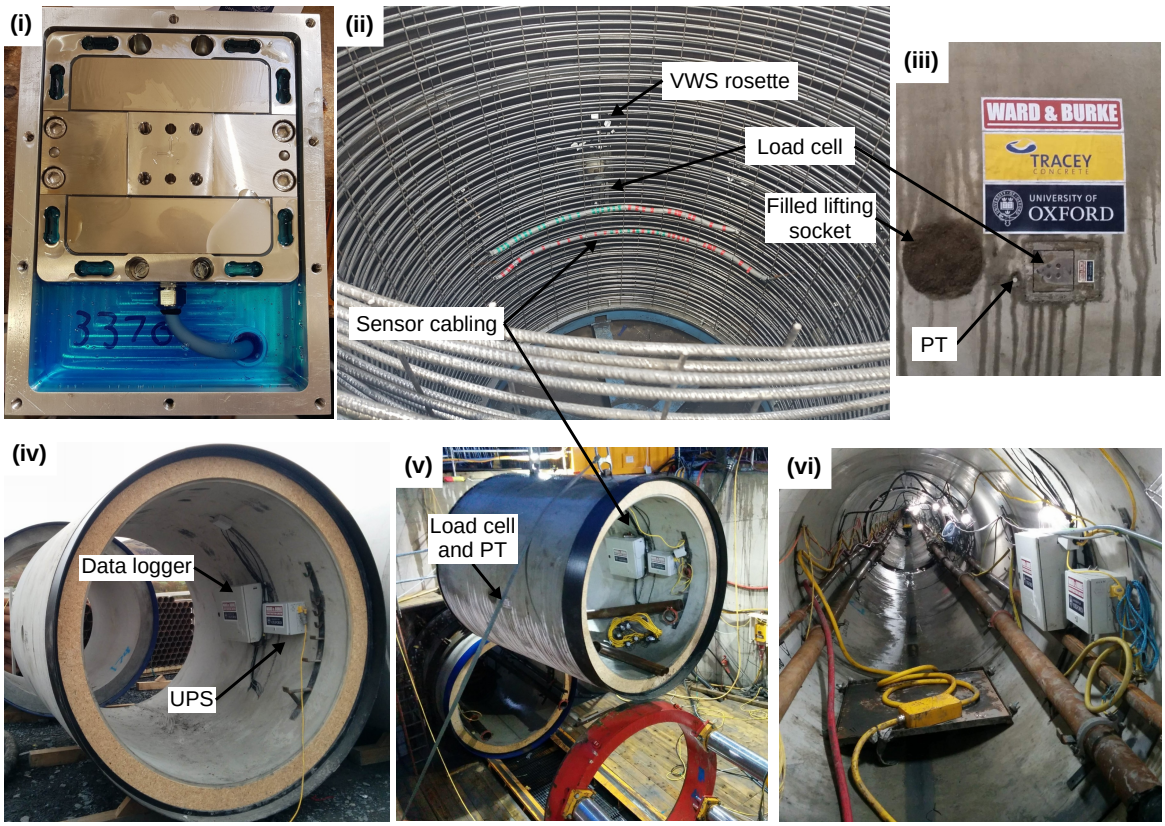


Figure 3.2: Development stages of the Castlerigg IP: (i) Interface load cell with waterproofing "magic gel", (ii) sensors and cabling before inside mould installation, (iii) load cell and pressure sensor after casting, (iv) IP on site, (v) IP being installed, and (vi) IP during tunnelling.

Once on site, the data was logged using a National Instruments cRIO data-logger (for the pressure transducers and load cells) and Soil Instruments VWLog8s (for the VWS). These were connected to an uninterruptable power supply (UPS) and mounted onto the pipe wall. The UPS was designed to provide continuous power to the data loggers for periods of up to three days, so that during weekend shut downs, when power to the tunnel was turned off, the instruments would still be able to record data. Immediately prior to pipe installation, 24 hour baseline readings were taken for all sensors with the pipe under self-weight load only. This was particularly important for the VWS sensors as it was not possible to record the strains during curing and therefore establish a control reading. Following this, the pipe was installed into the drive as pipe number 177 of 418, approximately 537 m behind the head of the TBM. This location allowed the conditions recorded by the IP to be representative of the pipe string, whilst also collecting as much data as possible.

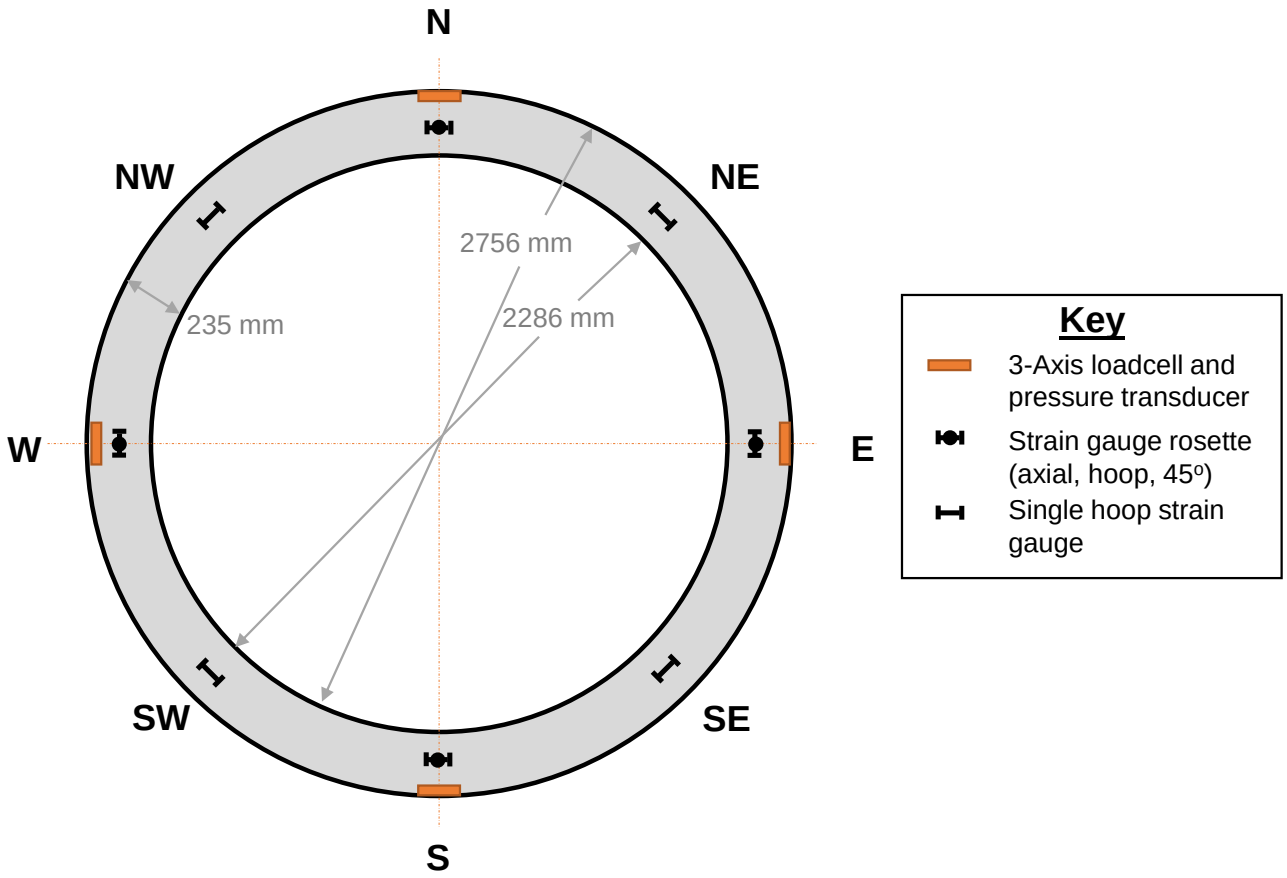


Figure 3.3: Schematic of the sensors installed into the Castlerigg instrumented pipe.

3.1.4 Putney tunnel drive

The second monitoring project in this research was located beneath the river Thames in Putney, London. The drive formed part of the Putney embankment foreshore site (PUTEF) of the Thames Tideway project. The £3.8 Billion "super sewer" project aims to reduce overflow events from the city's Victorian sewer network into the river Thames by 94% annually (Thames Water PLC (2021)). The scheme will intercept combined sewer overflows (CSOs) at 34 locations, and transport the waste, via a 15 mile long tunnel, to Abbey Mills pumping station for treatment.

At the PUTEF site, two CSOs are intercepted beneath Putney bridge to transport the wastewater along an L = 137 m, D_I = 2.286 m curved tunnel, to a drop shaft and connection to the main tunnel. An overview drawing of the tunnel is included in B. The cover H was between 2.3 m and 5.5 m for the drive. At this level, the excavation face consisted of weathered

London clay overlain by river terrace deposits due to the close proximity to the riverbed. Due to the shallow cover, the tunnel pipes were designed to be more robust than typical - to ensure the tunnel was not damaged if a ferry or barge grounded on the riverbed above. To this end, a 5 mm thick steel 'can' was cast into each pipe 120 mm from the inside face of concrete. To accommodate this, the D_O was increased from 2.756 m to 2.98 m.

The tunnel was completed at a 1:500 downward gradient. At 80 m chainage there was an anti-clockwise horizontal curve (at a radius of 237 m, for 7°) to align the tunnel perpendicular to the bridge abutment. The TBM was launched from the concrete launch shaft on the 14^{th} of September 2019, but due to technical difficulties tunnelling did not commence until 19^{th} November. It was received into a temporary steel cofferdam to the east of Putney bridge on the 17^{th} of December by two 12 hour shifts working 6 days per week.

Lubrication was provided by 3-port lubrication pipes distributed throughout the drive. These were spaced at 12.5 m intervals along the string, although the pipes 1 (immediately behind the TBM), 2, 3, 6, 8, and 10 were also lubrication pipes. This allowed for ample lubrication behind the TBM in the mixed soil and grouting of the tunnel in front of the bridge abutment upon drive completion.

3.1.5 Putney instrumented tunnel pipe

An IP similar to the one deployed in Castlerigg was developed for the drive. The sensor arrangement is shown in Figure 3.4. 12 Soil Instruments ST4 VWS were cast into the concrete in rosette formations at the N, E, S, and W locations on the outermost reinforcement layer. At the E position the 45° strain sensor was destroyed during cage installation, so only axial and hoops strains were logged. An additional axially orientated VWS was installed at each of the NE, SE, SW, NW locations to record the axial stress distribution within the pipe wall around the curve. Five Soil Instruments ST2 VWS were also welded to the outside face of the steel can to record load transfer to the can during jacking. Four of the sensors recorded the axial strain (at the N, E, S, W locations) and one sensor (at the N location) measured the hoop

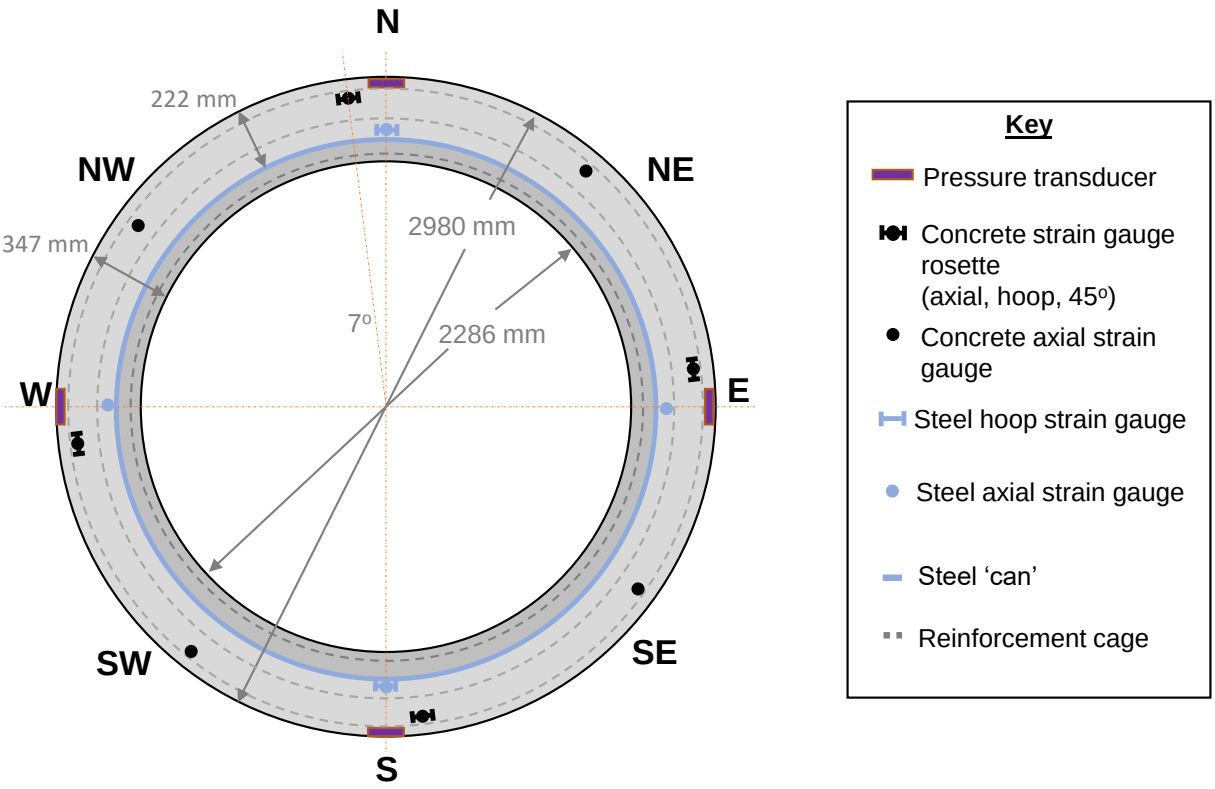


Figure 3.4: Schematic illustration of the sensor layout for the Putney IP. Note the additional steel 'can' cast within the pipe wall.

strain. Due to the 2.5 m length of the pipes, the cast-in lifters obstructed the VWS locations. The concrete sensors were therefore rotated 7° in an anti-clockwise direction as shown in Figure 3.4 and Figure 3.5 (i). Figure 3.5 (ii) and (iii) show the IP after casting, and during logging, respectively.

During the Castlerigg tunnel drive, the electronic load cells developed faults due to water ingress (Section 4.4) and were not deployed to the Putney IP. Instead, four WIKA S-20 pressure transducers (PTs) were installed at the N, E, S, W ordinates on the pipe. These were mounted without filter caps, to reduce damping, but had a protective rubber cap which was removed immediately before the pipe was installed into the drive.

The sensor cabling exited to the top of the concrete mould, which formed the leading face of the pipe during tunnelling. This enabled the sensors to be connected to the data loggers during the casting process, meaning that a 'whole life' strain history for the pipe could be recorded.

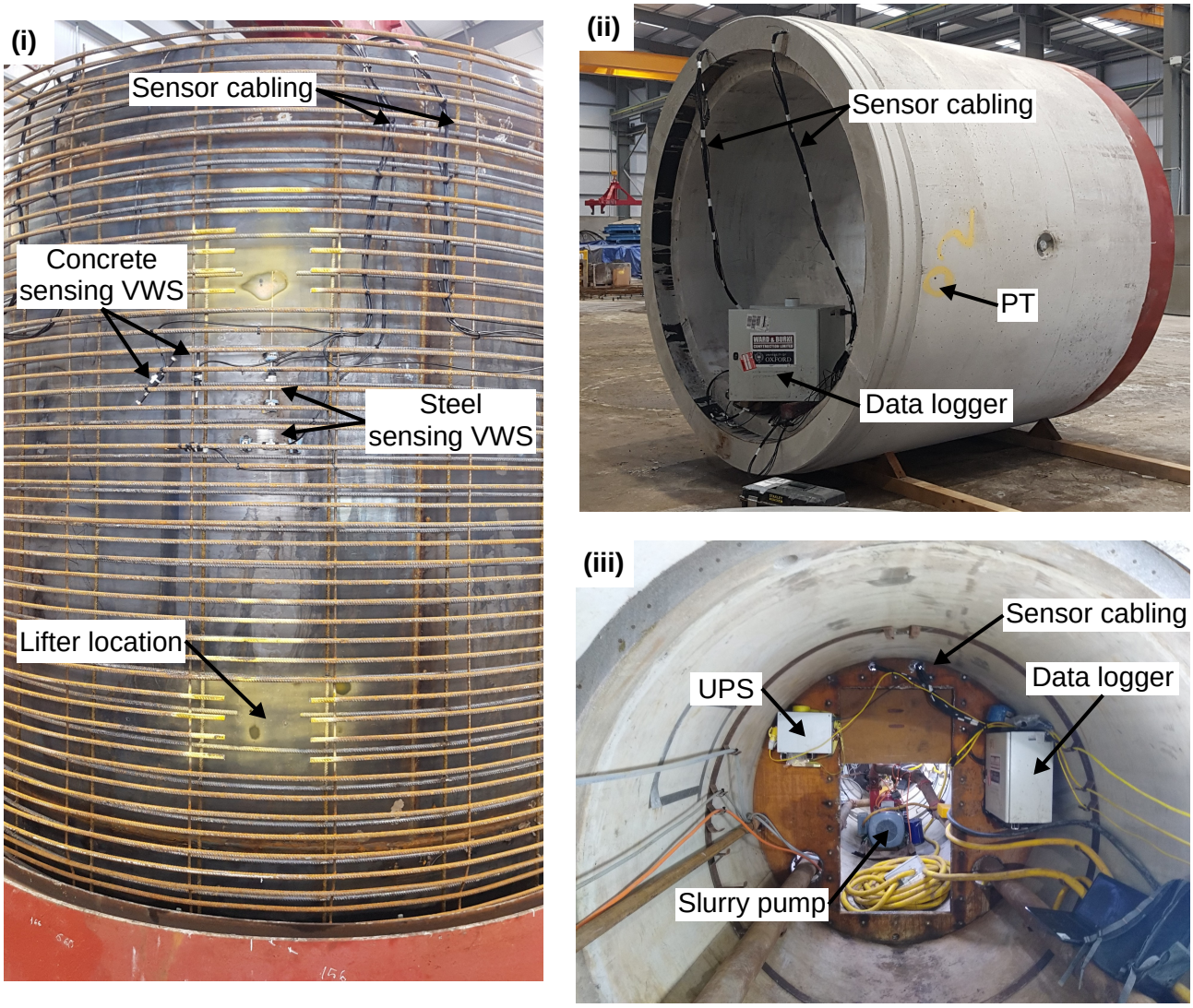


Figure 3.5: Putney instrumented pipe during different stages of the project: (i) VWS on the reinforcement and steel can, (ii) the IP after casting logging zero data in the casting facility, (iii) IP during data logging during the drive.

Before the pipe was delivered to site, a steel bulkhead was installed to enable pressure testing and grouting of the tunnel section ahead of the pipe in the permanent condition. The UPS and data logger were mounted to this, as shown in Figure 3.5 (iii). Baseline readings were then taken for 24 hours before the pipe was installed as pipe number 5 of the drive, starting 10 m behind the TBM.

In addition to the IP, distributed lubricant pressure monitoring was also installed on the drive. Pressure sensors were incorporated into the lubrication system between the control box and the port through the pipe wall. Although less accurate than direct measurement from the tunnel overcut, this approach is expedient and as such it is more likely to be taken up by

industry for future projects.

Figure 3.6 (i) shows the distributed pressure sensor fitted to the lubrication stations 1, 3 and 5 of the drive (3 m, 14.5 m and 41 m behind the head of the TBM) on the feed to the *SW* lubricant port. These were fitted with a 3/4" diaphragm to avoid the Bentonite clogging the small sensor orifice. These were connected into the lubricant control box on the discharge side of the control valve via a T fitting. Another sensor (Figure 3.6 (ii)) was installed onto lubrication station 9 (91 m behind the TBM) and fitted with a larger 2" diaphragm. This is the standard tunnelling sensor fitted to the lubricant distribution line at ground level and was used to compare the relative merits of the smaller, cheaper, and easier to install 3/4" sensors. Due to size limitations at the lubrication station, this sensor was connected at the *SW* delivery port through the pipe wall and an additional cable was led back to the control box. The first method of connection (i.e. at the control box) resulted in the pressure sensor being further from the delivery port, but allowed it to be left in-situ between tunnel drives. Whilst the second method provided a pressure reading closer to the delivery port, the sensor was exposed (and therefore more likely to be damaged) and had to be re-installed into each tunnel drive, making it less likely to be adopted in practice.

Data was gathered using the VMT guidance system for the tunnel drive via an additional input box (VMT GMBH (2019)). These are commonly used for connecting sensors at interjack locations to measure the interjack data and were installed with minimal additional time and cost. The data were displayed in the control container in real time during the tunnel drive to provide information to the TBM operator and supervising engineer.

3.1.6 Historical drive database

HK tunnelling systems record detailed tunnelling information by default in two databases. The first, confidential database, is available only to HK technicians and is used for diagnosis of the equipment and identification of faults. The second database provides information to the site team on key tunnelling parameters, these are given in Table 3.3, below. This table also includes

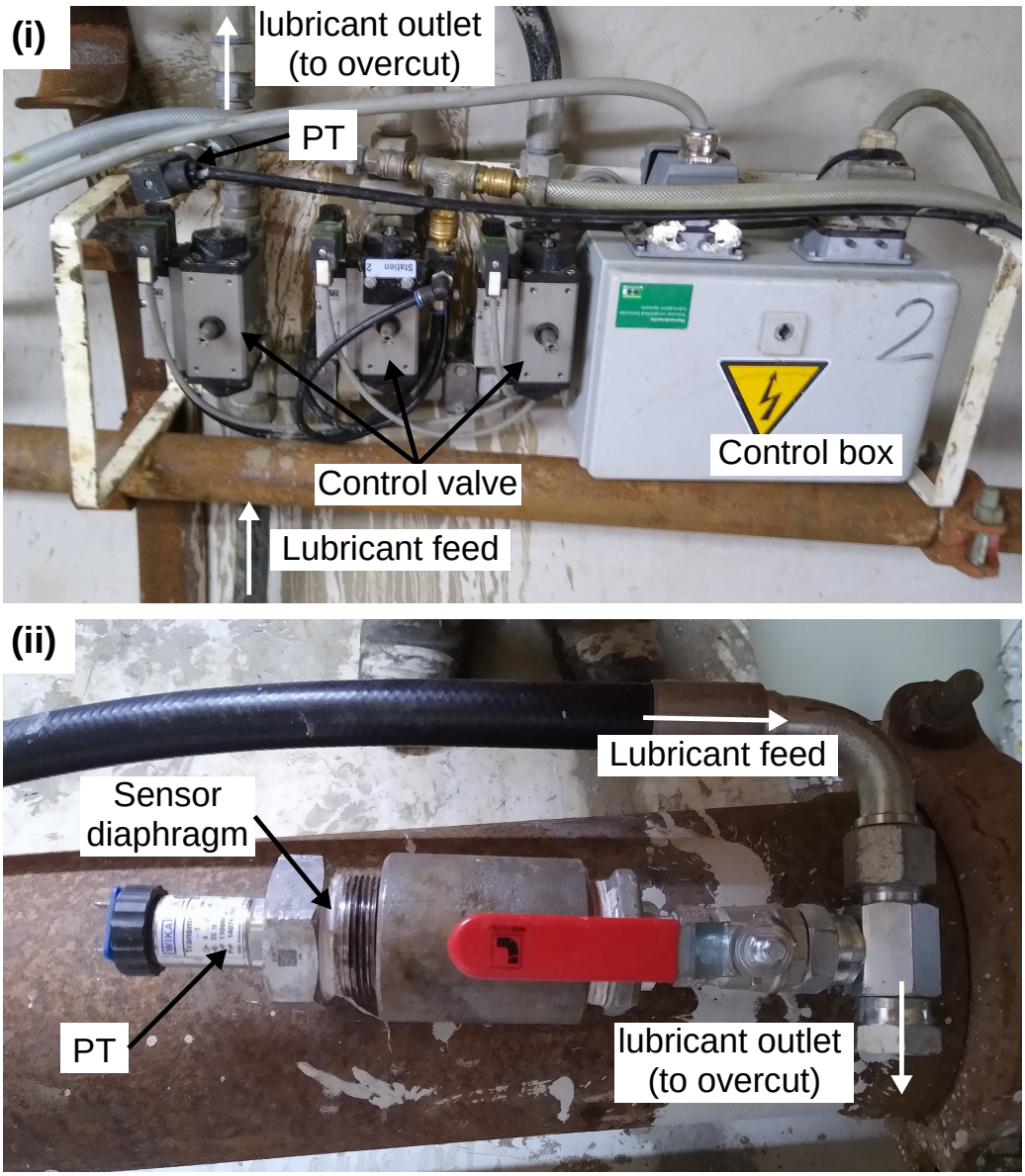


Figure 3.6: Overcut pressure sensor connections: (i) 3/4" at lubrication station, (ii) 2" at delivery port.

guidance data, such as the deviations from desired alignment. The type of guidance required for a drive varies depending on the alignment. For short and straight drives, a laser defines the desired profile and a receiver target on the machine calculates the deviations. These are then displayed in the control container to guide the TBM operator. For more complex alignments, such as those with curves, a VMT guidance system is typically used (VMT GMBH (2019)). In this system, a robotic total station is used in the tunnel to calculate the TBM position using the length of the tunnel and reference targets within the tunnel pipes. Information stored by this system is shown in Table 3.4.

These parameters were compiled into a database of tunnel drive data for interpretation alongside additional information collated from the tunnel sites. Where available, information such as TBM operators logs, ground condition logs, alignment drawings and site investigations, lubrication mix designs, and lubricant mixing logs were also stored, so that a more detailed understanding of the tunnel drive process could be developed. From this database key parameters, such as P, R and F can be examined, to identify trends in the data which indicate SLS interface behaviours.

Table 3.3: Parameters recorded in the HK system database

No.	Parameter
1	Time
2	Date
3	Chainage
4	Advance Rate
5	Cutting head hydraulic pressure
6	Cutting head speed
7	Horizontal and vertical deviation
8	Total jacking force
9	Pitch, roll, and yaw of TBM
10	Steering cylinder stroke
11	Steering cylinder pressure
12	Steering cylinder average stroke
13	TBM temperature
14	Pore pressure in excavation chamber
15	Feed pump(s) power(s) and RPM(s)
16	Return pump(s) power(s) and RPM(s)
17	Slurry feed line flowrate and pressure
18	Slurry return line flowrate and pressure
19	Interjack forces
20	Bentonite line pressure
21	Active Bentonite line
22	Bentonite volume pumped
23	Bentonite distribution box
24	Bentonite distribution valve
25	Bentonite command time
26	Bentonite valve open duration
27	Bentonite volume pumped
28	Input ground type
29	Interface friction condition
30	Target Bentonite amount

Table 3.4: Parameters recorded in the VMT system database

No.	Parameter
1	Pipe number
2	Horizontal and vertical deviation at cutting edge
3	Horizontal and vertical deviation at the TBM
4	Horizontal and vertical deviation at target in machine
5	Machine tenancies
6	Northing, easting, elevation of cutting head
7	Northing, easting, elevation of machine pipe
8	Northing, easting, elevation of target in machine
9	Northing, easting, elevation of all target prisms
10	Northing, easting, elevation of total station
11	Angles to target locations
12	Roll of reference pipes and total station pipe

3.2 Laboratory elemental lubricant testing

3.2.1 Scope of parametric study

To identify changes in the salient Bentonite properties which occur during pipe-jacking a parametric study was completed. The objective of the study was to establish the relative dependence of Bentonite filtration rate, filter cake formation, viscosity, and yield stress on the following controlled variables:

1. **Bentonite type** - both Tunnel Gel and Hydraul-ez Bentonites were examined.
2. **Concentration** - tests were conducted at water/Bentonite ratios of between 12:1 and 24:1 (8.3% to 4.1%).
3. **Additive concentration** - the effect of TK60 and PAC-L at concentrations of 0.5, 1, 2, and 4 kg/m^3 were examined.
4. **Temperature** - samples were tested at ambient temperatures (18^oC to 23^oC) and at 15^oC, 20^oC, 30^oC, 40^oC, and 50^oC to examine the effect of temperature on Bentonite behaviour.
5. **Filtration pressure** - the effect of altering the filtration pressure on the filtration rate was assessed at pressures of 25 kPa, 50 kPa, 100 kPa, 200 kPa, 300 kPa, 400 kPa, and 500 kPa. The tests at lower pressures ($<$ 100 kPa) were of particular importance as these were close to the observed over pressures in overcuts during typical field tunnel drives.

3.2.2 Sand selection

The objective of the sand selection was to identify a sand with a particle distribution that would allow a filter cake to form, whilst limiting the Bentonite's penetration into the sample - to limit the size of the testing apparatus required. Praetorius and Schößer (2017) and Min et al. (2013) identified that the transition from internal to external filter cake formation occurred when soils had a 10% passing fractions $D_{10} \approx 1$ mm: in soils with $D_{10} > 1$ mm an internal filter cake typically forms, whilst an external cake is expected to develop for $D_{10} < 1$ mm.

A sand with a D_{10} close to this threshold was selected - 14/25 grade Leighton Buzzard sand. The 14/25 sand was procured from Aggregate Industries Leighton Buzzard facility (Aggregate Industries (2022)) for this research as similar sands had been used in previous studies such as Royston (2018), Richards (2019), and Mayall et al. (2020). A test program was conducted to determine the properties of the two tonnes of 14/25 used during the research. The results, and basis of the values, are shown in Table 3.5.

Table 3.5: Summary of the salient 14/25 sand properties.

Parameter	**Symbol**	**Value**	**Unit**	**Basis**
Maximum density	γ_{max}	17.0	kN/m^3	3 tests
Minimum density	γ_{min}	14.2	kN/m^3	10 tests
Particle specific gravity	G_s	2.66	-	Supplier
Minimum void ratio	e_{min}	0.566	-	3 tests
Maximum void ratio	e_{max}	0.834	-	3 tests
Particle shape	-	Sub angular to rounded	-	Supplier
Critical state friction angle	ϕ'_{cs}	33.2	°	14 tests
10% passing fraction	D_{10}	0.74	mm	5 tests
50% passing fraction	D_{50}	0.91	mm	5 tests
90% passing fraction	D_{90}	1.09	mm	5 tests
Coefficient of uniformity	C_U	1.44	mm	Supplier
Coefficient of curvature	C_Z	0.96	-	Supplier

Tests were completed to calculate the maximum density of the sand (γ_{max}). When completed to the BSI method (British Standards Institution (1990)), these yielded $\gamma_{max} = 16.2kN/m^3$ which was considerably less than the value obtained for a similar sand quoted in Richards (2019). Testing to the same standard was also completed on the samples used by Richards (2019) which yielded γ_{max} lower than reported in the research. As such, 3 tests were completed to the BSI method but compacting the sand in 10 layers (as opposed to three in the standard). These tests yielded γ_{max} = 17.0 kN/m^3, with a variation of less than ± 0.1 kN/m^3, which was used for further calculation.

3.2.3 Selected lubricants and additives

Tunnel Gel, manufactured by Cebo Holland (Cebo Holland BV (2019)), is the primary Bentonite lubricant considered, due to its use in the field drives analysed during this study.

It is a pre-mixed Sodium Bentonite produced in Greece, but the manufacturer publishes no additional information about its constituent components, or mechanical properties. For comparison, *Hydraul-Ez* is also considered. This is produced by Cetco (Cetco Minerals Technologies (2019)) and is supplied as pre-mixed Sodium Bentonite originating in Wyoming (U.S.A). It is described as a "200 mesh" Bentonite with a "special polymer additive", though Cetco do not publish information on what the polymer additive is. A US standard 200 mesh corresponds to a maximum particle size of 75 μ m within the Bentonite clay.

Two commonly used additives were also used, PAC-L and TK60. These are described as a filtrate reducer and viscosifier, produced by Halliburton and Morrison Mud respectively (Halliburton (2021); Mudtech LTD (2022b)). These are typically added to Bentonite lubricants at concentrations of between 1 kg/m^3 and 4 kg/m^3 or, in the case of TK-60, mixed with water alone to form a polymer slurry.

3.2.4 Sample preparation

All samples for testing were prepared using an identical method. Up to 10 kg of water was first weighed, then placed in a suitable mixing vessel. The temperature, pH, hardness, and conductivity of the water were measured, such that the water was only used if the values were within the limits recommended by Praetorius and Schößer (2017) i.e. a pH > 7, hardness < 250 ppm $CA^{2+} or Mg^{2+}$, and conductivity < 600 $\mu S/cm$. There was some variation in properties during the test program and these are summarised in Table 3.6, below.

Table 3.6: Summary of salient laboratory and mixing water parameters.

Property	**Unit**	**Mean value**	**Range**
Laboratory temperature	^oC	21	± 5
Mixing water temperature	^oC	12	$+2, -1$
Mixing water pH	-	7.8	± 0.3
Mixing water hardness	ppm	180	-
Mixing water conductivity	$\mu S/cm$	350	-

A variable speed mixer was positioned such that the mixing blades were $\sim$ 25 mm from the base of the mixing vessel. The water was then set to mix with the blades rotating at 960

rpm. The required quantity of Bentonite clay (weighed to 0.1 g accuracy) was slowly added, to ensure that the clay fully dispersed within the water. Once all of the Bentonite had dispersed, additives (weighed to 0.1 g accuracy) were also added (if appropriate). The mixing speed was then incrementally increased to 2060 rpm for twenty minutes to ensure complete mixing of the slurry components at a high shear rate.

Samples were covered and left to hydrate for a minimum of 12 hours before use. Post-hydration, samples for density, filtration, and viscometer testing were mixed at 2060 rpm for at least 5 minutes to break down any structures formed during hydration. Samples in the SLS interface apparatus hopper were mixed using a set of blades attached to a battery drill, with a rotation of 1750 rpm, for at least 5 minutes before use.

3.2.5 Test methodologies

Once mixed, the density, or mud-weight, of the samples were tested using the methodology of American Petroleum Institute (API) recommended practice note 13B-1 (American Petroleum Institute (2003)), which is adapted from ISO standard 10414-1 (British Standards Institution (2011)). A mud balance cup (Figure 3.7) was filled with slurry, the cap installed, and any excess carefully removed from the outside. This was then placed onto the balance and the slide weight adjusted until a level balance point was found. The density and temperature of the sample were then recorded. Due to the potential variability of this test, a minimum of three readings were taken for each Bentonite mix.

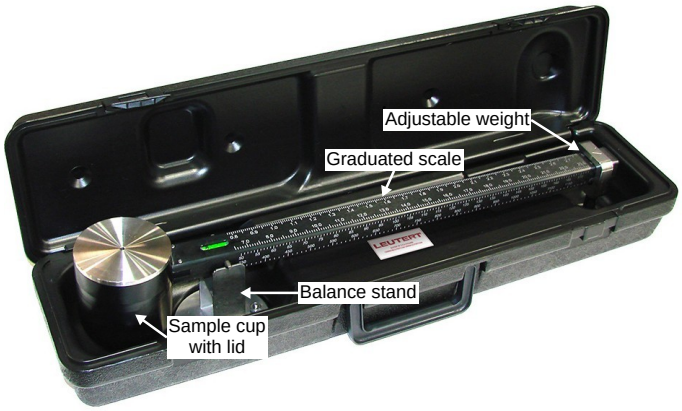


Figure 3.7: API mud balance apparatus.

The filter loss rate of the Bentonite mixtures was assessed using an API filter loss apparatus as shown in Figure 3.8. Due to limitations of the laboratory compressed air supply, 500 kPa pneumatic pressure was applied to the samples instead of the standard 689 kPa (American Petroleum Institute (2003)). This was deemed acceptable for two reasons: firstly, the filtration rate of Bentonite at lower filter pressures was of greater relevance to this research; and secondly, a parametric study was being completed to ascertain the relationship between pressure and filtration rate for the Bentonites.

To prepare a test, the mesh was covered by a sheet of filter paper and the pipework to the filtrate collection beaker was bled. The sample mixture was then carefully poured on-top of the saturated paper to ensure no air was entrained. Once the sample was 10 - 15 mm from the top of the chamber, the lid was secured in position, the pressure was then applied (via the opening of a ball valve) to filter the Bentonite mixtures through the 45.8 cm^2 filtration area of the cell. The weight of filtrate was recorded using a 2 kg load cell, logging at 1 Hz.

The pipework between the chamber and collection beaker was calculated to create a small suction pressure on the sample base of up to 0.2 kPa (depending on the exact configuration) due to the vertical height difference between the chamber and discharge to the beaker. This increased the effective filtration pressure slightly and was accounted for in the results. After 30 minutes of filtration, the test was halted, and pressure reduced to atmospheric. The volume of filtrate was then recorded and the sample removed from the chamber. The top of the filter cake was identified by gently washing the top of the sample to remove any unfiltered Bentonite mixture, leaving only the consolidated cake. Finally, samples of both the cake and excess slurry were weighed and dried to ascertain the water contents.

Previous literature, such as Vryzas et al. (2017) and Mohammed (2017), determined the temperature filtration relationship varies between different Bentonite lubricants and as such temperature dependency testing was required as part of this research. To complete tempera-

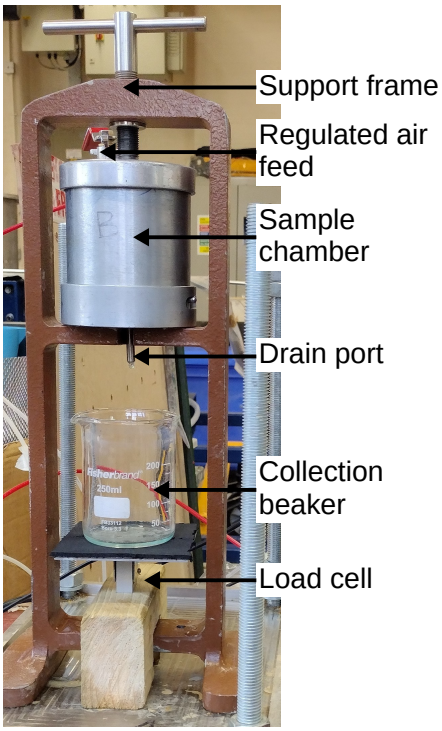


Figure 3.8: API filter press apparatus during testing.

ture dependency tests, the filtration apparatus was pre-heated to the test temperature before being filled as per the previous methodology within the heated chamber. To ensure uniform temperature within the sample and apparatus, both were left within a sealed chamber at test temperature for 90 minutes before the test commenced. The test then proceeded as previously described. During these tests, the rate of evaporation from the collection beaker was recorded and corrected for in the results.

Slurry viscosity and yield strength were measured using a 6 speed FANN model 35 direct reading viscometer, as shown in Figure 3.9. The rotation speeds of the instrument were 3, 6, 100, 200, 300, and 600 minute^{-1}. The viscosity ν_i (where i denotes the rotation speed) was recorded for the slurry by shearing the sample at the selected rate until the reading stabilised. To calculate the industry parameters of plastic viscosity ν_p, apparent viscosity ν_a, and plastic yield point Y_P the following procedure was used: i) the instrument was filled with slurry to the required level (marked by a notch on the wall of the sample cup), ii) the sample temperature was recorded, iii) the sample was sheared at 600 minute^{-1} until a steady state reading was reached

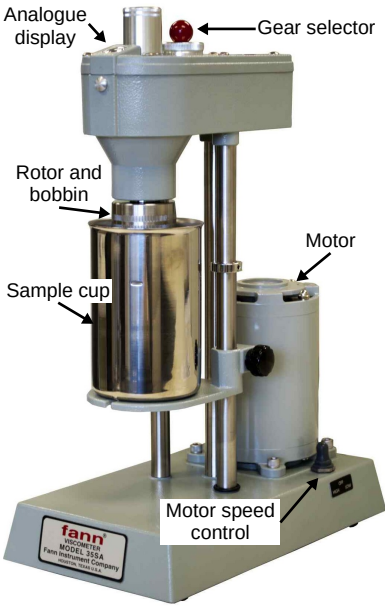


Figure 3.9: Viscometer apparatus (courtesy www.fann.com).

and recorded, and iv) the shear rate reduced to 300 minute^{-1} and the viscosity recorded once steady state was reached. From these two readings ν_p, ν_a, and Y_P were calculated as:

$$\nu_p = R_{600} - R_{300} \tag{3.1}$$

$$\nu_a = \frac{R_{600}}{2} \tag{3.2}$$

$$Y_P = 0.48(R_{300} - \nu_P) \tag{3.3}$$

where R_i indicates the dial reading at a given shear rate i.

Tests were conducted to ascertain the relationship between yield stress and time since shearing. These tests consisted of mixing the sample at a shear rate of 300 minute^{-1} until steady state before shearing at 600 minute^{-1} for 30 s. At this time the instrument was stopped for a given duration (10 seconds, 10 minutes, or 30 minutes) before being restarted at the lowest shear rate (3 minute^{-1}) and the peak reading recorded.

To convert the dial gauge readings from the FANN instrument into SI units the following equations were used:

$$\nu_N = S.\phi.f.C \tag{3.4}$$

where ν_N is the Newtonian viscosity, S is the speed factor (from Table 3.7), f is the spring

factor (1 for the F1 spring used), C is the rotor-bob factor, and ϕ is the dial reading. The viscometer was used in the "R1-B1-F1" configuration, meaning that the standard bob, rotor, and torsion spring were used. The corresponding C in this case was 1.

Table 3.7: Speed factors used in converting FANN 35 dial gauge readings into viscosities and shear values.

Instrument speed (rpm)	**Speed Factor** (-)
3	100
6	50
100	3
200	1.5
300	1
600	0.5

Shear stress τ (with units of kPa) was then calculated as follows:

$$\tau = \frac{k_1.k_2.\phi}{10} \tag{3.5}$$

where k_1 is 386 dyne per cm per degree deflection, and k_2 is the "shear stress constant for effective bob surface" (0.01323 for the configuration used).

Finally, the shearing rate is calculated as:

$$\gamma_r = k_3.N \tag{3.6}$$

where N is the rotor speed (rpm), and k_3 is the shear rate constant (1.7023 for the R1-B1 rotor - bob combination).

3.3 Shear box apparatus

3.3.1 Apparatus overview

One of the potential sources of frictional increase during tunnel stoppages is the filter cake surrounding the tunnel pipe shearing, or the tunnel pipe shearing against the filter cake. To assess the extent of the filter cake's influence on friction, a bespoke consolidation shear box apparatus was developed to quantify the shear stresses of consolidated Bentonite filter cakes. The consolidation shear box consisted of two PTFE sections, as shown in Figure 3.10, with a

58.5 mm diameter, 50 mm deep, circular sample chamber confined by a top cap with double O-ring seals. PTFE was selected as the shear box material to reduce friction during shearing. An additional recess, 10 mm wide, was machined into both of the sections to minimise sample - box contact, and further reduce friction, during shearing.

To apply a normal stress to the sample during consolidation and shearing, load was applied to the top cap via a kentledge frame to achieve stresses of 12.5 kPa $< \sigma_N <$ 300 kPa. Drainage was provided through the top cap by machined grooves, whilst a 10 mm layer of epoxy stabilised sand, 2 mm below the shear plane, provided the bottom drainage. Filter paper was used to stop Bentonite penetration into the sand during testing.

3.3.2 Test procedure

To prepare a consolidation shear box test, the two sections of the apparatus were first clamped together. The drainage lines were bled with water and the lubricant was then prepared as detailed in Section 3.2.3 and, once aged, placed into the sample well until 10 mm below the rim. The top cap was installed and depressed to bleed out any air between the cap and sample. The loading frame was then installed before the dial gauges were positioned to record consolidation settlement, and kentledge load applied. Photographs of the apparatus during consolidation as shown in Figure 3.11.

To commence the test, the drainage valves were opened until either the desired consolidation time, or degree of consolidation had been reached. The drain lines were then closed and the clamping screws (holding the two sections of the shear box together) were removed. Stand-off screws were then used to achieve 1 mm clearance between the two shear box sections during shearing. Finally, the shear test was conducted at a rate of 1.2 mm per minute in both forward and reverse directions to achieve undrained conditions at the shear interface, as these were experienced during the field studies discussed in Chapter 4. During testing, the vertical displacement of the top-cap (δ_v) was recorded, alongside the shear displacement (δ_h) and actuation force. As the shear interface area changed during a test (up to 13.0% over δ_h

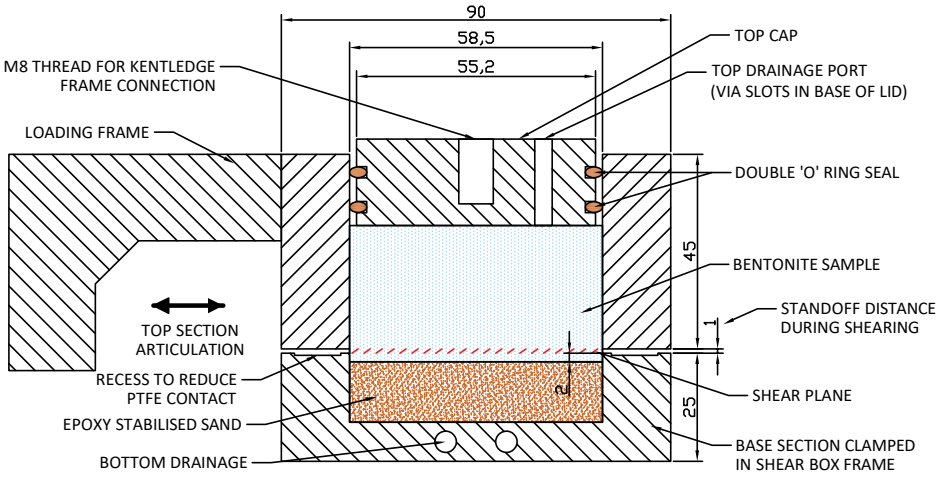


Figure 3.10: A section drawing through the consolidation shear box apparatus with key features and dimensions labelled.

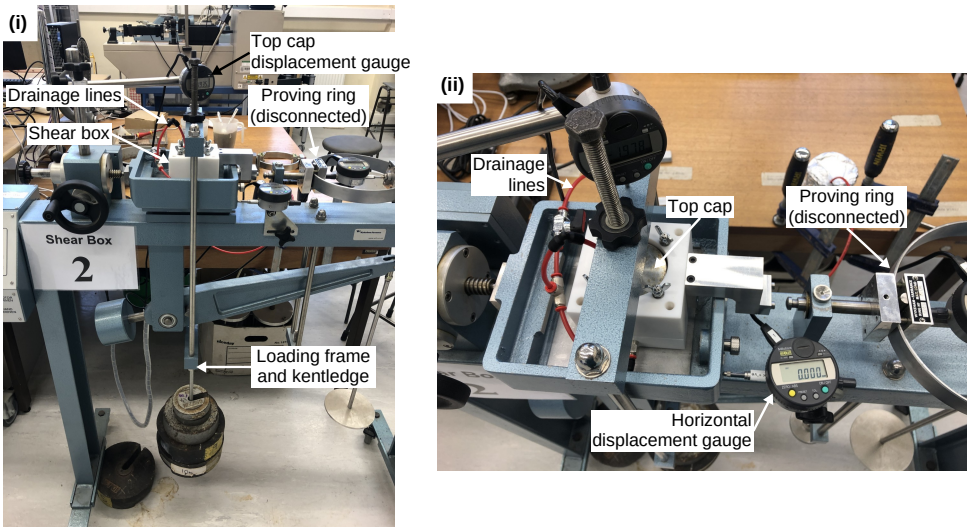


Figure 3.11: Overview of the consolidation shear box apparatus during testing.

= 6 mm), it was calculated and corrected for in the results. After the test, the top cap was removed and consolidated Bentonite lubricant carefully extracted to measure the water content of the resulting mixture.

3.4 Permeameter apparatus

3.4.1 Apparatus overview

The bespoke permeameter apparatus was developed to investigate how changes in mix and pressure change the infiltration (or spurt) distance of Bentonites into sand. It was also intended to identify consolidation and/or filtration mechanisms in the tunnelling lubricant at the SLS interface using detailed pore pressure measurements. Once these had been identified for a baseline case, a parametric study examining the effects of Bentonite concentration, filtration

pressure, and additive concentration on filtration rate and filter cake formation was to be completed. The API filter press was deemed insufficient to achieve these objectives, as to accurately recreate the overcut conditions in the field the Bentonite must penetrate into soil (not mesh as in the API filter press). The penetrating Bentonite wave-front must also be allowed to stagnate within the soil sample naturally, i.e. without reaching the edge of the apparatus. This requires a soil sample thickness which is not possible in the filter press.

A bespoke permeameter was therefore fabricated, consisting of an acrylic cylinder 140 mm in diameter and 350 mm high, similar to Min et al. (2013) and Xu and Bezuijen (2019). A drainage layer consisting of mesh was installed to the column 10 mm above the base and sealed around the perimeter, providing free drainage to the base of the column whilst preventing lubricant from penetrating into the drainage line. To allow access to the top of the column, a stainless steel top-cap was manufactured with two O-ring seals. This was restrained by a reaction frame, as shown in Figure 3.12.

Pressure was applied using the regulated laboratory air supply, with a maximum design pressure of 150 kPa within the column. Pressures to be tested in the column were initially determined using the equations proposed by Atkinson and Potts (1977), described in Section 2.3. These equations yielded overcut pressures (P_a) in the range 3.9 kPa to 7.8 kPa for a tunnel axis depth of 5 m, soil friction angle of 34°, and soil density of 18 kN/m^3. These magnitudes are less than those predicted by Terzaghi's soil arching theory (Terzaghi (1943)) (41 kPa) and pressures observed during the field monitoring during the Putney tunnel drive ($\sim$ 50 kPa - 80 kPa). Due to this variability, a test program was conducted considering 25 kPa $\leq P_a \leq$ 100 kPa in 25 kPa increments. As the discharge to the collection beaker was below the apparatus, the discharge pipe generated a suction of 2 kPa at the base of the chamber, which was corrected for in the results.

Pressures were monitored using 689 kPa capacity pressure sensors supplied by Omega

(OMEGA Engineering (2021)) which were connected to the column through capillary lines tapped through the column at 20 mm increments. A National Instruments (NI) cDAQ using 24 bit NI-9237 modules was used to provide 40 mPa resolution on pressure measurements. Filtrate weight was recorded using a 10 kg capacity load cell, connected to the reaction frame. As the test apparatus was effectively earthed, the noise in the signals was determined to be negligible.

All sensors were zeroed at the beginning of testing to remove the influence of Bentonite head. During testing, the permittivity of individual bands of the system were calculated, where a 'band' is defined as the layer of soil between two pressure sensor locations, as shown in Figure 3.13. To calculate permittivity, the pressure drop between the sensors (ΔP_i) and weight of filtrate (ΔW) were calculated for a given time step (Δt). The permittivity was then calculated, using equation 3.7, for typical timesteps of 1 $s^{1/2}$ (elapsed since the start of the test).

$$K_{i,t} = \frac{\Delta W}{\Delta t.A_c.\rho} \frac{\Delta X_i.\nu_v}{\Delta P_i} \tag{3.7}$$

where $K_{i,t}$ is the permittivity of the band i mm from the soil - lubricant interface at time t, ΔX_i is the distance between the sensor locations, ρ is the density of the filtrate water (taken as 1000 kN/m3), A_c is the plan area of the column apparatus (0.0154 m^2), and ν_v is the dynamic viscosity of the filtrate water.

3.4.2 Sample preparation

To prepare a sand sample within the permeameter apparatus, the column was first filled with water before the drainage lines and capillary tubes were bled to remove any air. The required depth of saturated sand was then wet pluviated through the water column, to ensure uniform sample preparation and removed any air. Once the sand was at the correct depth, the water level was drained to the sand surface, which was then levelled by carefully removing any excess sand. For tests where a large spurt distance was anticipated (such as those at high

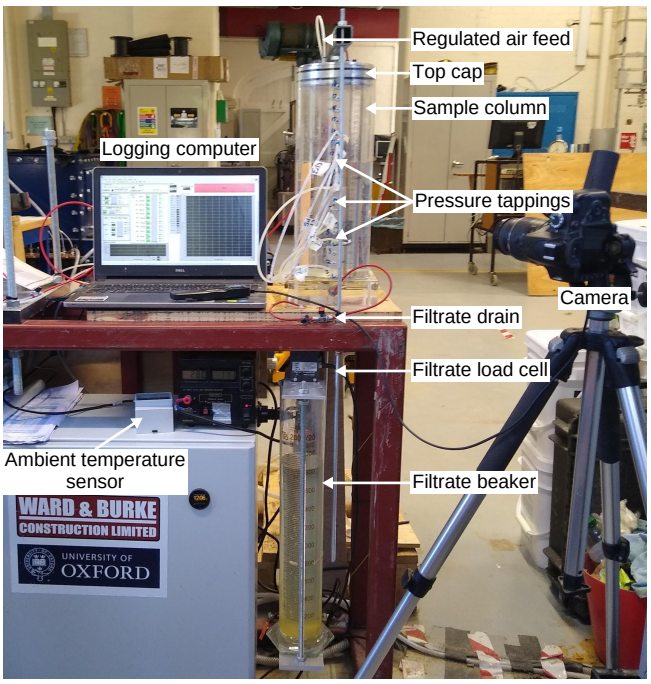


Figure 3.12: Bespoke permeameter apparatus before filling with sand and lubricant sample.

Bentonite mix ratios or applied pressure) this method was modified to allow for a greater sample depth within the column. In these cases, the sand interface was prepared to 40 mm - 60 mm below the top cap using the wet pluviation method. The void between this and the top cap was then completely filled with lubricant and any air purged. An external reservoir of lubricant was connected through a 1/2" port in the top cap and air pressure applied to this reservoir. A limitation of this method was that, during the initial stages of a test, the rapid flowrate of the lubricant through the pipework resulted in decreased pressure within the column. The applied pressure was manually adjusted to compensate for the losses. However, this did increase variability in the applied stress during the first 10 minutes of tests, after which, the flow rate slowed, and the losses reduced.

To confirm the repeatability of the sample preparation method, both the global and local density of multiple samples were assessed. The global density was determined by measuring the volume of the cylinder to the sand fill depth using water (V), before the dry weight of the sand sample prepared using the wet pluviation method described above was measured (W).

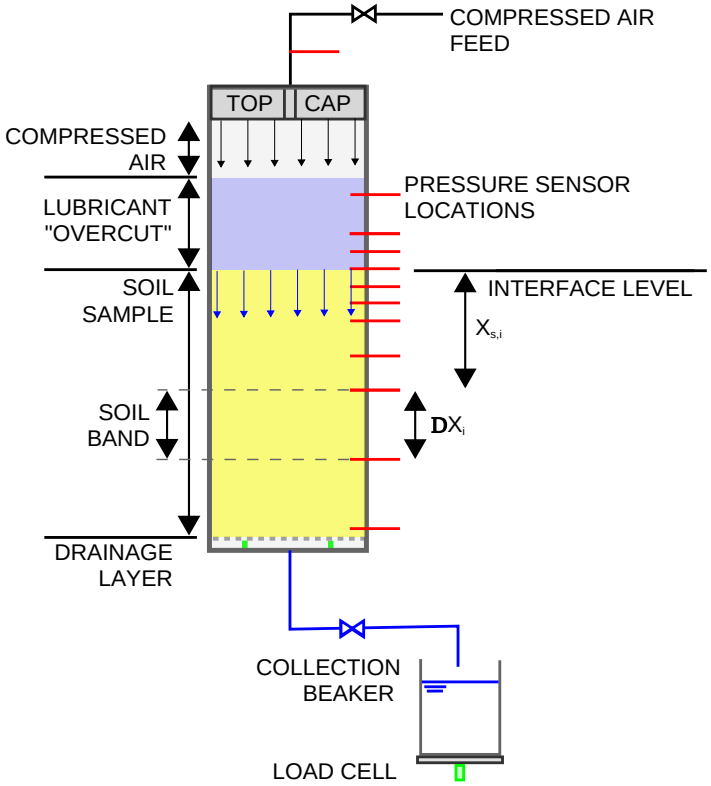


Figure 3.13: Schematic of bespoke permeameter apparatus with salient features labelled.

The density was then determined using:

$$\gamma = \frac{W}{V} \tag{3.8}$$

Relative density was then calculated as:

$$D_r = \frac{\gamma_{max}}{\gamma} \frac{\gamma - \gamma_{min}}{\gamma_{max} - \gamma_{min}} \tag{3.9}$$

To examine the uniformity within the sample, cone penetration tests (CPTs) were conducted on samples using the apparatus developed by Mayall (2019) and previously used for the characterisation of 14/25 Leighton Buzzard sand by Richards (2019) and Mayall et al. (2020). The 8 mm diameter CPT probe was penetrated into the 240 mm deep sample 200 mm to avoid overloading the mesh in the base of the permeameter or the CPT probe tip. The tip resistance, q_c, was then used to calculate the relative density of the sample using empirical correlations of the form:

$$D_r = a_1 + a_2.ln(\frac{X_c}{a_3}) \tag{3.10}$$

where a_1, a_2, a_3 are fitting constants and X_c is the normalised tip resistance:

$$X_c = \frac{q_c/p_{ref}}{(\sigma'_v/p_{ref})^{1/2}} \tag{3.11}$$

where p_{ref} is a reference pressure of 100 kPa and σ'_v is the vertical stress in the soil. The vertical stress profile of the soil was assumed from the global density measurement through:

$$\sigma'_v = (\gamma - \gamma_w)X \tag{3.12}$$

where X is the depth below the soil surface. As the fitting parameters were calculated using dry samples the results were corrected using the method devised by Jamiolkowski et al. (2003) to account for reduced friction in the saturated case using Equation 3.13.

$$D_{r,sat} = D_r(0.9813 + 0.0232X_c) \tag{3.13}$$

Fitting coefficients from Mayall (2019) and Templeman (2023), shown in Table 3.8, were used to calculate D_r from the results. The Mayall (2019) analysis utilised the same sand fraction and supplier as this study, though γ_{min} and γ_{max} varied slightly. The calculated D_r profiles and average D_r between -30 mm $\geq X \geq$ -200 mm are shown in Figure 3.14.

Table 3.8: Fitting coefficients for relative density calculations from Mayall (2019) and Templeman (2023).

Source	**Sand type**	a_1 (-)	a_2 (-)	a_3 (-)	γ_{min} (kNm^{-3})	γ_{max} (kNm^{-3})
Mayall (2019)	14/25 LB	-22.39	16.48	1	14.43	17.64
Templeman (2023)	14/25 LB	-45.02	25.53	1	14.2	17.0

The global D_r which was calculated to be 0.25 ± 0.2 for the samples assessed. Analysis using both Mayall (2019) and Templeman (2023) parameter sets provide a good fit to the data, with Average D_r similar to the globally calculated value. The D_r of the column increased with depth from 0.15 at X = -40 mm to 0.35 at X = -200 mm. These changes correspond to a decrease in void volume of 5% between the top and bottom of the column, which was deemed acceptable.

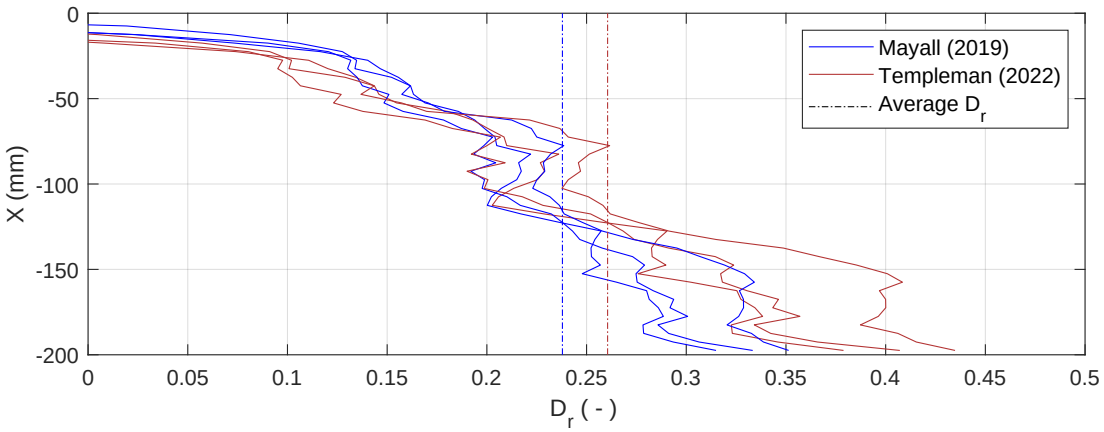


Figure 3.14: D_r profile of prepared permeameter samples. D_r calculated using Mayall (2019) and Templeman (2023).

The permeability of the sand-column system was assessed to allow comparison to the tests using Bentonite. Samples were prepared as detailed above before water was flushed through at pressures of between 25 kPa and 100 kPa. The permeability of the system was then calculated to be 3.4 m/s $\pm$ 0.5 m/s. The variability of the measurement was due to noise in the load cell caused by the rapid filling of the collection beaker.

3.4.3 Test procedure

To complete a permeameter test, lubricant samples were first prepared and aged following the procedure described in Section 3.2.3. The lubricant was then placed onto this interface, ensuring no air was entrained within the sample. The top cap was installed and clamped into position using the reaction frame. The test was then started by setting the required test pressure using the regulator. This was then applied to the sample over 30 s and, once the pressure had stabilised, the drain line was opened, and the time recorded. During the spurt phase, the lubricant wave-front location was recorded using a Nikon D3200 camera and timer at intervals of between 1 s and 60 minutes, depending on the rate of advance. Pressures were logged at 1 Hz for the start of the test, with the rate reduced to 0.1 Hz as the test progressed.

Once the desired test duration had elapsed, the pressure was released, and the top cap was removed. Samples of the slurry and filter cake were taken at 10 mm increments between 50 mm and the interface. These samples were weighed, dried, and re-weighed to calculate the

water content. The depth of filter cake was recorded together with any qualitative observations about its appearance and consistency. 1" core samples were taken, photographed, and dried to confirm the depth of the lubricant wave-front within the sample matched the perimeter of the column. The column was then emptied, and pressure readings were recorded, to ensure the pressure transducers had not experienced zero drift during the test.

4 | Field study results

4.1 Analysed tunnel drives

From the tunnel drive database described in Section 3.1.6, 14 drives have been extracted for analysis: the Castlerigg instrumented tunnel drive ($D1$), the Putney instrumented tunnel drive ($D2$), five drives in Hull, UK ($D3$ - $D7$), and seven drives in Dublin, Ireland ($D8$ - $D14$). The Castlerigg and Putney tunnel drives were selected as these were monitored during construction using IPs. The Hull and Dublin drives have been selected as each provided multiple drives with the same: TBM and operator, tunnel pipes, lubricants, and tunnelling equipment, thereby removing these elements as potential influencing factors on the data. In addition, as the Dublin and Hull drives were geographically close together, the ground conditions were similar along their length.

The Hull drives were predominantly in soft peat and clay, whilst the Dublin group were in sands and gravels, with Drives 'C' and 'D' encountering some limestone along its alignment. A summary of the key parameters of these case studies is given in Table 4.1. The table also provides details of the lubricant mix used in each case study, with all except the Putney drive (D2) using Tunnel Gel (TG) Bentonite at an 18:1 (Bentonite : water ratio by weight) and, in some instances, TK60 and PAC-L polymers, and the lubricant pipe spacing along the drive, which varied between 12.5 m and 20 m depending on the ground conditions.

In Putney, the client restricted the use of Bentonite lubricants due to a perceived risk of Bentonite polluting the river Thames, similar to Taylor (2021). For this reason, a lubricant formed of TK60, PAC-L and Sloop was used. Sloop is a proprietary polymer designed to mimic the properties of traditional Bentonite lubricants (Mudtech LTD (2022a)). The polymer mixture was tailored by the site operatives to match the Marsh funnel time of the 16:1 TG mix originally intended for the drive.

Table 4.1: Summary of key information for field tunnel drive case studies.

Drive Number (-)	**Drive name** (-)	**Drive length** (m)	D_O (m)	**Ground type** (-)	**Lubricant make-up** (-)	**Lubricant pipe spacing** (m)
D1	Castlerigg	1137	2.756	Mudstone[1]	TG:TK60:PAC-L	20
D2	Putney	137	2.980	Clay / gravel[2]	TK60:PAC-L:Sloop	12.5
D3	Hull A	165.5	1.490	Peat / soft clay	TG	16
D4	Hull B	47.2	1.490	Peat / soft clay	TG	16
D5	Hull C	141.4	1.490	Peat / soft clay	TG	16
D6	Hull D	195.2	1.490	Peat / soft clay	TG	16
D7	Hull E	266.2	1.866	Peat / soft clay	TG	16
D8	Dublin A	602	1.866	Gravel	TG	16
D9	Dublin B	387	1.866	Gravel	TG	16
D10	Dublin C	338	2.224	Gravel[3]	TG	16
D11	Dublin D	336	2.224	Limestone[4]	TG	16
D12	Dublin E	387	2.224	Gravel	TG	16
D13	Dublin F	154	2.224	Gravel	TG	16
D14	Dublin G	546	2.224	Gravel	TG	16

[1] The first 200 m and final 100 m of the drive were in Glacial till soils.
[2] Drive was a mixed face of gravel over clay. Varying between almost fully gravel at the start of the drive to almost fully clay in the centre.
[3] Drive through Limestone first 60 m.
[4] Drive with partial face of Limestone and gravel.

4.2 Tunnel advance rates

To gain insight into the shearing conditions experienced at the SLS interface during field tunnel drives it is essential to quantify the tunnel advance rates, as well as the frequency and duration of tunnel stoppages. To achieve this, the data collected from the 14 tunnel drives are examined in this section for use guiding both the elemental and scale laboratory experimentation described in Chapters 5 and 7 respectively.

Figure 4.1 presents the relationship between tunnelled chainage (i.e. the location of the TBM face; x) and elapsed time (t), for the 14 selected tunnel drives, grouped into the four

main site locations. Stoppages are notable in the figure as horizontal lines and can be broadly grouped into two types:

1. **Short duration** - defined as $t_s \leq 14$ h and are typically caused by pipe changes, alignment surveys, or overnight breaks in tunnelling. Overnight breaks in tunnelling were observed to typically be up to 14 h due to the time taken to shut down the tunnelling equipment at the end of a 12 h shift and restart it the following morning. These stoppages are routine during tunnelling, as shown by the high frequency in Figure 4.2, and should be anticipated during all tunnel drives.
2. **Long duration** - defined as $t_s > 14$ h and are typically caused by either: weekend breaks in tunnelling (e.g. at $t = 4.5$ days in D3), or mechanical breakdowns of the TBM or supporting equipment (e.g. $t = 10.5$ days in D6 or $t = 6.5$ days in D2). These are considerably less common during tunnelling.

The difference in frequency of the two classes of stoppage is shown in Figure 4.2 (i), where the frequency of stoppage per 1 m advanced (N_1) is compared across the examined tunnel drives. From the figure it is clear that stoppages ≥ 14 h are significantly less frequent than those < 14 h. Variability between different drive groups is also apparent, which suggests a relationship between ground conditions and number of stoppages.

The penetration rate (P_r) is typically defined as the rate of change of tunnelled chainage (i.e. $\frac{dx}{dt}$) which varies between a few mm per minute to ≥ 300 mm per minute, depending on various factors including: ground conditions, TBM diameter, and separation plant effectiveness. Two subtle variations on this definition are considered here:

1. Net advance rate ($\overline{P_r}$). This is defined simply as the chainage divided by the total elapsed time and is given in units of mm per minute. It gives a measure of the overall productivity of the tunnel drive, but does not account for variations in P_r during the advances.
2. Average time stopped ($\overline{t_s}$). This measures total time stopped during the tunnel drive

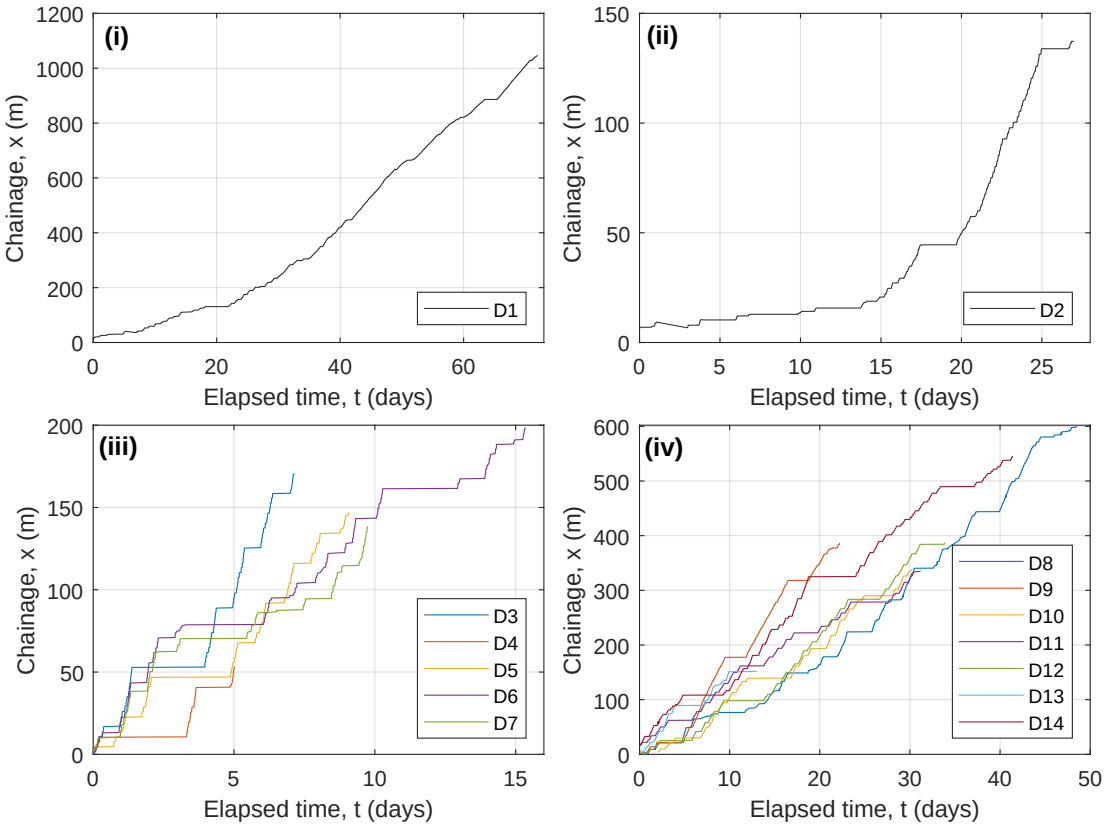


Figure 4.1: Time histories of tunnelled distance for the 14 tunnel drives examined in this study. Drives are split into the four locations: (i) Castlerigg, (ii) Putney, (iii) Hull, (iv) Dublin. Note that D1 and D2 contained IPs.

(t_s) and is given units of hours per 100 m advanced. In this analysis, stoppages of < 1 h are not considered as part of this metric. The metric is used to differentiate between drives with high and low values of P_r and t_s, which could result in similar calculated $\overline{P_r}$ values. The stoppages themselves can be further broken down into the bands proposed by Pellet-Beaucour and Kastner (2002) for comparison. The bands are defined as: (i) $1 \leq t_s < 1.5$, (ii) $1.5 \leq t_s < 3$, (iii) $3 \leq t_s < 14$, (iv) $14 \leq t_s < 20$, and (v) $20 \leq t_s$.

$\overline{P_r}$ and $\overline{t_s}$ are plotted for the 14 drives considered in this study in Figure 4.2 (ii) and (iii) respectively. Although $\overline{P_r}$ and $\overline{t_s}$ appear linked in most cases, there are outliers which demonstrate the importance of both metrics. For example, $D11$ has a slightly lower $\overline{P_r}$ than average for the Dublin drive group (D8 to D14), but has a significantly higher $\overline{t_s}$ due to long duration stoppages coupled with a high P_r whilst tunnelling. The data also show that, with

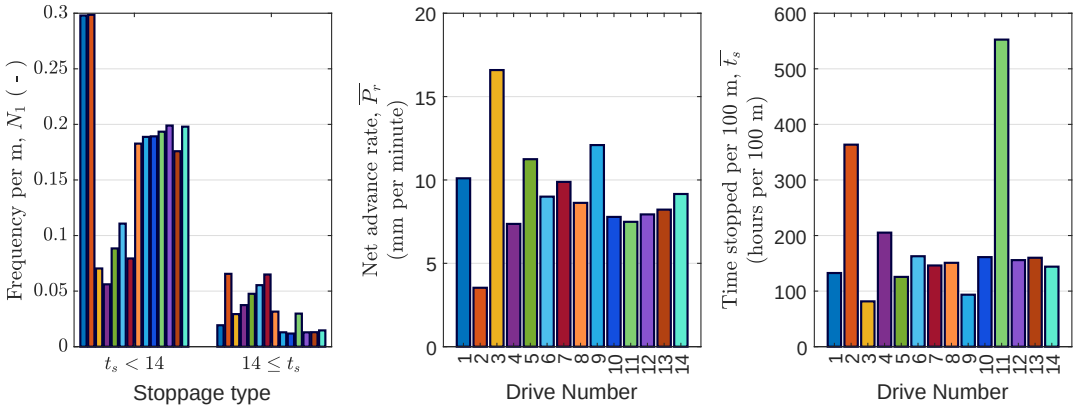


Figure 4.2: Advance related parameters calculated from the 14 assessed tunnel drives: (i) The number of short ($<$ 14 h) and long ($\geq$ 14 h) stoppages per 1 m advanced, (ii) the net advance rate ($\overline{P_r}$), and (iii) the time stopped per 100 m advanced ($\overline{t_s}$).

the exception of D3 and D9, both the Dublin and Hull drive groups have similar P_r and T_s values, despite the frequency of short and long stoppages being different.

4.3 Axial force measurement

In Figure 4.3, the development of jacking force P and face resistance R measured by the TBM during drive D1 is shown as a function of chainage. The drive was conducted with P of under 10,000 kN, and R typically in the range 400 kN $< R <$ 1200 kN. There was a peak in R between 800 m $< x <$ 900 m of $>$ 2000 kN, where a fracture in the rock was encountered and higher water pressure was measured at the face of the TBM. The measurements from four VWS cast into the IP wall in the axial direction were used to calculate the axial force in the IP (P_{IP}), 537 m behind the TBM, as follows:

$$P_{IP} = \frac{\sum_{i=1}^{4} \epsilon_i}{4} A_w.E_p \tag{4.1}$$

where ϵ_i is the axial strain measurement of sensor i, A_w is the pipe wall area and E_p is the pipe wall Young's modulus. This approach assumes that the pipe wall has uniform axial strain across its width and uses a calculated value for E_c, as it was not possible to test the concrete directly. To validate these assumptions, the calculated P_{IP} should match P during the initial launch, as the IP was directly attached to the jacking frame, from which P is calculated. For

D1, these values aligned well with an error of 6% to 8% between P and P_{IP} during the advance, and a similar magnitude of difference (250 kN to 330 kN) was noted between P and R during the TBM launch, thus validating the adopted approach to infer P_{IP} from strain measurements.

It is evident from the data that the friction on the pipe string (i.e. P - R) was highly variable during the drive. For example at between x = 380 m and x = 420 m chainage P reduced from 4500 kN to 3000 kN whilst R remained relatively constant. This example corresponds to the commencement of 24 hour working and a decrease in the number of stoppages occurring, whereas a large peak in P of $>$ 8500 kN occurred after a long stoppage at 890 m. The difference between P_{IP} and R also varied throughout the drive, demonstrating that the friction in 537 m of tunnel string between the IP and the TBM varied during the drive.

The other instrumented tunnel drive at Putney (drive D2) exhibited more relative variation in R during the drive, as shown in Figure 4.4. The reduction in R throughout the drive was largely a result of TBM control, as the slurry pressure in the excavation chamber was reduced as the drive advanced to avoid blow-out (whilst maintaining sufficient face support). The reduction in P between 25 m and 40 m chainage was due to the commencement of lubrication, as a technical issue had prevented its use prior to this. The effects from stoppages can also be observed in the drive, for example at 44 m and 134 m chainage there were 54 and 41 hour stoppages respectively. These resulted in a ΔP of 750 kN and 900 kN respectively.

Due to debonding of the concrete and steel 'can' within the Putney IP wall, the stress state within the wall could not be accurately determined and therefore P_{IP} could not accurately be calculated. Hence it is not shown in Figure 4.4. The debonding occurred as there were no shear studs connecting the steel can to the concrete external or internal pipe lining. This meant that only surface adhesion was maintaining the joint. It was found that under load, the pipe would deform slightly, and this would cause the two components to separate. Additionally, as the internal concrete lining shrunk during curing, it separated from the steel can. This allowed

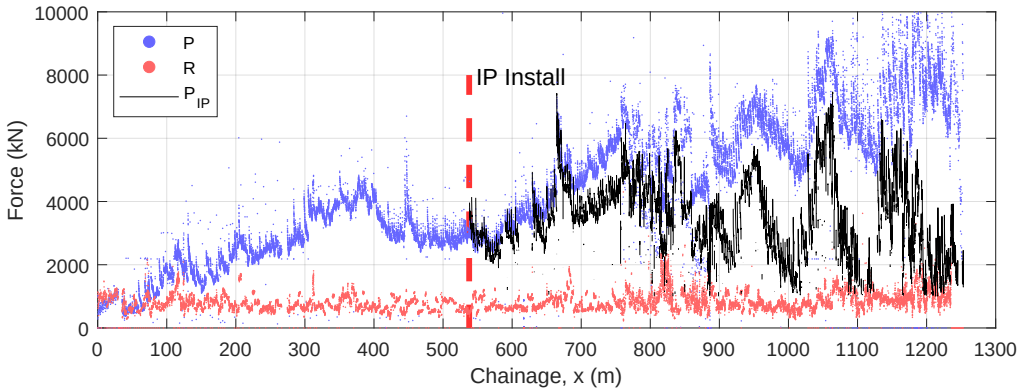


Figure 4.3: Development of total jacking force (P), face resistance (R), and IP axial force P_{IP} with chainage during the Castlerigg instrumented tunnel drive, D1.

slippage to occur at the joint, such that the stress state in the pipe wall could not be accurately predicted.

Data from drives D3 - D8 in Hull are plotted in Figure 4.5. In the soft clay ground conditions at Hull, P and R are similar for all drives - demonstrating low interface friction on the pipe string during jacking under steady state conditions. The D8 tunnel drive gave erroneous R readings throughout the drive, due to the diameter of the steering cylinders being input into the control program incorrectly. To correct this, a mean ratio of the head force to total jacking force ($\frac{R}{P}$) was calculated over the first 5 m of the drive and the derived factor was applied to the R data to correct the scaling error. Stoppages during tunnelling resulted in peaks in the forces, for example 54 m chainage in D3 where a 62 h stoppage resulted in a ΔP of 342 kN. Also, a timber obstruction was encountered at a chainage of 110 m in drive D6, which resulted in an increase in R and P for 20 m until the obstruction cleared the cutting head of the TBM.

Drives in gravel, such as drives D8 - D14 in Dublin, have historically presented with larger P and R values than those in clay due to an inability for the lubrication system to maintain a stable overcut. A significant difference between R and P is shown in Figure 4.6, highlighting the friction forces observed during the drives, despite the use of automated lubrication systems and industry best practice techniques. The low interface friction apparent in the first 50 m of drive D10 (Figure 4.6 (iii)) was due to the drive tunnelling through predominantly Limestone,

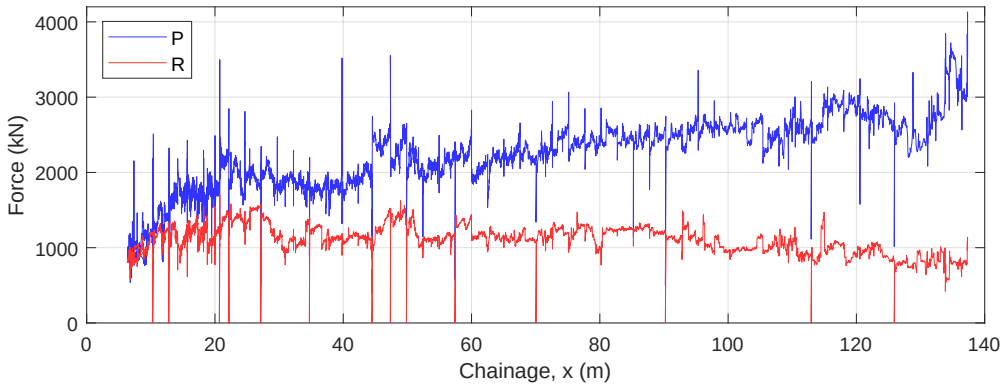


Figure 4.4: Development of total jacking force (P) and face resistance (R) with chainage during the Putney instrumented tunnel drive, D2.

after which the friction increased due to the remainder of the drive being in gravel. The effect of stoppages are also visible in the data, although their impact is less significant due to the already higher interface friction. For example, at 444 m in drive D8 a 62 hour weekend stoppage resulted in $\Delta P = 1500$ kN with near zero difference in R.

To ascertain the resultant location of axial force within the pipe string, the axial strain measurements recorded by the IPs during drives D1 and D2 were used. For drive D1, the resultant force magnitude, radial offset from the centre, and phase were calculated. The phase of the resultant force was measured anticlockwise from the N position (i.e. $W = 90^o$) and the deviation from the pipe centre was normalised by $\frac{D_O}{2}$. The results from this analysis are shown in Figure 4.7.

These data show that during the straight D1 drive, the resultant axial force was located within the top half of the pipe section for 75 % of the distance advanced, suggesting that the friction force on the pipe extrados was concentrated in the top half. As the pipe is buoyant in the lubricant, this result shows that during an advance the top section of the pipe was in contact with the soil, or filter cake formed at the lubricant-soil interface. This contact resulted in a higher interface friction than at the base of the tunnel where the pipe was in contact with the lubricant. This difference led to the resultant force location being in the top half of the pipe. It also suggests that the pipe overcut was free from fines, which have been shown to

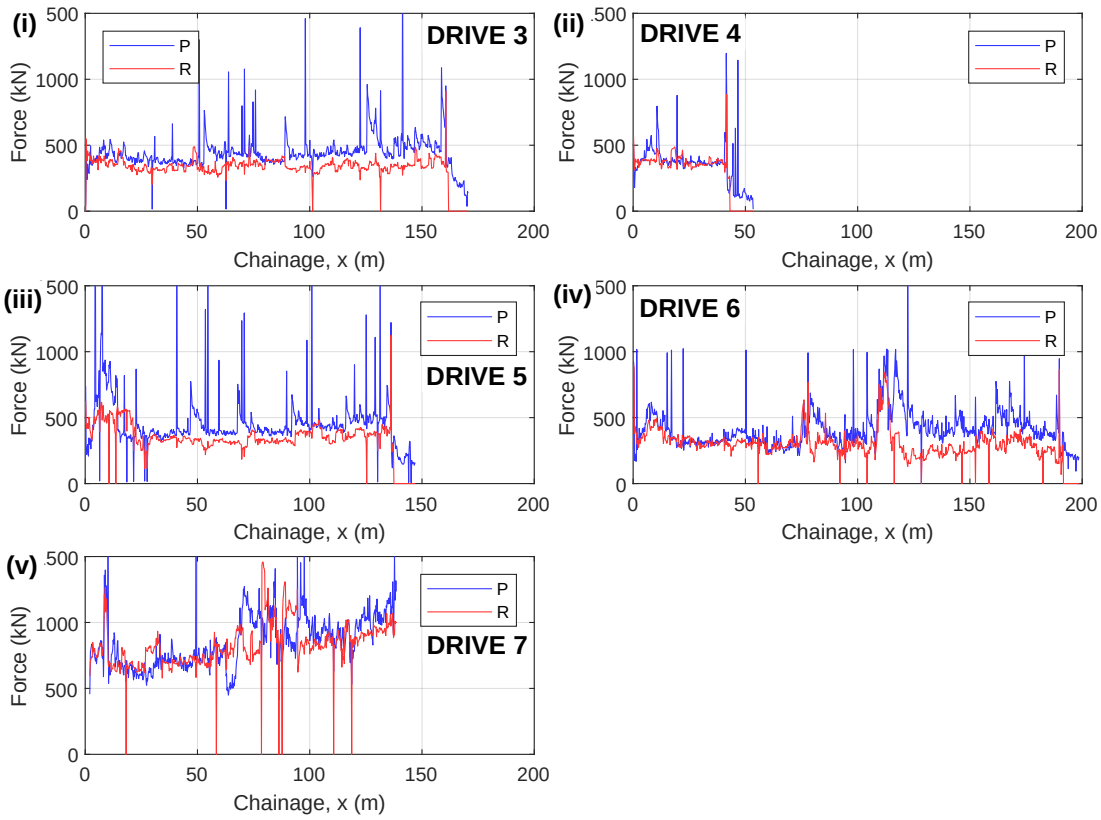


Figure 4.5: P and R variation with distance tunnelled for drives D3 (i) to D7 (v) in the Hull group of tunnel drives in soft clay.

generate friction at the bottom of the tunnel bore.

The calculated resultant force deviation reduced during periods of high axial load, whereas deviation increased as the axial force reduced during pipe changeovers. This was due to the compression of the packing material between the pipes distributing the load more evenly at higher axial force. The resultant force increase after stoppages is also evident, for example at 127 m IP chainage in Figure 4.7 (iii), where a 20.4 hour stoppage led to an increase of 3243 kN increase in thrust load through the IP.

Due to a VW logger failure during the Putney drive D2, the strains of the steel can within the pipe wall were not recorded. As the interaction between the can and the reinforced concrete section of the wall altered the force transmission, accurate resultant force locations were not possible to calculate. Instead, the measured strains from the eight sensors in the pipe wall are assessed. The development of axial strain measured by the eight VWS with IP chainage is

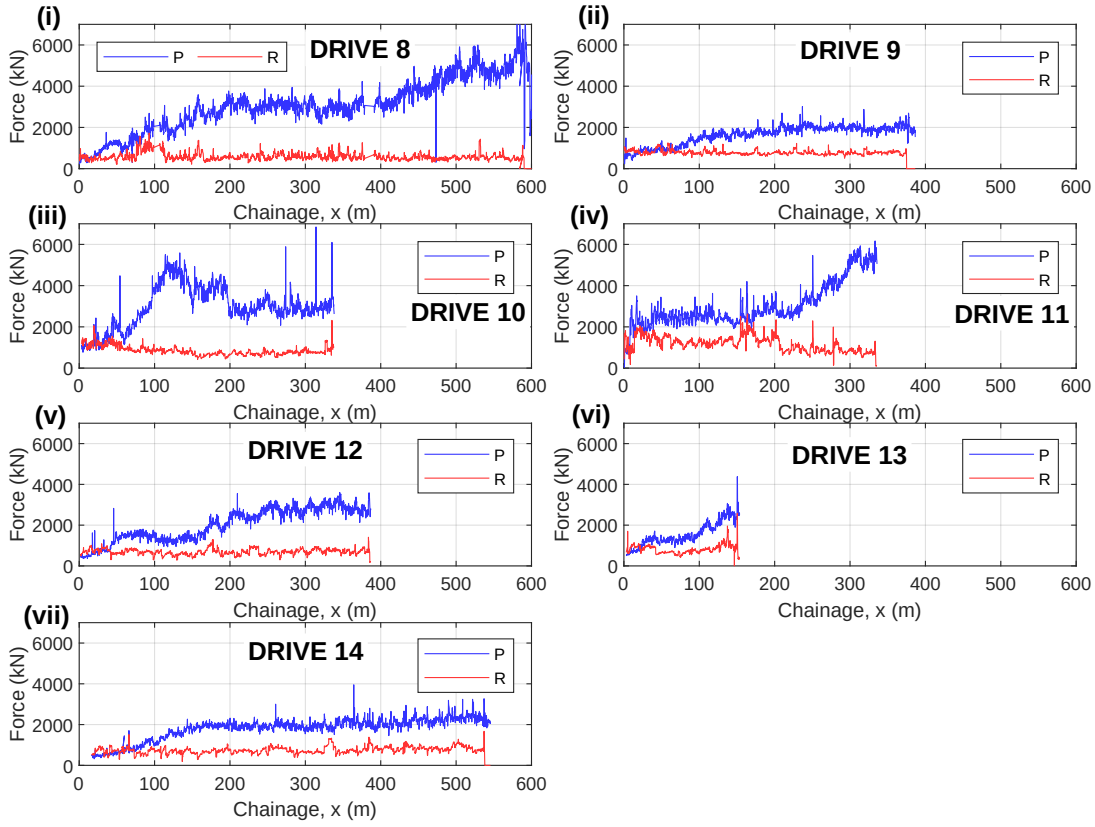


Figure 4.6: P and R variation with distance tunnelled for drives D8 (i) to D14 (vii) from the Dublin group.

shown in Figure 4.8, with compressive stresses shown as negative. The plotted strains ($\Delta\epsilon$) are compared to the zero reading recorded before the pipe was lifted into the launch excavation.

The effect of the drive curvature on the force distribution is shown in Figure 4.8 by the strain gauge in the E position measuring large compressive strains of up to -76 $\mu\epsilon$ between 70 m and 100 m IP chainage (as it was located on the inside of the curve). The N, S, and W sensors all show tension during this period, with a maximum value of 25 $\mu\epsilon$. These data also show a noticeable 'saw tooth' pattern in the results, with $\sim$ 500 mm at the start of every pipe advance recording less compressive strain in the pipe (e.g. at 77.5 m chainage). This was caused by compression of the pipe string as it overcame the interface friction after a new pipe was installed resulting in the measurement wheel for the drive (which logs the distance advanced at the launch shaft) recording a forward movement before the TBM itself began to advance. As the pipe string compressed, the load through the IP increased to the level required

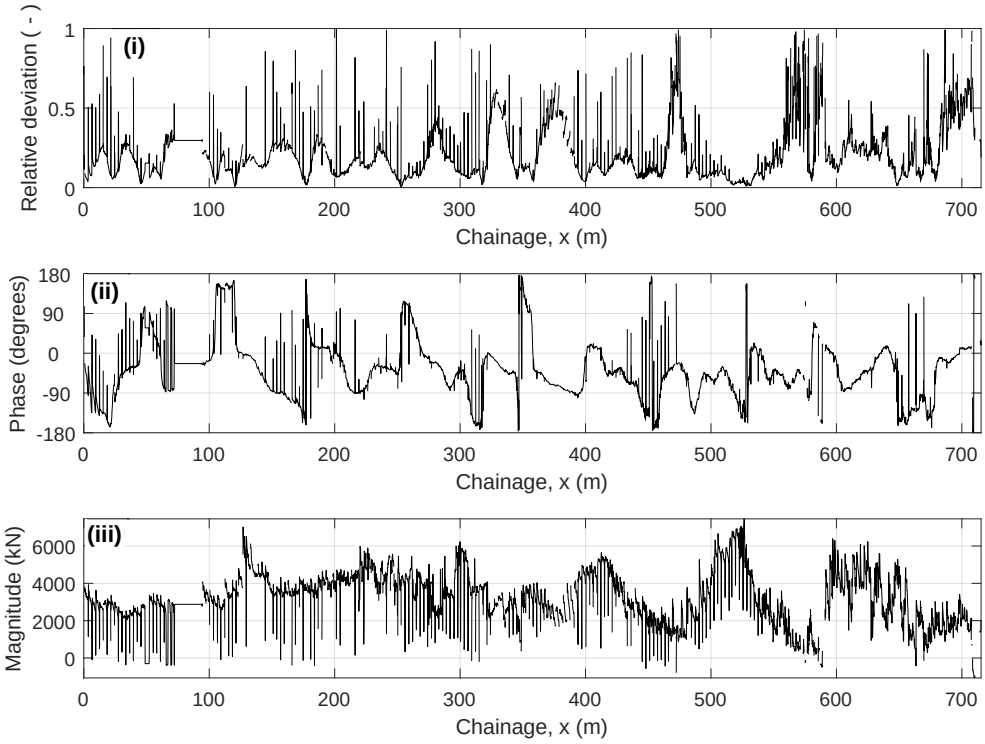


Figure 4.7: Axial force variation with IP chainage from D1: (i) the resultant axial force relative deviation from the IP centroid, (ii) the resultant phase, and (iii) magnitude (P_{IP}).

to advance the TBM and pipe string, similar to the previous reading.

These data also demonstrate that friction was generated in the lower half of the pipe throughout the drive. During a given advance the S, SE, and SW sensor record more compressive strain than the N, NE, and NW sensors respectively, particularly during the curve (i.e. between 70 m to 100 m chainage). This shows the resultant force location was in the bottom half of the pipe, which would have been due to the friction between the pipe extrados and the tunnel bore as the pipe was not buoyant in the fully lubricated overcut, due to the increased wall thickness.

4.4 Interface friction

The force data from the monitored tunnel drives demonstrates that the P - R relationship varies throughout the different tunnel drives. The cause of the variation is the interface friction

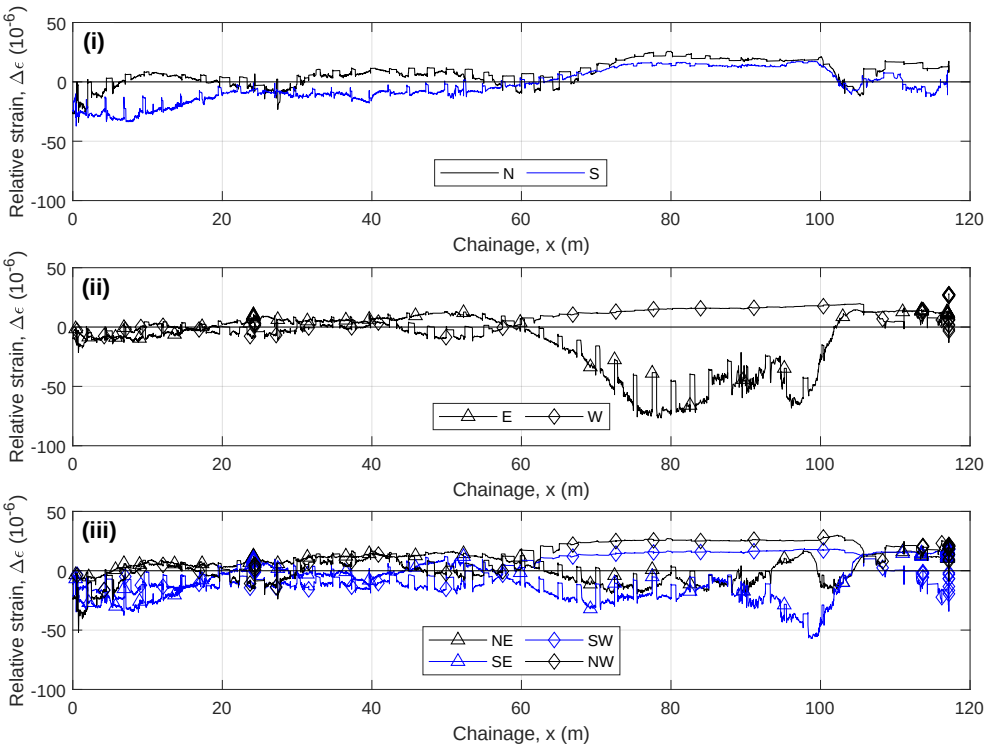


Figure 4.8: The development of axial strains with IP chainage measured during D2. Sensors are plotted in diametrically opposite pairs: (i) N - S, (ii) E - W, (iii) NE - SW and SE - NW. Compressive strains are defined as negative.

(τ) between the pipes and surrounding ground, which is calculated as follows:

$$\tau = \frac{P - R}{\pi . D_O . x} \tag{4.2}$$

where x is the current tunnel chainage. Figure 4.9 highlights this variation by plotting the development of τ with increasing chainage in the four tunnel groups considered. Where there are multiple tunnel drives in a given location, i.e. drives D3 - D7 in Hull or drives D8 - D14 in Dublin, the average friction of the group ($\overline{\tau}$) is shown as well as the individual drive friction, where $\overline{\tau}$ is calculated using a moving average of all individual τ values within a window of one pipe length.

The drives in soft clay at Hull (D3 - D7) recorded the lowest friction values of 0.2 kPa $< \tau <$ 0.6 kPa after the first 30 m. The largest frictions were observed in the drives in gravel with 0.6 kPa $< \tau <$ 3.5 kPa measured during drives D2 and D8 - D14. Nevertheless, these values are significantly lower than those previously quoted in the literature; e.g. Yonan (1993) ($>$ 25

kPa), or Stein (2005) (3 kPa $< \tau <$ 5 kPa), which highlights the improvements in lubrication effectiveness since the previous research was published, particularly in the soft clay and rock conditions.

Figure 4.9 (iii) and (iv) show similar friction values across the drives in each group, which also demonstrates the consistency of modern tunnelling techniques. This means that an empirical model of force prediction is suitable for tunnel drives, due to the highly consistent friction data. The peak in Figure 4.9 (iv) at $x = 110$ m shows drive D10, where problems with the tunnel lubrication system resulted in insufficient lubricant being delivered and higher interface friction measurements. These were resolved and the re-introduction of lubrication is shown to reduce τ to the normal range.

To assess the impact of stoppages on τ, periods of > 1 h duration were extracted for further analysis. 1 h was selected as a minimum time period for analysis because it was found that the large number of stoppages of < 1 h duration had significantly different τ responses. Due to the large number of these stoppages logged on each drive it was not possible to identify the causes of the different τ responses and draw meaningful conclusions from the data. Therefore, by reducing the number of events (through increasing their minimum duration) it was possible to identify the causes of the different τ responses and identify the relationships and trends in the data.

The difference in τ before and after a stoppage ($\Delta\tau$) was calculated for all stoppages with $t_s > 1$ h. To avoid erroneous readings (i.e. those caused by the hydraulic jacking cylinders becoming fully extended), the minimum value of τ in the 50 mm advanced before the stoppage was used as the pre-stoppage value. Similarly, the maximum value of τ within 50 mm distance following the restart was selected as the restart value. $\Delta\tau$ was then defined as the difference between these values two quantities, the magnitude of the friction increase during the stoppage ($\Delta\tau$) the rate of friction increase ($\frac{\Delta\tau}{t_s}$) were calculated.

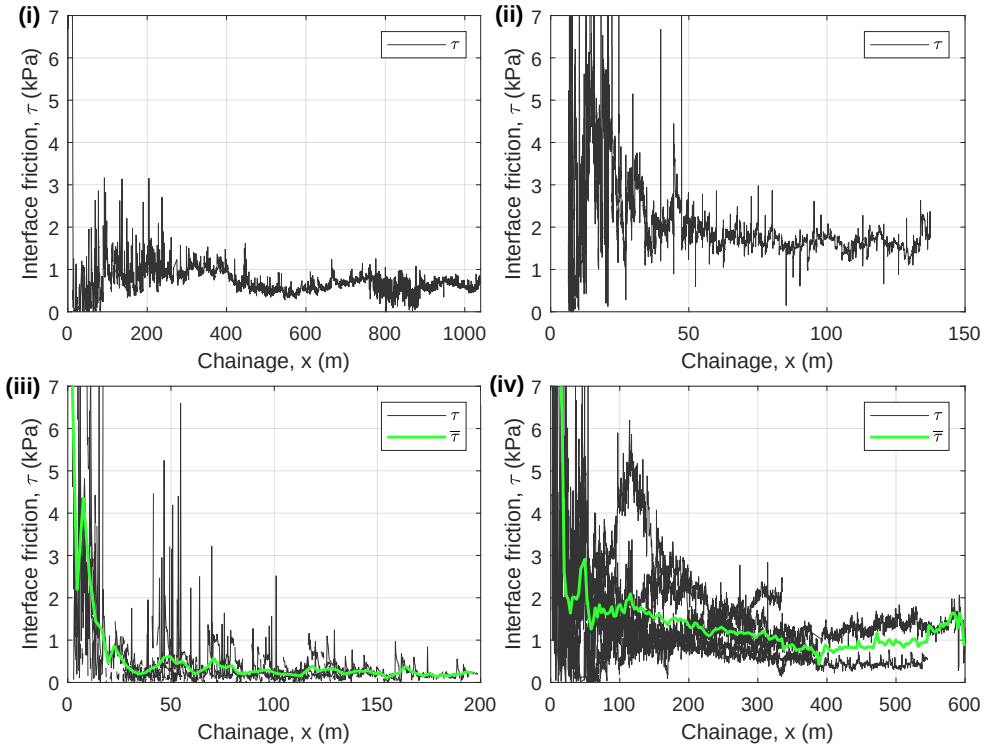


Figure 4.9: Interface friction stress calculated from the TBM data for: (i) D1 , (ii) D2, (iii) D3 - D7, and (iv) D8 - D14. Where more than one drive was completed, a 3 m moving average friction ($\overline{\tau}$) is plotted.

Figure 4.10 presents the $\Delta\tau$ during stoppages for the four tunnel groups. From the figure it is apparent that there is significant scatter within the results, especially during D2, and therefore the fitted log-linear trends can mask significant variation and should be used with caution. This scatter was also observed in previous studies of tunnel drive data, such as Pellet-Beaucour et al. (2002), and can be attributed to the variable site conditions influencing the frictional behaviour during the stoppage (e.g. differing lubrication practice during stoppages or the cause of the stoppage). The variation in $\Delta\tau$ also follows the log-linear increase with t_s identified by Pellet-Beaucour et al. (2002), although the magnitudes of the increase are smaller than reported by those authors.

Variations in $\Delta\tau$ with t_s caused by the different ground conditions can be identified by comparing the different drive groups. For example, drive D2 and D8 - D14 (through gravels) present larger maximum friction increases, of up to 10 kPa, when compared to D1 and D3 - D7, which were in rock and soft peat / clay, respectively. These results are also more scattered

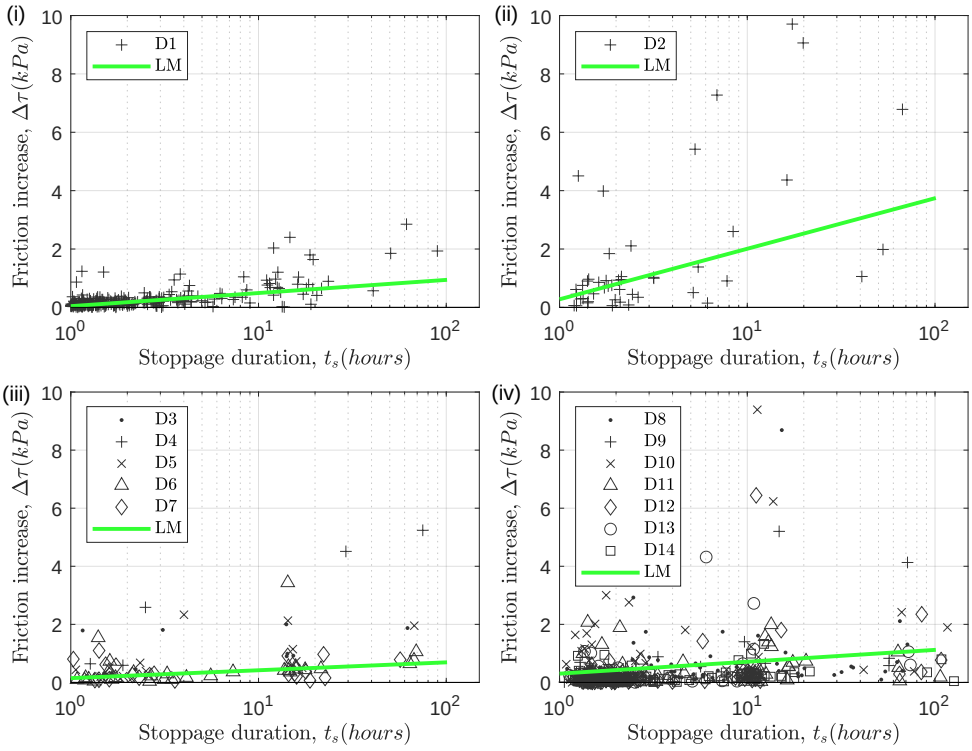


Figure 4.10: (τ) development with time stopped (t_s) for the four tunnel drive groups: (i) D1, (ii) D2, (iii) D3 - D7, (iv) D8 - D14. A least squares linear model (LM) has been fitted to each of the drive group data.

than those in rock or clay, highlighting the importance of gaining a better understanding of the SLS interface behaviour in granular conditions. Additionally, it can be observed that τ in these granular materials increases more quickly immediately after a stoppage (i.e. the apparent intercept of the fitted linear models is larger).

Figure 4.11 then presents the variation of $\frac{\Delta\tau}{t_s}$ with t_s for the four groups of drives. From the figure, it is clear $\frac{\Delta\tau}{t_s}$ decreases with t_s. A linear relationship with $ln(t_s)$ is observed, which is due to the underpinning time-dependent friction mechanisms, such as consolidation, following a linear relationship with log-time. The relationship can therefore be defined using:

$$\frac{\Delta\tau}{t_s} = a_s.ln(\frac{t_s}{t_{ref}}) + b_s \tag{4.3}$$

where t_{ref} is the reference stoppage time (1 hour) and the coefficients a_s and b_s for the different drive groups are calculated using a least squares method of fitting the data and are given in Table 4.2, alongside the coefficient of variation for the factors and R^2. The coefficients of

variation (a_s) are high (up to 0.82 during D2), highlighting the variation in the stoppage friction data from the drives caused by different factors influencing the stoppage behaviours. This equation is only valid for the range $\frac{\Delta\tau}{t_s} \geq 0$. This implies a limiting friction increase at longer stoppage durations, which could be caused by the underlying friction increasing mechanisms (such as filtration of the lubricant) reaching steady state. Figure 4.11 (iv) highlights this behaviour in the D8 - D14 (Dublin) drive group through gravels.

Drive D1 had both a low b_s (intercept) and a_s (gradient) value, denoting a small starting rate of friction increase which only decreases slightly for stoppages of longer duration. The values for the other drives present different trends, for example the Hull drives had an intercept value twice that of the Dublin drives, whilst the rate of decrease is over twice that of the Dublin group. These differences suggest the drives in soft clay, starting from a very low interface friction, had a rapid increase in friction at the start of a stoppage but $\Delta\tau$ plateaued at longer t_s. The Putney drive (D2) behaved similarly to the Dublin group, which suggests the ground conditions influenced the stoppage behaviour as both drive groups were in gravel. However, there were differences between Putney and Dublin, notably that Putney measured a more rapid increase in τ as soon as jacking ceased, which is attributed to the polymer lubricant used dissipating more readily into the gravel than a Bentonite due to the lack of filter cake formed.

Table 4.2: Summary of friction fitting coefficients, their coefficient of variation, and the overall R^2 of the model.

	Coefficient value		**Coefficient of variation**		
Drive (-)	$\mathbf{a_s}$ $\frac{kPa/hour}{log(hour)}$	$\mathbf{b_s}$ **(kPa/hour)**	$\mathbf{a_s}$ (-)	$\mathbf{b_s}$ (-)	$\mathbf{R^2}$ (-)
D1	- 0.0131	0.082	0.12	0.044	0.96
D2	- 0.0559	0.421	0.82	0.26	0.32
D3 - D7	- 0.0733	0.285	0.16	0.094	0.93
D8 - D14	- 0.0322	0.139	0.16	0.095	0.92

The stoppage data also showed that approximately 2.5% of stoppages under 14 h resulted in a decrease in τ, whilst few drives with $t_s > 14$ h resulted in decreases in τ. These reductions

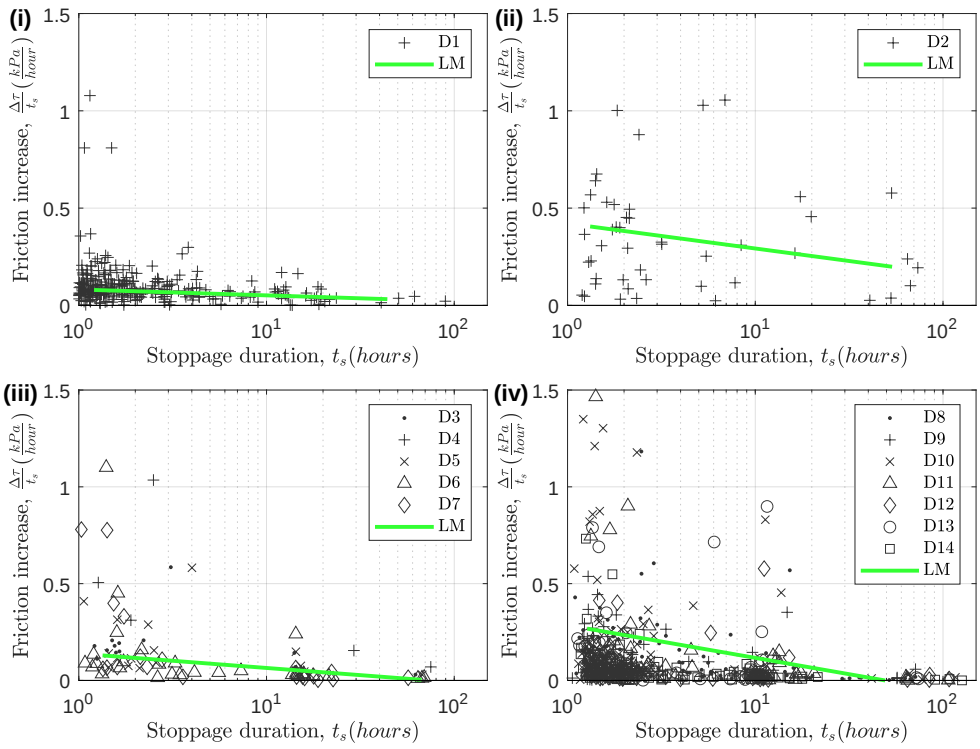


Figure 4.11: $(\frac{\Delta\tau}{t_s})$ development with time for the four tunnel drive groups: (i) D1, (ii) D2, (iii) D3 - D7, (iv) D8 - D14. A least squares linear model (LM) has been fitted to each of the drive group data.

typically resulted from one of three sources:

1. The stoppage was shortly after a longer stoppage, or large τ increase, and τ was tending downwards towards a steady state.
2. An improvement had been made to the lubrication during or before the stoppage. For example, the lubrication system was enabled before restarting on some stoppages, which resulted in lower τ values on restart.
3. Large steering deviations were experienced immediately after the stoppage. Steering deviations increased the load in the steering cylinders (from which R is calculated) as the TBM head was manoeuvred into a new alignment against the surrounding ground. These additional forces did not always correspond to additional jacking force, as lateral loading also occurs on the TBM head. As τ is the difference between the calculated R and P values, the increase in R resulted in a lower τ magnitude after the steering correction was applied.

Pellet-Beaucour and Kastner (2002) proposed an alternative method for the calculation of τ where no measurements of R are available, or where the data are uncertain. Those authors proposed that τ can be predicted by connecting the minima of the P envelope within a particular window (or bin). The intention of this approach was to calculate the friction of the pipe string over long bin lengths to identify trends in friction caused by changes during tunnelling, or for a tunnel overall. P values from the Castlerigg drive (D1) were used to validate this approach against the P - R method of calculating τ used in this research. For the analysis a bin length of 1 pipe (3 m) was used, as shown in Figure 4.12, to assess if the method was also suitable over shorter bin lengths.

The Pellet-Beaucour and Kastner (2002) method correlates well with the calculated τ values, giving a conservative estimate up to 760 m chainage. Between 750 m and 900 m chainage a discontinuity was encountered in the rock with groundwater ingress into the tunnel overcut and head of the TBM reported. This resulted in greater variation in the recorded P, R, and τ values at $x > 760$ m and hence the more variable agreement.

To quantify how interface friction varied during each pipe advance, the interface friction values were calculated during each advance of the longest monitored tunnel drive (D1). The calculated τ was averaged over bins of 60 mm (1/50th of the pipe length) and normalised by the corresponding peak value during each pipe advance. The corresponding advance distance and time were also normalised by pipe length and advance duration respectively. This exercise was completed for all pipe-length advances in the drive and the trends are presented in Figure 4.13. The figure shows τ decreases during each advance. The ramp up in force in the first 10% of the drive can be attributed to compression of the pipe string after a stoppage as the interface friction is overcome along the tunnel. The rapid decrease in the last 5% of the advances is attributed to a large number of the advances stopping before the full elapsed pipe length.

The distance normalised data show a plateau in jacking force between 10% and 30% of

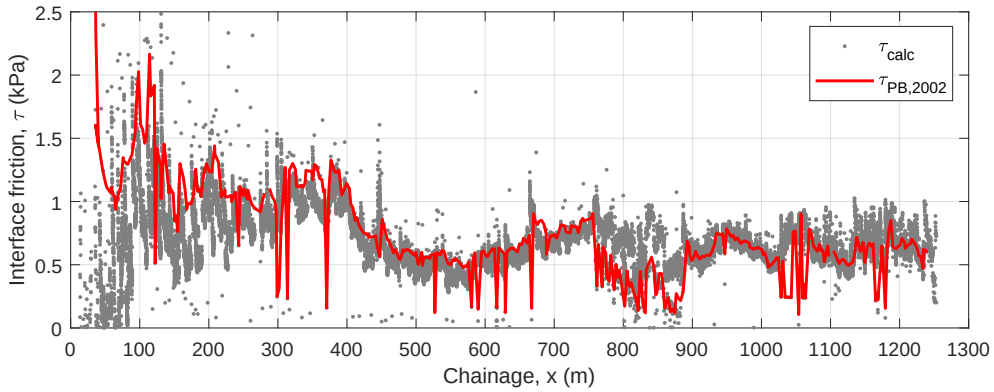


Figure 4.12: Comparison of calculated interface friction (τ_{calc}) and friction derived using the Pellet-Beaucour and Kastner (2002) method ($\tau_{PB,2002}$) using the Castlerigg (D1) tunnel drive data.

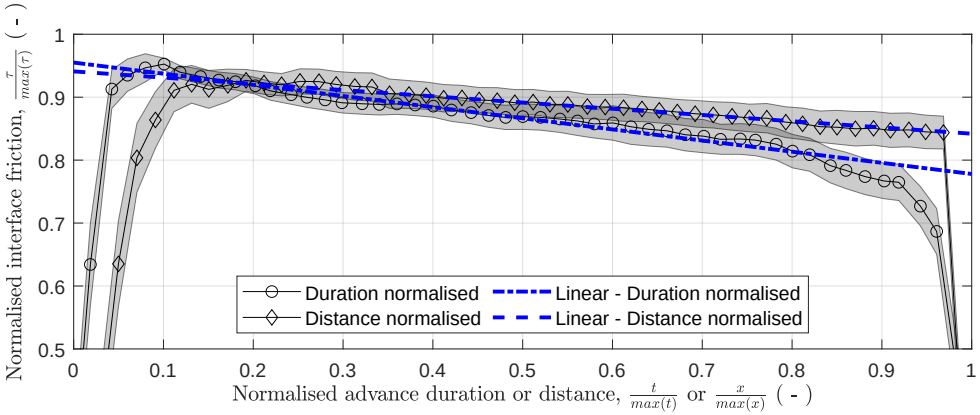


Figure 4.13: Development of normalised interface friction ($\frac{\tau}{max(\tau)}$) with normalised advance duration ($\frac{t}{max(t)}$) or distance ($\frac{x}{max(x)}$) from the Castlerigg tunnel drive (D1). Data are the mean of 121 pipe advances with the 95% confidence bounds shown in grey.

the advance, whilst the duration normalised data peaks at 10% before decreasing. The rates of decrease are then -0.117 and -0.0990 for duration and distance normalised respectively. Between 30% and 90% elapsed duration or distance, the variation in τ is highly linear, with the differences between the duration and distance normalised data explained by changes in P_r during each advance. Typically, P_r starts low as the maximum τ is overcome after a stoppage, then, as the τ reduces, P_r increases. This leads to the more rapid apparent decrease in the time normalised data when compared to the distance normalised data.

4.5 Local interface stress sensors

Tunnel interface frictions have been shown to be similar and repeatable across multiple drives in Section 4.4, which suggests that the governing interface friction mechanisms are similar

for all drives. To gain insight into the specific conditions at the soil-lubricant-structure (SLS) interface, the Castlerigg drive (D1) was instrumented with four interface load-cells located at 90^o intervals around the pipe. Up to 60 m of data was recorded by these sensors before they failed through Bentonite infiltration after between two and three days. This distance corresponded to measurements within the glacial till strata in the drive, not the mudstone.

Figure 4.14 presents the time series σ_N and τ measurements from the sensors: (i) and (ii) plot data from the N and S sensors, whilst (iii) and (iv) plot the E and W sensors. During tunnelling, σ_N variations caused by lubricant injections near the IP are apparent, e.g. at 0.9 days elapsed in Figure 4.14 (i). Six peaks in σ_N are visible - corresponding to lubricant injections from the three lubricant ports in each of the lubricant pipes either side of the IP, which shows that the overcut was hydraulically connected along this 40 m length. The increase in normal stress ($\Delta\sigma_N$) recorded during each injection was a maximum of 45 kPa and after each group of injections a residual increase of between 20 kPa and 40 kPa was recorded. This increase was above the required stability pressure for the overcut and resulted in a total stress increase of 300 kPa over 2 days, which would likely have increased the interface friction, as discussed further in Chapter 8.

The relationship between σ_N, τ and x is plotted in Figure 4.15. Interface changes during stoppages are apparent in the τ response of the sensors. τ increases of approximately 0.75 kPa are evident at 3 m intervals in the W and S sensors (for example at 10 m, 13 m, and 16 m chainage), before returning to steady state over 1 m advanced. A smaller peak is also visible in the E sensor data with little observable change in the N sensor during the same periods, showing that this stress increase is not uniform about the pipe extrados.

It is believed that lubricant ingress began in the N sensor at $x = 30$ m, or $t = 1.25$ days, due to a seal failure and resulted in the reduction in the measured normal stress to a value lower than the overcut pressure (P_a) logged by independent sensors. Between $0.75 < t < 1$ days

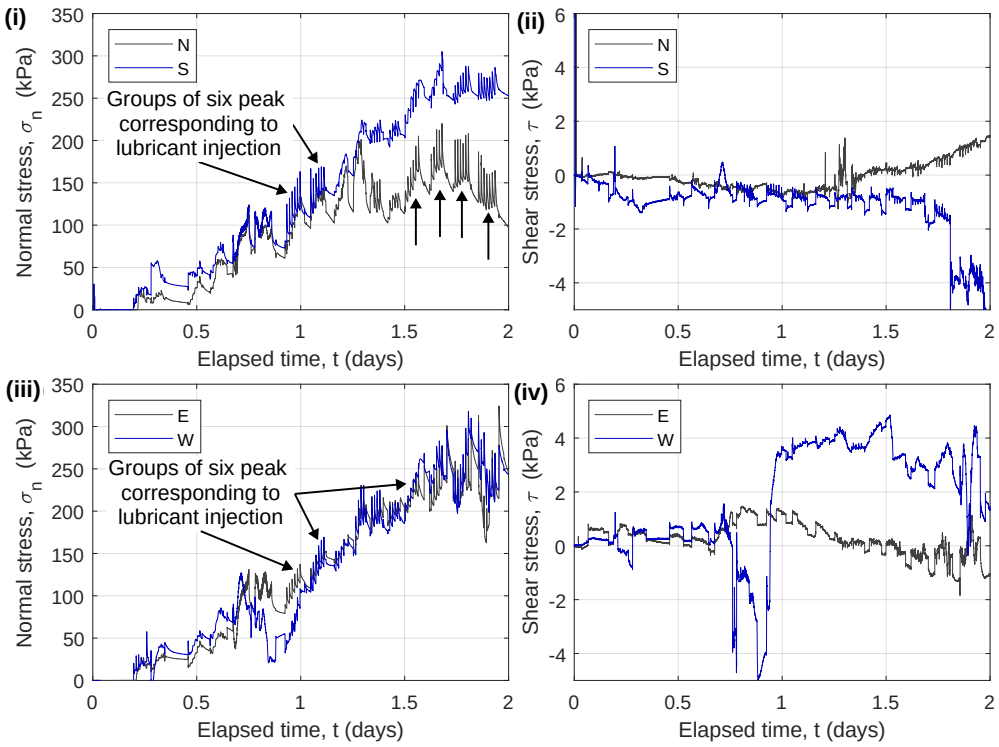


Figure 4.14: Development of σ_N and τ with time since IP install (t) for the four interface load cells in the Castlerigg (D1) IP: (i) σ_N for the N and S sensors, (ii) τ for the N and S sensors, (iii) σ_N for the E and W sensors, (iv) τ for the E and W sensors.

(19 m and 20.5 m) the W sensor experienced a decrease in σ_N and τ before recovering to a similar σ_N but higher τ value, 4 kPa compared to 0 kPa - 1 kPa for the E sensor. The increased τ value is then present for the remaining data, suggesting the W sensor was continuously in contact with the tunnel bore during that period.

4.6 Local overcut pressure monitoring

Monitoring of local P_a around the IPs was undertaken to develop an understanding of how P_a varies around the tunnel pipes during tunnelling and stoppages. These measurements were then used to guide laboratory experimentation as well as assess the effectiveness of modern lubrication techniques. The local P_a measurements from the four sensors in D1 are presented in Figure 4.16. P_a in excess of 1 MPa were observed during the drive, due to over injection of lubricant from the volume controlled lubrication system in the the low permeability mudstone. This resulted in leaks at the interjack station in front of the IP at t = 31.6 and 36.4 days. Three long duration stoppages are highlighted by arrows in the figure, e.g. at t = 12 days,

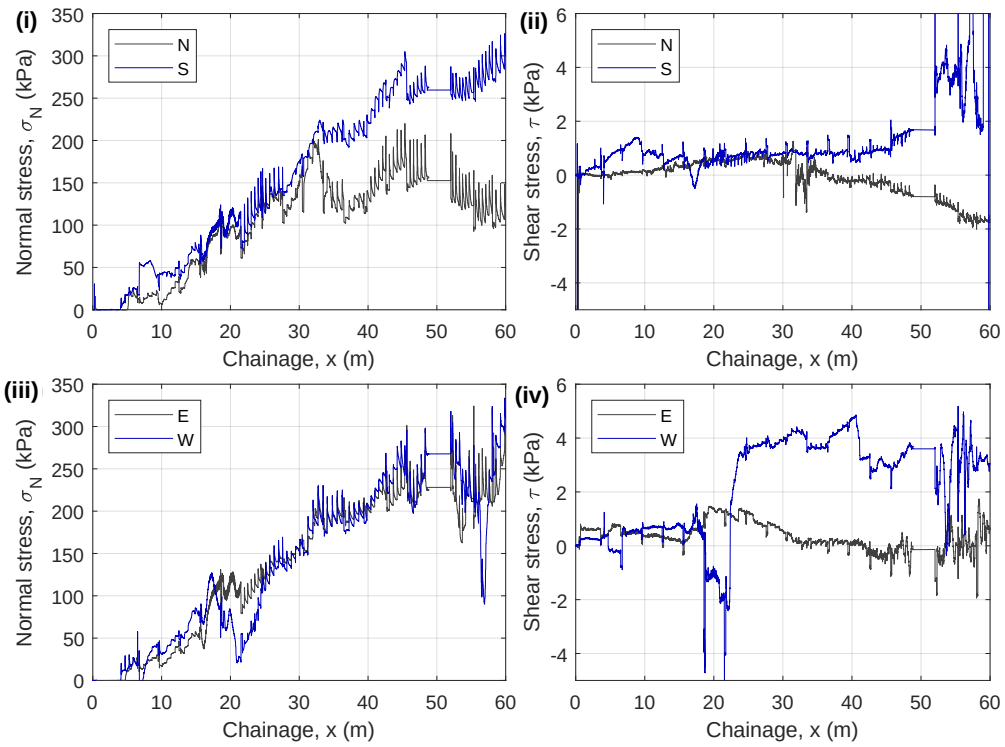


Figure 4.15: Development of σ_N and τ with IP chainage (x) for the four interface load cells in the Castlerigg (D1) IP: (i) σ_N for the N and S sensors, (ii) τ for the N and S sensors, (iii) σ_N for the E and W sensors, (iv) τ for the E and W sensors.

which show a significant decrease in P_a between advances. The end of tunnelling activities are shown by the red dashed line at $t = 41$ days, after which $P_a \approx$ hydrostatic ≈ 500 kPa.

Figure 4.17 plots the fractional decrease in overcut pressure ($\frac{\Delta P_a}{P_a}$) recorded by the N and W PTs during one stoppage during D1, as the S and E sensors exhibited a more damped response to pressure changes - caused by a loss of saturation behind the filter cap or clogging of the filter cap face From the figure, a log-linear relationship between $\frac{\Delta P_a}{P_a}$ and t_s is apparent during the stoppage and this was found to be common in all stoppages. To understand the average changes in P_a during the stoppages in D1, figure 4.18 plots the fractional decrease in overcut pressure recorded during 75 unlubricated stoppages in the drive, from which a mean and the 95% confidence intervals are shown in the figure.

At $t_s < 1$ hour, there were a significant number of stoppages that showed similar fractional changes in pressure and hence the 95% confidence interval (CI) uncertainty is small. For this analysis, the 95% confidence intervals were calculated as $\pm\ 1.96\frac{\sigma'}{n^{0.5}}$ from the mean value, where

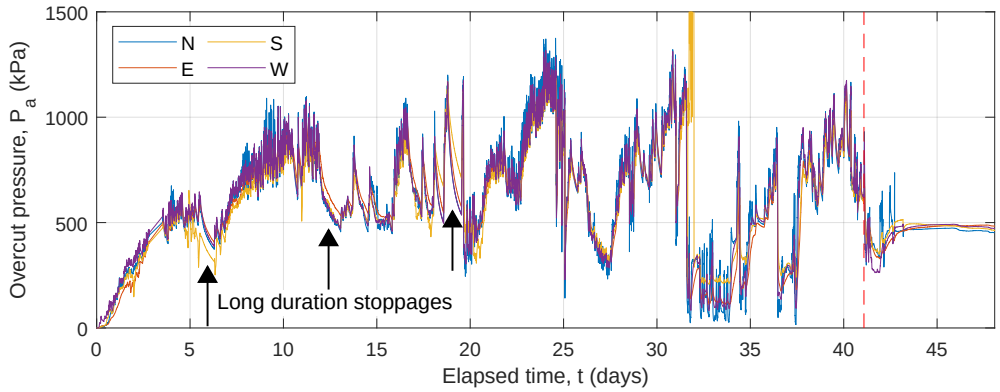


Figure 4.16: The development of overcut pressure (P_a) with time since IP install (t) for the Castelrigg tunnel drive (D1) measured by the four IP PTs. Long duration stoppages are indicated using arrows, as is the ceasing of tunnelling at 41 days.

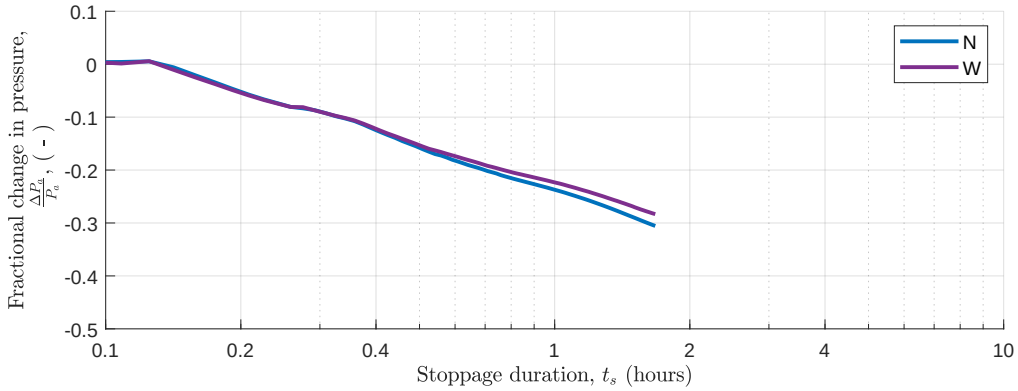


Figure 4.17: The fractional change in overcut pressure ($\frac{\Delta P_a}{P_a}$) during one stoppage on the Castlerigg tunnel drive (D1).

n is the number of measurements and σ' is the standard deviation. Between 1 h $< t_s <$ 2 h the number of data-points reduced, and the variation increased, which is reflected in the increased range of the 95% CI. Similarly, the step changes in both the mean and the CI bounds at t_s $>$ 2 h are due to individual stoppages ending, and the mean shifting correspondingly. Despite this variation, a linear relationship between ($\frac{\Delta P_a}{P_a}$) and log(t_s) is apparent in the results. The results for both the N and W sensors were also similar albeit damped, further demonstrating the hydraulic connectivity around the IP during the stoppages.

An identical analysis has been conducted for D2. Figure 4.19 presents the P_a measurements, where the end of tunnelling is again shown with a red dashed line, for D2 after $t = 15.9$ days. The cyclic variation of the overcut pressure before and after this time is due to hydraulic connectivity between the tunnel overcut and the tidal river Thames. During tunnelling, the pressure within

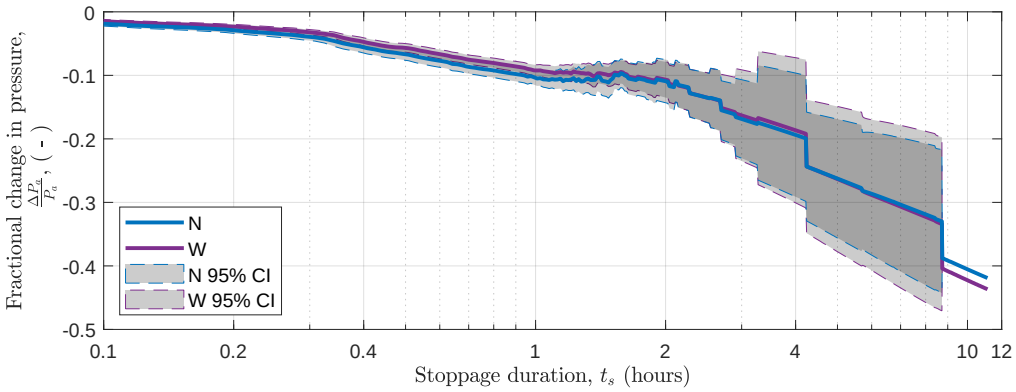


Figure 4.18: The fractional change in overcut pressure ($\frac{\Delta P_a}{P_a}$) during 75 stoppages on the Castlerigg tunnel drive (D1). The mean pressure and 95% confidence intervals (CI) are shown.

the overcut varied significantly and rapidly. A prolonged stoppage is evident from $t = 6.5$ days, with P_a tending towards hydrostatic conditions before tunnelling recommenced.

The hydrostatic pressure variation around the tunnel pipe is visible in Figure 4.19, especially during the stoppages. The D_O of 2.98 m in D2 equated to an anticipated hydrostatic pressure difference of 29.2 kPa between the N and S sensors, assuming $G_s = 1.0$ for the polymer lubricant. This offset is evident throughout the drive, for example at during the stoppage at t = 8.25 days where the difference in P_a between the sensors was 29.14 kPa. During periods of lubricant injection this offset is also maintained, which confirms hydraulic connectivity in the overcut around the IP, suggesting lubrication coverage around the whole IP.

The average hydrostatic pressure measured during the long stoppage at $t = 14$ days was 48 kPa. During tunnelling, P_a typically varied between 90 kPa and 60 kPa, meaning that in P_a was between 12 kPa and 42 kPa above hydrostatic, although peaks of over 60 kPa were observed. This is significantly lower than the excess P_a measured during D1, which was due to: (i) the higher permeability of the gravel surrounding D2, and (ii) the polymer lubricant used during D2 being unable to form a filter cake around the tunnel bore. This lack of filter cake resulted in the polymer lubricant dissipating into surrounding gravel more readily once tunnelling ceased.

Figure 4.20 presents the decrease in P_a with t_s for 11 stoppages recorded by the PT sensors

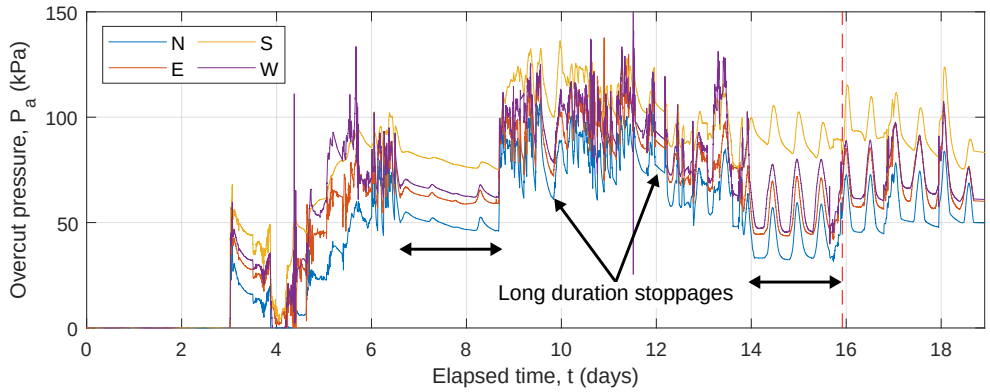


Figure 4.19: The development of overcut pressure (P_a) with time since IP install (t) for the Putney tunnel drive (D2) measured by the four IP PTs. Long duration stoppages are indicated with black arrows, and the end of tunnelling by a red dashed line at 15.9 days.

in the Putney IP. Stoppages where P_a was similar to the hydrostatic pressure are not shown in the figure, nor are stoppages during which the lubricant in the overcut was topped up by the contractor whilst the drive was stopped (with the objective of reducing friction or testing the lubrication system). The data show that the decrease in pressure was more varied than during D1, and also occurred at a slower rate. Discontinuities in the figure are caused by the influence of individual stoppages due to the small sample size.

At $t_s < 1$ hour ΔP_a is linear with t_s, which is a similar relationship to that observed during D1. The decrease in P_a of the S sensor is slower than the other sensors - which was due to the sensor being in contact with the clay invert of the tunnel and the contact damping the response for $t_s < 2$ hours. The smaller decreases in P_a for the longer duration stoppages ($t_s > 2$ hours) was due to the ineffective lubrication during the drive resulting in P_a being similar to u at the onset of the stoppage. This meant that the change in P_a, although log-linear, had a smaller magnitude than for the shorter stoppages. It is notable that the N, E and W sensors decrease at similar rates, which again demonstrates that the overcut conditions were similar at the three sensor locations.

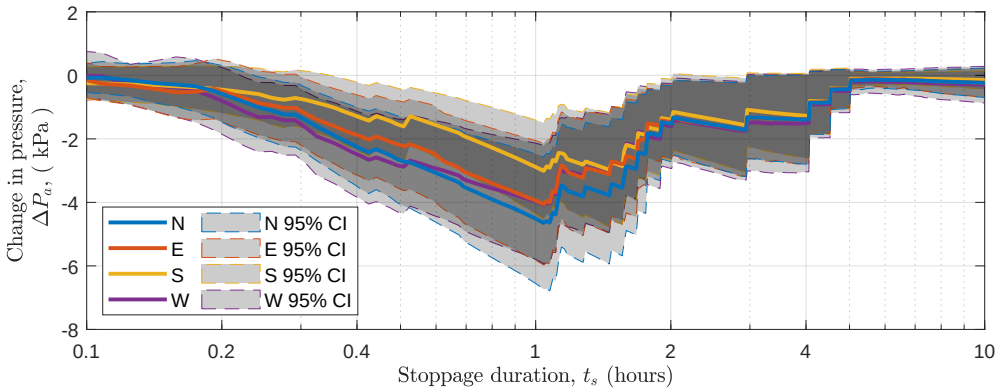


Figure 4.20: The change in overcut pressure (ΔP_a) during 11 stoppages on the Putney tunnel drive (D2). The mean pressure and 95% confidence intervals (CI) are shown for the four IP PTs.

4.7 Distributed overcut pressure monitoring

To assess how effective lubrication was along the whole drive, pressure sensors were also installed into the lubrication system of D2 at distances behind the TBM of: 14.5 m, 41 m, and 91 m (which corresponded to lubrication stations two, five, and nine). The development of overcut pressure with TBM chainage logged by the three stations is shown in Figure 4.21. These data confirm P_a was maintained above the hydrostatic pressure during the whole drive throughout the overcut length, except at 20 m TBM chainage, where the lubricant was drawn into the TBM head during excavation and the overcut pressure reduced to near zero. These data also show a lower overcut pressure in the first 5 m after the station left the launch shaft (i.e. at $x = 15$ m for station 2, $x = 58$ m for station 5, and $x = 107$ m for station 9).

This lower pressure was attributed to leaks from the tunnel overcut into the launch shaft through the rubber seal in the launch shaft wall. As the rubber gaskets used to provide a seal between the launch shaft and tunnel pipes are susceptible to damage during jacking, maintaining a continuous seal between the tunnel pipes and launch shaft for the duration of the pipe-jack was found to be difficult. This was observed to result in multiple small leakages during tunnelling, particularly on the Putney instrumented drive, where one of the rubber gaskets was damaged slightly during the launch of the TBM.

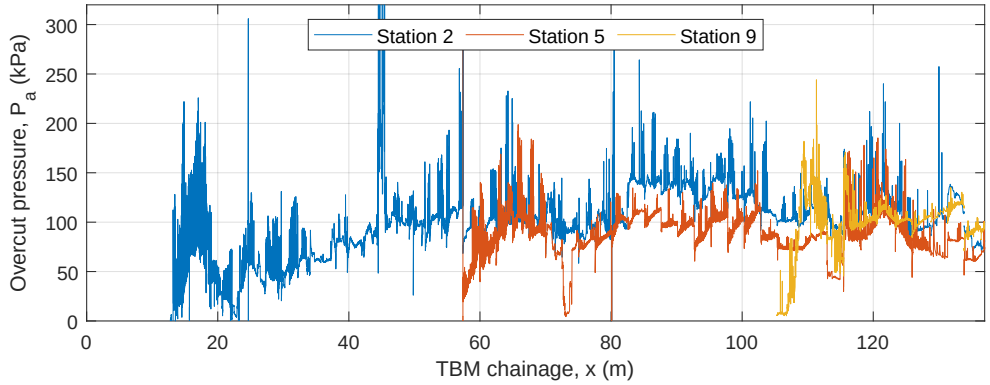


Figure 4.21: P_a recorded by the distributed pressure sensors in the Putney tunnel drive (D1).

A detailed view of the data between $t = 22$ days and 23 days is shown in Figure 4.22, during which the TBM advanced from $x = 78$ m to $x = 98$ m. In the time series data, the instantaneous reductions in P_a (e.g. at $t = 22.41$ days) were due to the system being switched off during pipe changeovers and reconnected after the stoppage. The peaks in the data are caused by lubricant injection at ports near to the sensor location. To obtain a more representative estimate of P_a in the overcut, the the minima of these values was taken. Two pertinent features of this interpreted P_a magnitude are evident: (i) P_a increases steadily in the overcut during tunnel advances, and (ii) P_a slowly dissipates towards the hydrostatic pressure during stoppages, as shown by the local pressure measurements. These factors result in P_a being typically 10 kPa to 40 kPa lower, and therefore close to hydrostatic pressure, upon restart of tunnelling after a stoppage, and the pressure does not immediately increase at the start of the advance.

The data also show that stations two and five were hydraulically linked as both stations recording similar variations in P_a throughout the drive. For example, between $t = 22.39$ and 22.42 days, a 45 minute stoppage resulted in a decrease in P_a of 15.1 kPa and 22 kPa at stations two and five respectively. During advances, the measured pressures also followed similar trends. For example, the peak in pressure recorded at 88.8 m chainage (shown in Figure 4.22 (ii)) is common to both sensors, and corresponded to a lubricant injection between the two locations.

As station 2 was connected to the lubrication station and station 5 was connected at

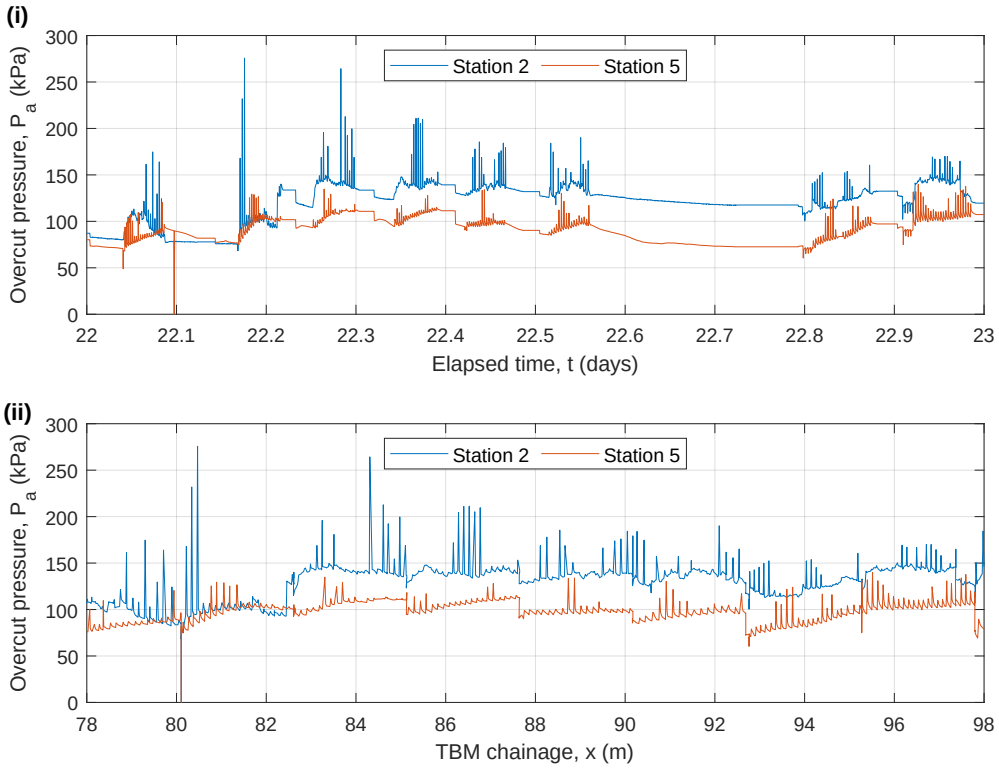


Figure 4.22: P_a recorded by the distributed pressure sensors in the Putney tunnel drive (D2) for the period 22 to 23 days elapsed. (i) presents the variation in the time domain, whilst (ii) presents the same data as a function of chainage.

the lubricant port, the results demonstrate that both methods of connection to the lubricant port record similar measurements throughout the drive. Connection to the lubrication station resulted in higher peak pressures during lubricant injection when compared to the sensor located at the port, for example at $x = 80$ m in Figure 4.22 (ii) (where station 2 measured $P_a > 200$ kPa during the injection). The sensor also measured a more damped response to changes in P_a when compared to the sensor mounted at the lubricant port, for example at $x = 92.5$ m where a rapid decrease in P_a is recorded by Station 5, but a slower decrease is observed in Station 2. Despite this, for future deployments, the most convenient method of connection can be used without having a material effect on the results as the minima of the pressure measurements can be used to estimate magnitudes and trends in overcut pressure.

4.8 Local overcut stability

Another source of friction during tunnelling is where the overcut locally becomes unstable and the soil comes into direct contact with the pipe. An example of this was identified in the

Castlerigg drive (D1) hoop strain data, recorded by the IP. Figure 4.23 presents typical data from the hoop direction VWS during the drive. Figure 4.23 (i) presents a polar plot of the measured strain in the eight circumferential VWS (shown indicatively in Figure 3.3). A grey dashed-line also denotes the average strain measured by the eight sensors, which is taken as the average strain in the pipe wall.

A 'bending strain' is defined as the difference between this average strain and the strain of each individual sensor as any any deviation from the mean strain will be caused by bending moments within the pipe wall. As the sensors were mounted on the external face of pipe reinforcement a negative bending strain indicates a sagging moment (outside face in compression) and a positive strain indicates a hogging moment (outside face in tension). The bending strains corresponding to the measured hoop strains in Figure 4.23 (i) are shown in Figure 4.23 (ii). In the figure, the N sensor recorded a sagging moment, which indicates that the top of the pipe is in contact with the tunnel bore (due to the pipe being buoyant in the fully lubricated overcut).

A possible obstruction in the tunnel overcut was noted in the IP data between $x = 270$ m and $x = 285$ m chainage. After the IP passed this chainage P_{IP} decreased by 1300 kN, whereas R and P varied by under 500 kN, meaning that the inferred obstruction was causing between 500 kN and 1300 kN of additional friction. During this period, the relative deviation of the resultant force through the pipe increased to 0.4 $\frac{D_O}{2}$ (from an average of < 0.2 $\frac{D_O}{2}$) and the phase to stabilise at approximately 21°.

The measured strains corresponding to this chainage are shown in Figure 4.24. The N and NE sensors (0^o and 45^o) show significant sagging strains in Figure 4.24 (ii). The SW sensor (225^o) also measured a smaller sagging strain. These measurements suggest a point loading applying a large bending moment to the pipe between the N and NE locations, which pushed the pipe into the tunnel bore on the opposite (SW) side. The mean compressive strain recorded by the sensors was was 95 % greater at this chainage, as shown in Figure 4.24 (i), whilst P_a

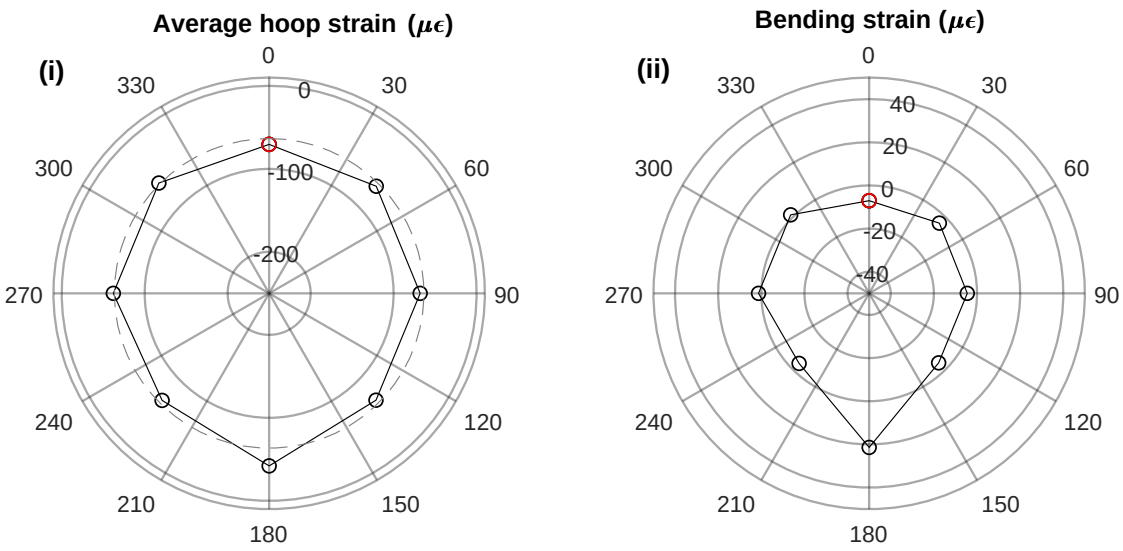


Figure 4.23: Measured IP strains at 133.2 m chainage: (i) tangential (hoop) strains, and (ii) bending strains. The mean hoop strain is shown with the grey dashed line in (i).

was $< 5\%$ higher. As mean compressive strain and P_a have been found to be linearly related, the action of the obstruction increased the mean strain in the pipe by approximately 90 %.

This result demonstrates the importance of maintaining a stable overcut, as a single obstruction led to an increase in friction of up to 1300 kN, which was over 30 % of the total jacking force. This analysis, coupled with the axial force measurement techniques in Section 4.3, also presents a method to assess intermediate forces on pipe string between the traditional R and P measurements, which can be used to guide lubrication by identifying regions of high friction.

4.9 Temperature

Previous research, such as Mostafa et al. (2007) and Ahmad et al. (2018), has demonstrated that lubricant slurry properties are affected by temperature. As overcut temperature is not normally logged during tunnel drives, the additional data provided by the two IPs deployed in this research was used to identify any changes which occur in tunnel overcut temperature during tunnelling. The thermocouples were situated 60 mm from the interface within the concrete wall as part of the VWS sensors. Although this 60 mm offset resulted in a small difference between the sensor temperature and lubricant temperature outside the pipe, it is believed this effect

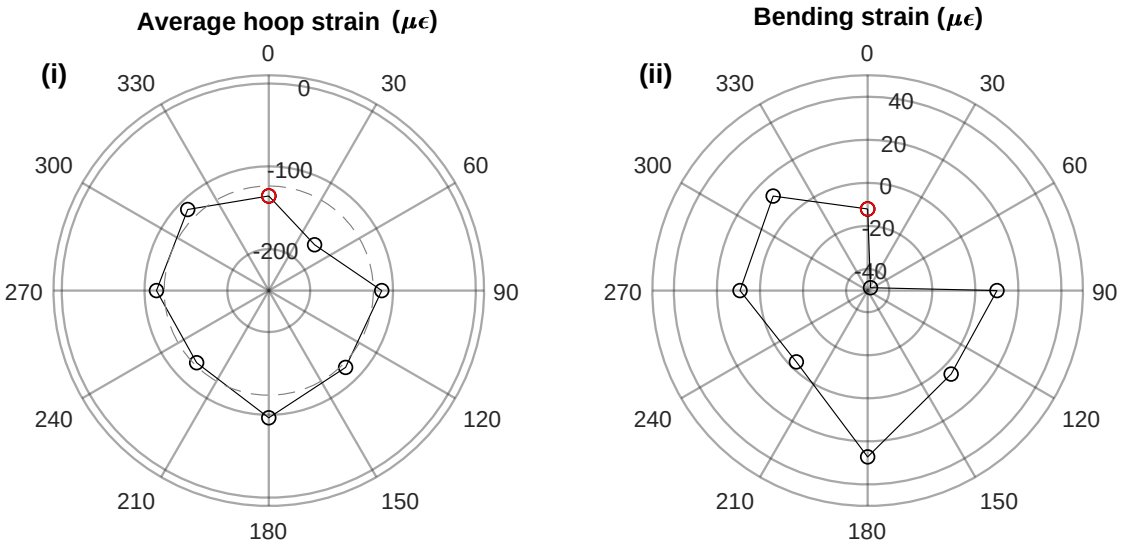


Figure 4.24: Measured IP strains at 283.2 m chainage: (i) tangential (hoop) strains, and (ii) bending strains. The mean hoop strain is shown with the grey dashed line in (i).

would be constant throughout the drive if the internal tunnel temperature was constant.

Figure 4.25 presents the recorded mean wall temperature and internal (enclosure) temperature throughout drives D1 and D2. The mean wall temperature is plotted as the distributed sensors measured similar temperatures on each drive, with a variation of < 1 ^{o}C between locations. From the data it is apparent that the IP in D1 experienced less variation in temperature than the IP in D2. This was due to the proximity to the TBM of the IP in D2 (10 m behind compared to 537 m in D1) resulting in the heat generated by the TBM having a larger effect on the internal temperature of the IP. Once the internal temperature had stabilised (at $x > 50$ m), both the D1 and D2 wall temperatures did not vary by more than 2 ^oC during the remainder of the drives. This finding means that temperature logging of tunnel overcuts during tunnelling is not required as the overcut temperature remains stable throughout the drive, as anticipated.

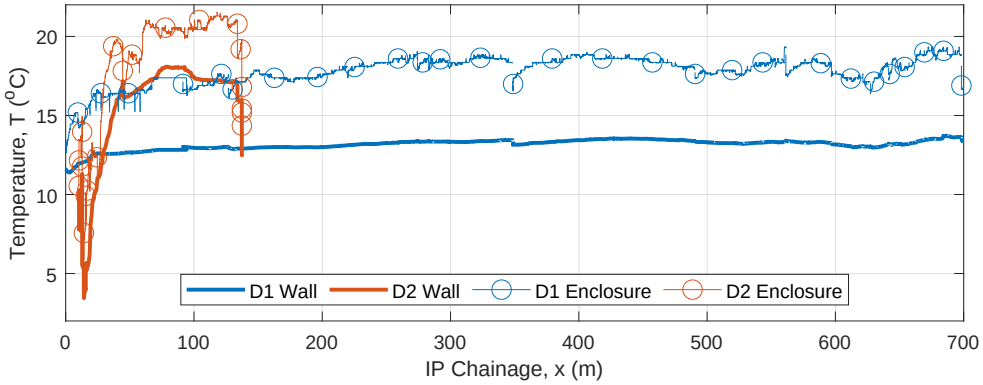


Figure 4.25: Pipe wall and logging enclosure temperature variation during the Castlerigg and Putney tunnel drives (D1 and D2).

4.10 Summary of field studies

This chapter has presented the findings of two instrumented tunnel drives conducted during this research. The results are complemented by data from 12 recent tunnel drives, split into two distinct groups in different ground conditions. The key findings from this work are summarised below:

1. Modern, automatically operating, lubrication systems are effective at reducing interface friction. Typical frictions recorded on the 14 tunnel drives varied from $\tau < 0.5$ kPa in soft clays to $\tau < 2$ kPa in gravels. Long stoppages, or failures within the lubrication system, resulted in large relative increases in the measured friction of up to 7 kPa. The magnitude of the increase is variable, due to the number of factors influencing the interface.
2. In pipes which are buoyant within the overcut, such as those in D1, the resultant friction location is predominantly within the top half of the tunnel pipe (75% of the advanced distance during D1). In drives which are not buoyant, the resultant is within the bottom half (D2). During periods of high axial force, such as after stoppages, this remains true, suggesting the pipe contact with the tunnel bore is the primary source of friction during both stoppages and in steady state conditions.
3. Tunnel drives with more frequent stoppages and lower net advance rates have higher interface friction. These stoppages can be placed into two groups, short and long dura-

tion. Short stoppages, of under 14 hours, happen highly frequently and are caused by routine overnight stoppages, pipe changes, and tunnel alignment surveys. Longer stoppages (caused by weekend stoppages, breakages, or equipment maintenance) happen less frequently and result in larger friction increases upon tunnelling restarting.

4. The rate of increase in friction during a stoppage ($\frac{\Delta\tau}{t_s}$), although variable, linearly decreases with $ln(t_s)$, such that a limiting value of $\Delta\tau$ is approached. The rate and apparent intercept of the relationship were consistent within each drive group analysed, showing consistency in the interface friction measurements for drives in a given ground type. This means that an empirical model, using this historical data, should be able to accurately predict the response of subsequent drives in the same ground type. It is of note that the relationships established masks variability, with larger friction increases possible.
5. Overcut pressures (P_a) vary significantly during tunnelling and between tunnel drives. Magnitudes $> 1\ MPa$ have been recorded during D1, but values of < 100 kPa are more typical (D2 and anecdotal records from other tunnel sites). During unlubricated stoppages these pressures decrease linearly with $ln(t_s)$, suggesting that the mechanisms governing pressure relief in the overcut during stoppages also have a logarithmic form. The rate of decrease also varies between tunnel drives and is dependent on P_a at the onset of the stoppage.
6. P_a measurements from the IPs in D1 and D2, and the distributed pressure monitoring system in D2, have shown that the overcuts of tunnels are hydraulically linked axially along lengths of at least 40 m and circumferentially around the tunnel pipes in all monitored ground conditions. This demonstrates that good lubricant coverage is achieved during injection around the tunnel pipes and this is maintained throughout the drives.

These results have demonstrated the variability of the soil-lubricant-structure interface around tunnels during installation under field conditions. Whilst key trends are apparent, they are

difficult to isolate and examine in detail to gain insight into the underlying mechanics. To isolate these key parameters, the elemental study of lubricant properties is presented in Chapter 5, before the novel soil-lubricant-structure interface test apparatus is used for a series of laboratory tests, described in Chapter 7.

5 | Lubricant testing results

5.1 Testing overview

To quantify the mechanics of the complex soil-lubricant-structure (SLS) interface, a detailed understanding of the properties of the lubricants used is required. To achieve this, the test methods and equipment described in Chapter 3 were used to gain insight into the salient properties of Tunnel Gel (TG) and Hydraul-ez (HZ) Bentonite lubricants used during the field studies analysed in this research. A parametric study was completed to establish the relationships between lubricant mix ratio, additive concentration, applied pressure, temperature and the Bentonite properties. A baseline lubricant mix, as well as lower and upper bounds for parameters in the study, has been defined based on typical mixes used during tunnelling and is shown in Table 5.1.

Table 5.1: Bounds of the parametric study of lubricants.

Variable	**Symbol**	**Unit**	**Lower bound**	**Upper bound**	**Baseline**[2]
Bentonite Type	-	-	-	-	Tunnel Gel
Bentonite mix ratio[1]	M	-	12:1	24:1	16:1
PAC-L concentration	$C_{a,p}$	kg/m^3	0	4	0
TK-60 concentration	$C_{a,t}$	kg/m^3	0	4	0
Temperature	T	^{o}C	15	50	20 $\pm$5
Applied pressure					
Filtration testing	P_a	kPa	25	500	500
Permeameter testing		kPa	25	100	50
Consolidation shear box testing		kPa	50	250	100

[1] Mix ratio is defined as the ratio of water/lubricant by mass.
[2] Baseline values for the parametric study.

This chapter first presents the results from elemental tests of filtration rate, viscosity, and yield strength conducted using the API filter press and viscometer apparatus. Consolidation and shear strength properties of the lubricants are then determined using the consolidation shear box apparatus. The permeameter apparatus test results are subsequently used to quantify the

infiltration and permittivity characteristics of the lubricant-soil interface. Finally, a summary of the key findings is presented.

5.2 Viscosity and filtration testing

5.2.1 Exemplar baseline mix results

To confirm the trends previously described in the literature for Bentonite lubricants and quantify properties of the baseline mix defined in Table 5.1 for comparison, a Fann model 35 viscometer was used to quantify the viscosity (ν) and shear stress (τ) relationships with shear rate (γ_r). Figure 5.1 presents the ν - γ_r relationship for the baseline mix, which was shown to linearly decrease in log-log space. Similarly, Figure 5.2 shows the dependence of τ on γ_r, which is shown to linearly increase with shear rate in log-log space.

The viscometer was also used to calculate the industry standard plastic and apparent viscosities (ν_p; ν_a) using the methods set out in Section 3.2.5. Measurements were taken of the 10 second and 10 minute yield stress (τ_{10s}; τ_{10m}), which are summarised in Table 5.2.

Table 5.2: Viscosity and yield measurements for the baseline lubricant mix.

Property	**Symbol**	**Unit**	**Value**
Plastic viscosity	ν_p	Pa.s	50
Apparent viscosity	ν_a	Pa.s	122
10 second yield stress	τ_{10s}	Pa	409
10 minute yield stress	τ_{10m}	Pa	480

The variation of filtrate weight (W) with elapsed time (t) during the baseline API filter press test is shown in Figure 5.3. As predicted by the literature, the trend is linear with root-time and can be used to calculate the filtration gradient, $f = 0.500\ \frac{N}{m^2.s^{0.5}}$. These results confirm the anticipated behaviour of the Bentonite lubricants and give confidence in the adopted testing procedures described in Chapter 3.

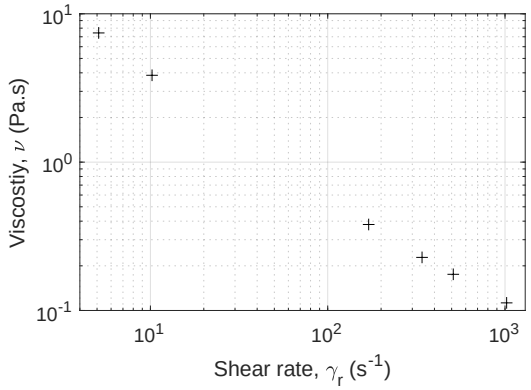


Figure 5.1: The variation of viscosity (ν) with shear rate (γ_r) for the baseline lubricant mix determined using a Fann model 35 viscometer.

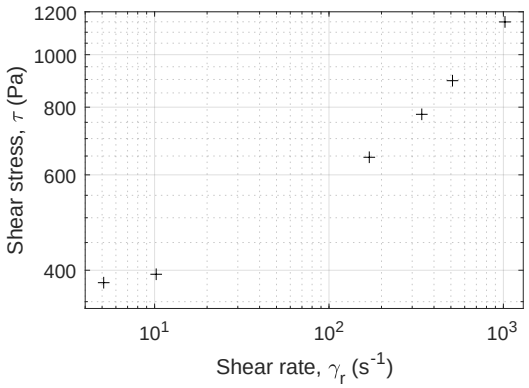


Figure 5.2: The variation of shear stress (τ) with shear rate (γ_r) for the baseline lubricant mix determined using a Fann model 35 viscometer.

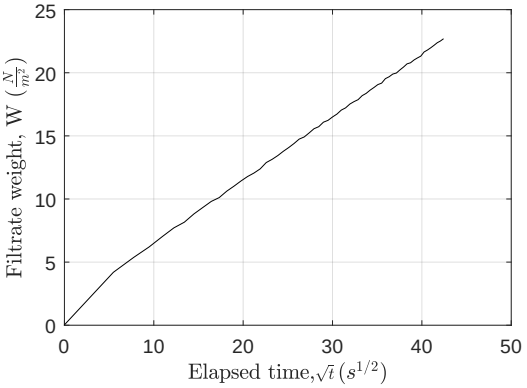


Figure 5.3: The variation of filtrate weight (W) with elapsed root-time (t) during an API filter press test of the baseline mix.

5.2.2 Compensation of temperature effects

Previous studies, such as Mostafa et al. (2007) and Ahmad et al. (2018), have shown that temperature influences the properties of Bentonite lubricant mixes. To allow comparison between field and laboratory results, as well as compensate for the variable laboratory temperature during testing, a series of tests were conducted to quantify the influence of temperature on shear behaviour, yield stress and filtration rate for the baseline mix. To quantify these relationships, samples were placed in an insulated environmental chamber to be heated or cooled.

Figure 5.4 presents the dependence of ν on temperature (T) at a representative shear rate of $\gamma_r = 1020\ s^{-1}$. From the figure, a linear relationship between ν and T is visible. This was true

for all γ_r tested, although the goodness-of-fit measurement decreased with γ_r due to the minor changes in ν caused by T at low γ_r being similar in magnitude to the noise in the measurements. To predict the variation of ν with T and account for the γ_r dependency Equation 5.1 is used.

$$\nu_c = (a_\nu.\gamma_r + b_\nu)(T - T_{ref}) + \nu \tag{5.1}$$

where a_ν and b_ν are fitting parameters derived using linear regression from the tests at constant γ_r with varying T.

A linear relationship was also observed for the influence of T on τ_0 and f. The relationships can be characterised by the following linear models:

$$\tau_{0,c} = a_t.(T - T_{ref}) + \tau_0 \tag{5.2}$$

$$f_c = a_f.(T - T_{ref}) + f \tag{5.3}$$

where a_t and a_f are a fitting parameter, T_{ref} is the reference temperature (20^{o}C), f_c and τ_c are the filtration rate and yield stress magnitudes corrected to 20^oC.

Table 5.3 gives the back-calculated constants for the properties examined in this study. The negative value b_ν shows that ν decreased at higher T, whilst the negative a_ν value indicates the influence of T is also more significant at higher γ_r. These results confirm the findings of previous studies and quantifying the dependencies for the Bentonite in this study. The table also presents the parameters normalised by the value under reference conditions, showing the relative effects of temperature on each parameter. The analysis shows that the f and τ of the Bentonite are the most sensitive to T and are therefore crucial to correct for in the results.

Table 5.3: Temperature dependency coefficients

Coefficient	**Application**	**Unit**	**Value**	**Normalised value**
$a_{\tau 10s}$	τ	$\frac{Pa}{^oC}$	-2.32	-5.68 10^{-3}
a_f	f	$\frac{N}{s^{0.5}.^oC}$	2.73	5.46 10^0
a_ν	ν	$\frac{Pa.s^2}{^oC}$	-0.00151	-0.916 10^{-3}
b_ν	ν	$\frac{Pa.s}{^oC}$	-0.110	-66.7 10^{-3}

The proposed relationships allow the temperature dependency of the lubricant mixture to be

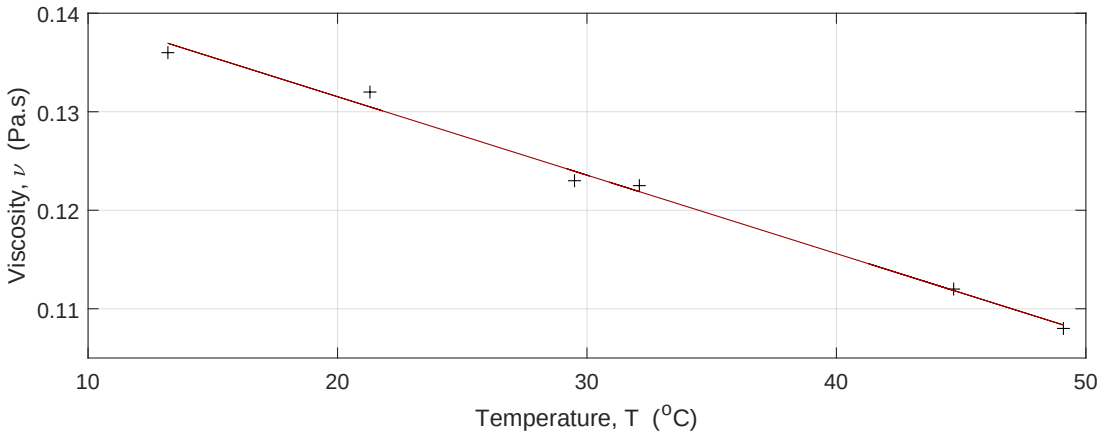


Figure 5.4: The relationship between viscosity (ν) and temperature (T) of the baseline mix for a shear rate (γ_r) of 1020 s^{-1}.

compensated for in the laboratory test data. As such, all data presented in the following sections are corrected to an effective temperature of 20^{o}C. The property variations with temperature will also influence the effectiveness of Bentonite as a lubricant in the field. For example, reduced shear strength and viscosity would lead to increased penetration depth of the Bentonite into the surrounding soil and reduce the ability of the Bentonite to form a filter cake. Temperature is unlikely to have changed the interface mechanics during a field tunnel drive, as the Castlerigg and Putney IP data have shown overcut temperatures to remain relatively constant during tunnelling. However, there may be significant T (and thus performance) differences between the Bentonite T during batching (when measurements are taken) and in the actual tunnel overcut, which is not currently considered in field practice.

5.2.3 Effect of lubricant type

To examine the variation between different proprietary Bentonite lubricants, HZ was compared to the baseline TG lubricant mix by preparing and testing mixtures in an identical manner to the baseline tests. The relationship between γ_r and ν for both Bentonites is shown in Figure 5.5. Both followed a similar linear relationship in log-log space, with the HZ viscosity 11.7% higher than TG at $\gamma_r = 5.11\ s^{-1}$, which reduced to 6.3% higher at $\gamma_r = 1020\ s^{-1}$.

The other measured properties, ν_a, ν_p, f, τ_{10s} and τ_{10m} were found to also be similar, and are presented in Table 5.4. The development of τ_0 with t varied between the two Bentonites. τ_{10m}

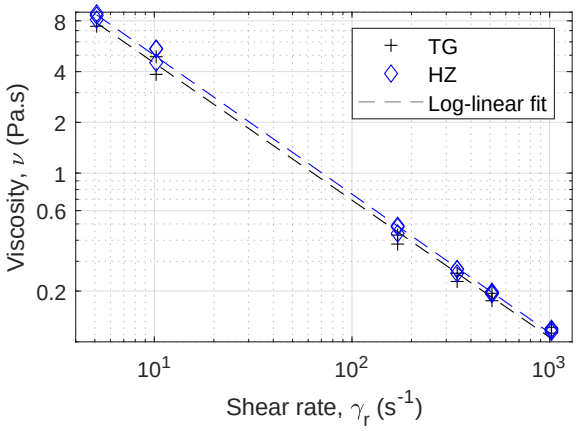


Figure 5.5: The development of viscosity (ν) with shear rate (γ_r) for TG and HZ Bentonite mixes under baseline conditions.

increased 20% compared to τ_{10s} for the TG mix, but decreased 3% for HZ. This resulted in τ_{10m} being 9.8% lower for HZ than TG, despite τ_{10s} being 10% higher. These results demonstrate that the characteristics of both Bentonite lubricants are very similar for the baseline conditions, with the exception of the yield stress magnitudes. This difference is probably due to the polymer inclusion within both Bentonites altering their thixotropic behaviour, but without additional information regarding their make-up it is not possible to determine the exact cause. To ascertain if there are differences in the Bentonite characteristics under different conditions, both products were assessed during the parametric study described in the following sections.

Table 5.4: Measured Hydraul-ez properties and comparison to the baseline valves.

Property	**Symbol**	**Unit**	**Value**	**% difference**
Plastic viscosity	ν_p	Pa.s	41.0	- 2.4
Apparent viscosity	ν_a	Pa.s	119	- 2.4
10 s yield stress	τ_{10s}	Pa	449	10
10 m yield stress	τ_{10m}	Pa	434	- 9.8
Filtration rate	f	$\frac{N}{m^2.s^{1/2}}$	0.511	2.1

5.2.4 Effect of pressure

As the overcut pressure has been shown to vary during tunnel drives, it is important to understand the dependency of f on P_a. To this end, tests with P_a ranging between 25 kPa and 500 kPa were conducted using the API filter press on the baseline mix and identically prepared HZ mix. Figure 5.6 presents the results of these tests, which show a linear relationship between

f and $ln(P_a)$ for both Bentonites. The filtration rates of both Bentonites are similar throughout testing, such that any differences in the behaviour could not be identified from the results.

5.2.5 Effect of mix ratio

In the field, the most common way to adjust the Bentonite lubricant properties 'on the fly' is to adjust the mix ratio (M). The literature, monitored field tunnel drives, and industry consultation have revealed that mix ratios of between 14:1 and 24:1 (water : Bentonite by weight) are typical. The influence of varying M on the Bentonite's salient properties was examined for both TG and HZ within this range.

Figure 5.7 shows the influence of M on ν_a and ν_p for both TG and HZ. The results show a linear relationship between both the viscosity parameters and concentration, definted as $\frac{1}{M+1}$ for the range of mix ratios in the study. The figure also shows that the variation in the HZ mix ν_a was similar the to TG mix, but the change in ν_p lower for HZ when compared to TG (by 28%). These results show that both Bentonites' viscosities at high shear rates vary similarly with M, but at lower shear rates HZ maintains a higher viscosity in comparison to the baseline TG mix, as ν_p is influenced by the difference between the viscometer readings at 600 rpm and 300 rpm.

Figure 5.8 shows the influence of M on τ_{10s} and τ_{10m}. The relationship between yield stresses and M was linear in log - log space. The relationship between τ_{10s} and M was similar for both mixes, with a 4.5% steeper gradient for the baseline mix. The gradient of the τ_{10m} response was also similar (with the baseline mix decreasing 2.8% less steeply than the HZ) but baseline mix had a magnitude 20% larger than HZ at $M = 16$.

Finally, the dependency of f on M was assessed using the API filter press at baseline pressure. Figure 5.9 presents the variation in f for the range $14 \leq M \leq 30$ as a ratio to the $M = 16$ value. f for TG increased 31% faster than for HZ, which resulted in TG mixtures depositing material more rapidly in the filter press during testing at higher pressures.

These results have shown that TG and HZ behave similarly as M increases. The key

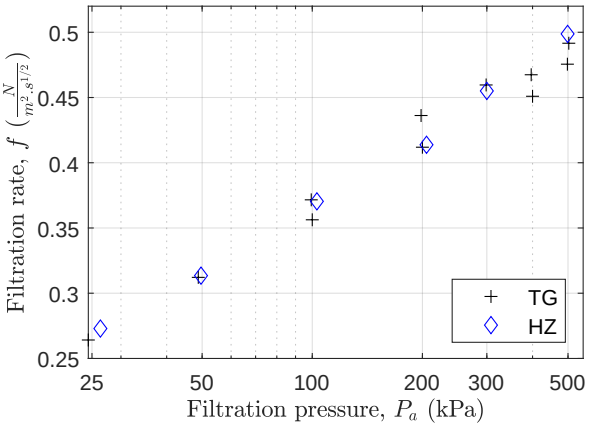


Figure 5.6: Relationship between filtration pressure (P_a) and filtration rate (f) for the baseline TG and HZ Bentonite lubricant mixes.

differences are that: (i) the 10 minute yield stress (τ_{10m}) of the baseline TG mix is larger than the HZ mix at all M, and (ii) the baseline mix has a larger filtration rate at higher M. These differences will influence the penetration of the Bentonites around tunnel drives in the field as the higher yield stress will reduce lubricant penetration into the soil and the larger filtration rate will increase the deposition rate of the filter cake which forms at the SLS interface.

5.2.6 Effect of additives

The effects of PAC-L and TK60 additives on the baseline and HZ Bentonite lubricant mixes were quantified using the Bentonite properties ν_a, ν_p, τ_{10s}, τ_{10m}, and f. Bentonite samples were prepared with PAC-L and TK60 concentrations (C_a) of between 0 kg/m^3 $\leq C_a \leq$ 4 kg/m^3 of mixed lubricant at a mix ratio of $M = 16$. These limits were selected as field tunnel drives monitored in this study used concentrations $<$ 1 kg/m^3 and the manufacturer's recommended maximum concentrations were up to 4 kg/m^3. Figures 5.10 and 5.11 present the change in ν_a and ν_p with increasing additive concentration, respectively, with trends in the measurements identified using linear regression analysis of the measurements. The results are shown as a ratio of the viscosity at a given additive concentration to the no-additive baseline result. In the figures, data points which exceeded the measurement range of the viscometer are omitted.

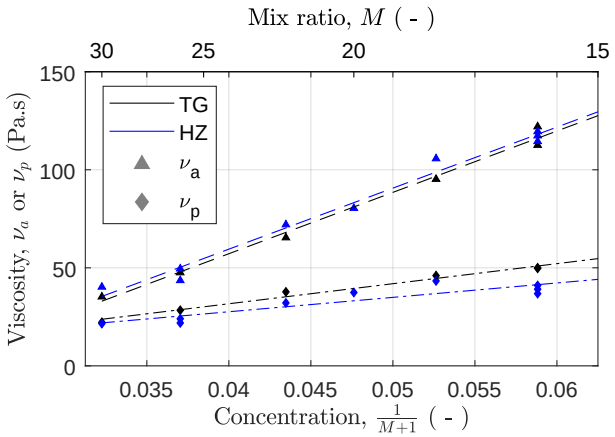


Figure 5.7: The relationship between viscosity (ν_a and ν_p) and mix ratio (M) or concentration ($\frac{1}{M+1}$) for TG and HZ lubricant mixes measured using a Fann model 35 viscometer.

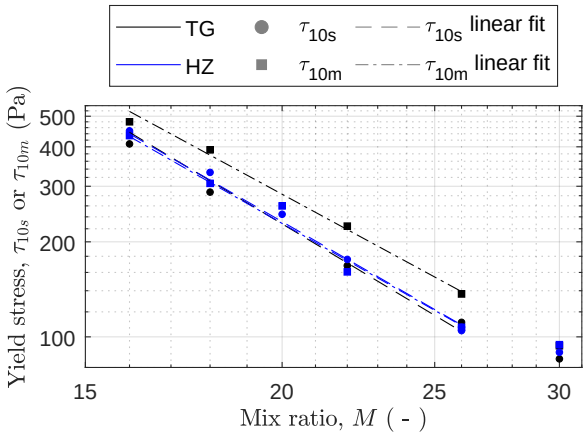


Figure 5.8: The relationship between mix ratio (M) and yield point (τ_{10s}, and τ_{10m}) for TG and HZ lubricant mixes measured using a Fann model 35 viscometer. Trends have been fitted to the linear region of the data ($16 \leq M \leq 26$).

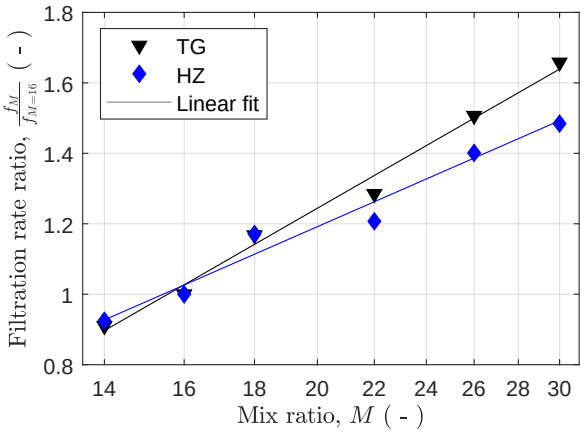


Figure 5.9: The relationship between mix ratio (M) and filtration rate ratio ($\frac{f_M}{f_{M=16}}$) for TG and HZ lubricant mixes at $P_a = 500$ kPa in an API filter press apparatus.

PAC-L was found to increase both ν_a and ν_p significantly at low concentrations, especially for the baseline TG sample which recorded 30% and 50% increases in ν_a and ν_p respectively at $C_a = 1$ kg/m^3. PAC-L was not as effective at increasing the ν_a and ν_p of the HZ, with 10% and 20% increases measured at the same concentration. As the calculation of ν_a is specific to $\gamma_r = 1020\ s^{-1}$, and ν_p measures the difference between the $\gamma_r = 1020\ s^{-1}$ and $\gamma_r = 511\ s^{-1}$ viscosities, a larger proportional increase in ν_p shows that the polymers increased viscosity at

higher shear rates more than at lower rates. The results also show TK60 had a less of an effect on ν_a and ν_p than PAC-L. For example, at 4 kg/m^3 TK60 concentration in the baseline TG sample ν_p increased by 8%, whereas in the HZ sample a 58% increase was measured.

Figures 5.12 and 5.13 show the dependence of the τ_{10s} and τ_{10m} on C_a, respectively, which were found to be linear. The influence of PAC-L on τ_{10m} was notably similar for both mixes and PAC-L was found to increase both τ_{10s} and τ_{10m} more than TK60 for both the baseline TG and the HZ samples. These results contradict the manufacturers guidance, and previous literature such as Li et al. (2016) and Al-Maamori et al. (2016), which found that TK60 should increase viscosity and yield stress more than PAC-L. This could be due to the proprietary Bentonites used in this research already containing polyacrylamide polymers of a similar type to TK60, which reduced the TK60's effectiveness at increasing yield stress or viscosity further. It is also of note that TK60 reduces interface friction coefficients significantly, which may have resulted in slippage between the viscometer and sample during testing at high concentrations, resulting in lower measured values. This phenomenon has recently been documented by Wang et al. (2018), Fernandes et al. (2019), and Chen (2020) who report that a significantly roughened interface is required to obtain representative measurements, which was not possible during this research. These sources of uncertainty are considered further in the permeameter testing.

The relationship between f and C_a was assessed using the API filter press at the baseline pressure. Figure 5.14 shows that PAC-L is significantly more effective at reducing f than TK60, e.g by 25% at 4 kg/m^3 concentration compared to 3.7% for TK60 at the same concentration. This small variation resulted in scatter in the TK60 results, although the decreasing trend is still clear. The reduction in filtration rate caused by the PAC-L also reduced the rate of filter cake deposition at the soil-lubricant interface as the smaller filtrate volume resulted in fewer Bentonite platelets being deposited at the interface. However, the relative influence of this effect and the changes in viscosity and yield stress caused by additive inclusion are not clear

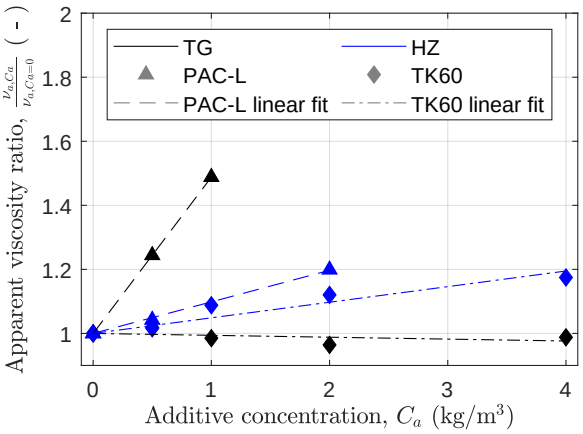


Figure 5.10: The relationship between additive concentration (C_a) and apparent viscosity ratio ($\frac{\nu_{a,Ca}}{\nu_{a,Ca=0}}$) for TG and HZ lubricant mixes.

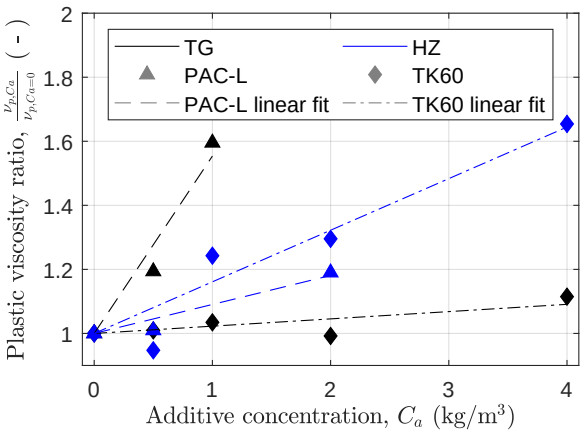


Figure 5.11: The relationship between additive concentration (C_a) and plastic viscosity ratio ($\frac{\nu_{p,Ca}}{\nu_{p,Ca=0}}$) for TG and HZ lubricant mixes.

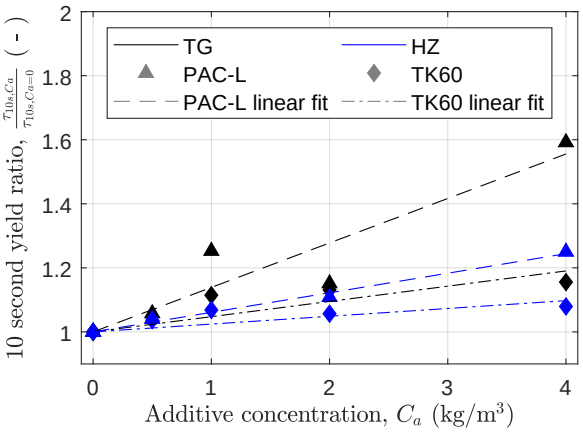


Figure 5.12: The relationship between additive concentration (C_a) and 10 second yield stress ratio ($\frac{\tau_{10s,Ca}}{\tau_{10s,Ca=0}}$) for TG and HZ lubricant mixes.

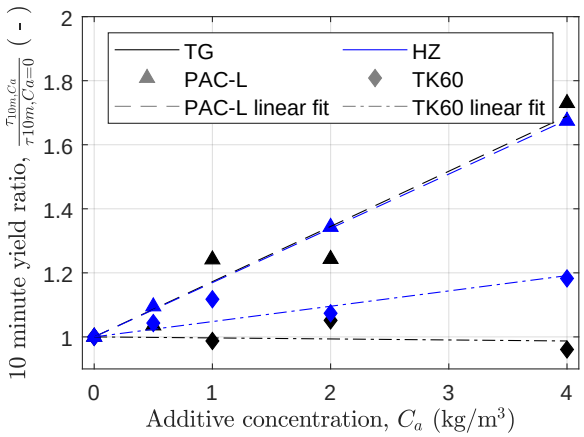


Figure 5.13: The relationship between additive concentration (C_a) and 10 minute yield stress ratio ($\frac{\tau_{10m,Ca}}{\tau_{10m,Ca=0}}$) for TG and HZ lubricant mixes.

from these separate tests. To assess their influence on the SLS system permeameter testing was completed on the additive containing Bentonite samples.

5.3 Consolidation shear box testing

5.3.1 Exemplar calculations

The consolidation shear box apparatus described in Section 3.3 was used to examine the influence of P_a and M on the peak and critical shear stresses (τ_p and τ_{cs}) of consolidated Bentonite mixes as well as the resulting water content WC. During consolidation, the top cap

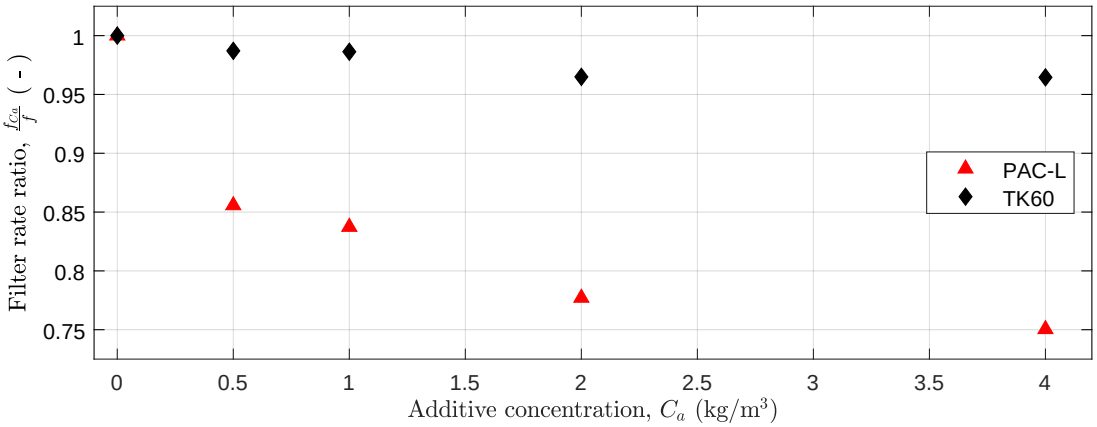


Figure 5.14: The decrease in normalised filtration rate ($\frac{f_{ca}}{f}$) with increased additive concentration (C_a) for TG and HZ Bentonite lubricants with PAC-L and TK60 additives.

vertical displacement was used to calculate the time to 90% consolidation (t_{90}) and consolidation coefficient (C_v), using the method proposed by Taylor (1948), to determine if primary consolidation of Bentonite could complete within the duration of typical stoppages. The Taylor method is standard industry practice and allows comparison to other results, for example those described in Shukla et al. (2009). With reference to Figure 5.15, the following procedure was used to calculate c_v and t_{90}:

1. The top cap displacement during consolidation was plotted against root - time.
2. A trend was then fitted to the linear portion of the data using linear regression, which is termed the primary consolidation stage.
3. The y-axis intercept was determined by extrapolation, which is termed the apparent displacement for zero consolidation (δ_0), and the gradient of the fitted line was also calculated.
4. As Taylor (1948) noted that using the unfactored equation under-predicted t_{90}. The corrected line is drawn from δ_0 with abscissa equal to 1.15 times that of the theoretical curve.
5. The intercept of this new line and the measured data was then defined as t_{90}.

6. C_v was then calculated as:

$$C_v = 0.848 \frac{H_{Dr}^2}{t_{90}} \tag{5.4}$$

where H_{Dr} is the drainage length which, due to double drainage used in these experiments, was set equal to half the initial sample height.

Once primary consolidation was complete, the samples were sheared to determine the peak and critical state shear stress (τ_p and τ_{cs}). Figure 5.16 presents exemplar results, from the shearing of the baseline TG mix, which show τ_p and τ_{cs}. Horizontal displacements of $\delta_h = 6$ mm were required to reliably achieve τ_{cs} after τ_p.

5.3.2 Effect of consolidation pressure

The influence of P_a on the consolidation rate and shear shear strength of Bentonite was explored for the range 50 kPa $\leq P_a \leq$ 250 kPa to ascertain the likelihood for a Bentonite filled overcut to consolidate at different overcut pressures and quantify the shear strength of the filter cake formed. Figure 5.17 shows the relationship between c_v and P_a for both the baseline mix and HZ. The calculated c_v values showed considerable scatter and therefore identifying a trend is difficult, however slight increase in c_v with P_a is apparent in the data. The scatter is assumed due to partial blockages or leaks in the drainage system of the apparatus, which could not be identified during the testing, and the slow consolidation rates.

These results showed that larger P_a resulted in larger c_v and therefore shorter consolidation times for TG. Tests were also completed on an identically prepared HZ mix at $P_a = 100$ kPa and 200 kPa for comparison and these were found to exhibit a similar response to the baseline samples. The calculated t_{90} magnitudes were between 13 hours and 80 hours for the 25 mm high samples tested, which (when quadrupled to allow for single drainage) means that consolidation of the Bentonite in the tunnel overcut may be possible during longer stoppages.

Figure 5.18 presents the variation in WC with P_a after consolidation. Larger P_a resulted in lower WC of the consolidated Bentonite, which (when considered with the larger c_v at larger

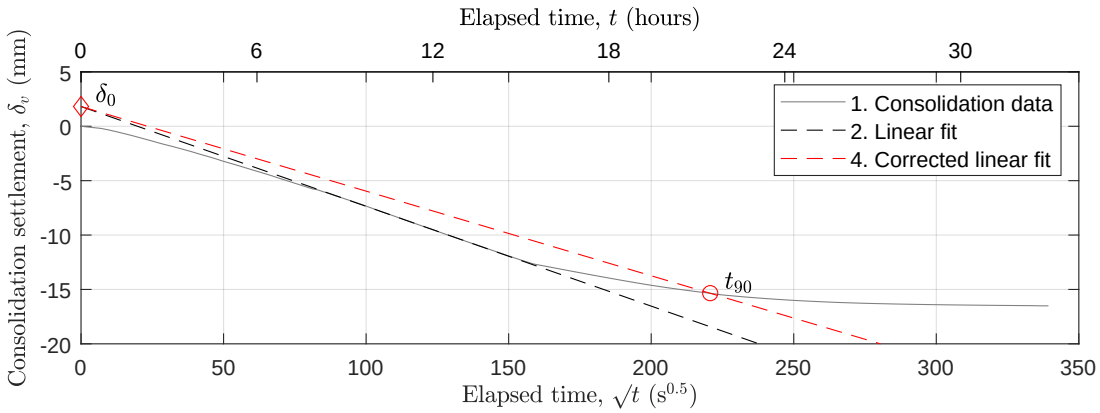


Figure 5.15: A graphical representation of the method for calculating t_{90} and c_v proposed by Taylor (1948), fitted to the baseline condition TG consolidation data.

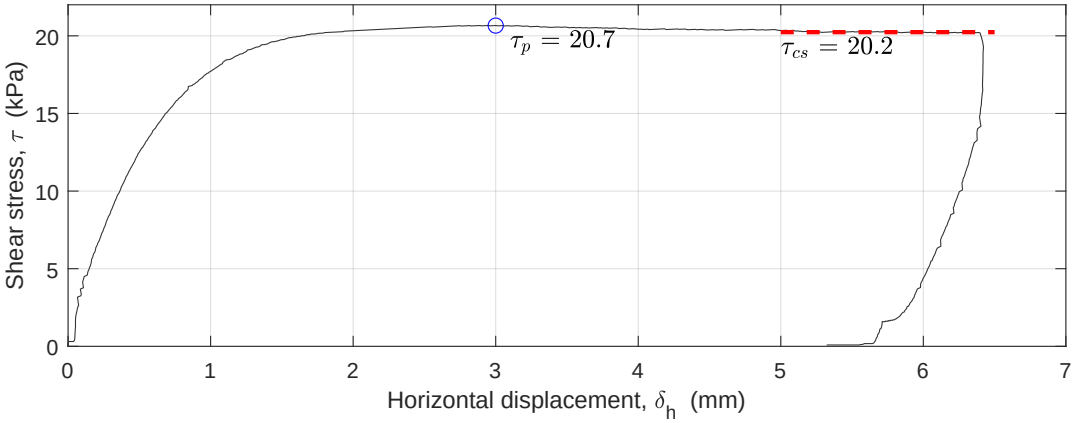


Figure 5.16: Shear box exemplar data from the baseline TG sample.

P_a) means that the higher P_a achieved a greater degree of consolidation in less time. This is an important observation for tunnelling, as it means that Bentonite in tunnel overcuts can consolidate quicker at higher overcut pressures.

Figure 5.19 presents the measured τ_p and τ_{cs} of the samples after consolidation. The magnitudes were found to vary linearly with P_a for both Bentonites. At higher stresses, the difference between peak and critical shear stress reduced, e.g. from 5.3% for TG at $P_a = 50$ kPa to < 0.1 % at $P_a = 250$ kPa. The difference between the TG and HZ stresses were small at 100 kPa ($< 4\%$). The TG measurements at $P_a = 200$ kPa are outliers to the observed trends, as significant variation between τ_p and τ_{cs} was measured, and is not representative of the TG behaviour.

The magnitudes of the normalised shear stress $\frac{\tau}{P_a}$ were similar for both mixes at

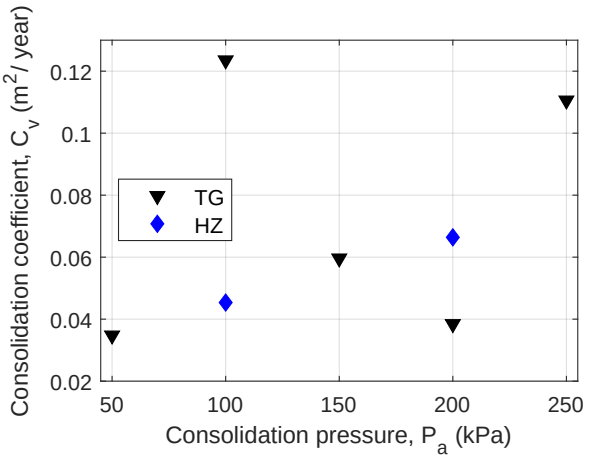


Figure 5.17: The relationship between applied consolidation pressure (P_a) and consolidation coefficient (c_v) for TG and HZ lubricant mixes.

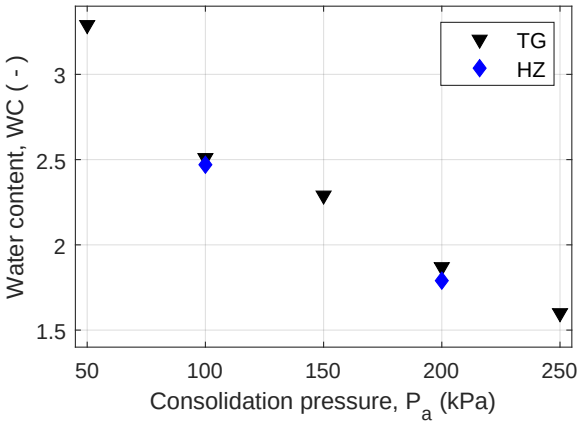


Figure 5.18: The relationship between applied consolidation pressure (P_a) and resulting water content (WC) for TG and HZ lubricant mixes.

~ 0.2, although it increased slightly to 0.26 in the $P_a = 50$ kPa TG sample. This is similar to other commonly used laboratory clays, such as Kaolin ($\frac{\tau}{P_a} = 0.253$), Martin (1994). The magnitudes of τ_p and τ_{cs} are greater than the interface friction increases recorded during field tunnel drives, which suggests complete consolidation of the Bentonite lubricant in the tunnel overcut may not occur in field drives.

5.3.3 Effect of mix ratio

To assess how varying M influenced the consolidation characteristics of the TG Bentonite, samples were prepared with $14 \leq M \leq 22$ and consolidated at the baseline pressure. Comparative samples were also prepared using HZ. Figure 5.20 shows the relationship between c_v and M, which appears linear in the range of M considered. This trend suggests that mixtures with a lower M consolidate more quickly than those with larger starting M values, although the impact is significantly less than the that of P_a within the bounds of this study.

Figure 5.21 shows a similar trend between the WC of the consolidated cake and M, where the WC increased with M, but the effect is significantly smaller than that observed for a variation in P_a, shown in Figure 5.18. Finally, Figure 5.22 shows the measured τ_p and τ_{cs}, which decreased slightly as M increased. Additionally, at higher M values, τ_p was larger than τ_{cs}, i.e. 11% for the $M = 22$ sample compared to 2.9% for the $M = 16$ sample. This means

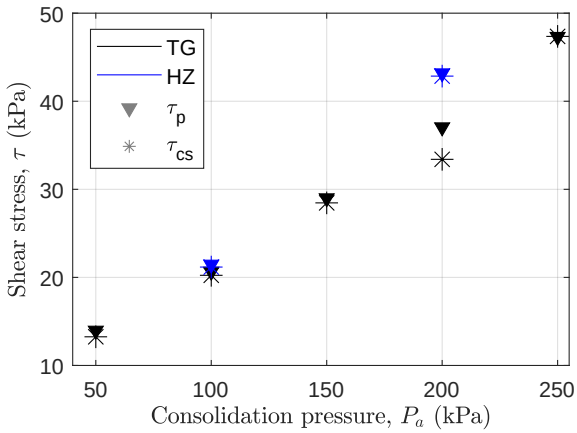


Figure 5.19: The influence of P_a on τ_p and τ_{cs} of consolidated TG and HZ lubricant mixes.

that although a similar critical state friction may be reached, the peak value for lubricants with higher starting M will be larger.

5.3.4 Water content - shear strength relationship

To determine if τ_p and τ_{cs} were dependent on the WC of the consolidated sample alone, irrespective of M or P_a, the results were plotted in WC - τ space for all tests. Figure 5.23 shows that, although scatter is apparent, τ_p and τ_{cs} decrease with increasing WC of the resulting filter cake. The HZ data at $WC = 2.85$ ($\tau \approx 32$) are outliers to the trend. In the remaining data, the difference between τ_p and τ_{cs} increases with the WC of the consolidated samples. The difference for TG samples increases from < 0.2 kPa at WC < 1.6 to 0.72 kPa at WC > 3.2, which is small but non-trivial when considering the low skin frictions recorded during tunnelling.

These results demonstrate that the properties of the consolidated filter cake are primarily dependent on its WC (as anticipated) and independent of the starting conditions for freshly prepared Bentonites. τ_p and τ_{cs} are also similar for both TG and HZ. P_a has a larger influence on WC than the starting M for the parameter ranges considered. This means the shear strength of a filter cake within the tunnel overcut will depend primarily on the overcut pressure during tunnelling and any stoppages.

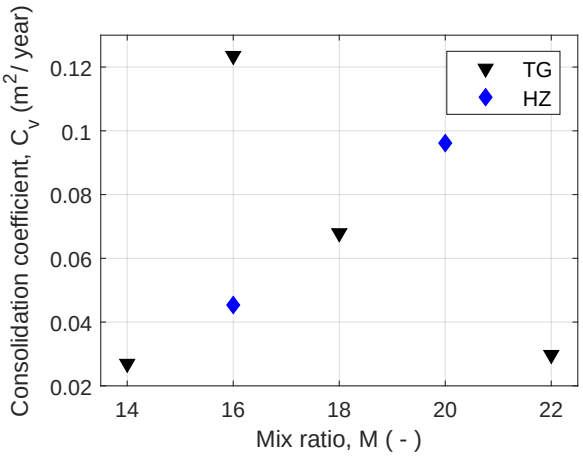


Figure 5.20: The relationship between mix ratio (M) and consolidation coefficient (c_v) for TG and HZ lubricant mixes.

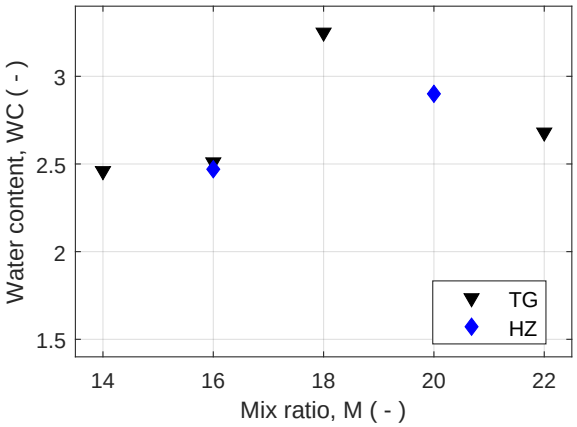


Figure 5.21: The relationship between mix ratio (M) and resulting water content (WC) for TG and HZ lubricant mixes.

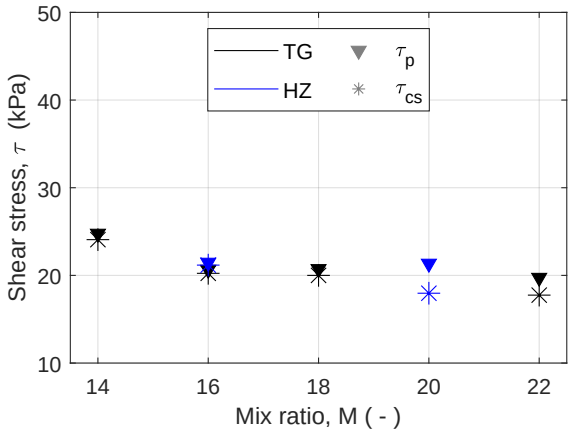


Figure 5.22: The relationship between mix ratio (M) and consolidated peak or critical state shear stress (τ_p and τ_{cs}) for TG and HZ lubricant mixes.

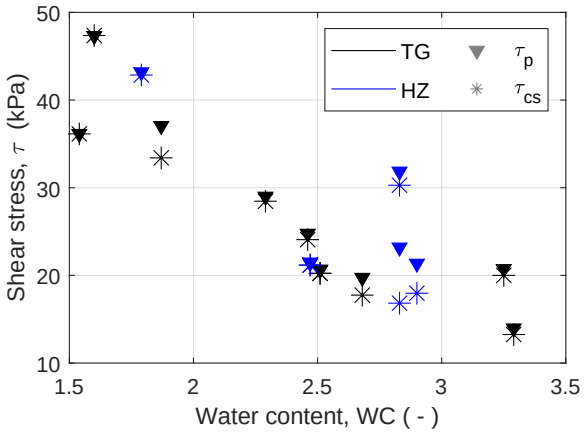


Figure 5.23: The relationship between water content (WC) and consolidated peak or critical state shear stress (τ_p and τ_{cs}) for consolidated TG and HZ lubricant mixes, obtained using a consolidation shear box apparatus.

5.4 Permeameter testing

5.4.1 Exemplar calculations

The permeameter apparatus described in Section 3.4, and shown schematically in Figure 5.24, was used to determine the pore pressure distribution around the soil-lubricant interface and determine the influence of M, P_a, and C_a on the pore pressures (u), penetration distance (X), and permittivity (K) for both the baseline TG and HZ lubricant mixtures. Figure 5.25 presents typical u measurements from a 7 day baseline test. Data from five pressure transducers

(PT) are plotted, located between 20 mm above and 80 mm below the soil-lubricant interface and labelled X_{20}, X_{00}, X_{-20}, X_{-40}, X_{-80}. These were located to capture any steep variations in the u profile with depth which occurred near to the soil-lubricant interface. The development of u is shown as a function of root-time, as previous testing (such as Larsen (1938), Ahmad et al. (2018), and Sims (2020)) had revealed a linear relationship between filtration rate and root-time.

As well as the direct pore pressure measurements, the permittivity of the different sections of column were calculated. These were termed the 'band' permittivity, with each 'band' being the section of the column between two pressure sensors, e.g. between $X = 0$ mm (the interface) and $X =$ -20 mm (the first pressure sensor within the sand). To calculate the permittivity, the pressure difference between two sensors (ΔP_i; where i denotes the sensor location) and change in filtrate weight (W) were calculated during a given time step (Δt), which was typically 1 $s^{1/2}$. The permittivity (K_i) was then calculated using equation 5.5.

$$K_i = \frac{\Delta W}{\Delta t.A_c.\gamma_w} \frac{\Delta X.\nu_v}{\Delta P_i} \tag{5.5}$$

where ΔX is the distance between the sensor locations, γ_w is the density of the filtrate water, A_c is the plan area of the column apparatus (0.0154 m^2), and ν_v is the dynamic viscosity of the filtrate water.

These calculated values yielded the resistance to the Bentonite flow in each section of the column. As the change in effective stress on the soil resulting the applied pressure and band permittivity could be calculated for each band utilising the difference in u across the band, the depths at which P_a was transferred to the soil structure were also found. These corresponded to where the 'support pressure' would be applied to the soil structure at the SLS interface under field conditions.

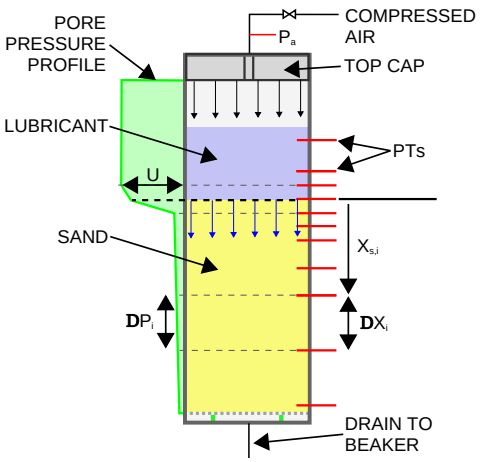


Figure 5.24: Schematic of the permeameter test apparatus with key features labelled.

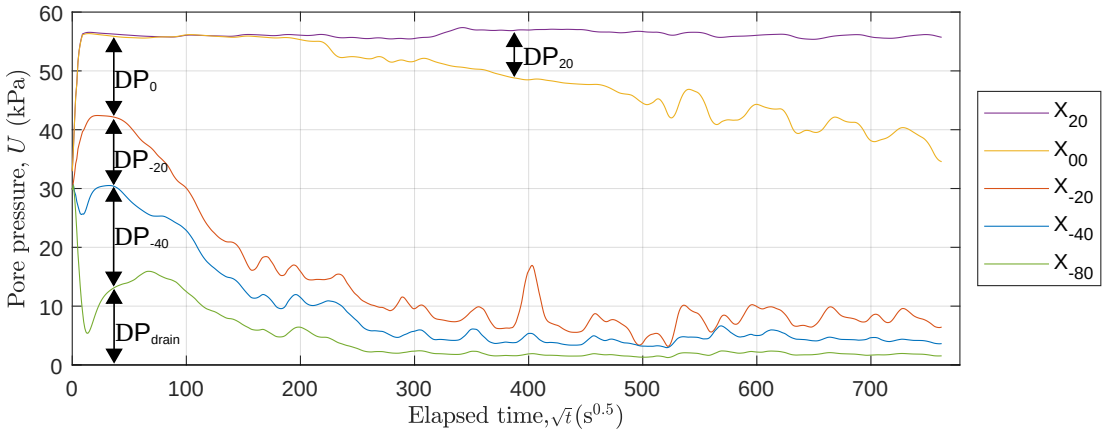


Figure 5.25: The typical pore pressure (u) response with elapsed time (t) for five pressure transducers around the interface of the permeameter apparatus. The pressure differences are labelled ΔP_i where i denotes the location of the top pressure sensor relative to the interface.

5.4.2 Typical results

Figure 5.27 shows the lubricant penetration into the sample for the first 100 $s^{1/2}$ of the baseline test. In the first 10 $s^{1/2}$, the infiltration rate is rapid and near-linear with root-time. This is defined as the infiltration, or 'spurt', phase (Xu and Bezuijen (2019)). After this time, the wave-front advance rate slows significantly as the filter cake begins to form at the interface, before stagnating at approximately 60 $s^{1/2}$ in this test.

Figure 5.28 shows the pore pressure measurements from six PTs during the baseline test alongside the wave-front location for the first 60 $s^{1/2}$ of the test. The high rate of infiltration at the start of a test resulted in an initial drop in P_a due to the high flow rate of air required

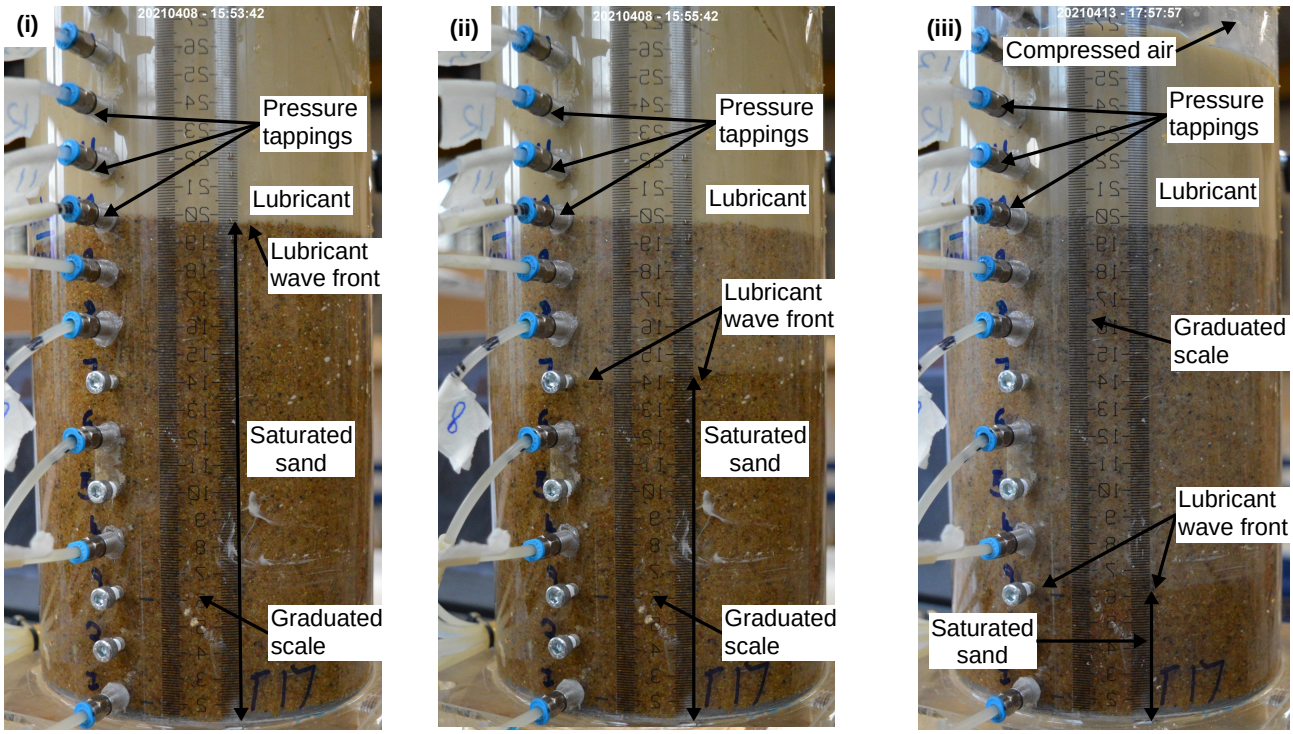


Figure 5.26: Photographs of the lubricant penetration with elapsed times of: (i) 0 $s^{1/2}$, (ii) 11 $s^{1/2}$ (2 minutes), and (iii) 660 $s^{1/2}$ (5 days) with salient features labelled.

to the apparatus. This is apparent in the figure as P_a increases from 35 kPa to 57 kPa (steady state for the test) after 10 $s^{1/2}$. Similarly, during the infiltration phase, the hydraulic losses in the small diameter drainage pipework resulted in $u > 0$ kPa at the base of the sample, as shown by the X = -180 mm sensor response between $0 < t < 15$ $s^{1/2}$. The drainage pipework was required to be small diameter to promote droplet formation into the collection beaker during the latter stages of the test, when the filtration rate was low. This effect was common in all results, so it was deemed not to affect the comparisons made between tests.

The result of the wave-front passing a PT was that the measured u began to increase, such as at $t = 9$ $s^{1/2}$ for the X = -40 mm sensor in Figure 5.28. This was due to the increased dynamic pressure losses in the Bentonite lubricant between the PT location and the wave-front location. Following the initial increase in u a plateau is reached, such as at $t = 27$ $s^{1/2}$ for X = -40 mm sensor, demonstrating that the behaviour of the soil-lubricant interface was changing as the filter cake formed and the permittivity of the SLS interface, and therefore the filtration rate, decreased.

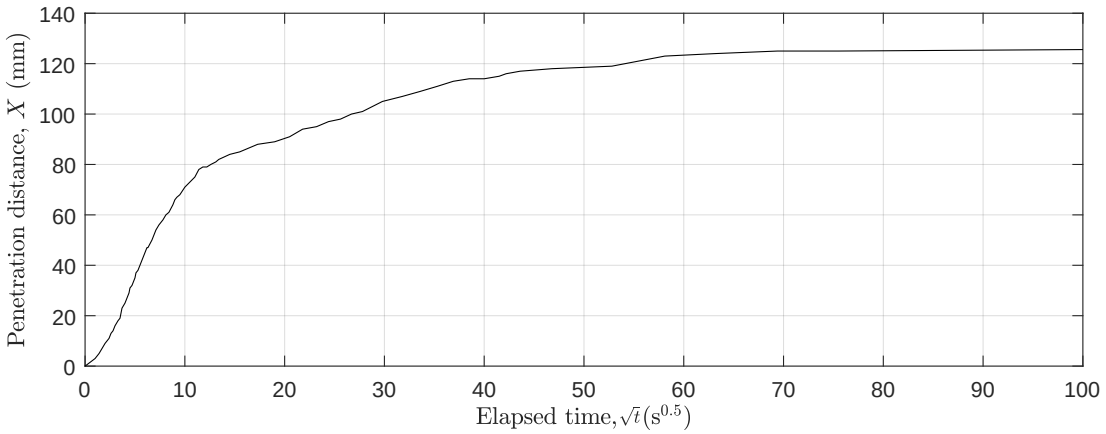


Figure 5.27: The increase in wave-front penetration (X) with root-time (t) during a baseline permeameter test. The slowing in the rate of advance at 11 $s^{1/2}$, caused by filter cake formation, is apparent before the wave-front stagnation at $t \approx 60$ $s^{1/2}$.

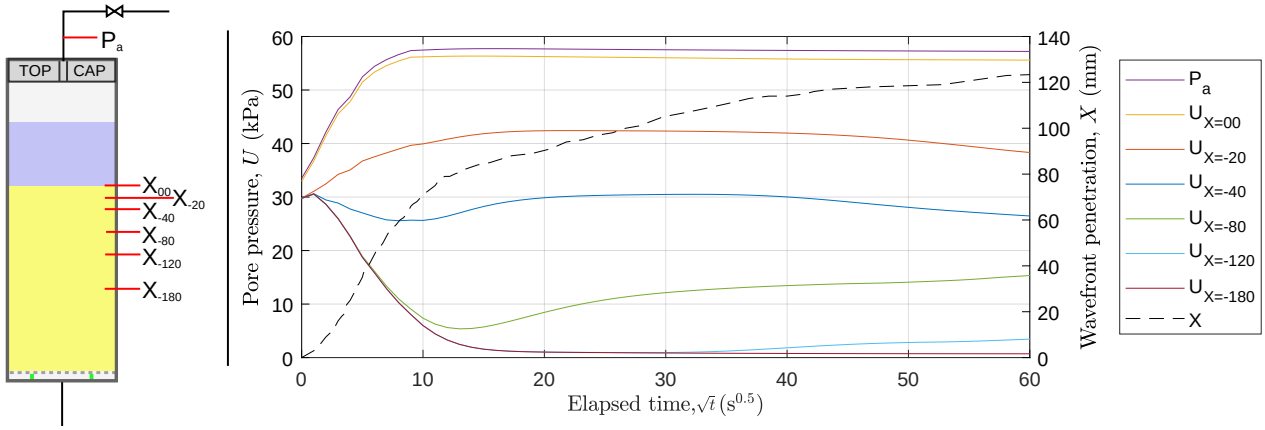


Figure 5.28: The pore pressure (u) response and Bentonite wave-front penetration (X) in the first 60 $s^{1/2}$ (1 hour) of the permeameter baseline test.

The pore pressure measurements at three discrete times for the same test are shown in Figure 5.29. These times (11 $s^{0.5}$ (2 minutes), 294 $s^{0.5}$ (1 day), and 660 $s^{0.5}$ (5 days)) correspond to key behaviour changes at the SLS interface during the test. Figure 5.29 (i) shows the initial condition during the infiltration (or spurt) phase of penetration. At this time the pore pressure reduces linearly through the sand sample as the Bentonite infiltrates into the pore space. Figure 5.29 (ii) then shows the pressure distribution after the filter cake has formed in the region 0 mm $<$ X $<$ 20 mm. Finally, after 5 days, figure 5.29 (iii) shows the filter cake thickness has increased such that the X = 0 mm sensor u measurement has also begun to reduce. These trends can also be observed in the time series data for the same test, shown in figure 5.25.

The changes in the u measurements throughout the tests were caused by changes in the

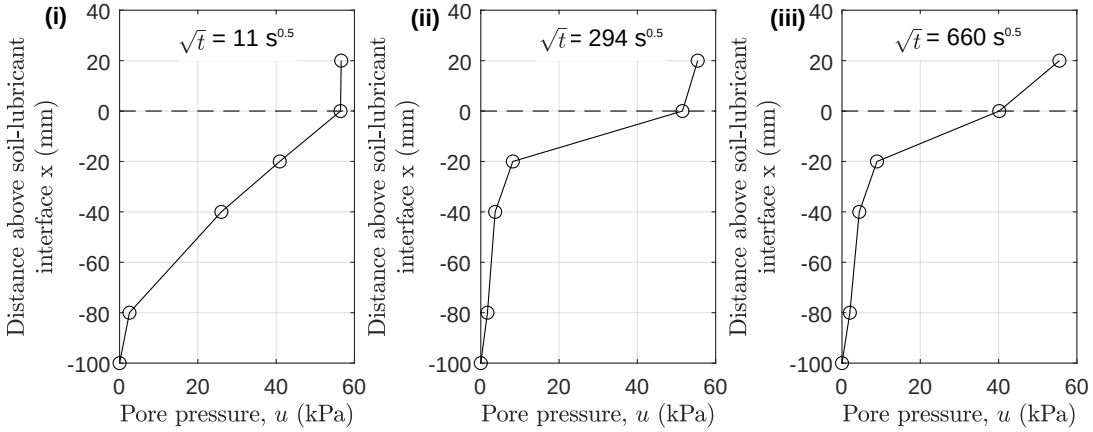


Figure 5.29: Typical pore pressure (u) measurements within the permeameter apparatus at three times during test shown in Figure 5.25: (i) 11 s$^{0.5}$ (2 minutes), (ii) 294 s$^{0.5}$ (1 day), and (iii) 660 s$^{0.5}$ (5 days).

permittivity of different bands between sensors. Figure 5.30 presents the permittivity of the 0 mm > X ≥ -20 mm and -20 mm > X ≥ -40 mm bands within the permeameter (K_0 and K_{-20} respectively) in the first 60 $s^{1/2}$ of the baseline test. The transition in the wave-front advance rate occurred as the calculated permittivity in the column decreases below the permittivity of the column system, i.e. between 12 $s^{1/2}$ and 20 $s^{1/2}$. At this time there is a notable change in gradient of the K_0 and K_{-20} permittivities, as the newly formed filter cake limits the infiltration into the sample. The very high permittivities before this were due to the negligible ΔP between the sensors in the initial stages of the test.

Once formed, the low permittivity filter cake at the soil-lubricant interface was observed to continue to decrease in permittivity for the duration of the test. This relationship was log-linear in root-time space and caused the filtration rate to also reduce linearly throughout the test. At low flow rates, the incremental filtrate weight (ΔW) used to calculate the permittivity in Equation 5.5 reduced such that the signal to noise ratio increased significantly. As the permittivity behaviour was expected to be log-linear with root time, linear models were fitted to the data to identify the trends. Figure 5.31 plots the measured and fitted data for the baseline test between 20 mm above and 40 mm below the interface. To avoid the influence of the rapidly changing permittivity during filter cake formation the model is fitted from 100 $s^{1/2}$

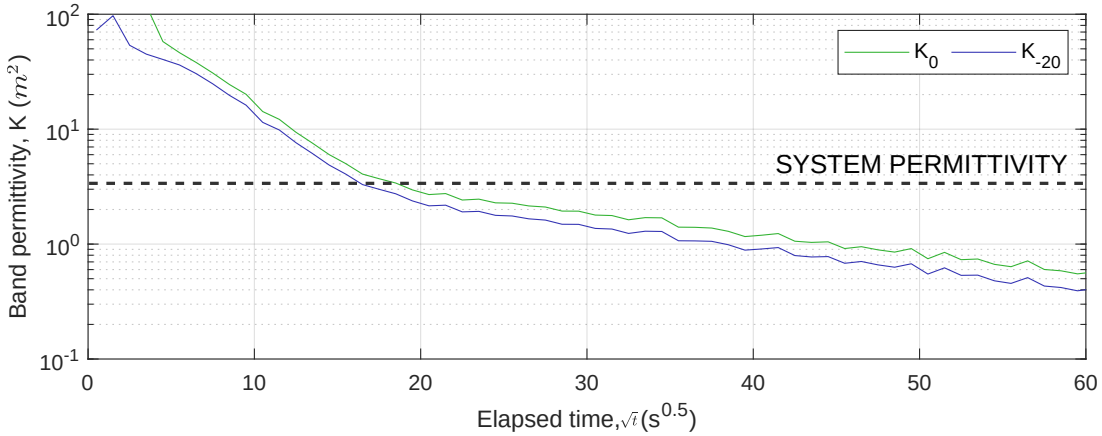


Figure 5.30: The typical permittivity development with time for the soil bands 0 mm $> X \geq$ - 20 mm (K_0) and -20 mm $> X \geq$ -40 mm (K_{-20}).

$\leq t^{1/2}$.

The trends in band permittivity were found to be influenced by P_a, M, and C_a. Two common trends were observed in the results. First, the permittivity of the bands further from the interface (e.g. K_{-40} in Figure 5.31) did not reduce significantly during the test. This shows that, once the filter cake forms, additional Bentonite platelets did not filter through the cake into the sample pores, as the permittivity does not reduce. Secondly, the bands at and just above the interface decreased in permittivity significantly during the test, as shown by low final permeability of the K_{20} band in the figure, which shows that the filter cake continued to form on the surface of the soil sample throughout the test.

Figure 5.32 shows the effect of the decrease in permittivity at the interface within the soil sample. Measurements of u below the interface decrease began to decrease after $t = 20$ $s^{1/2}$ and reduced significantly by t = 200 $s^{1/2}$. Finally, as the filter cake thickness increased, u at the interface ($X = 0$ mm) began to decrease after $t = 200$ $s^{1/2}$. The sensors within the soil recorded near zero u during this period of the test, demonstrating the permittivity of the interface is significantly lower than the Bentonite infiltrated the soil sample.

Figure 5.32 also shows variation in u close to the interface, e.g at $t = 400$ $s^{1/2}$ for $X =$ -20 mm sensor. This was caused by the 'fresh' Bentonite mixture from the top of the sample penetrating to the sensor location. There are three possible reasons for this: (i) the filter cake

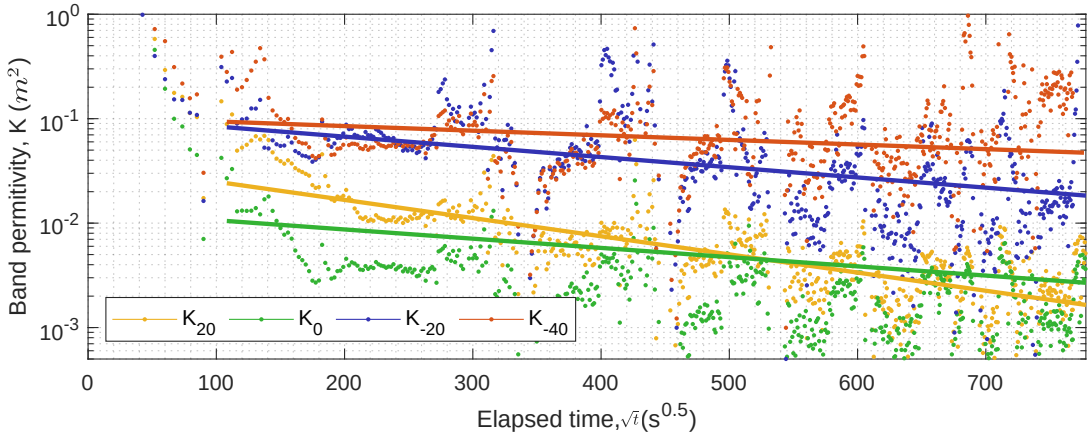


Figure 5.31: Development of permittivity (K) for 20 mm deep bands about the interface with time for a baseline ($M = 16$, $P_a = 50$ kPa, TG) permeameter test.

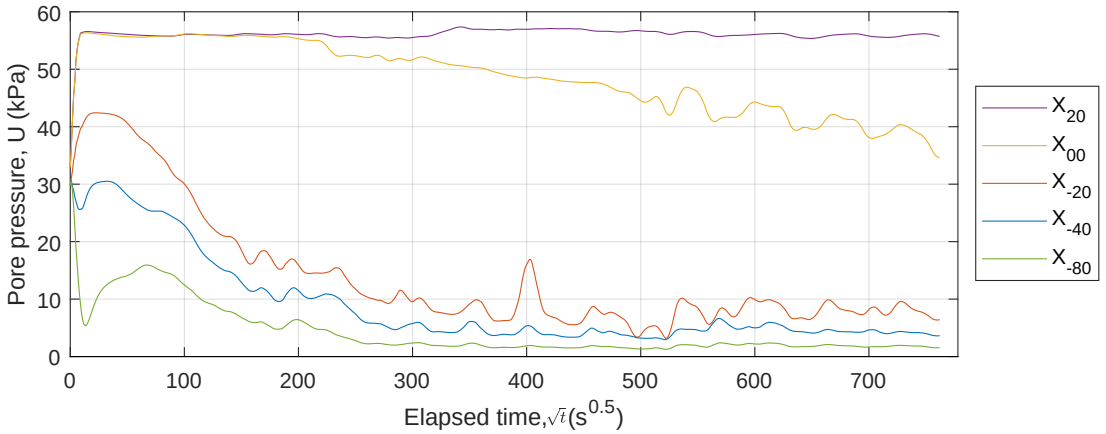


Figure 5.32: Development of pore pressure (u) with elapsed root-time (t) for five pressure transducers about the interface of the permeater apparatus during the baseline test.

formed at the interface ruptured, allowing the fresh Bentonite to pass through, (ii) Bentonite travelled along the interface with the chamber wall, or (iii) the pressure probes, which were in a vertical line down the column, disrupted the filter cake formation and allowed the fresh Bentonite to penetrate into the sample.

Edge effects have been discussed in Sanvitale et al. (2021) and Lin et al. (2021), where the interface between the sand particles and flat boundary of the column was shown to create larger pores than within the sample. These pores provided a preferential path for lubricant to flow. Lin et al. (2021) addressed this by the inclusion of ribs in the chamber wall to increase the boundary length. This was not possible in this research as the ribs would introduce dilation of the wave-front, and influence the penetration rate and distance. For this reason, infiltration

down the edge of the column was the probable cause of these increases in pressure, although it was not possible to detect such a phenomenon in the photographs taken during the tests.

Because of this, samples were taken from the centre of the column to ensure the penetration was similar to the recorded values at the chamber edges. These cores showed that the edge effects did not influence the penetration as the wave-front location was uniform throughout the sample. As such, it was believed any lubricant infiltrations were small and did not materially affect the results of the experiments. In future experiments it would be advised to modify the apparatus slightly to provide a rough interface at the soil-column boundary, and to arrange the pressure probes in a spiral around the circumference of the apparatus, to reduce the risk of any fresh Bentonite penetration being caused by the apparatus setup.

5.4.3 Effect of lubricant type

To quantify any differences in behaviour at the soil-lubricant interface related to the lubricant type, the HZ samples were compared to the baseline mix. Additionally, the penetration distances (X) of the Bentonite wave-fronts were compared to Equation 5.6, proposed by Praetorius and Schößer (2017).

$$X = \frac{d_{10}}{2\tau_0}\Delta P_a \tag{5.6}$$

where the τ_0 is not specified at a particular time (i.e. the API standard yield points measured at 10 s or 10 min). In the experiments, ΔP_a and D_{10} were identical, so any differences in X were inversely proportional to τ_0 of the Bentonites. The tests yielded $X = 122$ mm for TG and $X = 75$ mm for HZ. This result does not agree with the prediction of Equation 5.6, as the difference in the measured or calculated yield stresses (i.e. τ_{10m}, τ_{10s}, or Y_p) were 9.8% smaller and 10% and 8.4% larger respectively for HZ compared to the baseline mix.

These results show that X is influenced by factors other than τ_0 for the Bentonites and sand in this study. For example, the elemental testing in Section 5.2.3 identified that HZ had a higher viscosity at low shear rates when compared to TG (11.7% at $\gamma_r = 5.11$ s^{-1}). This

generated larger drag forces during lubricant infiltration, which resulted in lower permittivities of the sand-Bentonite mixture and filter cake formation occurring at smaller X values. It is therefore proposed that Equation 5.6 can be used to accurately predict the change in infiltration distance with P_a for a particular Bentonite, but the empirical factor of '2' must be calculated for each Bentonite product.

Figure 5.33 shows the overall permittivity of the soil-lubricant system within the permeameter after 100 $s^{1/2}$ elapsed, as this was when the permittivities were found to become linear with root-time, as shown by the linear models fitted to the data. HZ formed a lower permittivity filter cake at the soil-lubricant interface at t = 100 $s^{1/2}$, whereas the higher filtration rate of the TG observed in elemental testing resulted in faster deposition of material into the filter cake and a greater reduction in K during the test. This effect meant that both tests had similar K values at the end of the test, with HZ 0.2% larger than TG.

The scatter in both the TG and HZ data after t = 300 $s^{1/2}$ was due to the low ΔW in each time increment being similar to the electrical noise in the sensor reading. The periodic variation in the results was caused by temperature variation in the laboratory space, which was unavoidable during the test. The variation in K was partly due to an anticipated physical increase in K caused by the increased temperature influencing the properties of the Bentonites and partly due to temperature dependency of the filtrate measurement system which could not be fully corrected in the data. This was because the influence of sunlight on the system caused thermal strains of the apparatus which effected the load cell measurements in a manner that could not be repeated during calibration. As these variations were periodic, and the test extended through multiple cycles, it was deemed not to have affected the overall results.

5.4.4 Effect of pressure

The influence of P_a on spurt distance X was assessed using photographs taken of the column during tests on the M = 16 TG mix with P_a = 25 kPa, 50 kPa, 75 kPa, and 100 kPa. The results were normalised using the non-dimensional groups: $\frac{X}{D_{10}}$ and $\frac{\tau_{10s}}{P_a}$, which were selected

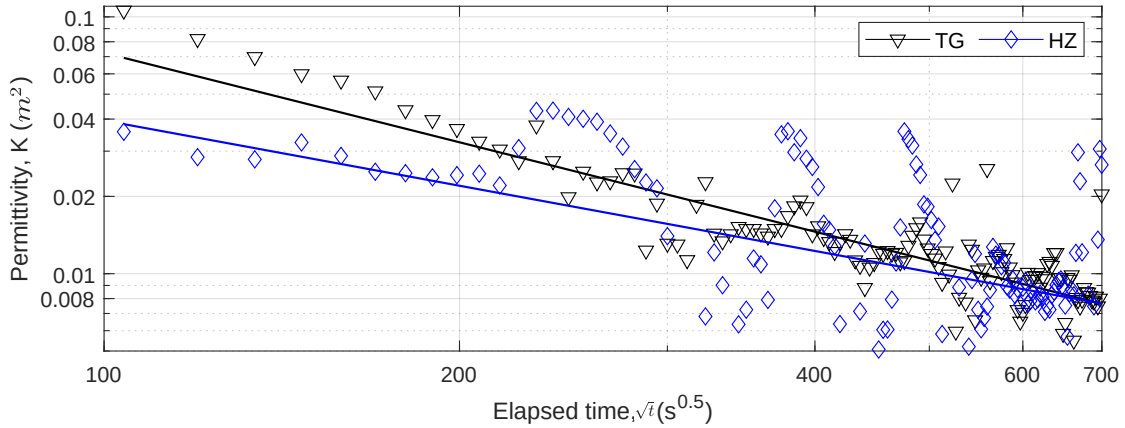


Figure 5.33: The development of permittivity of the soil-lubricant system (K) with time (t) for TG and HZ samples within the permeameter at $P_a = 50$ kPa.

as initial findings had shown D_{10} and τ_{10s} influenced the wave-front penetration distance, as proposed in Equation 5.6.

Figure 5.34 shows the results from the four tests in the range $0\ s^{1/2} \leq t \leq 55\ s^{1/2}$, after which stagnation occurred. Two infiltration regions were apparent in the results. Firstly an initial rapidly advancing phase which transitioned into a second linear region, with a slower rate of penetration, before the wave-front stagnated. P_a did not significantly influence the gradient of non-dimensional results, suggesting that the transition between the regions is defined by the Bentonite and sand properties alone, with the penetration distance proportional to P_a, and the dimensionless groups proposed successfully normalise the influence of P_a. This finding verifies the form of Equation 5.6, using the measured τ_{10s} to supplant the poorly defined τ_0 in the equation.

The overall permittivity of the system was found to be proportional to P_a for $P_a > 50$ kPa, e.g. 0.048 m/s and 0.032 m/s for $P_a = 50$ kPa and 75 kPa respectively at $t_s = 200$ s. At $P_a < 50$ kPa the permittivity of the system increased, which suggests that a more permeable filter cake was initially formed. The band permittivities, similar to those shown in Figure 5.31, were also calculated and are given in Table 5.5. The test with $P_a = 100$ kPa is not shown as the wave-front fully penetrated the permeameter after 60 $s^{1/2}$.

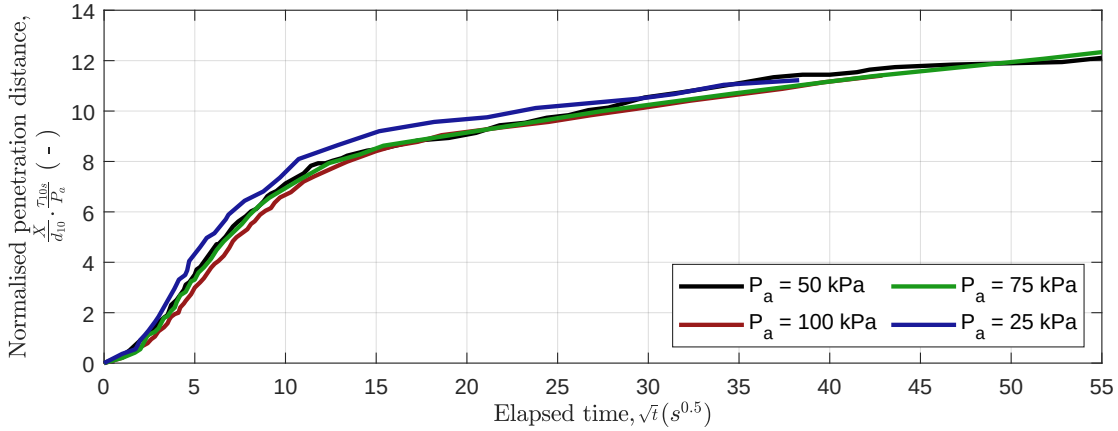


Figure 5.34: The development of normalised wave-front penetration ($\frac{X}{d_{10}}.\frac{\tau_{10s}}{P_a}$) with root time during tests of the baseline TG mix in the range 25 kPa $\leq P_a \leq$ 100 kPa.

Table 5.5: Trends in band permittivity (K) between 100 $s^{0.5} < t \leq$ 700 $s^{0.5}$ for tests with P_a = 25 kPa, 50 kPa, and 75 kPa.

Band	**Symbol**	**Permittivity gradient,** $\frac{K}{t^{0.5}}(mm.s^{-3/2})$		
		P_a **= 25 kPa**	P_a **= 50 kPa**	P_a **= 75 kPa**
20 mm $\geq X >$ 0 mm	K_{20}	0.0316	-0.0335	-15.1
0 mm $\geq X >$ -20 mm	K_0	-0.00852	-0.0116	-0.131
-20 mm $\geq X >$ -40 mm	K_{-20}	0.187	-0.0961	0.0756
-40 mm $\geq X >$ -60 mm	K_{-40}	0.564	-0.0689	0.275

Table 5.5 shows that the trends K for each band varied depending on P_a during the test. For example, larger P_a led to K_0 and K_{20} decreasing more rapidly, as the external filter cake formed. However, both the P_a = 25 kPa and 75 kPa tests resulted in increasing K_{-20} and K_{-40} values, which suggests washing out of the Bentonite plates within the soil pores, as the filtrate from the filter cake formation process washes through.

Figure 5.35 shows the non-dimensional filtrate weight for the tests. The non-dimensional weight is defined as $\frac{W}{P_a.A_c}$, where A_c is the plan area of the permeameter. The results demonstrate that for $P_a >$ 50 kPa the normalised weight was consistent. However, for P_a = 25 kPa the weight in the initial spurt phase was smaller (36% less than the baseline test at t = 100 $s^{1/2}$). The gradient of the linear portion (after t = 100 $s^{1/2}$) is also steeper in the P_a = 25 kPa test, showing that the non-dimensional filtration rate is higher.

These results have shown that there is a transition in behaviour at the soil-lubricant in-

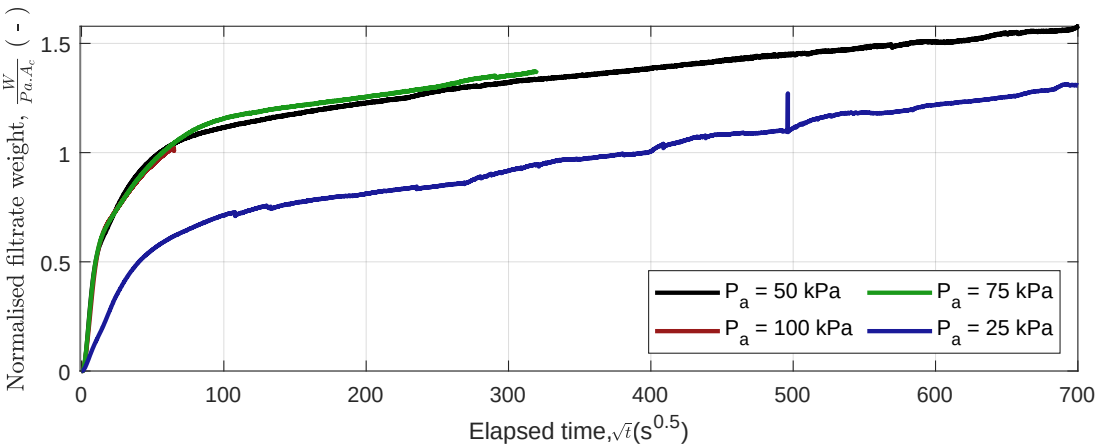


Figure 5.35: Normalised filtrate weight development with elapsed time (t) for baseline Bentonite lubricant mix with P_a = 25 kPa, 50 kPa, 75 kPa, and 100 kPa.

terface at $P_a < 50$ kPa for the lubricant and sand in this study. The infiltration and filter cake formation processes which occur at higher pressures do not occur in the same way below this threshold, which results in a more permeable boundary at the interface and less filter cake deposition. As initial P_a magnitudes during lubricant injection in the field exceed 25 kPa, the consistent behaviour of the higher stress tests will be present in field conditions.

5.4.5 Effect of mix ratio

The effect of varying mix ratio was assessed using TG with M = 12, 16 and 24. Figure 5.36 shows the relationship between non-dimensional penetration distance ($\frac{X}{D_{10}} \frac{\tau_{10s}}{P_a}$) and M for all tests. The results show that P_a does not influence the normalised penetration of the same mix M, confirming the findings in the previous section. As M decreased the penetration distance also decreased, which demonstrates that the filter cake formation mechanism occurs faster with lower M, resulting in the smaller non-dimensional wave-front stagnation depth.

The overall permittivity of the samples was calculated between t = 200 $s^{1/2}$ and the end of the tests, as this portion of the data was linear in log-log space and avoided any influence of the initial spurt phase at large M. Figure 5.37 presents linear models fitted to the tests data in this range. At t = 700 $s^{1/2}$, $K_{M=24}$ (the permittivity of the M = 24 sample) was significantly larger than $K_{M=16}$ at the same P_a (by 350%). This resulted from a larger permittivity at t = 200 $s^{1/2}$ and 24% slower decrease in K throughout the test for the M = 24 sample. The M

= 12 and $M = 16$ samples have similar permittivity at $t = 200\ s^{1/2}$ but $K_{M=12}$ decreases 18% faster than $K_{M=16}$ throughout the test, resulting in a lower permittivity at $t = 700\ s^{1/2}$.

The differences in permittivity were also observed in the filtrate weights measured during testing. Figure 5.38 shows the time history of the normalised filtrate weight ($\frac{W}{P_a.A_c}$) during the tests. The non-dimensional filtrate weights have been zeroed at t = 200 $s^{1/2}$ to show the influence of the initial infiltration phase and the resulting gradient after filter cake formation. In the initial phase the filtrate weight increases rapidly before the filter cake forms and the rate decreases to become linear with root-time. The results show that the $M = 12$ sample had a 21% lower filtration rate, when compared to $M = 16$ sample, which is similar to the calculated difference in permittivity. The $M = 24$ rate was 220% higher than the $M = 16$ gradient at the same pressure, which was again similar to the difference in permittivity of the samples at $t = 200\ s^{1/2}$.

These results have shown that Bentonite lubricant mixes with lower M values will penetrate less into the soil surrounding a pipe-jack, as they more readily form an external filter cake. Once formed, the cake will have lower permittivity - reducing subsequent filtration through it. Testing at lower P_a also results in more permeable filter cakes being formed for both the $M = 16$ and $M = 12$ mixes, as predicted in the previous section. These will lead to faster rates of filtration of the lubricant in the tunnel bore during tunnelling.

5.4.6 Effect of additives

The influence on additives on the soil-lubricant interface were explored using two tests on baseline mixes with 4 kg/m^3 of PAC-L or 4 kg/m^3 TK60 added during mixing. The effect on the overall permittivity of samples aligned with the results of the elemental testing, as both additives resulted in lower permittivities after 200 $s^{1/2}$. The permittivity of both samples then decreased more slowly than in the base case, with $\frac{\Delta K}{\Delta t}$ 30% smaller for the PAC-L test and 17% smaller for the TK60 test. These smaller gradients resulted in higher permittivity at 7 days elapsed, 6.7% for PAC-L and 5.7% for TK60.

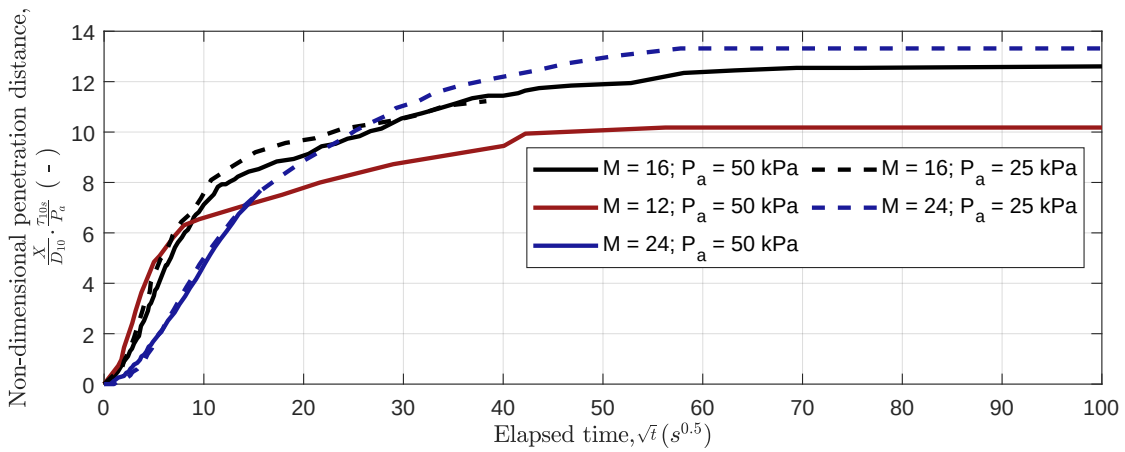


Figure 5.36: The development of normalised wave-front penetration ($\frac{X}{d_{10}}.\frac{\tau 10s}{P_a}$) with root time during tests of TG at M = 12, 16, and 24.

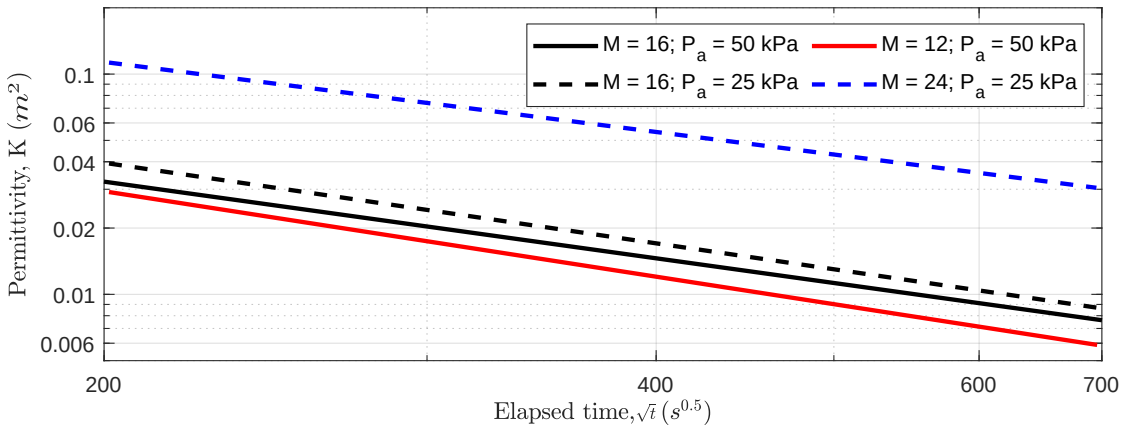


Figure 5.37: The development of permittivity of the soil-lubricant system (K) with time (t) for samples within the permeameter for M = 12, 16, 24 and P_a = 25 kPa and 50 kPa.

Figure 5.39 shows the non-dimensional filtrate weight measurements, which were zeroed at t = 200 $s^{1/2}$ and demonstrate the different ways in which the TK60 and PAC-L affected the behaviour of the lubricant-soil system. The TK60 inclusion reduced the infiltration distance before stagnation and resulted in the transition to the linear, filter cake building, region occurring sooner. This is shown by the more rapid transition from the initial steep filtration rate to the slower, linear, section between t = 40 $s^{1/2}$ and 60 $s^{1/2}$. Once the transition had occurred, the filtration rate was 15% greater than the baseline mix, similar to the calculated permittivity difference.

The PAC-L mixture had a different effect on the system. Initially, the rate of wave-front infiltration was slower than the baseline case, and the wave-front stagnated later (82 $s^{1/2}$ com-

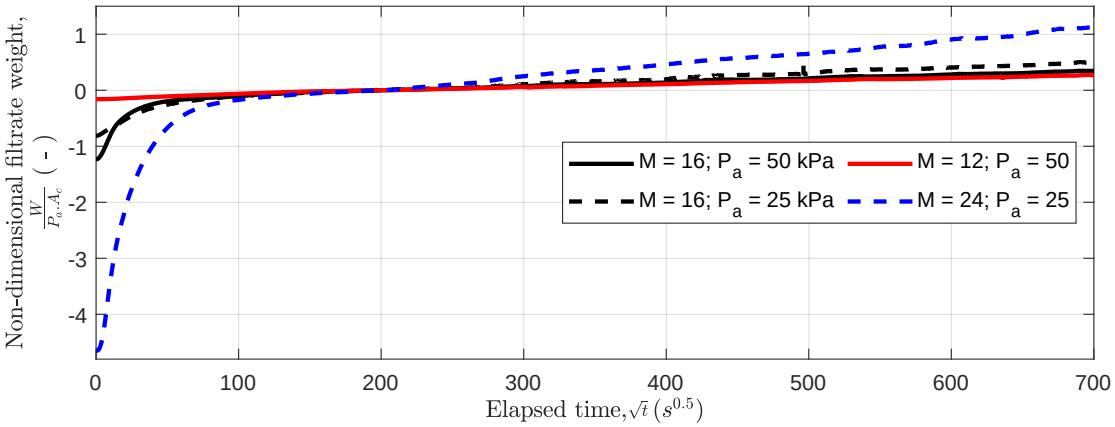


Figure 5.38: The non-dimensional filtrate weight of TG samples with different M values, zeroed at t = 200 $s^{1/2}$ to show the different spurt and linear behaviour.

pared to 58 $s^{1/2}$). Once stagnation occurred, the filtration rate gradually decreased until t = 200 $s^{1/2}$ where the rate is lower than both the baseline and TK60 containing mixes. The rate then increased between 400 $s^{1/2}$ and 450 $s^{1/2}$ until it was 16% greater than the baseline case, similar to the TK60 test. These differences in the filtration rate were due to the different water content (WC) of the filter cake formed, as well as the behaviour of additives, which are discussed in more detail in the following section.

5.4.7 Filter cake water content

Water contents were measured at the end of each test by taking lubricant samples at 10 mm ± 5 mm intervals between X = 50 mm and X = -10 mm. Figure 5.40 presents WC of samples collected from the presented permeameter tests. Samples taken at X > 30 mm were found to be the same WC as the original mix in all tests, demonstrating that only the Bentonite in close proximity to the interface was affected by the filtration mechanism. This means that the Bentonite was not undergoing a traditional consolidation process. Instead, u away from the Bentonite filter cake was found to be constant during testing and the WC of samples taken after testing were found to be consistent with WC of the prepared sample. This suggests that a 'filtration' mechanism was occurring at the lubricant-soil interface, i.e. the Bentonite in the wider sample was not influenced by conditions at the interface, but that water was filtered from the slurry immediately adjacent to the filter cake region only and the Bentonite platelets

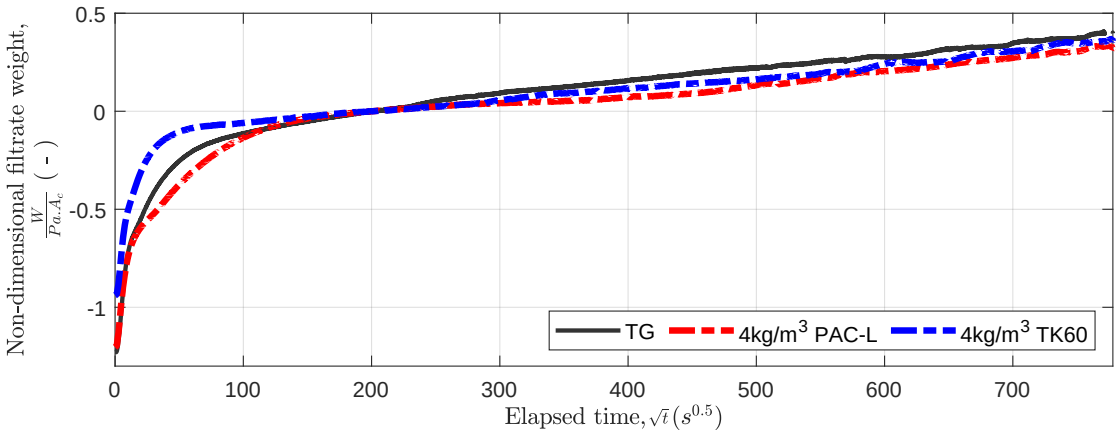


Figure 5.39: Normalised filtrate weight development with elapsed time (t) for Bentonite lubricant mixes with C_a = 4 kg/m^3 PAC-L, and 4 kg/m^3 TK60.

deposited into the cake.

The filter cake region was typically up to 20 mm thick, with the exception of the $M = 12$ test where it was 30 mm. This is shown by the WC of the samples matching that of the fresh Bentonite mix in Figure 5.40 at $X > 20$ mm. Within the filter cake region, the sample WC decreased linearly between the boundary and soil-lubricant interface level. The HZ samples contained higher water contents in this region, but at the interface and in the sample were slightly lower than the TG samples, i.e. $WC = 5.35$ compared to 5.39 at the interface. As the HZ tests had higher permittivity at the end of the test period, it can be deduced that the larger WC of the cake resulted in it being more permeable.

Variation of M had more influence on the WC of the samples. For example, at the interface level a reduction from $M = 16$ to $M = 12$ reduced the associated WC by 1.5%, whereas increasing the ratio to $M = 24$ increased WC by 26% (under $P_a = 25$ kPa for both samples). These results differed from the consolidation shear box experiments, where the starting M of the lubricant mixtures was not found to have a significant influence on their consolidated WC. The difference in findings was believed to be due to the primary consolidation of the lubricant at the soil-lubricant interface not completing during the permeameter tests.

The inclusion of PAC-L in the $P_a = 50$ kPa test increased WC at the interface and in the filter cake to similar magnitudes to the $P_a = 25$ kPa sample. However, the inclusion of TK60

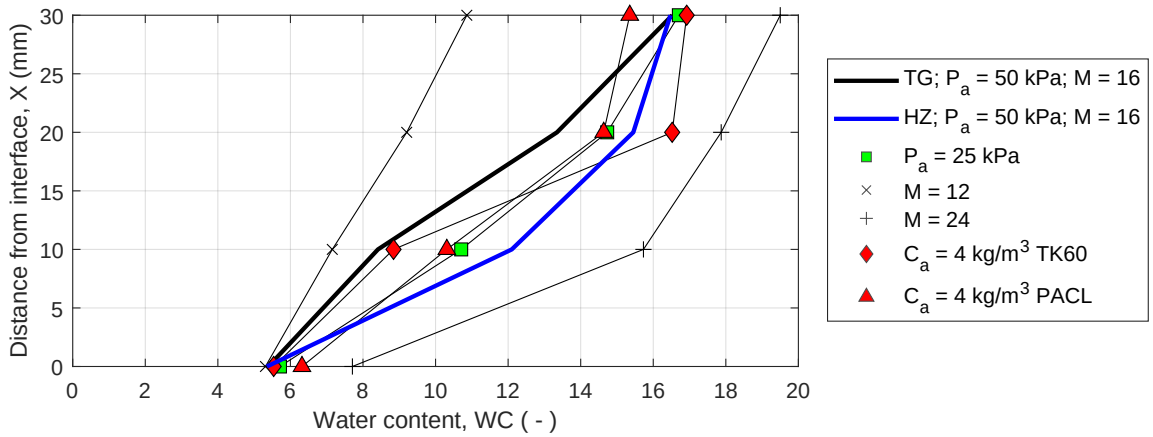


Figure 5.40: Water contents from lubricants taken after the 7 day permeameter tests.

had little effect on the WC at the interface and within the filter cake, but reduced the depth of external filter cake formed during the experiments to 10 mm (from 20 mm). These results explain the different filtration and permittivity behaviours, as the thinner cake formed by the TK60 sample was more permeable at the end of the test, as was the PAC-L containing cake due to its higher WC.

5.4.8 Filter cake penetration resistance

To qualitatively assess the differences between the resulting soil-lubricant mixtures after testing, the change in penetration resistance of the samples was measured. The CPT probe (described in Section 3.4) was penetrated through two baseline test samples after testing, one of which contained 4 kg/m^3 TK60. Figure 5.41 presents the data from the penetrations, which show the peak penetration resistance was within 10 mm of the lubricant-soil interface. This was due to the low WC Bentonite lubricant in the pore space in this region stabilising the sand and increasing q_c. The baseline sample had 90% higher tip resistance compared to the sample containing TK60. This was due to the TK60 sample containing higher WC Bentonite at the interface, which has been shown to reduce the shear strength of the Bentonite during consolidation shear box testing. The reduction may also have been partly due to the TK60 polymer reducing the interface friction between the probe and soil, although this effect could not be quantified.

Both sample's tip resistance below the peak were higher than the untested sample due to the sample D_r increasing as effective stresses were transferred to the soil structure by the low permittivity filter cake. In the region 50 mm $< X <$ 150 mm q_c varied between the two tests. In the TK60 containing test the Bentonite wave-front stagnated at $X = 90$ mm, compared to $X = 120$ mm in the baseline test. This is apparent in the results as q_c remained constant in the Bentonite infiltration zone, but increased once the tip passed into the saturated sand sample.

These findings are important as they (qualitatively) demonstrate that the soil strength has been increased by the presence of the Bentonite and consolidated filter cake. This increase in soil strength at the soil-lubricant interface will have a stabilising effect on the tunnel bore around pipe-jacked tunnels, even if P_a subsequently reduces, which will reduce the risk of overcut collapse and the increased interface friction caused.

5.5 Summary of lubricant testing

In this chapter, the results from a program of testing on tunnelling lubricant has been presented. The behaviours of two proprietary lubricants, Tunnel Gel and Hydraul-ez (TG and HZ), have been quantified using an elemental filter press, mud-balance, viscometer, and consolidation shear box apparatus. A parametric study has been completed to quantify the influence of pressure, mix ratio, and inclusion of two common additives (PAC-L and TK60) on the salient lubricant properties. More complicated soil-lubricant interface interactions have subsequently been assessed using a permeameter apparatus and the findings can be used to explain the response of the soil-lubricant-structure interface apparatus introduced in the next chapter. These results will also form the background of the empirical design method developed in Chapter 8. The following key conclusions arise from the work presented in this chapter:

1. Both TG and HZ Bentonites have similar basic properties, with differences in plastic viscosity, apparent viscosity, and filtration rate under 2.5%. HZ had a 10% higher yield at 10 s compared to TG, which did not vary with time. The yield of TG increased with

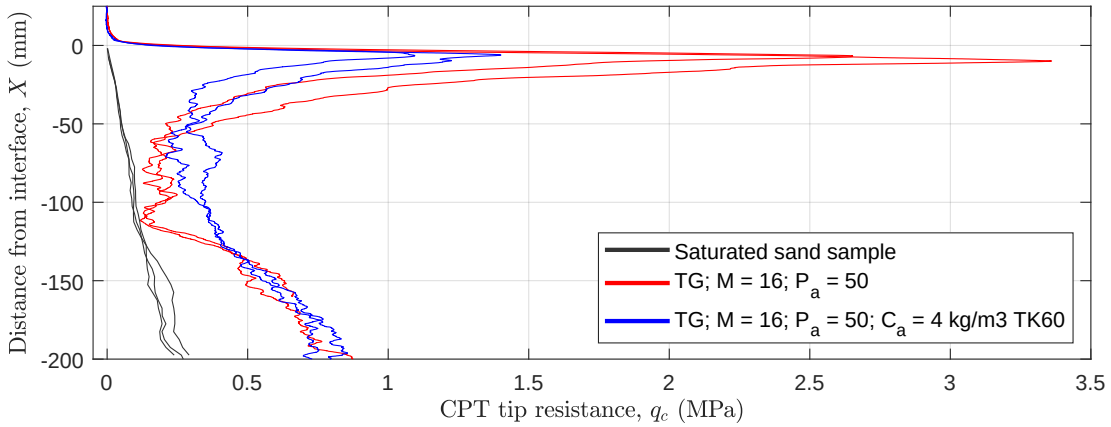


Figure 5.41: CPT probe tip resistance (q_c) variation with distance from the lubricant-soil interface (X) for a prepared saturated soil sample, baseline TG sample, and sample containing TK60, both after a 7 day test with $P_a = 50$ kPa.

time to be 9.8% greater than HZ after 10 minutes, which could lead to larger interface friction increases during stoppages in tunnelling.

2. The soil-lubricant interface in tunnel overcuts develops in two stages: firstly, the infiltration (or 'spurt') phase, where the Bentonite penetrates into the soil and is resisted by dynamics drag forces. Secondly, a filter cake formation phase, which is characterised by lower permittivities at the soil-lubricant interface. The location, permittivity, and deposition rate of the filter cake is influenced by the lubricant make-up and applied pressure. Once the filter cake has formed, no further Bentonite penetrates into the sand, but the Bentonite already within the sand from the infiltration phase stabilises it. Because of this, the API filter press tests do not accurately represent the behaviour of Bentonite at the soil-lubricant interface, as they do not capture the infiltration behaviour of the Bentonite.

3. The time taken to 90% consolidate 25 mm deep samples of TG and HZ in the consolidation shear box varied between 13 hours and 80 hours depending on the sample mix ratio and consolidation pressure. This is equivalent to between 52 hours and 320 hours in a singly drained tunnel overcut of the same thickness. As stoppages of this duration were logged during field monitoring, it is possible for a tunnel overcut to complete 90% primary

consolidation during a stoppage.

4. The WC of the fully consolidated TG and HZ filter cake decreased with increasing P_a, whereas the starting M had a negligible relative effect, as anticipated. Filter cakes with lower WC had higher peak and critical state shear stresses and there was a linear relationship between WC and peak and critical shear stress. Both shear stresses were similar (typically within 2%) and the peak stress varied between 13 kPa (P_a = 50 kPa) and 48 kPa (P_a = 250 kPa). These shear stresses are higher than the increases observed in the field, which shows that consolidation is not the only cause of increased interface friction during tunnel stoppages.
5. The influence of additives on Bentonite behaviour is complex. Both TK60 and PAC-L increased the lubricant viscosity and reduced the filtration rate of TG and HZ during elemental testing. PAC-L was more effective at reducing the filtration rate, with a 25% reduction at 4 kg/m^3 (compared to 4% for TK60).
6. TK60 reduced the infiltration distance of the Bentonite into the sand at the lubricant-soil interface, whilst PAC-L increased the distance but reduced the rate of infiltration. Both additives resulted in filter cakes with higher WC and permittivities than the baseline mix, leading to faster filtration rates after the 7 day permeameter tests.

6 | Soil-lubricant-structure interface apparatus development

6.1 Introduction

To complement the field monitoring study, a novel experimental apparatus has been designed to faithfully recreate the soil-lubricant-structure (SLS) interface around tunnel pipes during installation in the laboratory. This allows rigorous assessment of the factors influencing changes in tunnel overcuts during pipe-jacking. Key aspects of pipe-jacking captured by the apparatus include: a) overcut creation, b) support fluid delivery, c) large interface shear strains, and d) intermittent shearing (i.e. shearing with stoppages).

To recreate realistic overcut conditions the SLS contact area (apparatus plan area) was made as large as possible within the constraints of the available facilities. Figure 6.1 shows a schematic of the apparatus, which comprises a 1 m long, 1 m high, 500 mm wide test chamber. Test pieces, with concrete interfaces representative of tunnel pipes, are passed through the sealed, soil filled, chamber whilst sensors monitor the interface conditions. The apparatus is controlled by a computer system managing the actuation, lubrication, and boundary conditions. The chamber dimensions allow for a 50 mm to 100 mm deep pressure bag (to control total normal stress), overlaying a ∼600 mm deep soil sample, and the test piece (TP) interface 270 mm from the base of the chamber.

6.2 Apparatus design

6.2.1 Chamber construction

The chamber boundaries were required to minimise friction between the soil sample and chamber, whilst minimising lateral displacement of the test chamber under load. Previous studies (such as Talesnick et al. (2014)) have shown that movement of the soil-structure interface

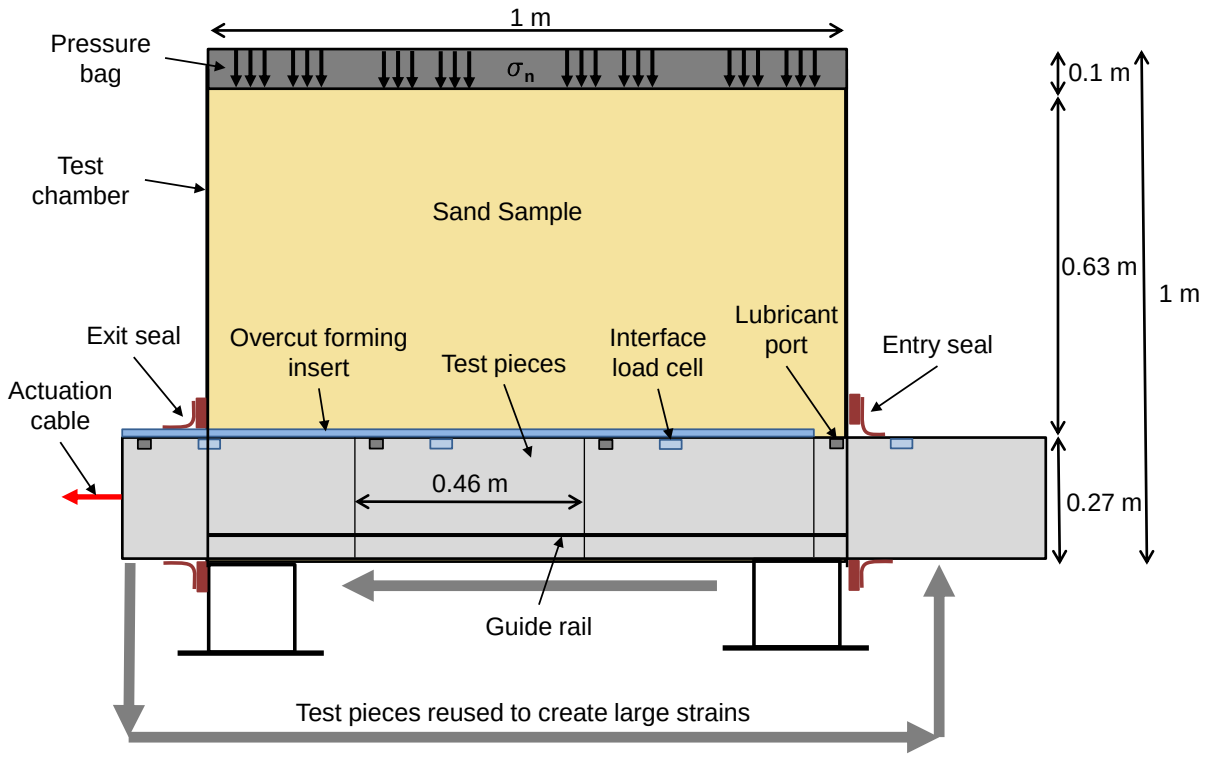


Figure 6.1: 2D schematic section through test apparatus highlighting key features and dimensions.

can alter the stress state in the soil being observed. Although it is expected that the soil sample within the test apparatus will be disturbed during testing by the injection of lubricant, the design sought to minimise chamber wall deformation using 150 × 75 × 18 kg/m parallel flange channel sections arranged as two stiffeners around the chamber at the midspan of the side walls. A simple finite element (FE) analysis of the system was completed using NASTRAN, an FE package inbuilt within the Autodesk Inventor program, to predict the maximum displacement under load. This modelling predicted a maximum deformation of 0.75 mm at 200 kPa internal pressure, which was 0.15% of the chamber width.

To seal between the panels forming the chamber, 1.5 mm thick neoprene gaskets were used with an additional bead of silicone sealant to eliminate any potential water paths. It was expected that the gaskets would increase the compliance of the chamber joints resulting in increased deformations under loading, so these were quantified during apparatus commissioning. All bolts passing through the chamber had countersunk heads which were coated in silicone sealant before being installed to prevent leakage.

To minimise friction at the chamber boundaries, a bespoke lining was developed. Brachman et al. (2001) provided an extensive review of different boundary linings used in a similar chamber for buried pipeline testing. Based on that study, a system of two 0.5 mm thick PTFE sheets, lubricated by a thin layer of LM2 lithium grease, was devised for the apparatus. The first sheet was bonded to the internal wall of the chamber and the lubricating grease was applied to the exposed face to form a thin, uniform, layer. The second sheet was placed loosely on top, allowing the sheet to move independently of the chamber wall. Simple shear box tests, conducted on a sample of this arrangement, showed that shear friction in the arrangement was constant at ~ 1 kPa over a normal stress range of 10 kPa to 100 kPa. This demonstrated that the film of grease between the two PTFE sheets was effectively lubricating the interface, so that the shear friction was that of the grease itself and independent of the applied pressure.

To form entry and exit seals around the test pieces, 10 mm thick Neoprene rubber gaskets were used. The gaskets were cut to the profile of the test pieces, but undersized by 25 mm to increase the contact area. A 40 mm wide strip of additional neoprene was bonded at 90° to the gaskets to provide additional tear resistance and increase the contact area between the seal and test piece. Figure 6.2 shows the exit seal of the chamber where the neoprene seal is visible. To ensure robust contact, the seals were clamped against the test pieces using 'fish plates' which were tightened against the test pieces before filling the chamber with the soil sample to ensure no sand entered the seals at the start of the tests. The fish plates consisted of angled sections to which D profile rubber strips were bonded to provide a degree of flexibility to the seal.

The interface between the TPs and chamber walls was sealed using two, 50 mm wide, 1.5 mm thick neoprene foam strips. One strip was bonded to the edge of the test piece and the second to the chamber wall. To reduce friction during shearing, 0.5 mm PTFE strips were bonded over the foam, such that the shearing took place between the two strips. The interface between these strips was also greased during testing to further reduce friction.

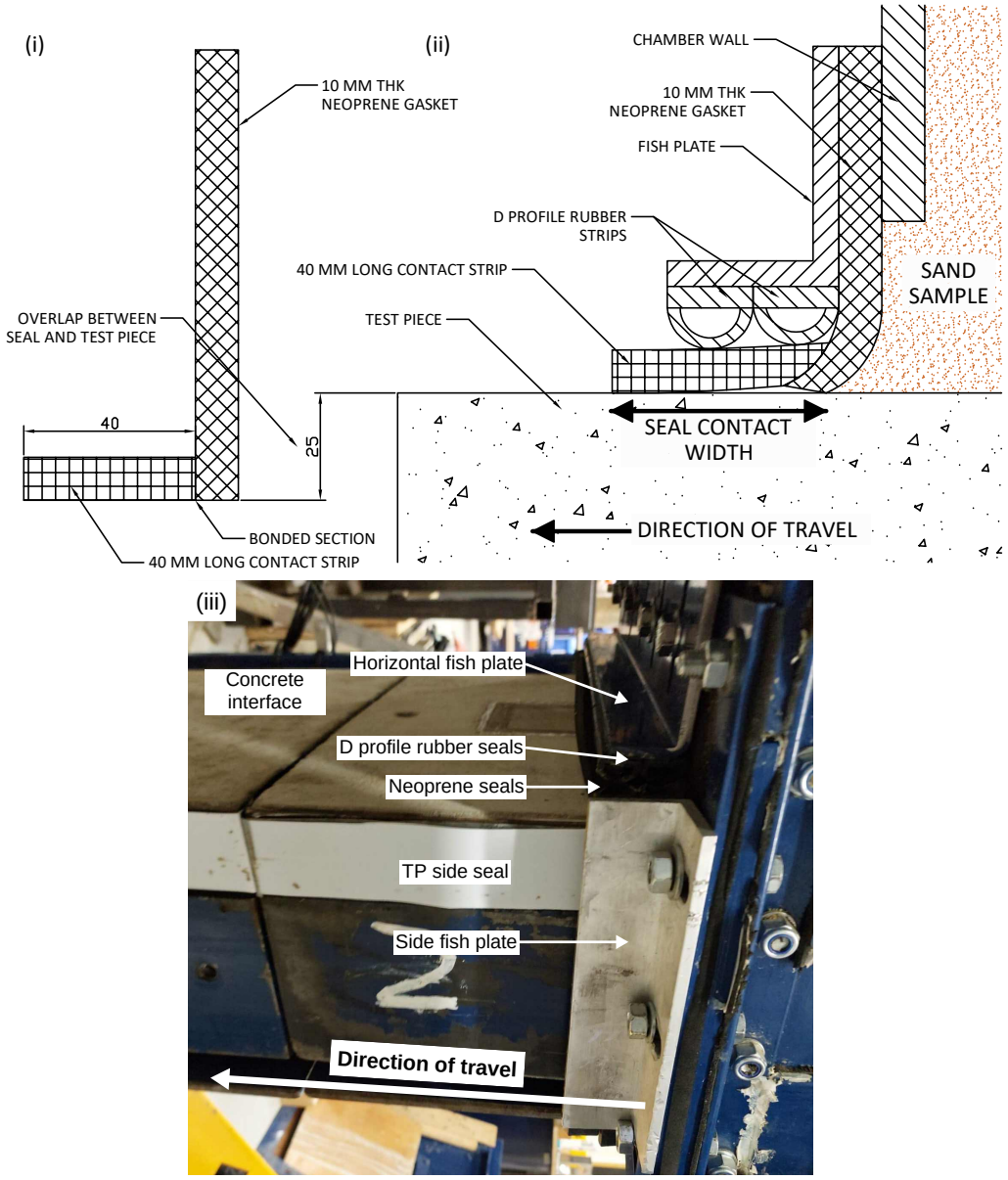


Figure 6.2: Test apparatus exit seal details: (i) Neoprene rubber seal shape, (ii) section through seal and test piece, (iii) photograph showing the exit seal with salient features labelled.

Total normal stress was controlled using a bespoke, water filled, pressure bag arrangement at the top of the test chamber. The bag was designed accommodate heave or settlement of the soil sample within the chamber (caused by sample dilation or lubricant injection or overcut contraction respectively) by expanding or contracting by $\pm$ 50 mm from an initial depth of 50 mm. To accommodate these movements, a highly elastic material was required. A 'food grade' 1.5 mm thick Nitrile rubber (NBR) was selected after trials of various rubber types (Natural, Neoprene, EPDM) and thickness (1.5 mm, 3 mm, 6 mm) were conducted. It was found that the NBR was flexible but had good tensile strength (8 MPa) and elongation at break (300%).

Figure 6.3 (i) shows the pressure bag in position over the prepared sample. The 875 mm x 1250 mm NBR sheet was concertinaed to form the corners, Figure 6.3 (ii), to avoid the requirement to cut and joint the rubber. The arrangement was held with temporary clamps before the chamber top plate was located on the bag, a small bead of silicone was injected around the perimeter (to ensure a watertight seal), and the clamping bolts were installed, sealing the chamber and bag.

6.2.2 Test piece construction

Bespoke instrumented TPs were designed for the apparatus. These were required to accurately recreate the lubricant-structure side of the SLS interface during tunnelling (by having a similar surface roughness to wet-cast concrete tunnel pipes) and delivering Bentonite lubricants using a similar method to field practice. In addition, the TPs were required to be re-usable during the tests so that large interface strains could be generated within the test chamber. Finally, the TPs were to house the sensors to measure the contact stresses at the interface.

Figure 6.4 presents an overview of the combined steel and concrete solution that was devised. Each TP was 460 mm long and 494 mm wide, with a height of 230 mm. A 50 mm deep recess in the top allowed a concrete insert to be fixed in place which covered 484 mm of the 494 mm TP width. A 'well' measuring 165 mm $\times$ 125 mm was incorporated into the test pieces to house the interface stress sensor, with a cable gland through into the TP. Figure 6.5 shows the final TP with concrete insert installed as well as the 0.5" port, located 45 mm from the leading edge of the TP, to deliver Bentonite lubricant to the interface.

The central area of the TPs was sealed from the chamber by spigot-socket joints such that no lubricant or sand could enter during testing. This provided a clean and dry region within the TP, through which the measurement and control cables, optical fibres, pneumatic feed, and lubrication feed were routed. The connection system between the TPs was also housed within this central area.

Figure 6.6 shows a section view through two TPs and the connection system. The system

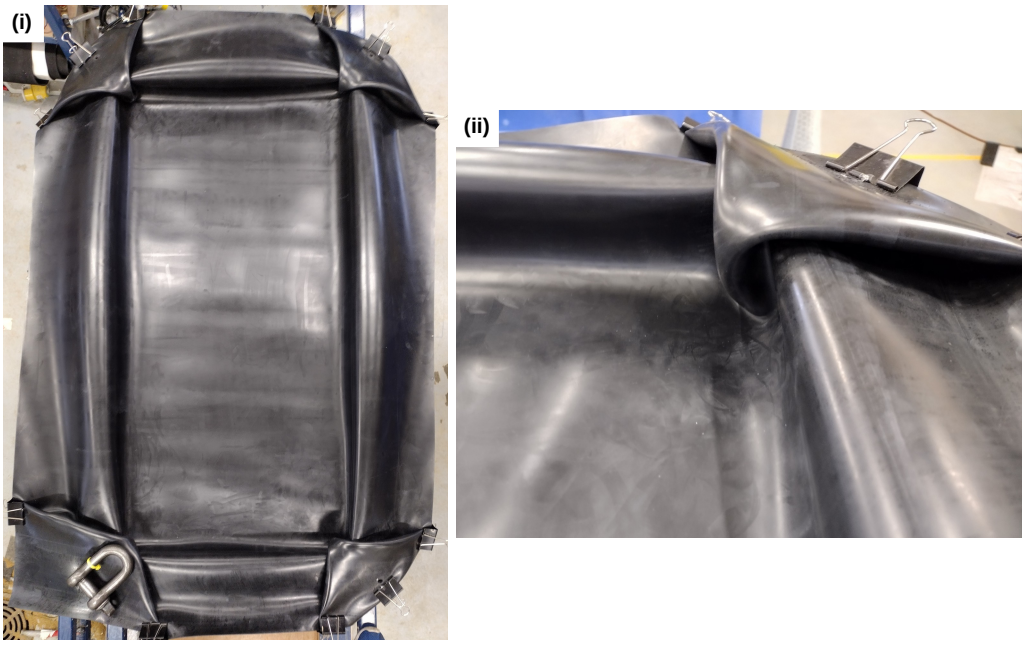


Figure 6.3: Pressure bag installation over a prepared sample: (i) plan view , (ii) concertina detail at the corners.

comprised a 50 kN S-type load cell to measure the force between the TPs. This was bolted to a bulkhead in the TP behind the load cell and to a rectangular bar section in-front through which two connection rods were located. These rods could be threaded into the bulkhead of the TP in-front of the load cell using socket cap bolts which were thread locked into the end of the rods. This arrangement meant that the TPs could be disconnected from the front (and reconnected from the rear) of the chamber during a test to allow large interface shears to be generated within the chamber by recycling the TPs after each advance. It also allowed for the TP joints to be pre-loaded during a test to avoid any joint movement during shearing.

The TPs were guided through the test chamber by two 10 mm thick, 45 mm wide, rails which are welded to the inside of the chamber 50 mm above the base. The TP was supported on these by four M30 ball transfer units (BTF) on each side. BTFs were selected over roller bearings because, in the event that sand particles infiltrated the bearing surfaces, it was anticipated the larger diameter balls would be able to either displace the grains or crush them more easily, thereby reducing any resistance increase.

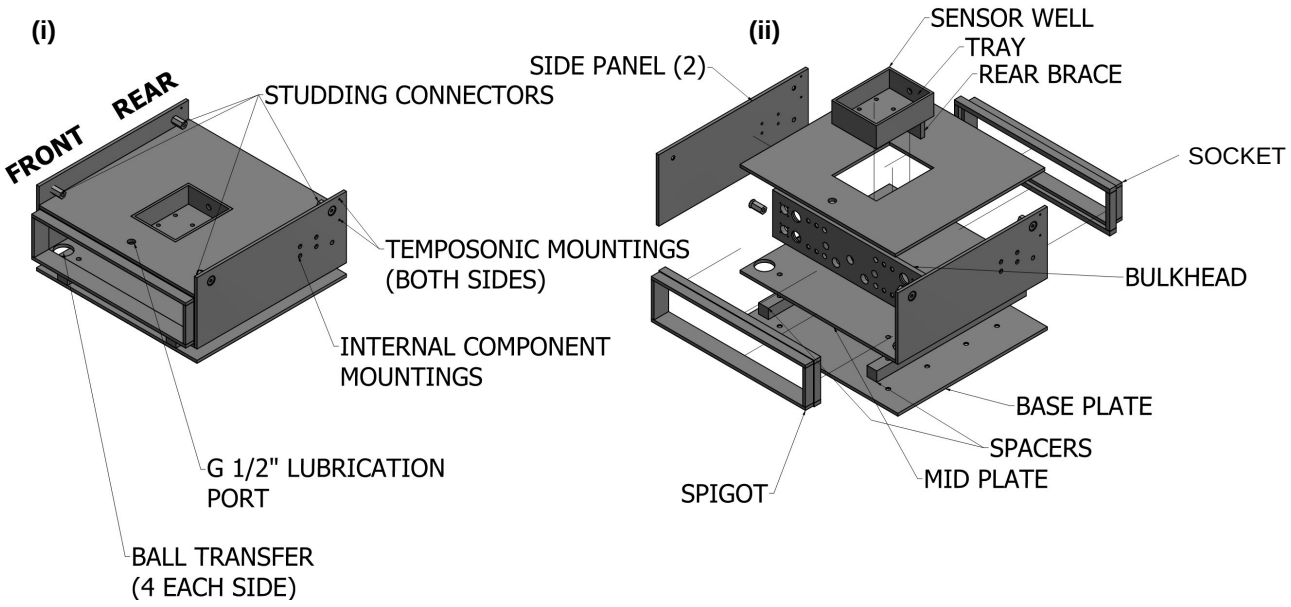


Figure 6.4: Extracts from fabrication model: (i) assembled metal test piece, (ii) exploded component view.

6.2.3 Test piece interface

As Staheli et al. (2006) and Reilly and Orr (2017) noted a dependency between tunnel pipe surface roughness and interface friction during pipe-jacking, it was essential to match the properties of the TP interface to those of field tunnel pipes. Those authors recorded mean wet-cast tunnel pipe surface roughness (defined as the average peak-to-valley height differences ($\overline{R}_a$)) of 24.8 μm and 24.2 μm, and standard deviations of 19.5 μm and 9.3 μm respectively.

To select the concrete mix for the TPs which matched these measurements, 100 mm $\times$ 100 mm samples were cast using different water : sand : cement ratios and greased MDF moulds, identical to those fabricated for the TP interface inserts. The samples used Hanson Multicem 32.5 MPa cement and Jewson's sharp concreting sand aggregate. A mix of 0.55 : 2.5 : 1 (water : sand : cement) was provisionally selected as it had good workability without excessive water bleed. To measure the roughness of the concrete, four samples were assessed using an Alicona G4 infinite focus optical profilometer. Figure 6.7 presents example results from the 15 profile measurements taken from each sample. This analysis yielded an $\overline{R}_a$ of 18.9 μm for the samples, similar to the field measurements of both Staheli et al. (2006) and Reilly and Orr (2017) and therefore deemed acceptable for testing.

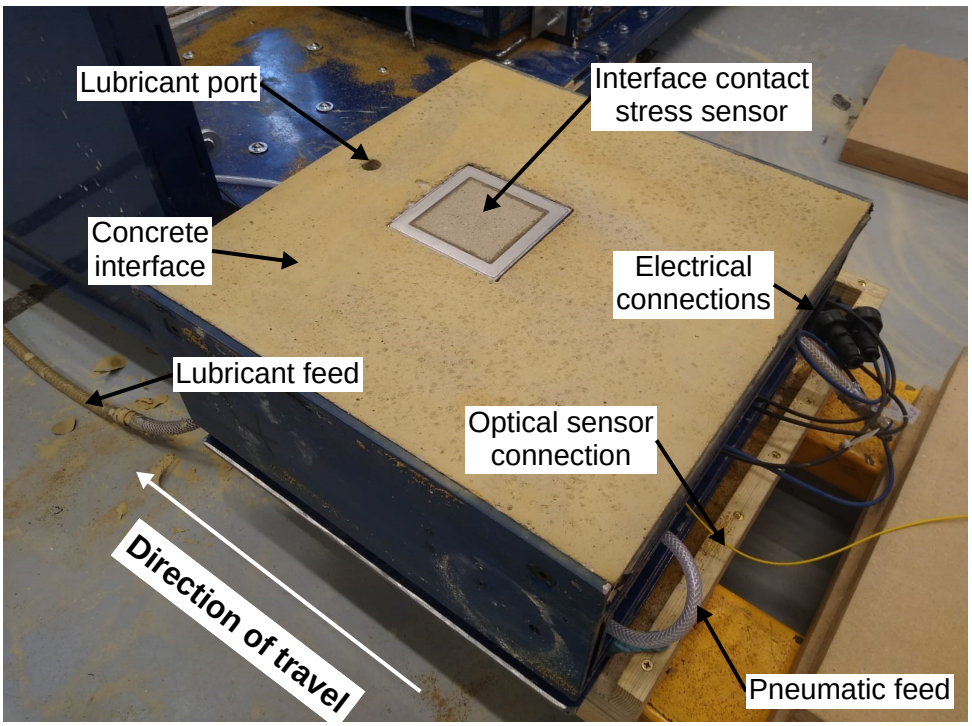


Figure 6.5: An overview of the assembled test piece with key features labelled.

Four M10 hexagonal studding connectors were cast into the corners of the concrete. Bolts were threaded through the metal TP walls into these to secure the concrete in place during testing and prevent any movement between the TP and concrete insert. To increase the resilience of the concrete, and avoid cracking during installation, a mesh was cast into the concrete 15 mm from the top surface. The cast TP interfaces were too large to be tested using the Alicona, but visual inspection of the surfaces showed they were similar roughness to the 100 mm samples cast using the same mix and method.

For tests requiring an overcut 18 mm thick varnished MDF 'overcut formers' were placed on of the TPs during the test setup and clamped in place using 2 mm thick aluminium plates which penetrated into the joints between the TPs. A Neoprene gasket was placed between the TP and former to ensure Bentonite did not penetrate along the connection. A schematic of the overcut formation process is shown in Figure 6.8. The sand sample was then prepared against this surface, 18 mm above the TP concrete interface. When the test commenced, the overcut formers travelled through the chamber with the first three TPs maintaining the overcut whilst lubricant was injected immediately behind the final former to maintain the overcut that was

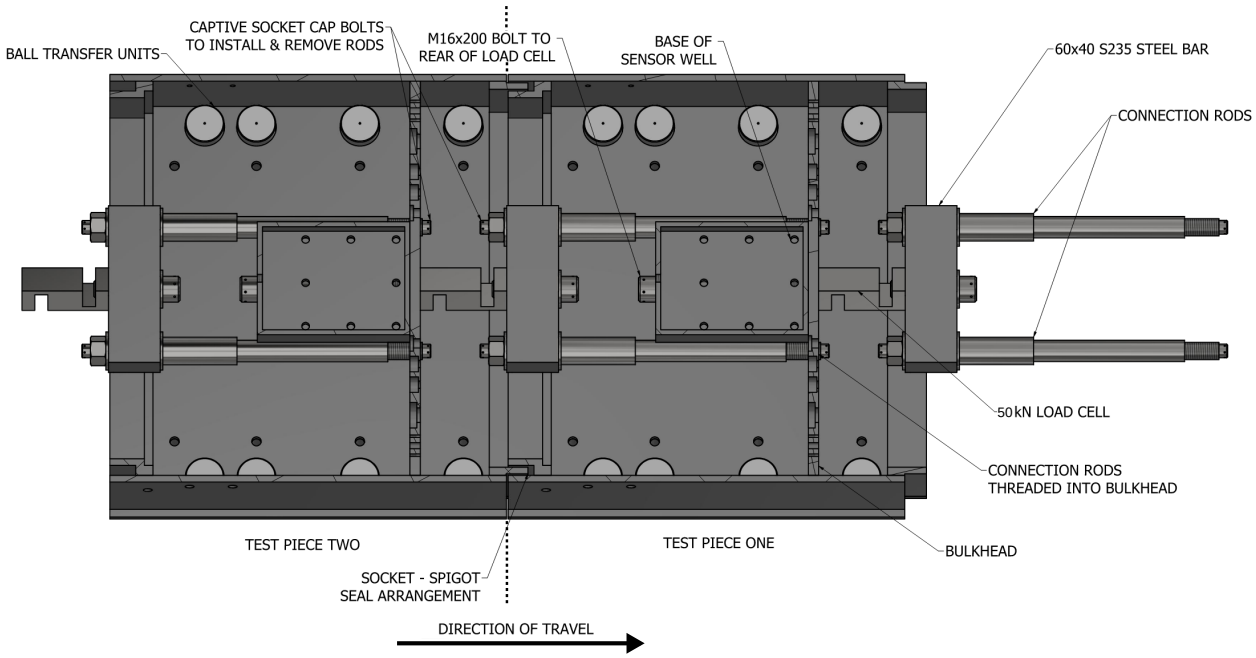


Figure 6.6: A 3D model showing a midsection view of two test pieces and three connection rods as installed during SLSI operation.

formed. At the end of each full advance, the overcut former was removed, so that the test piece interface was exposed for the remainder of the test.

6.2.4 Actuation system

The actuation system was specified to overcome the maximum expected friction forces within the test chamber plus any additional resistance offered by the seal arrangements. The maximum force required to actuate the test pieces was calculated using Equation 6.1:

$$F_a = F_{e1} + F_{e2} + \sigma'_n.L.B.(tan(\phi_{cs}) + \mu_2) \tag{6.1}$$

where F_a is the actuation force, F_{e1} and F_{e2} are the entry and exit seal resistances, σ'_n is the effective vertical stress at the interface, μ_2 is rolling resistance coefficient of the test pieces, ϕ_{cs} is the critical state soil friction angle, L and B are the internal length and width of the test chamber, and the TP interface is assumed fully rough. Table 6.1 presents the values used to calculate the design actuator capacity of 40 kN. To provide redundancy in the actuator, a capacity of 50 kN was specified to suppliers.

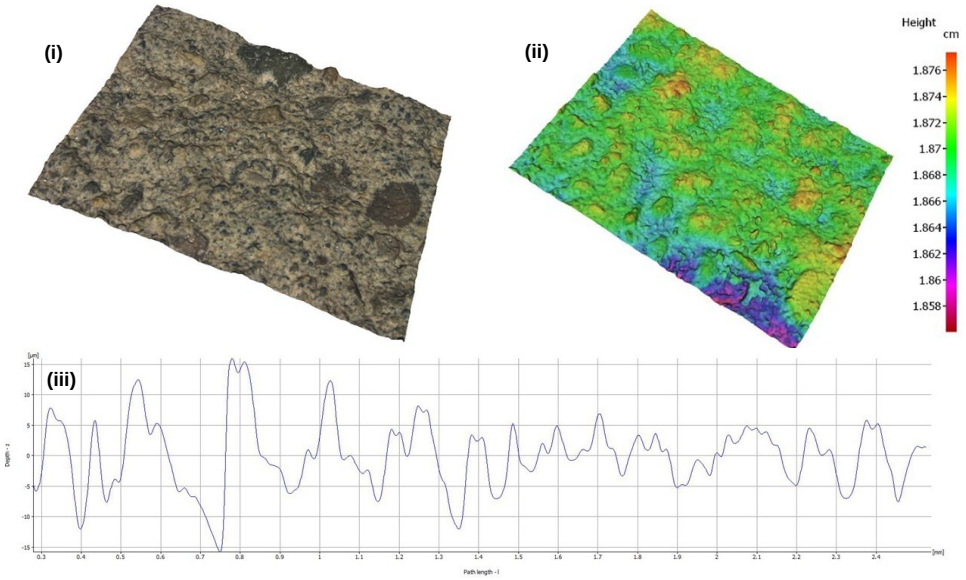


Figure 6.7: Example 100 mm x 100 mm test piece roughness analysis: (i) real colour image of test sample, (ii) heat map of test piece height, (iii) example roughness profile.

Table 6.1: Summary of the test apparatus loading assumptions.

Parameter	**Value**	**Unit**	**Source**
L	1000	mm	Design parameter
B	500	mm	Design parameter
F_{e1}, F_{e2}	5	kN	Determined empirically
$\sigma_n\prime$	100	kPa	Design parameter
μ_2	0.1	-	Assumed 10% applied load in friction
ϕ_{cs}	34.3	^{o}	Richards (2019)

To determine the power and encoder requirements for the actuator motor, the advance rate of the TPs through the chamber was determined. As field tunnel drives recorded advance rates of $<$ 10 mm/min to over 250 mm/min, 50 mm/min was selected as the maximum advance rate of the test apparatus to minimise power requirements, whilst falling within this range. To satisfy these requirements, a Zimm ZE-100-SL-TR standing screw actuator was selected, coupled to a NP025S-MF2-20 motor by 36:1 and 20:1 reduction boxes. This allowed a maximum actuator speed of 50 mm/min and a minimum of $<$ 1 mm/min. The motor was controlled by a SV2B5-Q-DE digital servo, which provided the power supply and logged the motor speed and actuator position.

The apparatus operated in a tension only mode during testing, as this allowed the actuator

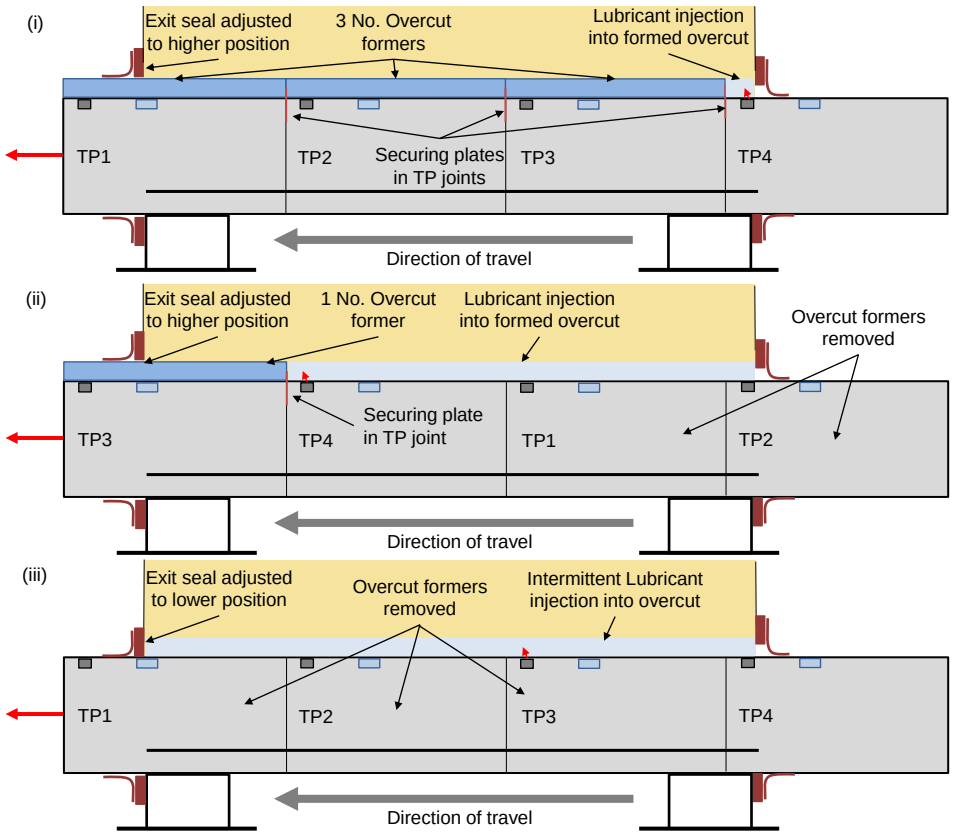


Figure 6.8: Schematic showing the overcut formation process: (i) the initial setup of the apparatus, (ii) the apparatus after two TP advances, (iii) the apparatus after four TP advances, with the fully formed overcut.

to be located adjacent to the test chamber which reduced the overall apparatus length. Figure 6.9 shows the final arrangement, with key dimensions and features labelled. To connect the actuator to the TPs, a 10 mm diameter, 7x19 316 stainless steel cable was used. The cable passed from the actuator around two 96 mm diameter aluminium pulleys before connecting to the test pieces via a 50 kN load cell. The pulleys were mounted into an end plate assembly which was braced back to the chamber and actuator by six 50 × 6.3 mm square hollow section members.

6.3 Data acquisition and control system

The data acquisition and control system for the apparatus was designed to store the sensor information from the apparatus and control the automated processes, such as total stress control. To achieve this, a program was developed using National Instruments (NI) LabVIEW. This controlled all systems within the apparatus and interfaced with external hardware, such

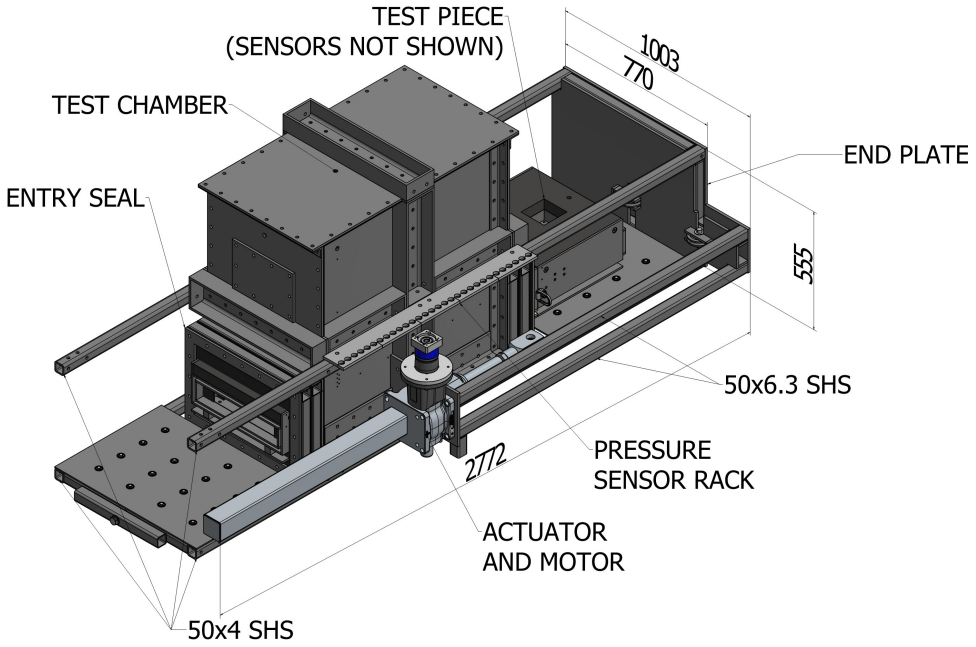


Figure 6.9: Test apparatus fabrication model with key features labelled.

as the Pump controller, via serial or Ethernet connections.

All the components of the data acquisition and control system were mounted on a mobile trolley which could be positioned away from the actuation cables of the apparatus. Figure 6.10 shows the layout of the trolley, with the electrical components mounted above the lubrication and pressure control system. To transmit data from the TPs to the logging cabinet on the trolley four 8-core electrical cables were used as well as 4 optical fibres. Similarly, a further cable connected the chamber mounted sensors to the cabinet.

PT data was acquired using NI-9208 16 channel ±20 mA current input modules connected to the negative wire from each sensor. Excitation was provided to all sensors by a common 24 V DC voltage supply. The PT on the lubricant feed line had a 0 kPa to 800 kPa (gauge) pressure range and was fitted with a diaphragm, whilst all other sensors were 0 kPa to 300 kPa (gauge), due to the high lubricant pressures noted during delivery in the field tunnel drives. All load cells used in the apparatus were of the full bridge type and logged using NI-9237 modules connected to the cDAQ chassis.

The location and displacement rate of the TPs were recorded in two ways. Firstly, the control program set the actuator velocity and logged its position at each data save interval.

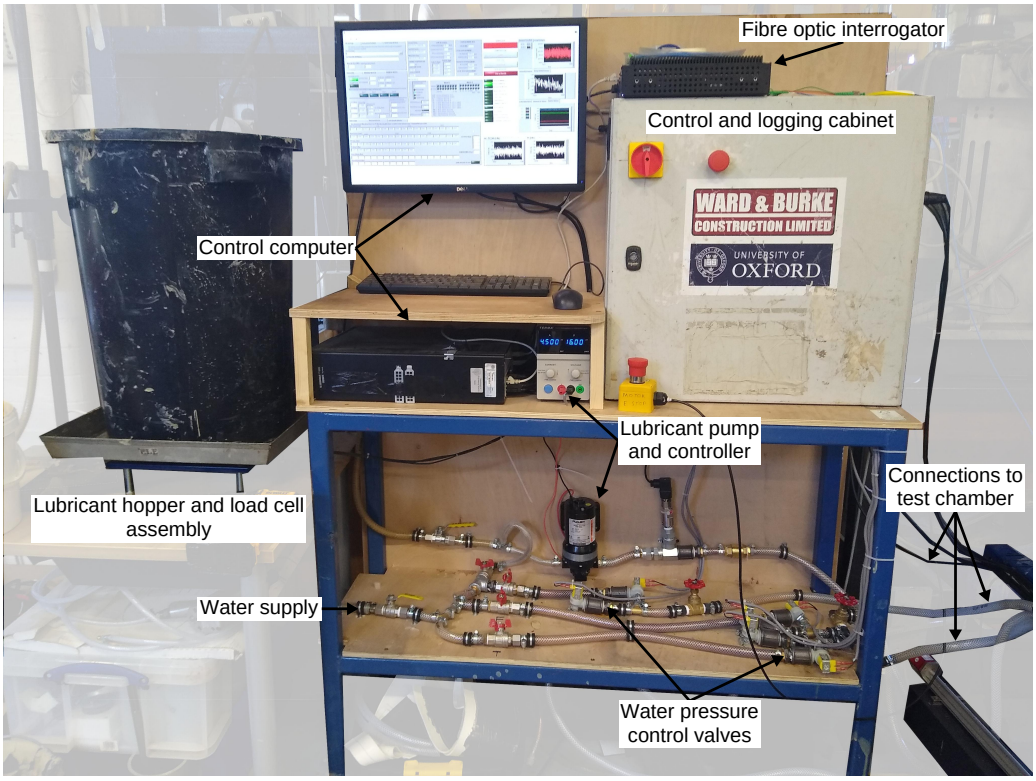


Figure 6.10: Photograph showing the layout of the control trolley and lubricant storage hopper.

Secondly, a Temposonic G-Series position sensor was connected to the rear of the TP on the entry side of the test chamber. This recorded the position throughout each advance and was used to control the advance displacement, thereby eliminating any discrepancies caused by compliance within the actuation system.

The fibre optic interface stress sensors used in the apparatus were connected into a Micron Optics si255 fibre optic interrogator. This produced the light source required for the sensors and logged their response. Communication with the interrogator used an Ethernet connection which was configured using proprietary LabVIEW scripts provided by the manufacturer.

Data was stored by the LabVIEW control program in two comma separated value (CSV) files. The first contained hardware information and test parameters such as: Pressure control valve states, lubricant pump voltage and current, solenoid valve states, actuator state, and lubricant hopper weight. The second "sensor" file contained the raw values from all the electrical and fibre optic instrumentation on the apparatus, i.e. the mA, mV/V, or nm readings from the sensors, for post processing. Additional ‘offset’ files were stored with the zero offsets for the

sensors. These were saved manually when values changed, for example if a pressure sensor was changed between tests.

6.4 Lubrication system

The lubrication system comprised four principal elements: i) a hopper for storing the lubricant, ii) three load cells for measuring the weight of lubricant in the hopper, iii) a pump and controller for dispensing the lubricant, and iv) a valve within each TP to enable lubricant to be dispensed from the selected TP. The hopper consisted of a black 75 l bin, with an outlet port drilled through the wall 25 mm from the base for lubricant delivery. During testing, the hopper lid was secured in place to minimise evaporation from the stored lubricant. The hopper was placed on a lightweight tray supported by three ±25 kg capacity full-bridge load cells which input into the control program. The weight of lubricant in the hopper was used to calculate the flow rate during testing as flow meter suppliers suggested this was more accurate for the range of flow rates required during testing. The lubricant flow rate was calculated as:

$$Q = \frac{\Delta W}{\gamma_L . \Delta t} \tag{6.2}$$

where ΔW is the change in weight of the hopper over a time increment Δt and γ_L is the lubricant density. To reduce signal noise due to pump vibrations, the calculated Q was passed to the control program through a five-point ($\sim$ 1 second) moving average which omitted $Q < 0$ litre per minute (LPM) or $Q > 10$ LPM readings. To pump the lubricant into the test apparatus, a Flojet Triplex series high pressure diaphragm pump was used. This pump provided a maximum 8 bar outlet pressure at a maximum Q of 5.4 LPM which satisfied the anticipated flow rates and pressure required in the apparatus. The 24 V DC power required by the pump was provided by a Tenma Digital DC power controller, which interfaced with the control program and allowed the pump excitation voltage to be set, in turn adjusting the flow rate. Within the control program, a simple PID controller adjusted the power supply voltage to compensate for errors between the target and actual lubrication rate at approximately 5 Hz.

Lubricant delivery to the interface was via a common 0.5" feed line, which was jointed at each test piece. Each of these joints contained a non-return valve which stopped any back flow of lubricant. Within each test piece, a 0.5" pneumatically operated ball valve opened to enable the release the lubricant into the interface, via the 0.5" port. These were operated automatically on a timed sequence by the control program (similarly to industry practice), or manually using switches in the program.

To validate the stability of the lubricant control program, 33 tests were conducted at flow rates between 100 g and 4000 g per minute with $M = 20$ Tunnel Gel lubricant. The lubrication system controlled the flow rates to within $\pm$ 3% of the set point at 400 g per minute or greater, whilst at lower flow rates the system failed to maintain steady state due to a combination of noise in the load cell readings and the pump 'stalling'. Stalling is where the pump continues to draw current but stops pumping and, once stalled, the supply voltage from the control program was increased until the pump restarted, resulting in a large and rapid change in the flow rate. This finding dictated that, for the testing, a minimum flow rate of 400 g per minute was required to ensure consistent lubricant delivery.

6.5 Lubrication rate calculation

The lubrication rate for the two different types of lubricated stage of the proposed SLS interface tests were then calculated. The first stage type consisted of continuous lubrication, similar to that experienced behind the TBM during tunnelling. To calculate the required mass flow rate the results from the permeameter testing (presented in Chapter 5) were used. First, the predicted spurt distance for the test σ_N was calculated using the relationships measured. This was then multiplied by the sample void ratio to give a specific volume of lubricant required to complete the spurt phase of infiltration. The required flow rate was then calculated by multiplying this volume by the test advance rate (set at 25 mm per minute) and the lubricant density, yielding approximately 500 g per minute for $\sigma_N = 30$ kPa. For the tests with an 18 mm

deep overcut, an additional mass of 225 g per minute was added to theoretically completely fill the overcut volume during these initial stages.

The second stage type was intermittent lubricant injection, which was used to replicate the lubrication of the SLS interface on the pipe string further from the TBM. In these sections the lubricant ports in the pipe string are distributed at discrete spacings, shown to be between 12.5 m and 20 m during field tunnel drives monitored as part of this research. The required rate of lubricant injection during these stages of testing was common to all tests, regardless of overcut. To align the experiments with industry practice, values for the 'top up' lubrication, from Praetorius and Schößer (2017), were used. This guidance was specific to HK TBMs with overcuts, the flow rate was calculated per unit interface area using data for a 1490 mm D_O tunnel, similar to some of those in the Hull field study. From this, a required mass flow rate of approximately 60 g per minute was calculated for the apparatus interface area. To generate periodic injection, this was delivered as a 15 s burst of lubrication at 500 g per minute every 2 minutes.

6.6 Total stress control

The pressure in the normal stress pressure bag, and hence the total normal stress at the interface, was controlled using two solenoid valves connected to a 0.5" feed pipe. These were actuated automatically by the control program using relay boards in the logging enclosure. The 'fill' solenoid was connected to the mains water supply (which had a pressure $>$ 200 kPa), whilst the 'discharge' solenoid was directed to the laboratory drain. A gate valve was fitted into the pipework between the solenoids and chamber to throttle the fill/empty flow rate and avoid an under-damped response to pressure changes. A pressure sensor was mounted through the chamber top plate to directly read the pressure within the bag. Using this reading, the control program maintained the pressure within $\pm$ 1% of the target stress. A visual (safety) check of the pressure within the bag was provided by an analogue pressure gauge installed onto

the inlet pipework.

6.7 Contact stress sensors

Each TP within the apparatus was designed to accommodate a contact stress sensor on its centreline, behind the lubricant delivery port. These sensors were installed to measure the total normal stress and interface friction at the SLS interface during testing. Two TPs were fitted with three axis electrical load cells and another two were fitted with novel six axis fibre optic sensors. The electrical load cells were identical to those used in the Castlerigg instrumented tunnel drive, each with a per axis capacity of 5 kN and the maximum deflections under load of 0.08 mm and 0.16 mm in the shear and normal directions, respectively.

Six axis contact stress sensors, developed within Oxford University (Templeman (2023)), were deployed in the other two TPs. The optical fibres are durable and immune to electrical interference or water ingress, making them ideal for field monitoring applications. They are commonly used for monitoring and temperature measurement applications, such as Jung et al. (2000); Majumder et al. (2008); Scott et al. (2019). The fibres used in this study were manufactured by FBGS (FBGS International (2022)), with 8 mm long fibre Bragg gratings (FBGs) at regular spacings along a bare optical fibre. FBGs work by shining a broad spectrum light source down an optical fibre, onto which grating(s) are etched. The light wavelengths equal to the grating spacing are reflected and the remaining wavelengths transmitted through the fibre. By connecting a detector to either end of the fibre the peaks in the reflected light, or corresponding troughs in the transmitted light are detected. Figure 6.11 shows an example reflection spectrum from a sensor used in this research.

The wavelength of these reflected peaks is affected by changes in the spacing of the grating lines induced by either mechanical or thermal strains in the fibre. The relationship between the wavelength shift and strain is defined by:

$$ln\frac{\lambda}{\lambda_{ref}} = k(\epsilon_m + f(\Delta T)) + g(S_1, S_2, \Delta T) \tag{6.3}$$

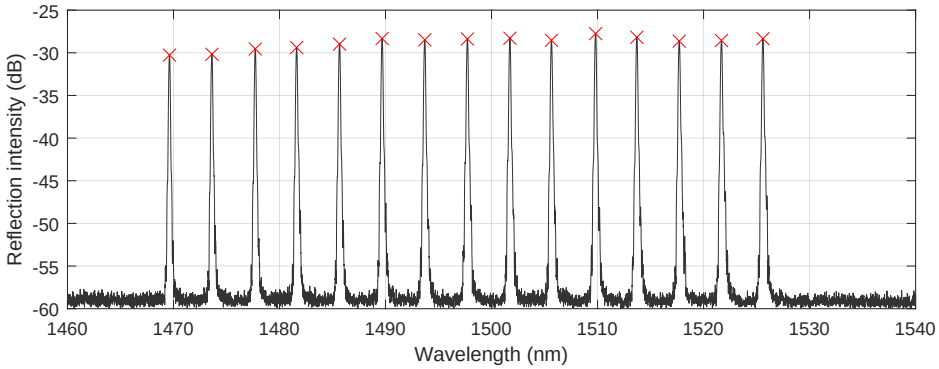


Figure 6.11: A reflection spectrum from one of the contact sensors used in this research. The 15 peaks from the FBGs are highlighted with red crosses.

λ and λ_{ref} are the current wavelength and reference wavelength of the grating, k the sensitivity to mechanical strain, and ϵ_m the mechanical strain acting on the fibre. ΔT is the difference between the current sensor temperature and the test reference temperature (T_{ref}). The sensor temperature dependency $g(S_1, S_2, \Delta T)$ is given by the equation:

$$g(S_1, S_2, \Delta T) = S_1.\Delta T + S_2((T - T_{ref})^2 - (T_0 - T_{ref}))^2) \tag{6.4}$$

where S_1 and S_2 are sensitivities of the fibre to temperature and T_{ref} is the reference temperature of the sensor and T_0 is the calibration temperature. The thermal strain function ($f(\Delta T)$) is defined as:

$$f(\Delta T) = (\alpha_s - \alpha_f)\Delta T \tag{6.5}$$

where α_s and α_f are the coefficients of thermal expansion of the substrate (the material the fibre is bonded to) and fibre, respectively. These three equations can then be rearranged to calculated ϵ_m at any temperature as:

$$\epsilon_m = \frac{1}{k}\left(ln\frac{\lambda}{\lambda_{ref}} - S_1.\Delta T - S_2\left((T - T_{ref})^2 - (T_0 - T_{ref})^2\right)\right) - (\alpha_s - \alpha_f)\Delta T \tag{6.6}$$

In traditional monitoring arrangements a dedicated temperature FBG is required to define ΔT. This must be isolated from mechanical strain via a non-straining configuration (as utilised by Mokhtar et al. (2012)) or independently attached in a clamp of known thermal expansion coefficient, as detailed in Acikgoz et al. (2022). The sensors developed by Templeman (2023) were novel in that the FBG arrangement also allowed the sensor to be calibrated for temperature

(by measuring the strain induced in the FBGs by temperature variation under zero loading and using these data as an input into the calibration algorithm), such that additional FBGs were not required.

Figure 6.12 shows a cutaway 3D model of the sensors developed. The FBGs were arranged around a thin 'sensing wall' attaching the 90 mm × 90 mm concrete sensor face plate to the sensor body. The sensitivity of the instrument was dependent on the strain in the FBG sensors under each loading condition. To optimise the FBG placement, FE analysis was conducted, using Abaqus FE (Simulia (2009)), to determine the locations of maximum strain under different load combinations. This process is described further in Templeman (2023).

Deformations at the soil-sensor interface have been shown to influence measured contact stress by Talesnick et al. (2014). To ensure the novel sensor was not more compliant than the electrical load cells, deformations were measured during calibration under the full normal and shear loads (N = 810 N, $T_x = T_y$ = 486 N) and found to be less than 10 μm, which is comparable to the shear and normal displacements of the electrical load cell under the same loading (8 μm and 26 μm, respectively).

To ensure the sensor face plates were representative of the TP interface, and tunnel pipes more generally, concrete covers were cast using the method and mix described in Section 6.2.3. These were bonded to a steel plate, which was in turn connected to each load cell. A 1 mm gap around the interface plate ensured the sensor was independent of the surrounding concrete. This was sealed using a thin bead of flexible silicone sealant, to ensure no lubricant penetrated into the sensor well and influenced the measurements.

6.8 Sand sample preparation

The air pluviation method was used to prepare the samples within the test apparatus. This involves dropping the sample soil into the chamber from a known height through a mesh to control the flow rate (Vaid and Negussey (1984)). Studies, such as Richards (2019), have

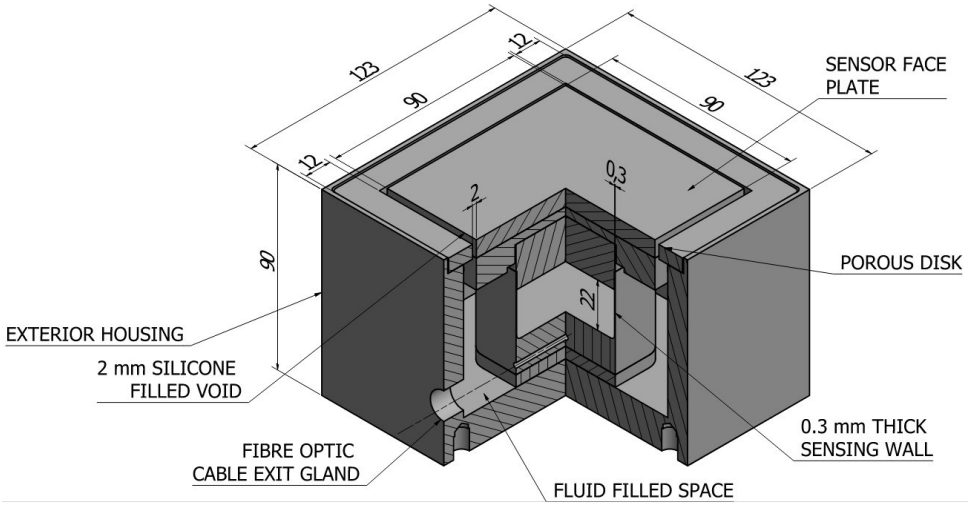


Figure 6.12: A cutaway 3D model showing the key features of the fibre optic stress sensor.

demonstrated that different mesh combinations alter the relative density of the sample produced. For example, a mesh with 20 mm diameter holes at 80 mm centre to centre (C/C) spacing produced a sample with $D_r = 0.6$, whereas 5 mm holes at 8 mm C/C produced a sample with $D_r = 0.8$ (Richards (2019)). The distance between the mesh and final sample surface has also been shown to have an effect on the sample density by Hariprasad et al. (2016). Those authors prepared samples from drop heights of 50 mm to 500 mm, through various mesh combinations, and recorded the resulting D_r. The results showed that a minimum drop height of 200 mm was required to achieve a uniform sample for sands.

Using this information, a simple plywood rainer was designed for use with the apparatus. A mesh with 5 mm diameter holes at 6 mm C/C was used to prepare samples from a drop height of 275 mm above the test chamber. Sand was fed through the mesh from a hopper and (due to restrictions on the height of the hopper) the chamber was filled in two phases, once the TPs had been installed.

To ensure the rainer produced uniform samples, the D_r profiles from cone penetration tests (CPTs) were compared to the average D_r calculated from the weight and volume of sand within the chamber. The CPT D_r was calculated using the same method as the permeameter tests, described in Section 3.4.

Figure 6.13 presents the calculated D_r profiles for three prepared samples with an average $D_r = 0.66 \pm 0.01$. Only depths from the interface (X) of < -350 mm are of interest to this study, as the lubricant did not penetrate further than 300 mm into the samples during testing. The sample was relatively uniform with D_r in the region of interest gradually increasing to an average value of 0.67. Closer to the interface with the test pieces, at $X <$ -500 mm, D_r increased again to a maximum value of between 0.69 and 0.75 at the TP interface.

As lubricant penetration into the soil has been shown to be influenced by its permittivity, the penetration of the lubricant was also theorised to be depend on the void ratio of the soil, as larger voids would increase the permittivity of the sample. The increase in D_r in the final 100 mm before the interface resulted in a maximum variation in the void ratio of < 3.6%, which was deemed acceptable for the testing. It is of note that in the figure the dip in D_r at $X =$ - 300 mm was located between the two sample rainings and was caused by the decrease in sand flow rate at the end of the first raining. These results also show good repeatability of the sample preparation process between tests.

6.9 Summary

This Chapter has described the design of a novel plane strain test apparatus developed to faithfully recreate SLS interface conditions during pipe-jacking at laboratory scale. The apparatus enables key features of the SLS interface in the field to be recreated, such as: large interface shear strains, intermittent lubricant injection from discrete ports, overcut creation, under controlled normal stress, as this has not been possible with the apparatus used in previous studies. The data acquisition and control systems have been described, as have the sensors used to record the interface conditions and the sample preparation equipment.

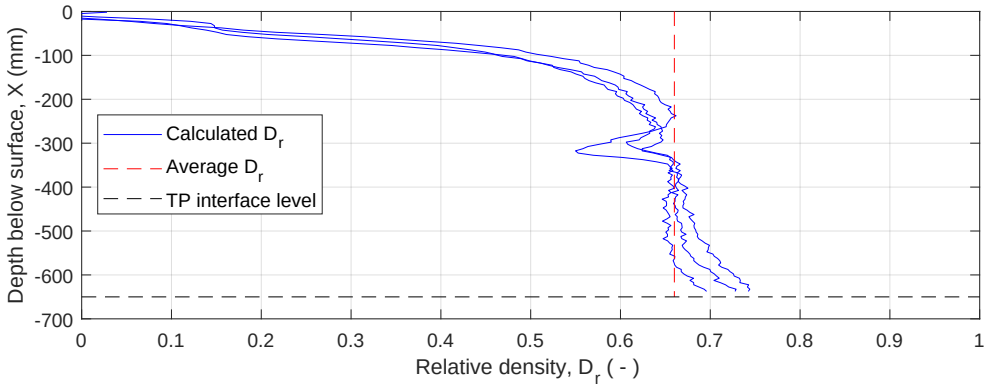


Figure 6.13: The change in relative density (D_r) with depth from soil surface (X) for three prepared samples within the SLS interface apparatus

7 | Soil-lubricant-structure interface apparatus results

7.1 Introduction

7.1.1 Testing objectives

The bespoke soil-lubricant-structure (SLS) interface apparatus described in Chapter 6 was used to conduct a test program examining the influence of a number of variables on SLS interface mechanics, particularly friction development. Variables considered included: i) Bentonite lubricant injection, ii) overcut presence, iii) normal stress, and iv) stoppage duration. The main objective of this testing was to inform development of an empirical model to describe changes in interface behaviour during tunnelling, as developed in Chapter 8, by providing the data to quantify the relationships between the elemental lubricant properties, identified in Chapter 5, and the results of field studies, detailed in Chapter 4.

Testing was initially conducted on an unlubricated SLS interface, for commissioning and validation of the apparatus performance. Following this, eight tests were completed using the apparatus to provide the data required for the empirical model. These tests can be broken down into three broad types: (i) 'short' - which examined unlubricated friction and the effects of initial lubricant injection, (ii) 'medium' - which examined the effects of a single stoppage, and (iii) 'long' - which explored the effects of large shear strains and multiple stoppages on the interface. The key parameters of each completed test, and its objective, are given in Table 7.1.

Table 7.1: Summary of completed SLS interface tests, their objectives, and key test variables.

Test number (-)	**Interface normal stress** σ_N [1] **(kPa)**	**Lubricant injection** (-)	**Overcut height** h_{oc} **(mm)**	**Total duration** t_{max} **(hours)**	**Total interface displacement** x_{max} **(mm)**	**Stoppage durations** t_s **(hours)**	**Objective(s)**
T1a	0 - 100	No	0	3	1000	0	Apparatus commissioning.
T1b	0 - 100	Yes	0	3	1000	0	Fibre optic load cell and lubrication system commissioning.
T2	30.6	No	0	6.5	3450	0	To quantify unlubricated friction.
T3	32.6	Yes	0	15	1220	0	Influence of partial lubrication.
T4	30.6	Yes	0	7.5	1970	0	Influence of lubrication with no overcut.
T5	30.6	Yes	0	23.5	4090	12	Influence of a single stoppage.
T5b	30.6	Yes	0	44	6780	12, 12	Influence of multiple stoppages.
T7	30.3	Yes	0	140	6869	3, 60	Influence of long duration stoppages.
T8	30.9	Yes	18	158	7545	12, 60, 60	Influence of overcut, long duration stoppages.
T9	50.3	Yes	18	3	1460	0	Influence of higher normal stress.
T10	50.4	Yes	18	158	9305	12, 60.5[2], 62[2]	Influence of higher normal stress, long duration stoppage.

[1] Variation in σ_N due to small soil sample height and D_r differences between tests.
[2] Variation in t_s caused by laboratory access restrictions.

7.1.2 Test structure

To ensure consistency, all tests followed a similar structure. Each test was broken down into a series of common stage types, which were repeated to form the test sequences. The stage types were as follows:

- **Setup Phase** (S). During this stage the soil sample was prepared, the pressure bag was installed, and the pressure increased to the set point for the test before any interface shearing was conducted.
- **Unlubricated advance** (L_u). This phase allowed the unlubricated friction to be recorded at the start of each test to ensure consistency of the interface conditions between tests and establish the magnitudes of the friction between the TPs and test chamber.
- **Continuously lubricated advance** (L_c). This phase consisted of an advance whilst lubricant was pumped at a consistent rate into the SLS interface from a single lubricant port. This recreated conditions immediately behind the TBM, where lubricant is pumped into the SLS interface either by a lubrication ring, or discrete ports on the TBM, continuously.
- **Intermittently lubricated advance** (L_i). This phase consisted of lubricant being pumped intermittently from a single port as the TPs advanced through the test chamber. This recreated the intermittent nature of lubrication of the SLS interface in the field, where the lubricant systems are configured such that only one port is open at any given time. This results in P_a fluctuations, such as those identified in Chapter 4, which were recreated within the test chamber.
- **Changeovers** (C). These were required to reuse the TPs in order to create large interface strains within the chamber. The stages were typically 1 hour duration to minimise the time where no shearing occurred at the interface, whilst ensuring a consistent duration between tests. This is also similar to the duration of changeovers recorded in the field

studies which typically varied between 30 minutes and 2 hours.

- **Stoppages (ST).** These were longer periods with no interface shear or lubrication of 12 h or 60 h duration which recreated typical overnight or weekend stoppages during tunnelling.

All tests without overcuts present began with L_u type advance(s) before L_c type advances, with lubricant injected into the interface (T3, T4, T5, T5b, T6, and T7). The overcut containing tests (T8, T9, and T10) began with L_c type advances immediately. The L_c advances were then repeated until the full length of the interface had been lubricated. Once this was achieved, L_i stages were completed before either the test was terminated (T4 and T9), or the first ST stage of the test.

In the medium and long tests, each ST was followed by L_u type advances to quantify the conditions at the SLS interface before lubricant re-injection. These conditions were representative of field conditions, as field data have shown that the tunnel advance is typically restarted as soon as lubrication recommences, which would result in fresh lubricant not being present in the whole overcut. Additionally, the SLS interface at a particular location may not be influenced by a lubricant port until three or four pipe length advances after the tunnel drive restarts, due to the typical lubricant port spacing of 12 m to 20 m.

Tests T3 and T5 were terminated after a single ST stage to examine the condition of the SLS interface, whilst T5b, T7, T8, and T10 continued with a set of L_i type advances, before another ST. The number of L_i advances varied slightly due to timing constraints, but a minimum of four advances were completed before the next ST to ensure all TPs had passed through the interface since lubrication restarted. The sequences of the eight tests conducted post-commissioning (i.e. T3 - T10) are shown in detail in Tables 7.2, 7.3 and 7.4.

Table 7.2: T3 and T4 test sequences, with the stage number (Nr), stage class (Cl), advance distance (Δx), and stoppage duration (t_s) identified where applicable.

T3				**T4**			
Nr. (-)	**Cl**[1] (-)	Δ_x **(mm)**	t_s **(h)**	**Nr.** (-)	**Cl**[1] (-)	Δ_x **(mm)**	t_s **(h)**
1	S	-	-	**1**	S	-	-
2	L_u	65	-	**2**	L_u	100	-
3	L_u	200	-	**3**	L_u	100	-
4	L_c	200	-	**4**	C	-	1
5	ST	-	12	**5**	L_c	120	-
6	L_u	460	-	**6**	C	-	1
7	C	-	1	**7**	L_c	75	-
8	L_u	460	-	**8**	L_c	390	-
				9	C	-	1
				10	L_i	460	-
				11	C	-	1
				12	L_i	460	-
				13	C	-	1
				14	L_i	125	-

[1] Stage classes (Cl) are: setup (S), unlubricated advance (L_u), constant lubrication advance (L_c), intermittently lubricated advance (L_i), stoppage (ST), and changeover (C).

Table 7.3: T5, T5b, and T7 test sequences, with the stage number (Nr), stage class (Cl), advance distance (Δx), and stoppage duration (t_s) identified where applicable.

T5				**T5b**				**T7**			
Nr. (-)	**Cl**[1] (-)	Δ_x **(mm)**	t_s **(h)**	**Nr.** (-)	**Cl**[1] (-)	Δ_x **(mm)**	t_s **(h)**	**Nr.** (-)	**Cl**[1] (-)	Δ_x **(mm)**	t_s **(h)**
1	S	-	-	**1**	S	-	-	**1**	S	-	-
2	L_u	100	-	**2**	L_u	265	-	**2**	L_u	200	-
3	C	-	0.166	**3**	C	-	0.166	**3**	C	-	0.166
4	L_c	330	-	**4**	L_c	465	-	**4**	L_c	265	-
5	C	-	1	**5**	C	-	1	**5**	C	-	1
6	L_c	90	-	**6**	L_c	465	-	**6**	L_c	465	-
7	L_c	465	-	**7**	C	-	1	**7**	C	-	1
8	C	-	1	**8**	L_c	465	-	**8**	L_c	465	-
9	L_i	465	-	**9**	C	-	1	**9**	C	-	1
10	C	-	1	**10**	L_i	465	-	**10**	L_i	465	-
11	L_i	465	-	**11**	ST	-	12	**11**	ST	-	3
12	C	-	1	**12**	L_u	465	-	**12**	L_i	465	-
13	L_i	465	-	**13**	C	-	1	**13**	C	-	1
14	ST	-	12	**14**	L_u	465	-	**14**	L_i	465	-
15	L_u	465	-	**15**	C	-	1	**15**	C	-	1
16	C	-	1	**16**	L_i	465	-	**16**	L_i	465	-
17	L_u	465	-	**17**	C	-	1	**17**	C	-	1
18	C	-	1	**18**	L_i	465	-	**18**	L_i	465	-
19	L_u	465	-	**19**	C	-	1	**19**	ST	-	60
20	C	-	1	**20**	L_i	465	-	**20**	L_u	465	-
21	L_u	465	-	**21**	C	-	1	**21**	C	-	1
				22	L_i	465	-	**22**	L_u	465	-
				23	C	-	1	**23**	C	-	1
				24	L_i	465	-	**24**	L_i	465	-
				25	ST	-	12	**25**	C	-	1
				26	L_u	465	-	**26**	L_i	465	-
				27	C	-	1	**27**	C	-	1
				28	L_u	465	-	**28**	L_i	465	-
				29	C	-	1	**29**	C	-	1
				30	L_i	465	-	**30**	L_i	465	-
				31	C	-	1	**31**	ST	-	60
				32	L_i	465	-	**32**	L_u	465	-
								33	C	-	1
								34	L_u	465	-
								35	C	-	1

[1] Stage classes (Cl) are: setup (S), unlubricated advance (L_u), constant lubrication advance (L_c), intermittently lubricated advance (L_i), stoppage (ST), and changeover (C).

Table 7.4: T8, T9, and T10 test sequences, with the stage number (Nr), stage class (Cl), advance distance (Δx), and stoppage duration (t_s) identified where applicable.

T8				**T9**				**T10**			
Nr. (-)	**Cl**[1] (-)	Δ_x **(mm)**	t_s **(h)**	**Nr.** (-)	**Cl**[1] (-)	Δ_x **(mm)**	t_s **(h)**	**Nr.** (-)	**Cl**[1] (-)	Δ_x **(mm)**	t_s **(h)**
1	S	-	-	**1**	S	-	-	**1**	S	-	-
2[2]	L_c	140	-	**2**[2]	L_c	140	-	**2**[2]	L_c	130	-
3	C	-	0.5	**3**	C	-	0.5	**3**	C	-	0.5
4[2]	L_c	450	-	**4**[2]	L_c	450	-	**4**[2]	L_c	450	-
5	C	-	0.5	**5**	C	-	0.5	**5**	C	-	0.5
6[2]	L_c	460	-	**6**[2]	L_c	420	-	**6**[2]	L_c	450	-
7	C	-	1	**7**	C	-	1	**7**	C	-	1
8	L_i	460	-	**8**	L_i	470	-	**8**	L_i	450	-
9	ST	-	12					**9**	ST	-	12
10	L_u	465	-					**10**	L_u	450	-
11	C	-	1					**11**	C	-	1
12	L_u	465	-					**12**	L_u	450	-
13	C	-	1					**13**	C	-	1
14	L_i	460	-					**14**	L_i	460	-
15	C	-	1					**15**	C	-	1
16	L_i	460	-					**16**	L_i	465	-
17	C	-	1					**17**	C	-	1
18	L_i	460	-					**18**	L_i	465	-
19	C	-	1					**19**	C	-	1
20	L_i	460	-					**20**	L_i	460	-
21	C	-	1					**21**	C	-	1
22	L_i	460	-					**22**	L_i	465	-
23	ST	-	60					**23**	ST	-	60.5
24	L_u	460	-					**24**	L_u	460	-
25	C	-	1					**25**	C	-	1
26	L_u	460	-					**26**	L_u	460	-
27	C	-	1					**27**	C	-	1
28	L_i	465	-					**28**	L_i	460	-
29	C	-	1					**29**	C	-	1
30	L_i	465	-					**30**	L_i	460	-
31	C	-	1					**31**	C	-	1
32	L_i	465	-					**32**	L_i	460	-
33	C	-	1					**33**	C	-	1
34	L_i	465	-					**34**	L_i	460	-
35	C	-	1					**35**	C	-	1
36	L_i	465	-					**36**	L_i	460	-
37	C	-	1					**37**	C	-	1
38	L_i	465	-					**38**	L_i	460	-
39	ST	-	60					**39**	ST	-	62
40	L_u	465	-					**40**	L_u	460	-
41	C	-	1					**41**	C	-	1
42	L_u	465	-					**42**	L_u	460	-

[1] Stage classes (Cl) are: setup (S), unlubricated advance (L_u), constant lubrication advance (L_c), intermittently lubricated advance (L_i), stoppage (ST), and changeover (C).

[2] Overcut being formed during this stage.

7.1.3 Chapter structure

This chapter first presents a summary of the results from the commissioning testing of the SLS interface apparatus, which quantified the key design parameters, such as: wall, axial, and test piece interface friction. Following this, sources of uncertainty in the data are discussed alongside their perceived impact on the experimental results. The results from the eight interface tests are then explored by examining first the influence of lubrication on the SLS interface without the presence of an overcut, before the influence of overcut inclusion, and finally the effects of stoppages on the overcut conditions. Observations from post-test analysis of Bentonite penetration, infiltration zone water content, and a summary of visual observations at the end of the test are also presented. To ensure consistency in presentation of these results, the sign conventions shown in Table 7.5 have been adopted.

Table 7.5: Sign conventions used in the presentation of apparatus chamber results

Component	Symbol	Unit	Sign convention	Notes
Interface normal stress	σ_N	kPa	Compressive negative	On sensor side of interface
Interface axial shear stress	τ	kPa	Backwards positive	On sensor side of interface
Axial position in test chamber	x_{ch}	mm	Origin at entry to chamber	-
Transverse position in test chamber	y_{ch}	mm	Origin at rear of chamber	Actuator side is the rear side
Advance distance	x	mm	Forwards positive	-

7.2 Commissioning results

7.2.1 Chamber deformations

To quantify the chamber deformations under internal pressure, two tests were completed where the test chamber was pressurised to 200 kPa to measure the deflections at the wall mid span. During the tests, the TP exit and entry ports were sealed, and the TPs were removed from the apparatus. A maximum deflection of 2.1 mm was recorded at the midspan of the

front face of the chamber, whereas the rear face deformed less due to the additional stiffness of the actuator support frame. The maximum deflection was larger than the design value due to compliance introduced by the gaskets between the chamber panels, but, as the deflection was $< 0.5\%$ of the chamber width, it was deemed acceptable for testing.

7.2.2 Chamber wall friction

The small scale tests of the chamber wall interface demonstrated that the wall friction angle was non-trivial and required accounting for in the calculation of normal stress at the SLS interface. Tests were therefore conducted where the pressure bag stress (P_a) was varied in the range 0 kPa to 100 kPa. Figure 7.1 presents the measured normal stress (σ_N) and applied stress ($P_a + \gamma.H$; where H is the sample height). The figure shows that σ_N is less than the applied stress during the incremental increases in loading, but greater during incremental unloading, demonstrating the presence of wall friction within the chamber.

At $P_a > 10kPa$, the friction loss was linearly proportional to P_a in both loading and unloading conditions. When $P_a < 10$ kPa the losses appeared to be insensitive to P_a, suggesting a minimum loss value of 4 kPa at the interface, but these values are below those used during testing. For the pressure range of interest, the wall friction angle (δ_w) was calculated as 5.4°. This value is similar to the 4.6° determined by Tognon et al. (1999) for a similar, albeit larger, experimental setup, but varied from the constant ≈ 1 kPa observed during small scale testing of the arrangement. This difference was believed to be due to the lubricating grease film dispersing more thinly over the larger chamber wall area, such that it's lubricating effect was less pronounced. It was found that injecting additional grease to the interface did not change this behaviour, therefore, to account for the wall friction during testing, σ_N was calculated as:

$$\sigma_N = (P_a + \gamma.H) - (\frac{\gamma.H}{2} + P_a).K_0.tan(\delta_w).A_w \tag{7.1}$$

where A_w is the area of the chamber walls in contact with the sand sample and K_0 is the coefficient of lateral earth pressure at rest for the 14/25 sand.

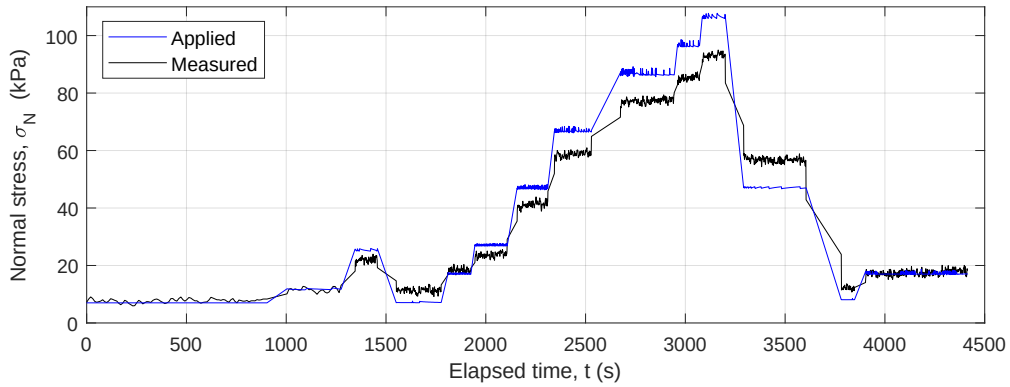


Figure 7.1: Theoretical vertical stress at the SLS interface ($P_a + \gamma.H$) and measured normal stresses by the test pieces (σ_N) during a static pressure test.

7.2.3 Concrete interface friction

Six interface friction tests were conducted on concrete test samples cast to fit within a standard 125 mm shear box apparatus. These were sheared against the 14/25 sand used in the apparatus and a mean interface friction coefficient (μ) of 0.96 was calculated from the results. Using the relationship between normalised roughness ($\frac{R_a}{D_{50}}$) and μ proposed by Knappett and Craig (2012), where the present value of $\frac{R_a}{D_{50}} = 0.021$, a $\mu \approx 0.9$ was predicted, slightly less than the calculated value.

During testing it was observed that the surface of the concrete was roughened by abrasion with the sand, which was not accounted for in the calculation of R_a as these measurements were taken on untested samples. Figure 7.2 shows a comparison between the as-cast TP concrete surface (7.2(i)) and the surface after five transits through the test chamber (7.2(ii)), where 'pitting' is visible. The pitting was formed when thinly covered air bubbles are exposed by the abrasive action of the sand and accounts for the measured μ value being slightly greater than the predicted.

This degradation of the concrete surface was also evident in the small scale shear results. Figure 7.3 shows the relationship between μ and the horizontal displacement (δ_h) for the first eight passes of an untested concrete sample against dense 14/25 sand in the shear box apparatus (Test 1). Pass one has a steady state $\mu = 0.94$, which increases to ~ 1 by pass eight. A

second test on the same sample, comprising of two passes, is also shown to demonstrate the repeatability of the peak and critical state response of the interface. Peak behaviour is observed in the first pass of both tests, however it dissipates after $\delta_h = 5$ mm. As the TPs in the apparatus were re-used during the SLS interface testing, $\mu = 1$ was adopted for all tests.

7.2.4 Apparatus axial friction

Tests were conducted without a sand sample to quantify the axial force required to overcome friction within the test apparatus. It was anticipated that the axial friction created by the entry and exit seals would vary slightly between tests (due to the differences in the clamping forces of the fish plates) and could only be estimated by testing without a sand sample, whereas the friction between the chamber walls and TPs was more constant and could be quantified during commissioning. Figure 7.4 presents exemplar data which shows the frictional force distribution within the apparatus. In the figure, load cell one (LC1) was connected to the actuation cable, with LC2 between the next TPs, then LC3, and then LC4. During the advance, test piece two (TP2), was passing through the chamber exit seal, whilst TP3 was completely within the chamber and TP4 was passing through the entry seal.

Within the test chamber, the friction was 0.3 kN per test piece, as shown by the difference between $LC2$ and $LC3$, which corresponded to a friction of 0.32 kN per m at the chamber wall - TP seals. The exit seal and side friction with the chamber is seen to add 1.8 kN to F_a, as measured by the difference between the LC1 and LC2 magnitudes. Similarly, the entry seal was between LC3 and LC4 and caused 0.7 kN of friction.

To quantify any changes in the friction magnitudes during testing, measurements were taken at the start and end of each test by actuating the TPs through the chamber without the sand sample present. If there was a discrepancy between the values, the friction values were taken to be constant at the after-test magnitude throughout the test, as it was anticipated that any additional friction was caused by sand ingress into the seals and would manifest quickly at the start of the tests.

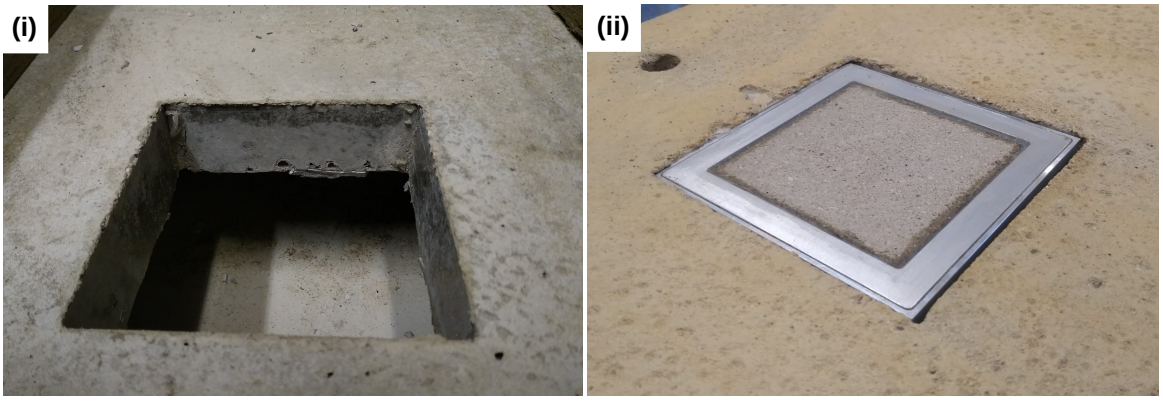


Figure 7.2: Photographs showing the surface condition of the TPs: (i) as cast and (ii) after five transits through the test chamber in contact with sand.

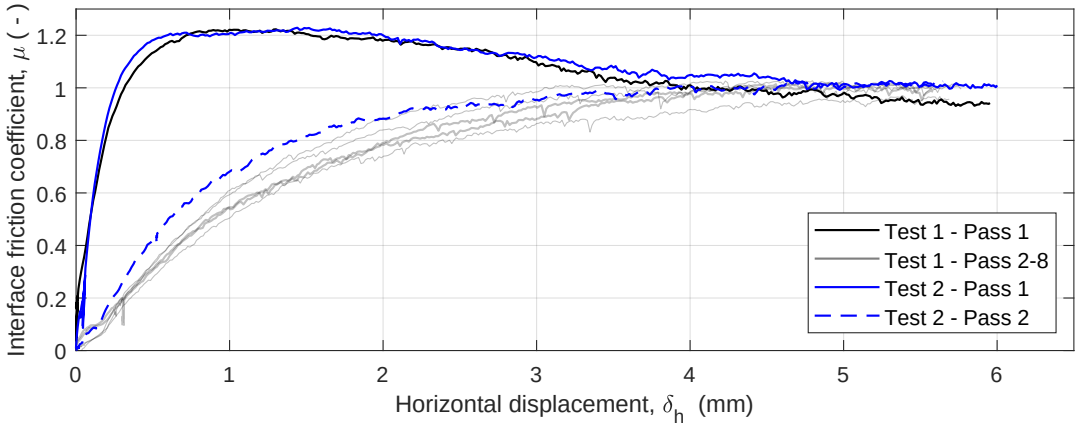


Figure 7.3: Interface friction coefficient (μ) development with horizontal displacement (δ_h) from two consecutive tests, totalling ten passes, between the cast concrete interface sample and dense 14/25 sand for $\sigma_N = 100$ kPa.

7.3 Sources of uncertainty

During commissioning, some sources of uncertainty became apparent which could not be fully isolated from the test data. Although none of these were felt to significantly influence the test results, they are described, alongside their potential impact on the tests, in the following section.

During testing, small leaks occurred at the TP - chamber seals when the lubricant at the interface was under higher pressures (i.e. when the injection port was close to the seal) or when features of the TPs (joints, lubricant ports, or overcut formers) passed through the seal. Despite the compression of the neoprene seal using flexible double rubber D profiles and the fish plates, the ports and joints allowed the lubricant a path out of the test chamber, as shown

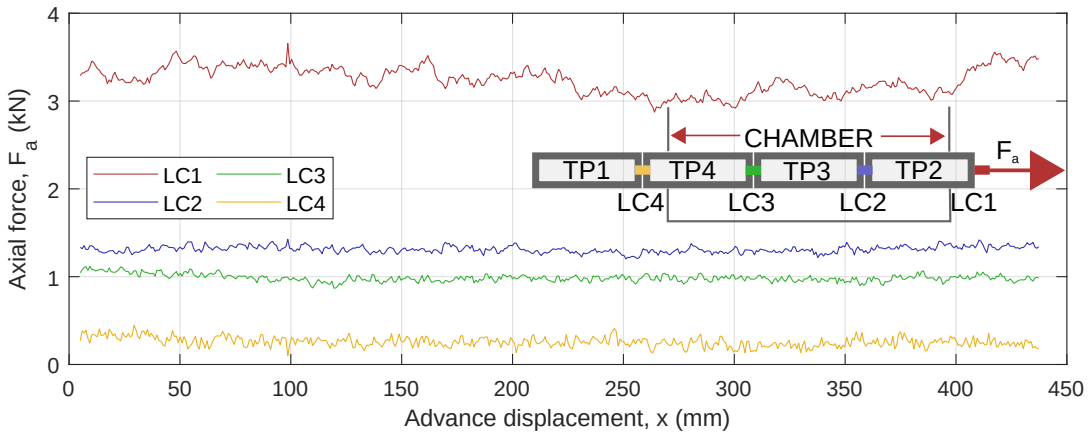


Figure 7.4: Axial load cell friction measurements from a $x = 440$ mm advance with no soil sample, showing the friction between the test pieces and seals.

in Figure 7.5(i). Leaks were confined to the centre of the TPs at the exit seal, along the line of lubrication injection, or at the top corners of the TPs where adequate compression of the seal was more difficult to achieve.

The leaks between the TPs and chamber boundaries were caused by sand contamination of the seals as the TPs passed joints in the chamber (i.e. at the windows and central panel joint). The slight bull-nose on the TPs, designed to stop the TPs tearing the entry and exit seals, allowed a small quantity of sand into the seal, despite the inclusion of a foam strip to fill the void and act as a brush to clean the seal. Figure 7.5(ii) shows the sand grains and lubricant contaminating the seal in a commissioning test. This infiltration prompted the addition of a second PTFE covered foam strip, bonded to the chamber wall, which reduced contamination of the joint by smoothing the chamber walls.

If, during testing, a large leak occurred (defined as > 1 l during a stage of the test) the test was abandoned and restarted, as this was deemed to have had a significant impact on the test results. Smaller leaks were tolerated, but did influence the total volume of Bentonite within the apparatus during the tests. The leaks primarily occurred whilst the apparatus was in motion, as during stoppages no visible signs of leakage were observed. Some small variations in pressure were recorded during stoppages, which are further discussed in the results.

During deconstruction of the apparatus after each test, it was found that a small quantity

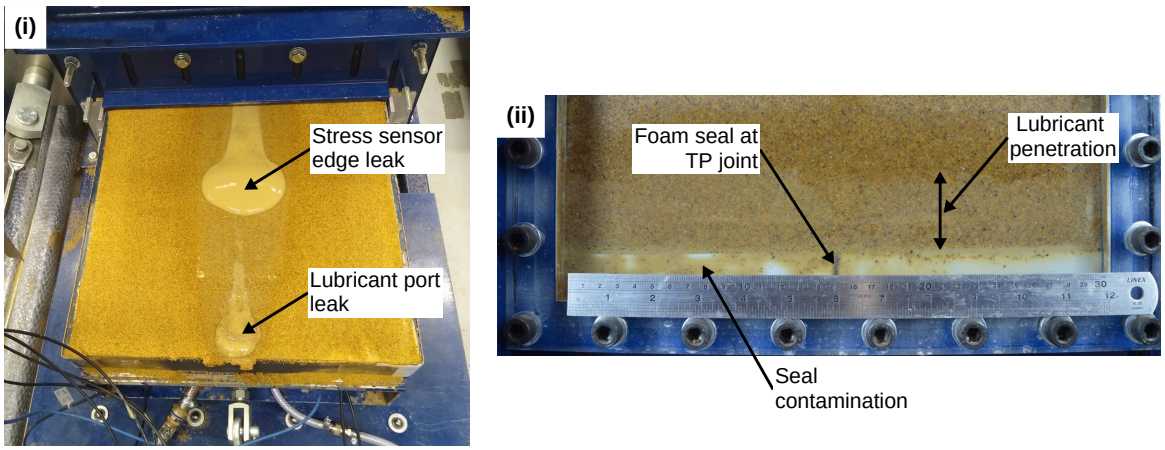


Figure 7.5: Photographs showing small Bentonite leaks at: (i) the exit seal, and (ii) the TP-chamber seal with notable features labelled.

($<$ 250 ml) of lubricant travelled between the two PTFE sheets in the chamber corners and collected under the pressure bag. This was seen to be due to the small gaps between the sheets at the corners providing a lower resistance path for the Bentonite than direct infiltration the sample itself. The penetration into the sand sample at the corner was small ($<$ 20 mm) and the penetration was not thought to effect the test results due to the small volume of lubricant involved.

During unlubricated tests, the rough interface of the TPs drew a thin layer of sand through the exit seal, as shown in Figure 7.6(i). The thickness of the layer depended on the position of the top fish plate and varied slightly between tests, but it was typically $<$ 2 mm. The sand was collected after each advance and found to weigh $<$ 600 g, which equated to $<$ 0.1% of the sand mass in the chamber lost per advance. During lubricated tests the sand loss was found to be significantly less, as shown in Figure 7.6(ii) for a lubricated test. This sand was not weighed (due to the Bentonite inclusion), but the loss was qualitatively assessed to be less than in the unlubricated case. As the mass of sand loss was small, and the pressure bag was designed to accommodate volume changes of the sand sample, this sand loss was not thought to influence the test results significantly.

During the tests the u at the interface was monitored using PTs mounted 330 mm behind the lubricant injection port of each TP. The filter caps used to prevent sand and Bentonite

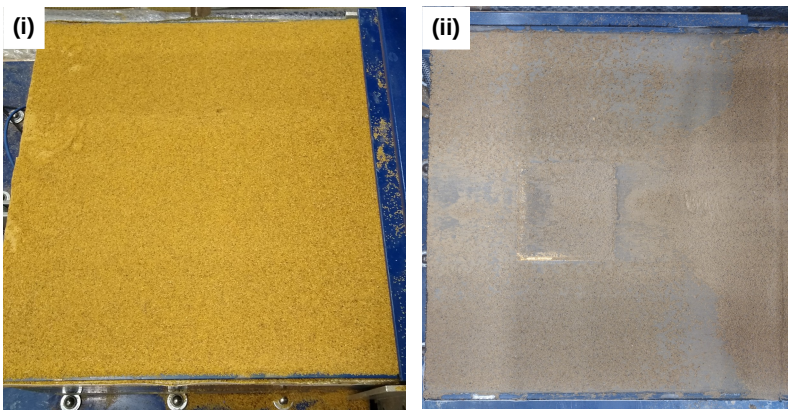


Figure 7.6: Photographs showing the sand and Bentonite drawn through the exit seal during testing: (i) unlubricated and (ii) lubricated.

from clogging the PT ports damped their response, such that instantaneous total and effective stress calculations were not accurate. During a test without filter caps, the pore pressure and total stress measurements from the test pieces were found to align well during the lubrication stages but the capillary tube to the PT quickly blocked with Bentonite which again damped the response. Therefore, the data from the local stress sensors are presented in terms of total stress during shearing to avoid any errors induced by damping of the PT measurements.

7.4 Unlubricated interface friction

After the setup stages an unlubricated (L_u type) advance was completed in all tests, except those with overcuts. This was for two reasons: firstly, the advance ensured the interface conditions at the start of lubrication were steady state (i.e. any peak effects had dissipated), and secondly it confirmed the predicted friction magnitudes from the entry and exit seals. For example, Figure 7.7 shows the measured interface friction angles from the TP1 stress sensor (δ_{TP1}) and axial load cell data (δ_G) during the first 100 mm advanced of $T3$. The axial load cell measures the average, or global, interface friction within the chamber, including the friction from the entry and exit seals and the TP - chamber wall seals. A corrected friction angle ($\delta_{G,c}$) is also calculated, which removes these friction components.

The TP1 data in the figure show a peak friction angle of $\delta_{TP1} = 32°$, followed by a reduction to a critical state angle of $\delta_{TP1} = 29°$, demonstrating that the interface had achieved critical

state within the first 100 mm advanced. The critical state angle of 29° was lower than the friction angle recorded during commissioning, a finding attributed to the advance being the first use of the new sensor face plate in the apparatus, and a lower μ value of the unabraded interface.

To confirm the consistency of the interface across the chamber the shear responses from two sensors (TP1 and TP4) are compared in Figure 7.8. The figure shows the change in normal stress ($\Delta\sigma_N$) and shear stress ($\Delta\tau$) at the interface during the first 100 mm advanced of test T4. The variation of $\Delta\sigma_N$ shows that the stress at the interface increased during the initial 50 mm of the advance, demonstrating that the sample dilated during shearing. The dilation resulted in the normal stress pressure bag draining during this period, with the pressure within the bag briefly increasing from 20 kPa (the target pressure) to 24.07 kPa at 25 mm advanced, before decreasing again. This increase is less than $\Delta\sigma_N$ observed at the interface (9.06 kPa), due to the wall friction in the chamber resisting the heave of the sample. As the stresses reduced to critical state, the τ and σ_N responses were similar for both TPs, demonstrating consistent interface conditions throughout the chamber. The results also show that the apparatus achieves critical state conditions after $x = 100$ mm at $\sigma_N = 30$ kPa, which is the desired condition for the large interface shear tests.

During commissioning it was noted that the sample surface deformed after shearing, by settling up to 40 mm at the entry seal end, whilst the exit side remained level. This settlement was created by sand being transported through the chamber from the entry to the exit seal end by the fully rough interface. The volume change resulting from this deformation exceeded the volume lost through the exit seal during the tests, confirming a small density increase around the exit seal of the chamber. This phenomenon was less apparent in the lubricated tests, and not observed in the overcut tests, demonstrating that the TP - sand interface was fully rough in the unlubricated condition, again confirming predictions of the small scale testing.

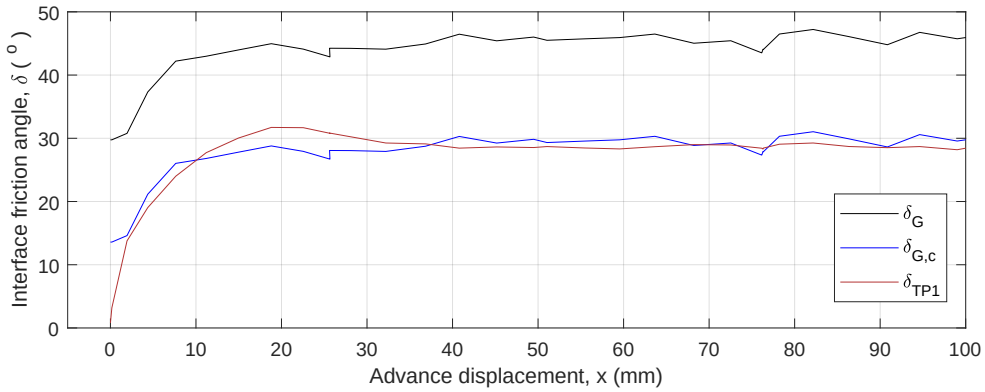


Figure 7.7: The development of the global, local, and global corrected interface friction angle (δ_g, δ_{TP1}, $\delta_{g,c}$) with advance distance (x) during the first L_u type advance of T3.

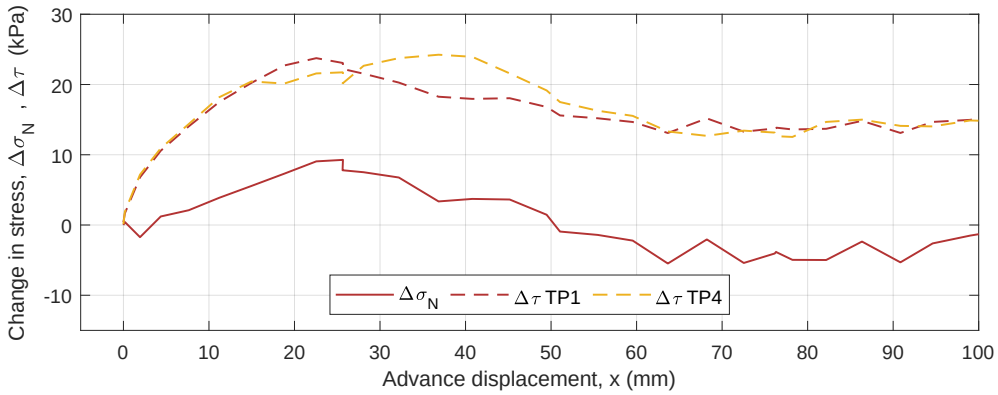


Figure 7.8: Typical change in normal stress (σ_N) and shear stress (τ) during the first 100 mm of the initial (L_u) stage of a test.

7.5 Influence of initial lubricant injection

7.5.1 Effect on local stress

The effects of lubricant injection were assessed in T3 - T7 and compared to the unlubricated advances described above. T3 - T7 began with continuous lubricant injection, at a rate of 500 g per minute, to simulate a SLS interface without an overcut in the field being filled for the first time immediately behind a TBM. Figure 7.9 presents representative measurements from TP1 during T3 stage 4 (TP1 being the local stress sensor immediately behind the injection port). For the first 20 mm of the advance, τ and σ_N are constant, demonstrating that the lubricant injection had not influenced the sensor. Between 20 mm $< x <$ 100 mm σ_N increased to 50 kPa and τ decreased to near 0 kPa. The coupling of the τ and σ_N measurements demonstrate that a low-friction boundary layer was being formed at the SLS interface by the lubricant injection.

As the lubricant first influenced the sensor whilst the leading edge of the sensor was 65 mm behind the original injection location (calculated using the advance distance of the TP), the measurements demonstrate that the lubricant was travelling along the SLS interface. During this period, the pressure bag intermittently drained to maintain the target pressure of $P_a = 20$ kPa, demonstrating that heave of the sand sample was occurring as the boundary layer formed.

Figure 7.10 shows σ_N response for T4 - T7 in the first 120 mm advanced. In T5b and T7 σ_N increases in a similar manner to T3, although the distance advanced before σ_N increases varied between 20 mm $\leq x \leq$ 40 mm. This suggests that lubricant spread at the SLS interface is a variable process and that the resistance to lubricant penetration into the sand, and the resulting lubricant pressure, controlled whether penetration occurred across the interface or into the sand sample. Figure 7.11 presents the τ response during the same 120 mm period of the first lubricated advance. These responses vary slightly between tests, as τ is only seen to decrease once σ_N increases. For example, τ during T5 decreases more rapidly than during T5b due to the earlier influence of the lubricant, as shown by the earlier σ_N increase.

A leak between the chamber seals and TP is apparent in the T4 data at $x = 88$ mm in Figure 7.10, evidenced by the decrease in σ_N. Despite the drop in σ_N, τ does not increase for the remainder of the advance, which demonstrates that a lubricating boundary layer had been formed at the interface and, until the layer had dissipated (either through filtration into the sand, abrasion by the interface, or dissipation around the interface) τ was independent of σ_N. The leak, and associated reduction in $\Delta\sigma_N$, resulted in a reduction in the thickness of the boundary layer, causing settlement of the sand sample which was identified as the pressure bag intermittently filled instead of discharging during this period.

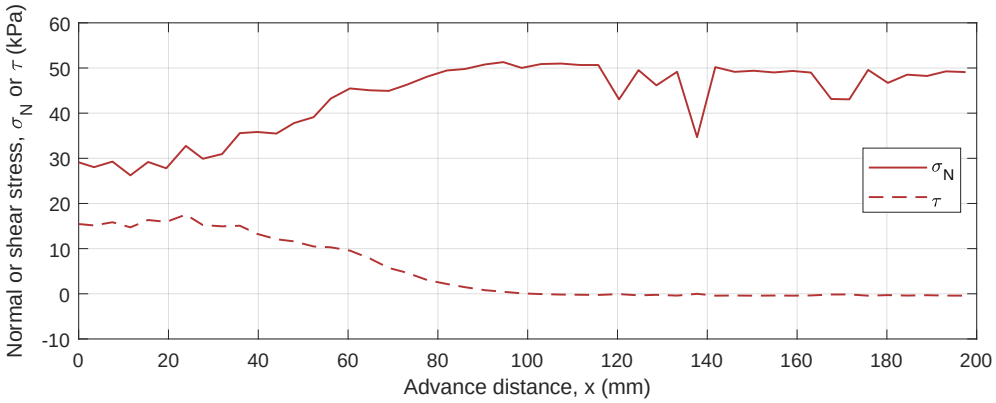


Figure 7.9: Normal stress (σ_N) and shear stress (τ) development during a 200 mm continuously lubricated advance, stage 6 of T3, measured from TP1, 130 mm behind the lubricant injection.

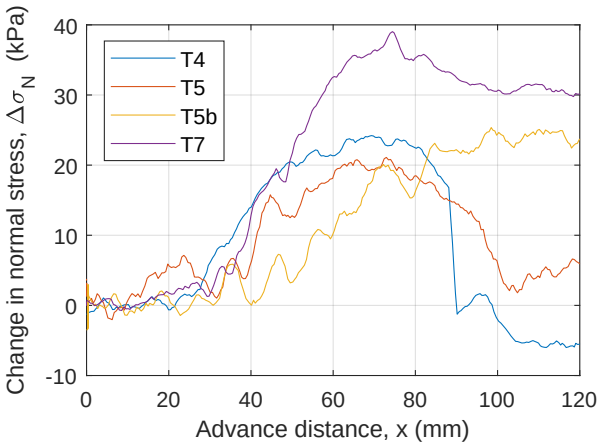


Figure 7.10: Normal stress change ($\Delta\sigma_N$) with advanced distance (x) during the first lubricated L_c stage of T4 - T7.

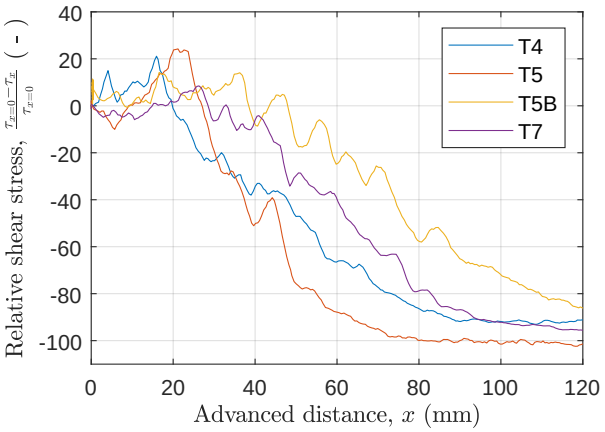


Figure 7.11: Shear stress change ($\frac{\tau_x-\tau_{x=0}}{\tau_{x=0}}$) with advanced distance (x) during the first lubricated (L_c) stage of T4 - T7.

7.5.2 Effect on global friction

The average interface friction across the whole of the test chamber (termed global friction) was calculated using the actuation force (F_a). Figure 7.12 shows the percentage reduction in global friction measured during the L_c stages of T3 - T7, when compared with the initial L_u type stage. From the figure, it is clear that during the first L_c advance ($ADV1$) the lubricant had a variable effect on F_a, due in part to the slightly different lengths of the advances. The lubricant maximum effectiveness in each test, except T5 which appears anomalous, was between 71% and 82% which is similar to the shear stress reductions observed in previous studies.

During these tests, the global friction values did not reduce to the same extent as the local

sensor values, suggesting that the lubricating effect of the injection was not uniform across the whole interface. This was confirmed by the pressures measured by observations from windows mounted through the chamber walls, through which the lubricant was not uniformly apparent at the chamber edge. The greater reduction in F_a observed in the test T5b and test T7 friction magnitudes was due to the increased σ_N at the interface (Figure 7.10) during the initial lubrication stage. The higher pressure of lubricant at the interface resulted in a broader spread of the Bentonite across the interface, forming a more effective boundary layer.

To examine the Bentonite spread in more detail, the penetration of the Bentonite into the soil sample was assessed using the chamber windows and observations of the TPs as they exited the test chamber. As only a single Bentonite injection occurred during T3, it provides reference to the initial spread of the lubricant. Figure 7.13 shows the Bentonite penetration at the exit window during the test at key stages:

(i) No Bentonite is apparent at the window, despite the lubrication port being in-front of the window and injection occurring.

(ii) Uneven Bentonite penetration is apparent at the window, with a bulb of Bentonite in front of a thinner layer along the interface behind.

(iii) The advance and Bentonite injection finish. The distribution of the Bentonite at the window is more even and shows penetration of up to 40 mm into the sand sample. No obvious separation has occurred between the sand and TP at the interface.

(iv) At $t_s = 1.5$ hours, Bentonite is apparent towards the front of the window, demonstrating that further spread of the Bentonite is occurring within the chamber. This is coupled with occasional filling of the pressure bag, which suggests the boundary layer thickness is decreasing as the Bentonite penetrates more into the sand.

(v) At $t_s > 12$ hours, further Bentonite penetration has stopped and a small area of partially saturated sand is visible around the fully lubricant-saturated region. The distribution of

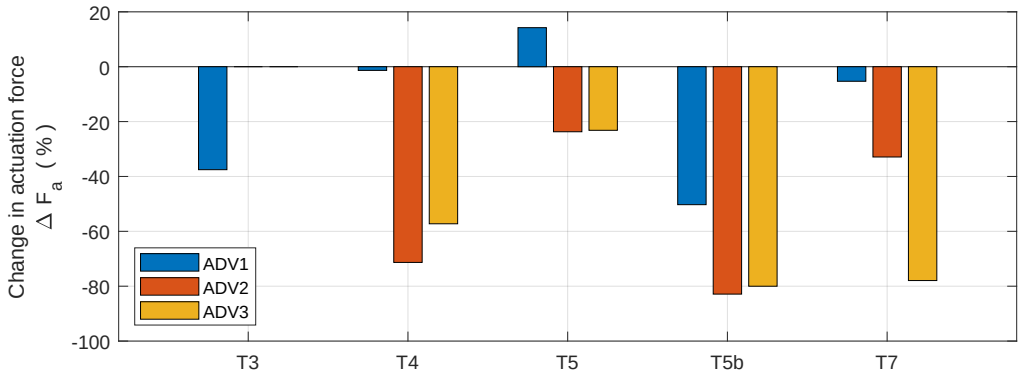


Figure 7.12: Percentage change in the actuation force (F_a) during L_c type advances (ADV) for tests without overcuts, compared to the F_a during the unlubricated, type L_u, advance.

Bentonite in the sand is more even and extends almost the full length of the chamber.

Figure 7.14 shows a plan view of the lubricating TP after it had exited the test chamber. The spread of the lubricant formed an angle of 130^o to the direction of advance. Outside of this region there was additional partially saturated sand which did not contain Bentonite, demonstrating that water had filtered out of the Bentonite during the test stoppage, as predicted by the permeameter testing.

In the image it is also possible to see an region of Bentonite with little sand content along the centre line of the TP. Either side of this zone a mixture of sand and Bentonite was observed, with reducing Bentonite content towards the chamber boundaries. The distribution of Bentonite showed that during lubricant injection the Bentonite had variable effectiveness; in line with the port, it separated the sand from the TP interface, forming a boundary layer, but further from the port it created a mixed interface of sand and Bentonite which was less effective at reducing interface friction.

This is an important finding as previous literature, based on smaller scale apparatus (such as shear boxes, small scale axis-symmetric testing, or triaxial apparatus) cannot model this spread phenomenon accurately due to the small test interface area. This small scale testing is not representative of current field tunnelling practice, which typically involves lubricant injection from three discrete ports evenly distributed around the tunnel circumference. This

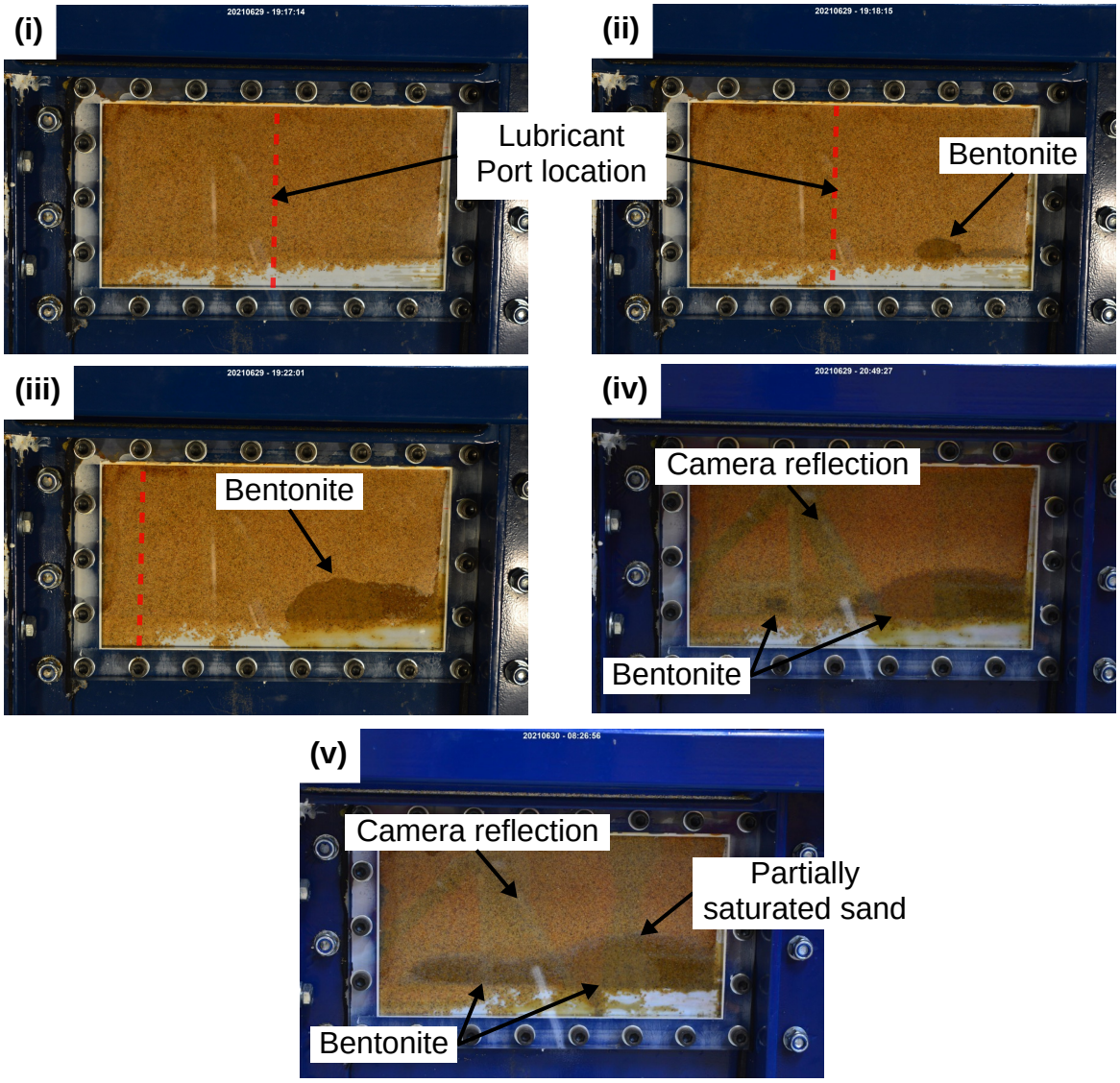


Figure 7.13: Photographs showing progressive lubricant penetration at the exit side window of the test chamber during T3.

can result in lubricant port separations of up to 3.1 m circumferentially for a large (2.98 m diameter) pipe, such as the one in the Putney tunnel drive, or between 1.56 m and 2.32 m for the smaller Hull and Dublin tunnel drives examined as part of this study.

7.6 Influence of intermittent lubricant injection

After the first port providing continuous Bentonite injection had passed completely through the chamber, the Bentonite delivery was changed to intermittent injection (L_i). During these advances, lubricant was delivered to a given port for 15 s every 2 minutes at 500 g per minute, similar to the intermittent lubrication observed during the field studies. The initial lubricant port was selected as the port closest to the entry seal after the L_c stages were complete. This

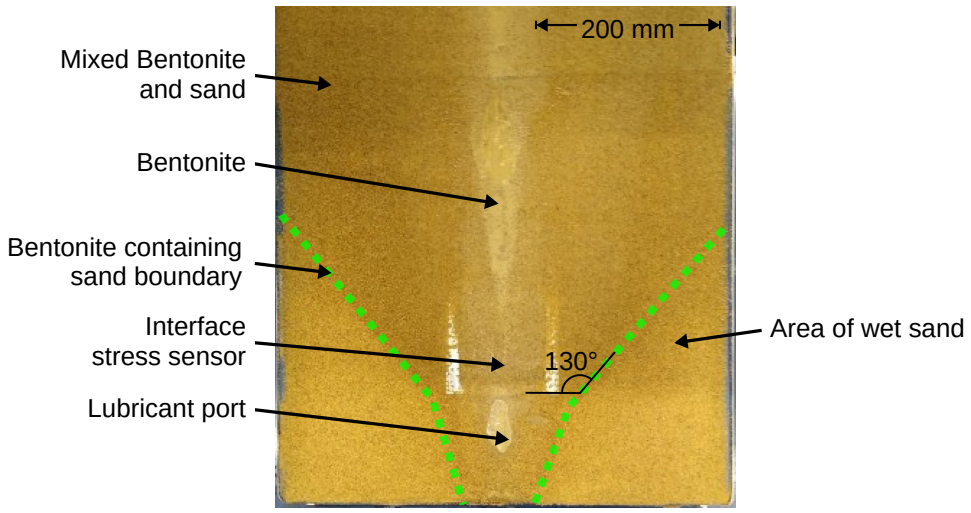


Figure 7.14: Photograph from T3 the spread of lubricant on the first injecting TP, in which the boundary between the visible wet and dry sand is highlighted.

port was then used for the subsequent two advances, before the next port closest to the entry seal was selected. This resulted in the injection lubricant port alternating between two TPs during the tests, for example from TP2 to TP4 then back to TP2 again and so on.

Figures 7.15 and 7.16 show representative σ_N and τ data for L_c and L_i type advances from the local interface stress sensors for the first 500 mm of the test chamber. During the L_c advance, σ_N was maintained in the range 45 kPa $\leq \sigma_N \leq$ 55 kPa; in contrast during the L_i stage σ_N varied widely, with peaks observed every 50 mm advanced correlating to the 15 s on - 105 s off lubrication regime. After each peak, a decrease in σ_N was measured due to dissipation of the lubricant before the next injection occurred. However, each lubrication cycle resulted in an increase in both the peak and residual σ_N. This increase was observed during the L_i advances and corresponded to draining of the pressure bag during the stages, demonstrating that the lubricant was remaining at the SLS interface and causing heave of the sand sample.

The friction caused by the entry seal is visible in Figure 7.16 for 0 mm $< x_{ch} <$ 75 mm. During this period, both shear and the normal stress data are not representative of the conditions inside the chamber due to the additional stress exerted by the seal arrangement. The τ response of both advances drops to near zero when the sensor has fully passed through the entry seal, which demonstrates that the boundary layer was effectively reducing interface friction.

The measurements from both the L_c and L_i stages are consistent for $x_{ch} > 350$ mm, irrespective of the variation σ_N observed, showing that τ was independent of σ_N at the interface during the advances.

To assess the overall effectiveness of the L_i injection stages, Figure 7.17 presents the percentage reduction in F_a, similar to Figure 7.12, for the L_i type stages before the first stoppage in T4 - T7 (ADV5, ADV6, and ADV7) when compared to the unlubricated (L_u) advance. The figure shows a variable response between the tests, with a 27% maximum reduction observed in T4 but a 90% reduction in T7. These differences demonstrate that the lubricant injections had varying degrees of effectiveness away from the central area of the chamber, where the local

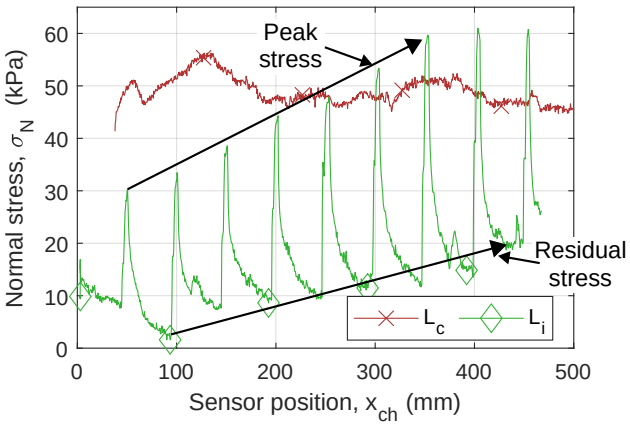


Figure 7.15: Local interface normal stress (σ_N) during L_c and L_i type advances. Stress development is shown with the sensor centre position in the chamber (x_{ch}) where $x_{ch} = 0$ is the entry seal location.

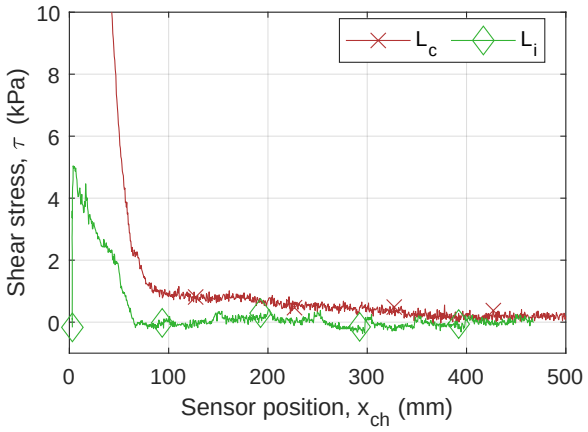


Figure 7.16: Local interface shear stress (τ) during L_c and L_i type advances. Stress development is shown with the sensor centre position in the chamber (x_{ch}) where x_{ch} = 0 is the entry seal location.

sensors measured near zero interface shear stresses throughout the tests. During T5b and T7, the L_c injection was more effective at lowering friction, which resulted in lower friction during the L_i stages as well.

This variability shows the sensitivity of the SLS interface to lubricant injection with no overcut. For tests where the pressure at the interface was not sustained during the initial injection (such as T5), the boundary layer did not form over the complete interface area and subsequent intermittent lubricant injection was not as effective at reducing friction. This was

due to the injected lubricant dissipating into the sand where a filter cake had not formed. The intermittent lubrication was more effective where the boundary layer formed over a larger area (i.e. T7) as it maintained the lubricant pressure at the interface - thereby maintaining the separation between the soil and structure.

The different lubricant spread around the SLS interface was also observed in the material the TPs drew through the exit seal during testing. Figure 7.18 presents images of T4 stage 8, T5b stage 12, and T7 stage 12, which are representative observations from the different tests. The sand-Bentonite mixture in Figure 7.18(iii) was uniform across the width of the TP, showing consistent conditions across the interface during T7. In contrast, Figures 7.18(i) and 7.18(ii), show a mixture of Bentonite and sand outside of the central region during T4 and T5b, similar to that observed in Figure 7.13. These poorly lubricated areas have a higher interface friction coefficient and result in the higher global interface friction observed, whilst the lubricated central region creates the low local friction measurements from the local TP sensors.

7.7 Influence of overcut

The influence of an overcut on SLS interface behaviour was explored in three tests. Test T8 was a long test, with two 60 hour stoppages, which examined how an 18 mm overcut altered the SLS interface conditions when compared to an equivalent no-overcut test, T7. T9 and T10 were conducted at a higher normal stress ($\sigma_N \approx 50$ kPa) to examine how interface stress influenced the SLS characteristics when an overcut was present. During T9 and T10 tests the Bentonite delivery rate was increased to account for the additional spurt distance resulting from the greater σ_N. T9 was a short test which isolated the changes induced by the higher σ_N on the overcut filling, similar to T4, whilst T10 followed the exact test procedure of T8, to isolate the effect of the higher pressure on the response after each stoppage. Figure 7.19 shows the overcut being formed during T8 stage 2. In the figure, the uniform thickness of the formed

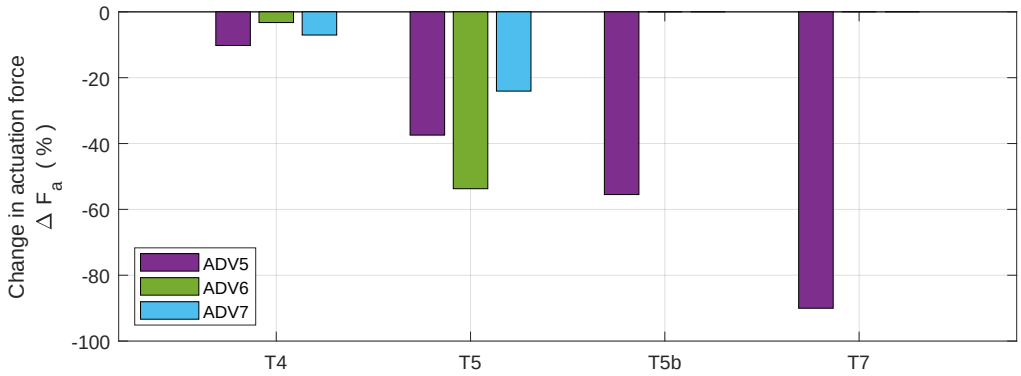


Figure 7.17: Percentage change in the actuation force (F_a) during L_i type advances (ADV) for tests without overcuts, compared to the F_a during the unlubricated advance.

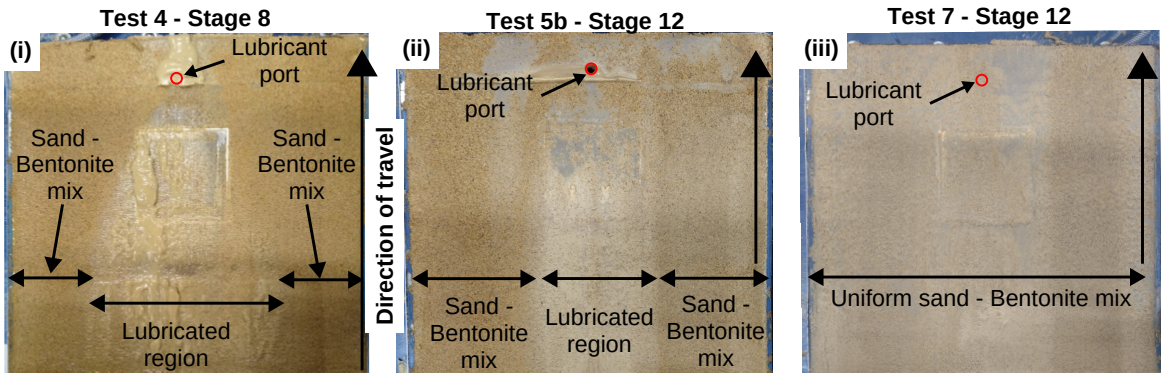


Figure 7.18: Photographs showing the sand and Bentonite mixture drawn through the exit seal during testing after: (i) T4 stage 8, (ii) T5b stage 12, and (iii) T7 stage 12.

overcut is visible, as is the penetration of the lubricant into the sand above.

Figure 7.20 presents σ_N measured by the local stress sensor on TP4 during T8 and T9. Figure 7.21 then presents the measured τ during the same period. In both figures, interaction with the entry and exit seals is observed at $x_{ch} < 75$ mm and $x_{ch} > 925$ mm and it should be noted that these data are not representative of the conditions at the interface. Similarly, at the end of ADV3 in both tests, the stress decrease between 825 mm $\leq x_{ch} \leq$ 925 mm was caused by leakage as the final overcut former exited the chamber and the exit seal was adjusted.

During the filling process, τ measured by the sensors was < 2 kPa and < 3 kPa in T8 and T9 respectively. In both tests, τ reduced as the TP moved through the chamber, which suggests that there was contact between the lubricant filter-cake and the TP, or the soil sample and the TP, in the first 400 mm of the chamber during T8, or 700 mm during T9. During ADV3 of T9,

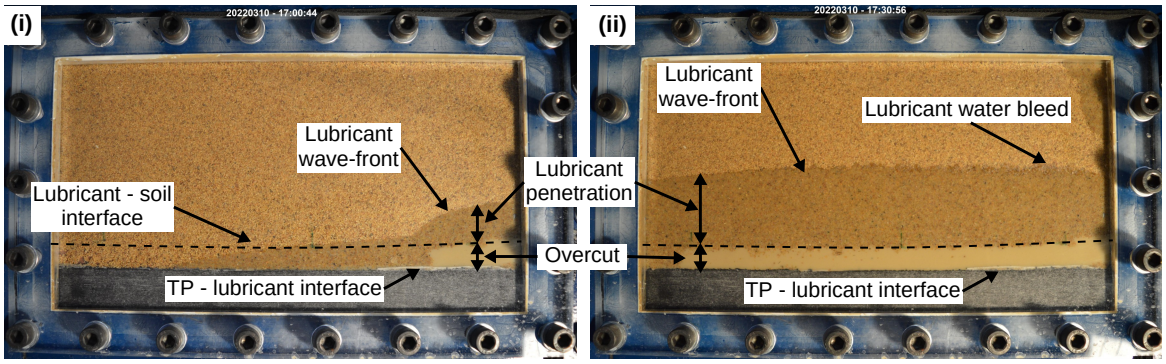


Figure 7.19: Photographs showing overcut formation during: (i) T8 stage 2, after 50 mm advanced and (ii) T8 stage 4, after 380 mm advanced.

σ_N increased to $>$ 30 kPa, whilst the measured τ decreased to near zero. This suggests that the overcut formation during ADV3 was forming a more effective boundary layer between the TP and soil during the advance. The higher σ_N is an indication of the more effective overcut

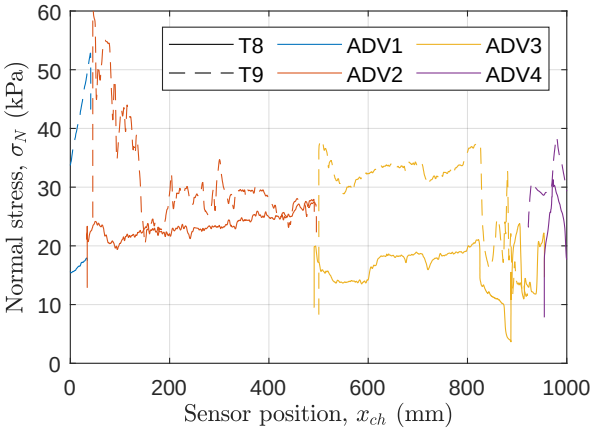


Figure 7.20: Measured total normal stress (σ_N) behind the lubricant port during the four overcut formation advances (ADV1 - ADV4) in T8 and T9.

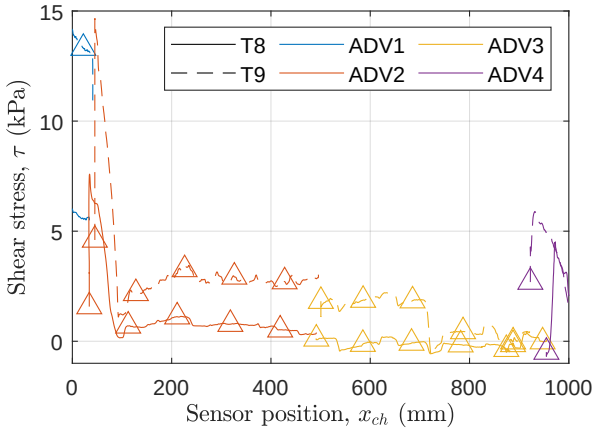


Figure 7.21: Measured shear stress (τ) behind the lubricant port during the four overcut formation advances (ADV1 - ADV4) in T8 and T9.

formation as it demonstrates that the resistance to the Bentonite penetrating into the sand sample had increased. This was due to filter cake formation (observed after the test) and a larger proportion of the lubricant was being retained in the overcut.

To assess the overall effectiveness of the overcut formation F_a (after correction for friction) was used. Figure 7.22 shows the development of F_a during the first four advances of T8 - T10, when the overcut was being formed. During T8 a load cell connection issue resulted in the data between x = 130 mm and x = 380 mm being lost. F_a during T9 and T10 was higher

than T8 due to the larger σ_N acting on the overcut formers increasing the friction. As the test parameters of T9 and T10 were identical, the similarity of the measured F_a for both tests demonstrates that the overcut formation process was highly consistent. Once the overcut had been formed ($x > 900$ mm), subsequent advances required only small actuation forces, with F_a measurements of near zero. These results demonstrate that the presence of the overcut reduced the interface friction to near-zero, regardless of the normal stress at the SLS, and was therefore significantly more effective than Bentonite injection without the presence of an overcut.

F_a during T8 - T10 was also more consistent throughout the tests when compared to the tests without an overcut. Figure 7.23 shows the variation in F_a for the tests without overcuts, whilst Figure 7.24 shows F_a measurements from T8 - T10 (with overcuts). From the figures, it is clear that the formation of the overcut at the start of shearing resulted in lower interface frictions, and hence actuation forces, throughout the tests.

These results demonstrate that the overcut formation process creates a more consistent boundary layer of Bentonite at the SLS interface, which remained present throughout the test. The effectiveness of the overcut was seen visually, as shown in Figure 7.25, as the TPs exiting the test chamber had little to no sand on the interface, unlike those of the no overcut tests shown in Figure 7.18. This also explains the variability in F_a observed in Figure 7.23, but not Figure 7.24, as the thinner layer of lubricant formed during T3 - T7 allowed concrete - sand contact during shearing and resulted in increased interface friction.

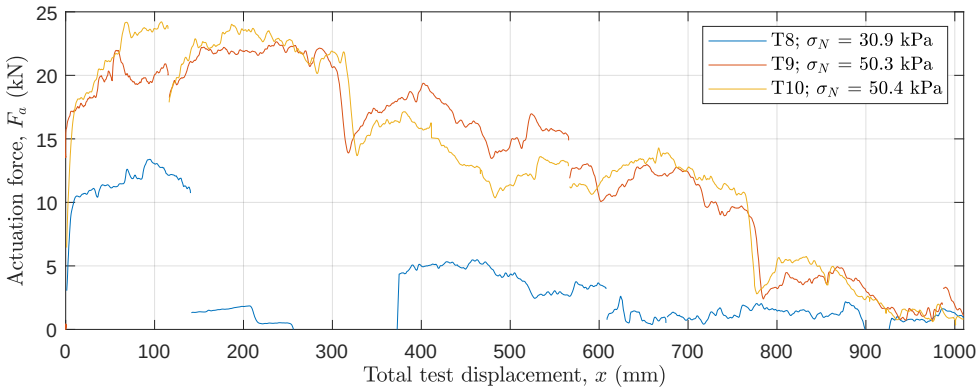


Figure 7.22: The development of total actuation force (F_a) with total test displacement (x) for tests with overcuts (T8, T9, T10) at different normal stress (σ_N).

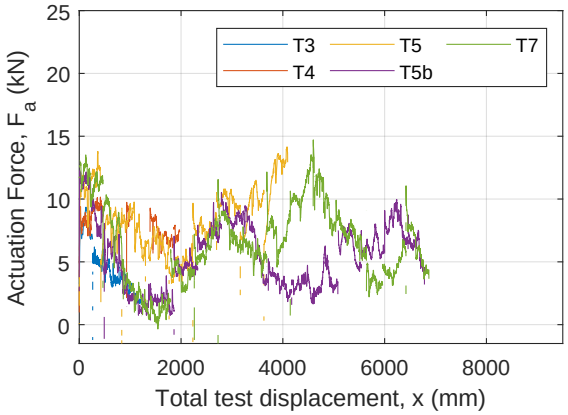


Figure 7.23: Actuation force (F_a) variation during the total test displacement (x) of the lubricated, no overcut, tests.

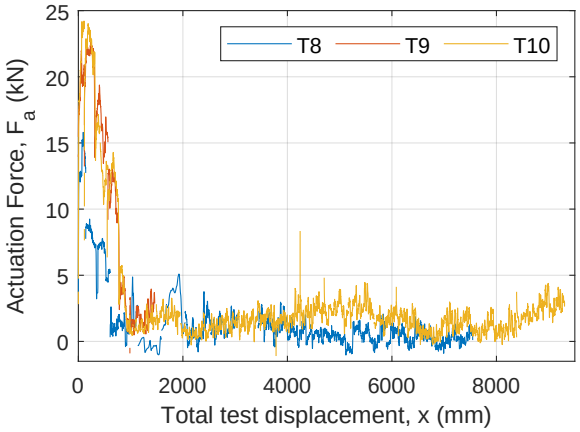


Figure 7.24: Actuation force (F_a) variation during the total test displacement (x) of the lubricated tests with an overcut present.

7.8 Influence of stoppages

7.8.1 Stoppage testing objectives

One of the main objectives of the laboratory testing program was to gain insight into the changes that occur at the SLS interface during stoppages. Field monitoring, discussed in Chapter 4, has shown that stoppages can be divided into two broad categories: routine short stoppages of $t_s < 14$ hours (caused by overnight breaks and pipe changeovers), and long stoppages of $t_s > 14$ hours (caused by weekends, public holidays, or equipment failure). Thus, stoppages of between 30 minutes and 62 hours were considered in the experiments. The tests also examined the influence of the overcut on the SLS behaviour during and after the stoppages

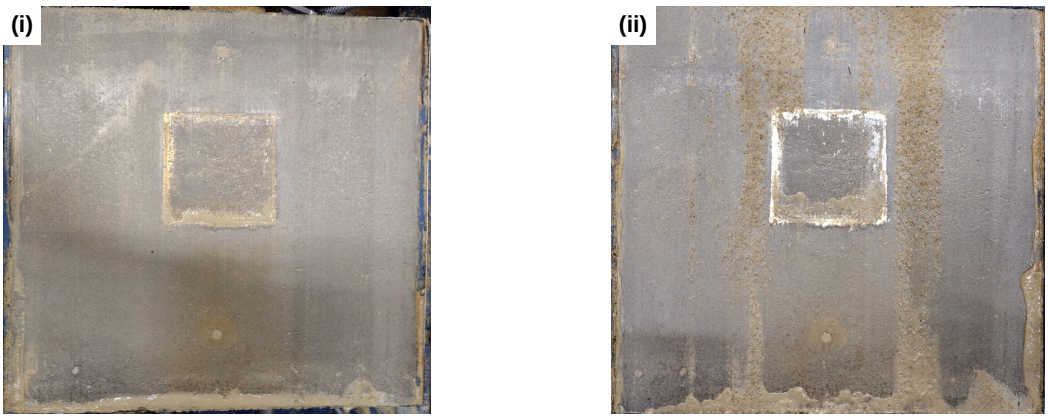


Figure 7.25: TP interface after the leaving the chamber after: (i) T8 stage 12, (ii) T10 stage 10.

to understand the benefits of overcut creation around tunnel pipes in the field.

Tests T5, T5b, T8, and T10 contained 12 hour stoppages, which were intended to replicate typical overnight stoppages observed on tunnel drives being conducted by a single (day) shift. Tests T7, T8, and T10 then also contained 60 hour stoppages, which replicated a weekend stoppage (from Friday afternoon to Monday morning). Although it was anticipated the behaviour in the first 12 hours of the 60 hour stoppage would be identical to the 12 hour, the shorter stoppage durations were required to assess the post-stoppage behaviour of the interface.

7.8.2 Intra-stoppage visual observations

A camera and timer were used to photograph the SLS interface at regular intervals during shearing and stoppages in T7 - T10. These images were used to identify visible changes which occurred during the tests and complement the measurements from the TPs. During T7 no visible changes of the interface condition were apparent after the initial injection of lubricant. This was by design, as the test objective was to monitor the conditions at the SLS interface where an overcut was not present, rather than form an overcut within the apparatus by excessive lubricant injection.

Figure 7.26 shows the SLS interface conditions during the stoppages in T8. Two key phenomena are apparent during each stoppage: firstly, the width of the overcut reduces significantly as the Bentonite lubricant filters into the sand above, and secondly the depth of the partially saturated sand region above the Bentonite penetration zone increases throughout the test,

irrespective of whether shear or lubricant injection was occurring.

Table 7.6 summarises the changes in the overcut, lubricant penetration, and partially saturated zone thicknesses observed during the T8 stoppages. The data show that the depth of the Bentonite penetration into the sand remained constant during the test after the initial 'spurt' phase was complete. During each stoppage, the overcut width decreased as water filtered out of the Bentonite into the sand. The magnitude of the decrease lessened throughout the test (from 25% in 12 h during the first stoppage to 25% in 60 h during the final stoppage) despite a similar starting overcut thickness. The thickness of the partially saturated sand region above the Bentonite increased throughout the test, but at a decreasing rate. For example, in the first 60 h stoppage it increased by 19 mm, whereas in the second 60 h stoppage it increased by 15 mm. These data suggest that during the second stoppage the SLS interface had a lower permittivity and hence less water filtered out of the overcut into the sand. This aligns with the findings of the permeameter experiments, where the permittivity of the interface (in the absence of shearing) was found to decrease linearly with log-time.

Table 7.6: Changes in Bentonite penetration depth (a), overcut width (b), and partially saturated sand region depth (c) during the T8 12 h and 60 h stoppages.

Stoppage	**Time stopped (t_s)**		**a**	**b**	**c**	**ΔA**	**ΔB**	**ΔC**
(-)	**($s^{1/2}$)**	**(h)**	**(mm)**	**(mm)**	**(mm)**	**(%)**	**(%)**	**(%)**
12 h	0	0	58	5	12	-	-	-
12 h	208	12	58	9	9	0	80	-25
60 h (1)	0	0	58	14	11	-	-	-
60 h (1)	190	10	58	22	10	0.7	58	-14
60 h (1)	465	60	58	33	6	0.7	137	-45
60 h (2)	0	0	58	35	12	-	-	-
60 h (2)	190	10	59	42	11	1.7	20	-8.3
60 h (2)	465	60	58	50	9	0	43	-25

Figure 7.27 shows the interface before and after the stoppages during T10, at similar times to Figure 7.26. For the higher interface normal stress (σ_N = 50.4 kPa), the overcut thickness was more variable than during T8 and the lubricant penetration was larger (100 mm compared to 58 mm). The 72% increase in penetration distance aligns with Equation 5.6, which states

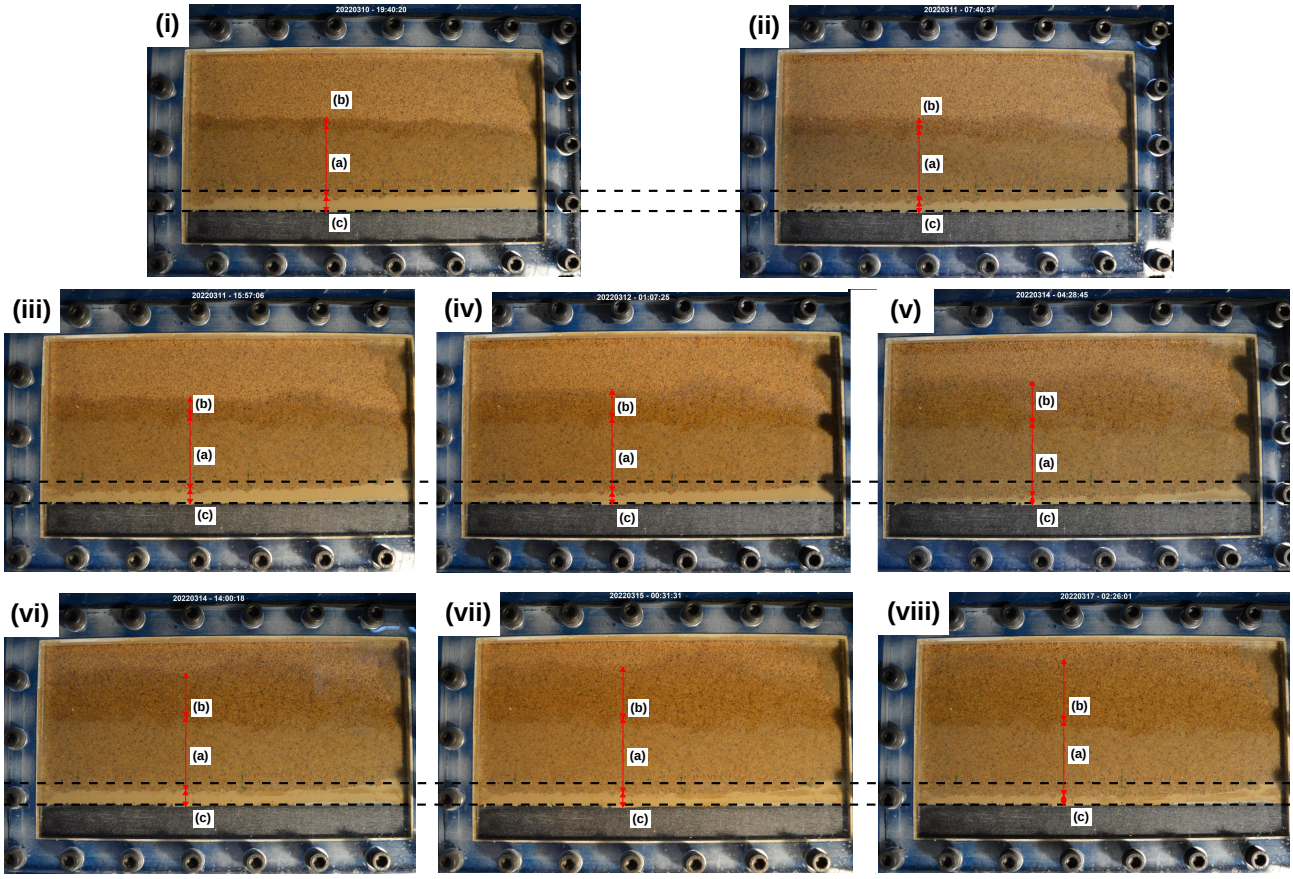


Figure 7.26: Photographs showing the overcut during stoppages in T8 at different elapsed times (t_s): (i) 12 h; $t_s = 0$ $s^{1/2}$, (ii) 12 h; $t_s = 208$ $s^{1/2}$, (iii) 60 h (1); $t_s = 0$ $s^{1/2}$, (iv) 60 h (1); $t_s = 190$ $s^{1/2}$, (v) 60 h (1); $t_s = 465$ $s^{1/2}$, (vi) 60 h (2); $t_s = 0$ $s^{1/2}$, (vii) 60 h (2); $t_s = 190$ $s^{1/2}$, (viii) 60 h (2); $t_s = 465$ $s^{1/2}$. Key features are labelled: (a) lubricant penetration zone, (b) partially saturated zone, (c) overcut.

that penetration is proportional to the pressure at the interface, which in this instance increased by 68%. The depth of penetration did not change significantly after the start of the test, which again aligns with the findings of the permeameter experiments, as these showed that once the filter cake formed no further lubricant penetration into the sample occurred.

Table 7.7 presents a summary of the measurements from Figure 7.27. The thickness of the partially saturated zone (B) was smaller during T10 when compared to T8, which shows that less water was filtering through the filter cake into the sand sample. This again confirms the permeameter test results which found the permittivity of the filter cake (after the spurt phase) decreased during higher pressure tests. During the 62 h stoppage it was not possible to measure the change in thickness of this zone as it permeated past the top of the window.

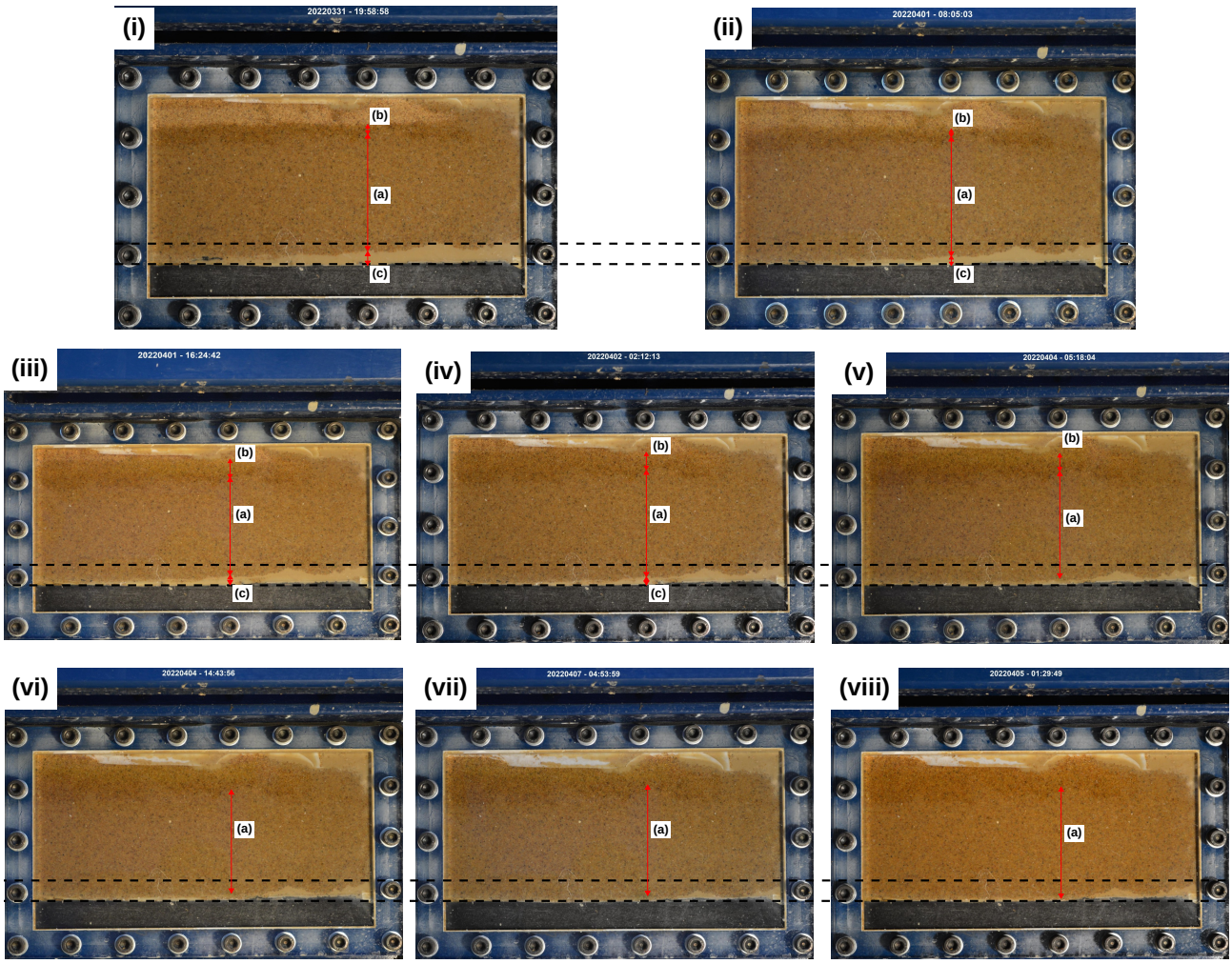


Figure 7.27: Photographs showing the overcut during a T10 at: (i) 12 h; $t_s = 0$ $s^{1/2}$, (ii) 12 h; $t_s = 208$ $s^{1/2}$, (iii) 60.5 h; $t_s = 0$ $s^{1/2}$, (iv) 60.5 h; $t_s = 190$ $s^{1/2}$, (v) 60.5 h; $t_s = 467$ $s^{1/2}$, (vi) 62 h; $t_s = 0$ $s^{1/2}$, (vii) 62 h; $t_s = 190$ $s^{1/2}$, (viii) 62 h; $t_s = 472$ $s^{1/2}$. Key features are labelled: (a) lubricant penetration zone, (b) partially saturated zone, (c) overcut.

Table 7.7: Changes in Bentonite penetration (a), overcut width (b), and partially saturated sand region (c) during the 12, 60.5, and 62 hour stoppages in T10.

Stoppage (-)	**Time stopped** (t_s) ($s^{1/2}$)	(**h**)	**A** (mm)	**B** (mm)	**C** (mm)	**ΔA** (%)	**ΔB** (%)	**ΔC** (%)
12 hour	0	0	98	8	11	-	-	-
12 hour	208	12	100	7	8	2	-13	-27
60.5 hour	190	10	99	16	7	0	-16	-30
60.5 hour	467	60.5	100	15	5	1	-21	-50
62 hour	0	0	97	[1]	6	-	[1]	-
62 hour	190	10	103	[1]	4	6.2	[1]	-33
62 hour	472	62	103	[1]	1	6.2	[1]	-83

[1] Saturated zone penetrated full height of window.

7.8.3 Intra-stoppage stress measurements

The contact stress sensors in the TPs recorded the changes in σ_N during each stoppage. Due to the influence of the preceding L_i stages, σ_N at the onset of the stoppages varied. To remove the dependency on starting pressure from the measurements, a non-dimensional pressure was defined for each stoppage as the ratio of measured σ_N to the applied normal stress ($P_a + \gamma.H$) at the onset of the stoppage. Table 7.8 shows the calculated values for the stoppages during T5, T7, T8, and T10.

Table 7.8: Applied and measured total normal stresses at the onset of each 12 h and 60 h stoppage. Where two stoppages of the same duration occurred, these are labelled (1) and (2).

Test	**Stoppage**	**Test piece**	**Normal stress**		
			Applied	**Measured**	**Non-dimensional**
(-)	(-)	(-)	$P_a + \gamma.H$ (kPa)	σ_N (kPa)	$\frac{\sigma_N}{P_a+\gamma.H}$ (-)
T5	12 hour	TP4	30.6	37.5	1.23
T7	60 hour	TP4	30.3	24.7	0.82
T8	12 hour	TP2	30.9	17.5	0.57
T8	60 hour (1)	TP1	30.9	65.1	2.11
T8	60 hour (2)	TP1	30.9	102.2	3.31
T10	12 hour	TP2	50.4	40.7	0.81
T10	60.5 hour	TP1	50.4	73.1	1.45
T10	62 hour	TP1	50.4	62	1.23

Figure 7.28 presents the changes in the non-dimensional normal stress measured during the stoppages in T5 - T10. Data from the 60 h stoppage in T7 and T8 (2) (i.e. the second 60 h stoppage) are incomplete due to data loss in the data logging program during these stoppages. The data all show a rapid decline at the onset of the stoppage as the lubricant filters through the filter cake at the SLS boundary. During this period, the width of the overcut reduced, as shown by Figure 7.26, which resulted in the sand sample settling in the chamber, as was confirmed by the pressure bag intermittently filling during these periods. The settlement of the sample resulted in arching within the chamber due to the wall friction and the measured σ_N decreasing below the applied stress.

This phenomenon explains the pressure response of the stoppages. During the first 60 h

stoppage of T8 (i.e. T8; $t_s = 60$ (1)) the settlement process of the sand was completed and, as a result, σ_N increased at the end of the test after 190 $s^{1/2}$ in T8 as the arching effects diminished. During the second stoppage, the lower permittivity filter cake slowed the filtration process, which resulted in the settlement process not completing during the test period and σ_N remaining less than the applied stress throughout due to the wall friction.

A difference in response between T8 and T10 was also apparent. During T10 the point of inflection in σ_N during the first 60 h stoppage was ∼300 $s^{1/2}$, whereas in T8 this occurred sooner (after ∼190 $s^{1/2}$). This demonstrates that the permittivity of the filter cake in T10 was lower than T8 as it reduced the rate of lubricant filtration out of the overcut. Similarly, during the second stoppage, σ_N continued to decrease throughout T10, whereas the point of inflection was ∼325 $s^{1/2}$ in T8, confirming the lower permittivity trend.

The 12 h stoppages show a similar response in all tests, where σ_N decreased rapidly before plateauing. During T5 (without an overcut), the decrease was slower than T8 or T10, but tended to a lower residual stress. Small peaks are apparent in the data, which were caused by the settlement of the sand-Bentonite mixture above the interface directly loading the sensor. Similar peaks with a smaller magnitude were also visible in the T7 data, which suggests that the sand sample was directly in contact with the load cell and no external filter cake had formed during the test. The decrease in T8 and T10 was initially faster, but tended towards a higher constant value, without visible peaks in the data - suggesting the SLS interface was maintaining a higher residual pressure during these tests.

7.8.4 Effect on post stoppage global friction

The change in global friction caused by the stoppages was assessed using the change in F_a measured during each test. As the actuation force in the apparatus varied during shearing, the pre-stoppage actuation force was taken as the mean of the last 50 mm before the stoppage as this corresponded to one lubrication cycle. Although the actuation force varied around this mean, averaging over one lubrication cycle was thought the most accurate way to establish a

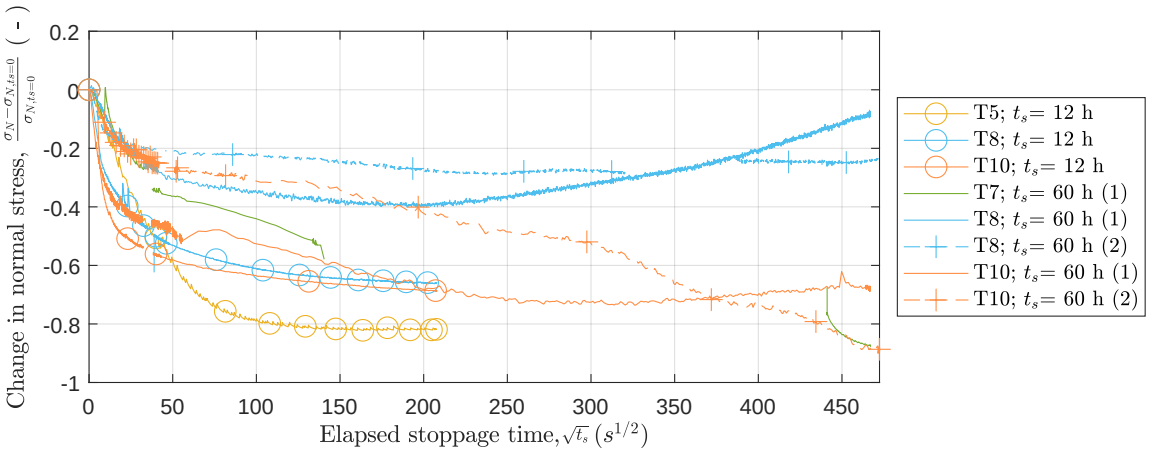


Figure 7.28: The change in total normal stress ($\frac{\sigma_N - \sigma_{N,ts=0}}{\sigma_{N,ts=0}}$) during 12 h and 60 h stoppages during tests both without an overcut (T5 and T7) and with an overcut (T8 and T10). Where two 60 h stoppages occurred the stoppage number is shown in brackets.

short-term representative value.

The response of the tests after the first 12 h stoppages are shown in Figure 7.29 and the changes in F_a are recorded in Table 7.9. T3 (with only a single lubricant injection) and T10 measured a small peak F_a after the stoppage, with T5 and T5b recording larger peak stresses of up to 5.8 kN, or 12 kPa. In test T8, F_a remained similar afters the stoppage, demonstrating (in this instance) that the conditions in the overcut during the stoppage had not significantly changed. The post-peak behaviour also varied between the tests. The average change in F_a (excluding the peak) ΔF_a was between 2 kN and 4.8 kN higher than the pre-stoppage level in T5 and T5b, whilst T3, T8, and T10 recorded little change.

The second advance after the stoppage was also unlubricated, which provided insight into the behaviour of the interface at a larger strain, and after a 1 h changeover. Both T5 and T5b again showed peak behaviour at the start of the advance (in the region 450 mm $\leq x$ - $x_s \leq$ 470 mm; where x_s is the distance at which the stoppage occurred), with increases in F_a of between 2 kN and 3.4 kN (4 kPa and 6.8 kPa) after the stoppage. The residual F_a also increased, showing that effectiveness of the Bentonite to lubricate the interface continued to decrease. In contrast to these results, F_a during the 1 h changeover decreased in both T8 and T10 by 0.34 kN and 0.70 kN respectively, suggesting the additional shearing had improved the effectiveness of the

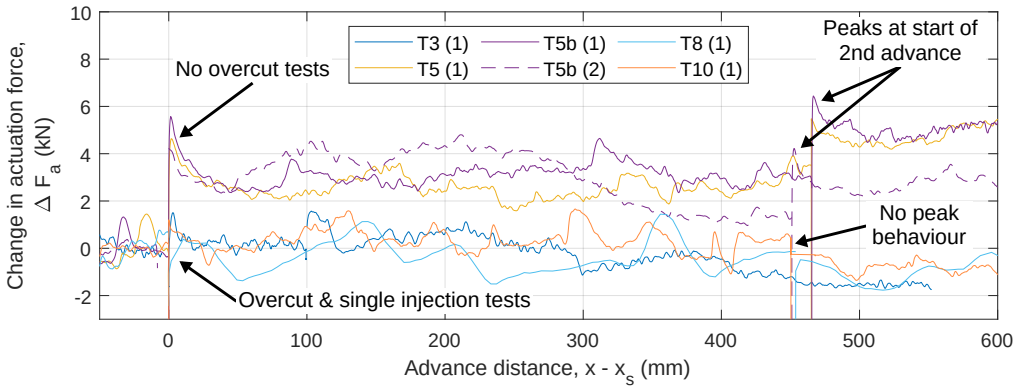


Figure 7.29: The change in action force (ΔF_a) measured in the first 600 mm advanced after the 12 hour stoppages (x - x_s; where x_s is the distance at which the stoppage occurred) after the single lubricant injection in T3, during the no-overcut tests T5 and T5b, and during the overcut tests T8 and T10. The stoppage number is shown in brackets.

boundary layer.

During the first $\sim$ 60 hour stoppages, the results between the overcut (T8, T9, T10) and no-overcut (T3 - T7) tests varied similarly to the 12 hour case. Figure 7.30 presents ΔF_a measurements after the 60 h stoppages in T7, T8 and T10. T7 measured ΔF_a = 7 kN (14 kPa) and a residual increase of 4.8 kPa. In contrast, the maximum peaks measured in T8 and T10 were 1.7 kPa and 5 kPa, respectively. However in both T8 and T10 there was no residual increase in friction.

The effects of multiple stoppages, and post-stoppage lubrication, were assessed during T7, T8 and T10 using the F_a measurements. During these tests, Bentonite was re-injected into the SLS interface after the first 60 h stoppage for four to six L_i stages before a second 60 h stoppage was completed. This sequence was intended to mimic field conditions, where the SLS interface is only directly re-lubricated periodically between stoppages.

The influence of Bentonite injection after stoppages without an overcut is shown by the trend in the T7 data observed in Figure 7.23. In the figure, the decrease in F_a observed between x = 4200 mm and x = 6000 mm correlates to the four L_i stages between the stoppages. F_a decreased linearly with the x during the subsequent advances, demonstrating that the additional lubrication was reducing τ at the SLS interface. The influence of the additional lubrication

Table 7.9: Changes in the peak and residual actuation force (F_a) and the advance distance these occurred at (x - x_s) after 12 h and $\sim$ 60 h stoppages during T3 - T10.

Test	**Stoppage**	**ADV**	**Peak F_a**			**Residual F_a**		
			ΔF_a		x - x_s	ΔF_a		x - x_s
(-)	**(h)**	**(-)**	**(kN)**	**(kPa)**	**(mm)**	**(kN)**	**(kPa)**	**(mm)**
T3	12	1	1.5	3	3	0	0	20
T5	12	1	4.6	9.2	2	2.1	4.2	60
T5	12	2	5.5	11	-	4.2	8.4	35
T5b	12 (1)	1	5.6	11.2	1.4	2.2	4.4	55
T5b	12 (1)	2	6.4	12.8	-	4.5	9	40
T5b	12 (2)	1	4.2	8.4	0.6	2.2	4.4	40
T5b	12 (2)	2	4.1	8.2	-	2.2	4.4	45
T7	60 (1)	1	7	14	1.4	2.4	4.8	25
T7	60 (1)	2	5.5	11	-	4.7	9.4	10
T7	60 (2)	1	4.9	9.8	1.5	1.7	3.4	50
T8	12	1	-0.5	-1	1.7	-	-	-
T8	60 (1)	1	-0.8	-1.6	1.6	-	-	-
T8	60 (1)	2	-0.5	-1	-	-1	-2	10
T8	60 (2)	1	0.9	1.8	0.9	-0.5	-1	45
T8	60 (2)	2	0.3	0.6	-	-0.2	-0.4	5
T10	12	1	1.2	2.4	1	-	-	-
T10	60.5	1	2.5	5	0	-1	-2	50
T10	60.5	2	0.6	1.2	-	0.2	0.4	5
T10	62	1	2.6	5.2	0	0	0	45
T10	62	2	2.4	4.8	-	1.1	2.2	25

during the overcut tests, shown in Figure 7.24, is less apparent due to the effectiveness of the formed overcut at reducing the friction at the interface both before and after the stoppages.

Table 7.9 also shows that the change in F_a for both the first and second stoppages varied as the tests varied. The first T7 stoppage had a much higher $\Delta F_{a,peak}$ than the second: 7.02 kN (14.0 kPa) compared to 4.88 kN (9.76 kPa). The change in friction between 0 mm and 100 mm advanced was also $\sim$ 1.2 kN less on the second stoppage when compared to the pre-stoppage level. This means that the additional lubrication after the first stoppage was effective at reducing τ at the interface and the lower permittivity of the sand-Bentonite mixture at the interface reduced the filtration rate of the lubricant from the interface, such that the Bentonite at the interface after the stoppage had a higher WC and hence a lower τ increase.

The T8 data show a small reduction in F_a of 758 N after the first stoppage but a peak of 861

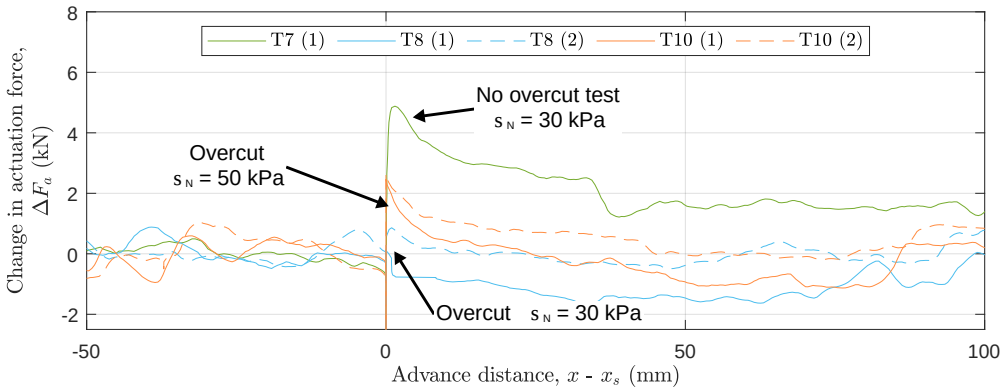


Figure 7.30: The change in action force (ΔF_a) measured measured in the first 100 mm advanced after the 60 h stoppages (x - x_s; where x_s is the distance at which the stoppage occurred) in the no-overcut test T7, and overcut tests T8 and T10. The stoppage number is shown in brackets.

N after the second. This demonstrates that the additional lubrication between the stoppages was insufficient to restore the SLS to the conditions prior to the first stoppage in this case, despite the overcut returning to a similar thickness. The average actuation force in the 100 mm after the stoppage is also larger following the second stoppage, which suggests contact between the TPs and the external filter cake (which had a lower WC and hence greater τ_0) than the injected lubricant.

These results demonstrate the influence of the overcut on the stoppage response of the SLS interface. The increased thickness of Bentonite lubricant resulted in filtration not being fully complete during the 12 h and 60 h stoppages at lower σ_N, which resulted in the concrete TPs shearing against a 'wet' Bentonite with lower friction upon restart. When filtration did complete, the external filter cake formed at the interface resulted in lower interface frictions than shearing against the sand - Bentonite mixture in the no-overcut tests. Finally, the overcut resulted in frictions reducing back to pre-stoppage levels after < 50 mm advanced in all cases. This demonstrates that once shearing was occurring at the interface the Bentonite adjacent to the concrete TP was in a similar state to before the stoppage.

7.8.5 Effect on post stoppage local friction

Changes in the response of the local contact stress sensors also varied between stoppages. Figure 7.31 shows example measurements from the contact stress sensors within the chamber

for the T3 (no overcut; single lubricated advance), T5 (no overcut; full lubrication), and T10 (overcut; full lubrication) after the 12 h stoppage, which show the three different behaviours at the interface. The T3 data shows a small peak in τ after the stoppage which degrades quickly, whereas the response in T5 demonstrates the peak behaviour recorded by the global measurements but at only 26% of the global peak increase magnitude. This peak also decreases back to the pre-stoppage friction level, similar to the global response of T8 and T10, after the stoppages. This confirms that the state of the SLS interface was variable across the chamber width during T5 as a result of the uneven lubricant distribution during the injections stages prior the stoppage. The uneven distribution of lubricant resulted in a thicker layer of Bentonite along the centre of the TPs before the stoppage, which behaved more similarly to the overcut tests. In contrast to this, the friction after the stoppage in T10 reduced slightly during the stoppage, demonstrating that the Bentonite lubricant was still fully effective in this region during the test.

Figure 7.32 shows the response from the local stress sensors after the 60 h stoppage. During T8, the interface sensor in TP1 was damaged, such that significant cross correlation occurred between the normal and shear stress measurements. This resulted in the large negative magnitude of $\Delta\tau$ recorded but was not thought to reduce the sensor's sensitivity significantly. Regardless of this offset, no peak behaviour is observed after the stoppage in either measurement.

During the stoppage in T10, two sensors were within the test chamber (TP1 and TP4) which showed good similar measurements. The sensors measured an increase in the residual τ of $\sim$ 2 kPa. The global (F_a based) measurement, did not record this increase in τ, suggesting that the lubrication effectiveness had decreased in the central section of the test chamber, but improved away from the centreline during the stoppage, offsetting the change.

The T7 behaviour varied within the chamber, as measured by TP1 and TP4 which were both within the chamber during the stoppage. The peak τ measured by TP4 was only 0.91

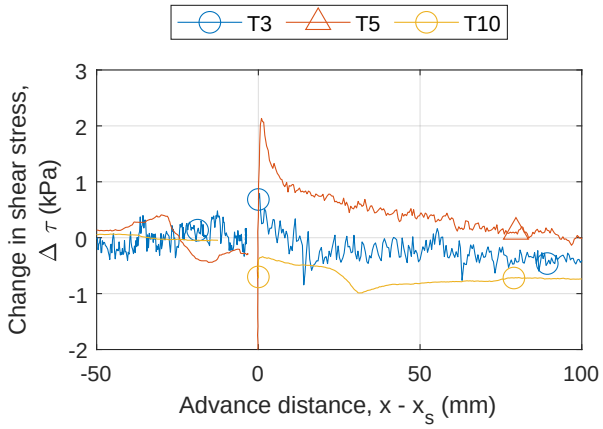


Figure 7.31: Variation in local shear stress measurements (τ) in the first 100 mm advanced after a 12 hour stoppage during T3, T5, T10.

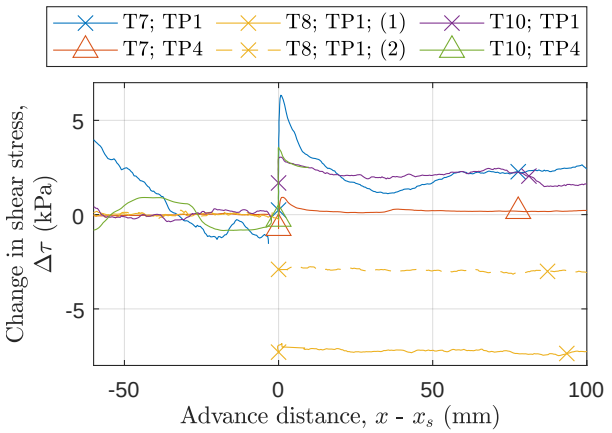


Figure 7.32: Variation in local shear stress measurements (τ) in the first 100 mm advanced after the 60 hour stoppages during T7, T8, T10.

kPa, whilst TP1 measured 6.3 kPa. The lower friction increase measured by TP4 demonstrates that there was unfiltered 'wet' Bentonite present towards the exit seal of the chamber, whilst the higher shear stress on TP1 (nearer the entry seal) was caused by contact with lower WC filtered Bentonite. This demonstrates that without a overcut the conditions at the SLS interface during a stoppage are influenced by the location of the preceding L_i stage, as before the stoppage these occurred close to the exit seal.

7.9 Post-test observations

7.9.1 Vertical Bentonite penetration

After the tests were completed, the chamber was disassembled, and the pressure bag was removed. Excavation was undertaken with a scoop until near to the zone of partially saturated soil, where vacuum excavation was used to carefully extract the remaining dry sand. This method allowed an accurate Bentonite/water penetration profile to be measured from the sample by excavating sand to approximately the same WC each time.

Figure 7.33 presents the data from: (i) T3, (ii) T7, (iii) T8, and (iv) T10, which show the key differences in profiles observed between the tests. The variable Bentonite penetration after the single lubricated advance is evident by the penetration depth (X) profile across the

chamber in 7.33(i) compared to the more uniform results in 7.33(ii) - 7.33(iv). This validated the differences observed between the local and global stress measurements, as the greater Bentonite penetration in the centre of the chamber demonstrates a preference for lubrication in line with the lubricant delivery port. Additionally, Bentonite was found not to have travelled backwards along the interface (towards $x_{ch} = 0$ mm) from the point of initial injection. Instead, the spread was lateral and lagged behind the injection port as shown by the smaller depth of penetration at $x_{ch} \approx 1000$ mm and $y_{ch} = 500$ mm compared to $y_{ch} = 250$ mm.

Tests T7 and T8 were conducted at similar normal interface stress ($\sigma_N = 30$ kPa) and show a similar penetration distance of 96 mm and 112 mm, after accounting for the 18 mm overcut. T10 resulted in a depth of Bentonite penetration of 150 mm, a 33% increase on T8, which was less than the 66% predicted by the increase in σ_N in Equation 5.6, and observed initially at the window during injection. This was due to the partially saturated sand zone in the chamber being thinner in T10 than T7 and T8 due to the lower permittivity filter cake formed at the SLS interface reducing the volume of water filtered from the Bentonite.

Overall, these surveys provided evidence that the lubricant penetration was slightly greater in the centre of the test chamber (i.e. closer to $y_{ch} = 250$ mm) than at the edges. The presence of the overcut during T8 and T10 reduced this effect, as the surveys were more uniform across the chamber width, further reinforcing the observations made at the chamber windows during testing, and explaining the different response of the local and global sensors. These findings are important for field tunnel drives, as they demonstrate the difficulties in generating the highly effective boundary layer and effective stress reduction around the full tunnel circumference without the presence of an overcut. They also explain the differences observed in previous experimental studies, such as those at small scale which did not detect these effects (i.e. Reilly and Orr (2017)) and large scale shear box type experiments (e.g. Namli and Guler (2017)) which uniformly distributed the lubricant but did not reduce the effective stress at the interface.

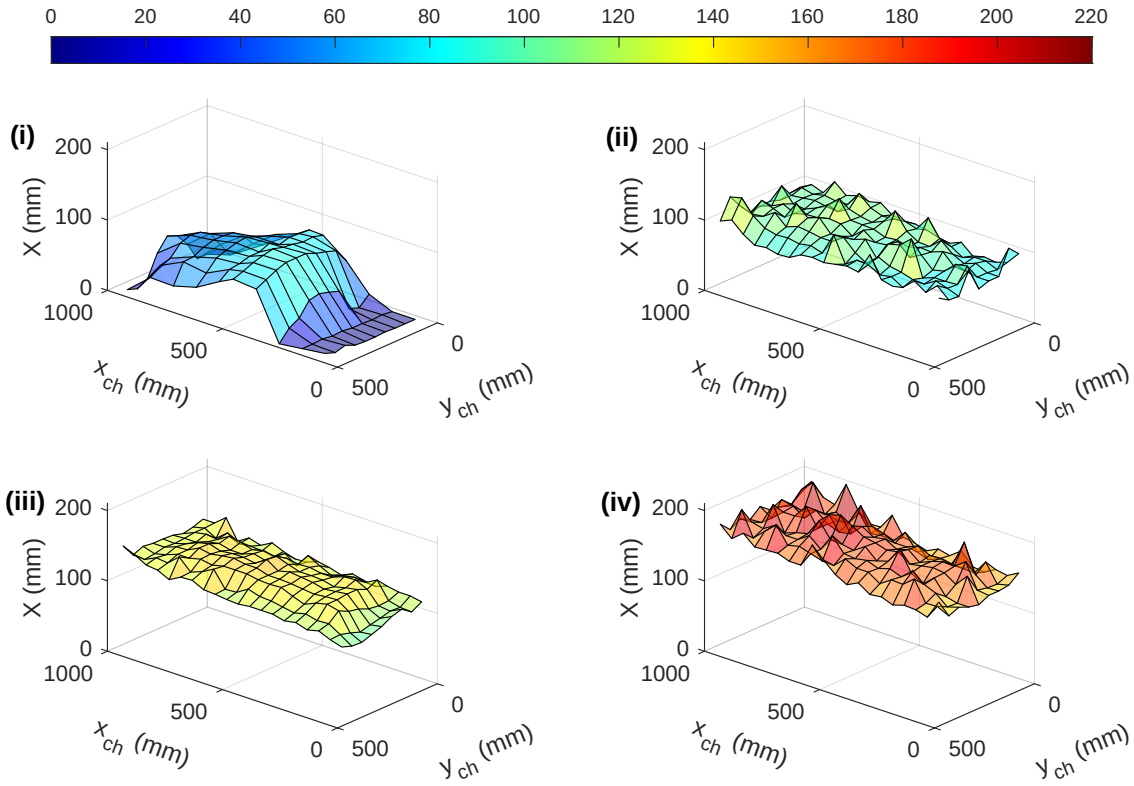


Figure 7.33: Post-test Bentonite penetration (X) after vacuum excavation from: (i) T3, (ii) T7, (iii) T8, (iv), T10.

7.9.2 Infiltration zone water content

Once the survey of Bentonite penetration survey was complete, the Bentonite-containing sand was then carefully excavated to measure any overcut thickness present and qualitatively assess the interface conditions. During the excavation process, samples were taken from the middle of the partially saturated region (measured using visible depth at the chamber window) and from three levels within the internal filter cake, as identified in Figure 7.34. These samples were then dried and weighed to ascertain their WC. The results of this analysis are shown in Figure 7.35 for T4, T5, T7, T8, and T10. After T4 and T5, no saturated-mid or cake-mid samples were taken due to the small thickness of the layers in those tests.

The results demonstrate the differences in WC at the lubricant-soil interface created by the presence of the overcut. WC measurements from samples taken after T8 and T10 were 420% and 365% larger than T7, as the filtration process did not complete in the overcut tests. The WC of the T10 sample was then 13% lower than T8, due to the higher normal stress at the

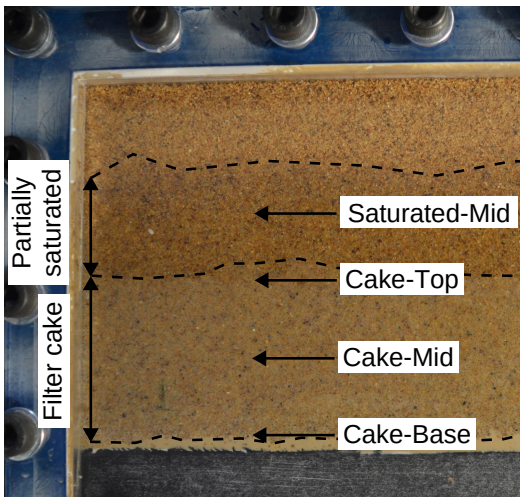


Figure 7.34: A photograph showing the locations of WC sampling points after the tests were conducted.

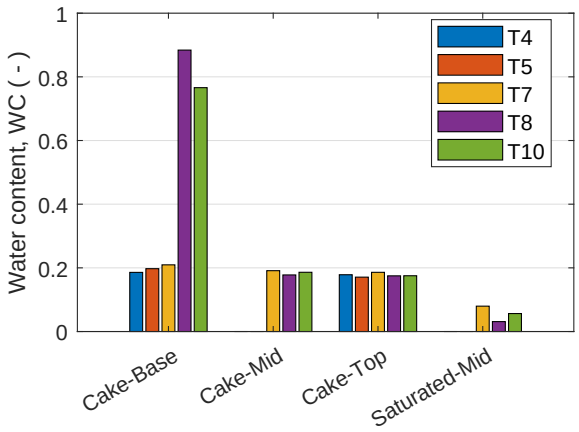


Figure 7.35: Post test water contents (WC) from T4, T5, T7, T8, and T10.

SLS interface resulting in a more consolidated filter cake. Within the filter cake, T7 had a 3% - 5% higher WC than the overcut test samples, which would have resulted in a higher permittivity filter cake as WC and permittivity have been shown to be related in the permeameter testing. The increased filtration of Bentonite from the interface also resulted in higher WC in the partially saturated sand layer above the interface after T7 as more water filtered from the lubricant. Similarly, the higher σ_N at the interface during T10 resulted in a greater rate of filtration when compared to T8, causing higher WC in the saturated region sample, despite the lower WC and hence permittivity of the interface.

7.9.3 Interface condition

Photographs were taken of the last TP to exit the chamber during each test and of the condition of the interface as the sample was removed. Figure 7.36 presents images of the interface in-situ conditions within the test chamber after the no-overcut test T7 and overcut tests T8 and T10. Similarly, 7.37 presents images of the TP and sand/lubricant side of the interface after removal from the chamber.

After T7, no separation of the sample and TP was apparent, as shown in both 7.36(i) and 7.37(i). In contrast, the interface after T8 (shown in 7.37(ii)) had an external filter cake present, with showed visibly 'wet' Bentonite at the concrete/lubricant side of the SLS interface

(7.36(v)). The visible cake was approximately 8 mm thick and was found to have a water content of 0.91, similar to the cake at the sand-lubricant side of the interface. The results from T10 also show a thinner external filter cake (7.36(iii)) although the TP side of the interface still contained 'wet' Bentonite with a ($WC = 0.92$) which the TPs were shearing against at the end of the test (7.37(iii)).

Photographs of the TPs as they exited the chamber also showed the differences in the SLS interface conditions after the stoppage. The T7 interface had significant sand adhered to the TP surface (which was similar to the conditions shown in Figure 7.25 during the test), whilst the T8 and T10 TPs had only Bentonite on their surface (7.37(ii) and 7.37(iii)). Additionally, differences were visible between the central section of the TP in T7, as had been the case throughout testing. Samples from the T8 and T10 Bentonite showed that it had WC of 0.91 after T8 and 0.82 during T10, similar to the WC of the Bentonite at the sand side of the interface.

7.10 SLS interface testing summary

This chapter has presented the results from eight tests using the bespoke SLS interface apparatus to examine the influence of lubrication, stoppages, and overcut inclusion on the characteristics of the SLS interface. Frictional and normal stress behaviour have been quantified using global and local stress measurements of the interface and relationships in the recorded data have been identified. The conclusions of this work are presented below:

1. Without an overcut, lubricant does not distribute evenly across the interface. When

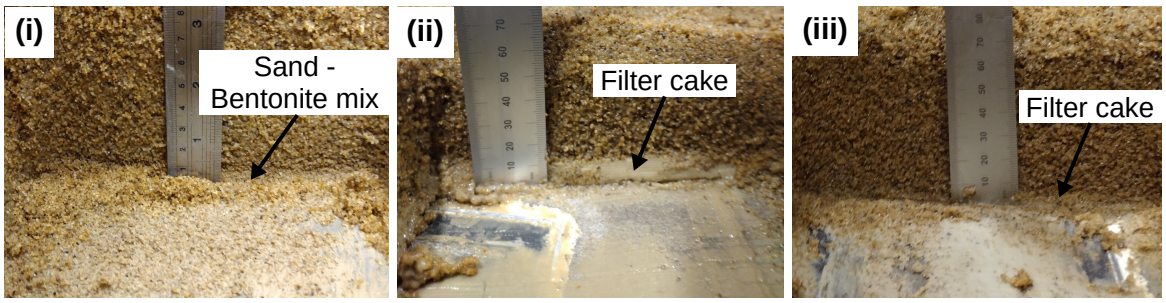


Figure 7.36: Photographs of the SLS interface condition in-situ within the chamber after testing was complete following: (i) T7, (ii) T8 and (iii) T10.

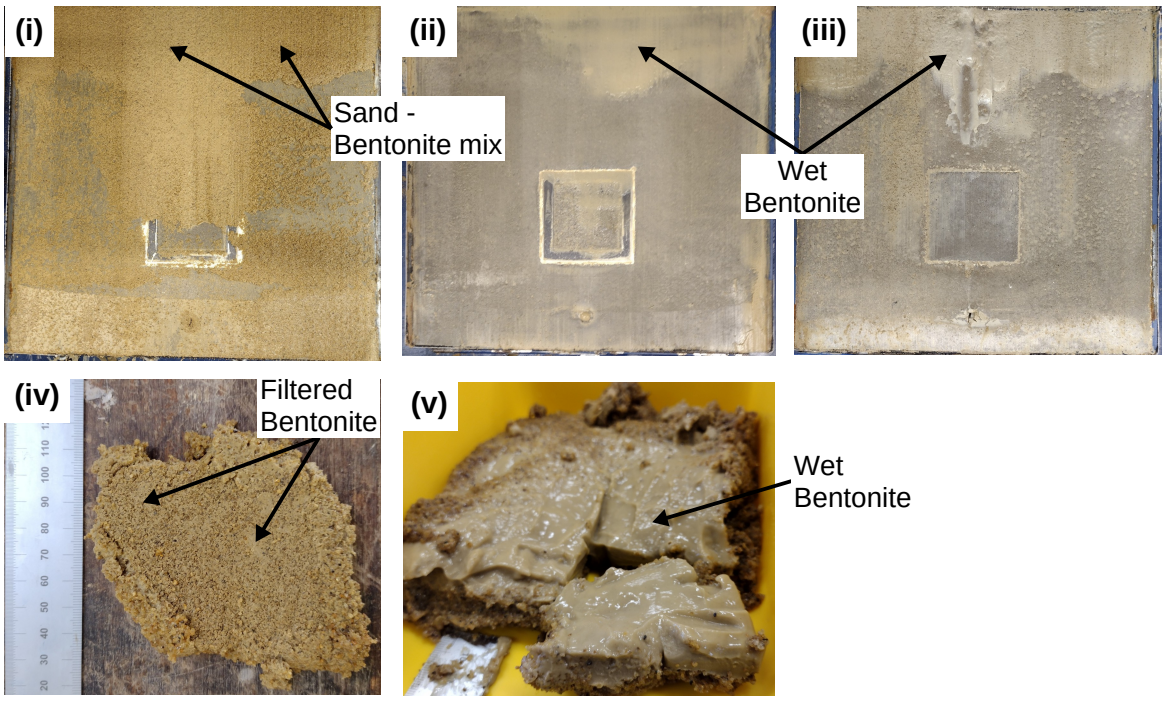


Figure 7.37: Photographs of the SLS interface condition (when removed from the test chamber) after testing was complete: (i) T7 TP surface, (ii) T8 TP surface, (iii) T10 TP surface, (iv) T7 sand surface, and (v) T8 sand surface.

initially injected, the lubricant first penetrates into the sand around the lubricant port and lubricates a small area of the interface. Once the permittivity of the sand-Bentonite mixture decreases and pressure at the interface increases, the lubricant travels along the interface further and lubricates a larger area. When the lubricant is travelling laterally across the interface it is less effective at creating a boundary layer between the soil and structure, which results in very effective lubrication in-line with the lubrication port, but a lower overall effectiveness of lubrication across the whole interface. This has significant implications for field practice, where typically only three discrete lubricant ports are spaced around the pipe circumference, and explains the differences observed between previous small and large scale laboratory studies of interface friction.

2. The inclusion of an overcut, with immediate lubricant injection post-formation, yields an even distribution of lubricant across the SLS interface and the creation of a boundary layer between the soil and structure. Once formed, the lubricant boundary layer creates more consistent SLS interface conditions which result in consistently lower interface friction.

3. Tests containing overcuts enabled an external filter cake to form at the soil side of the SLS interface, as the cake was protected from abrasion by the newly injected lubricant beneath. Tests without an overcut did not form this additional filter cake, and had partial sand-concrete contact at the interface during shearing, especially after stoppages.
4. During stoppages, the overcut width decreases as water filters from the Bentonite at the interface, through the infiltration region into the sand sample. This results in a filter cake at the interface, which builds up on the external face of the sand. As the interface is singularly drained by the soil, the highest WC Bentonite remains at the structure side of the interface. This means that, upon shearing restarting, the interface friction is low if there is still only a small amount of high WC Bentonite present at the interface.
5. The filtration rate of water from the Bentonite lubricant at the SLS interface is dependent on the initial penetration of the Bentonite lubricant into the soil and resulting permittivity of the filter cake formed at the SLS interface. Tests without an overcut resulted in a higher WC in the infiltration region, and hence a higher permittivity filter cake, which lead to faster filtration of Bentonite at the interface. This means that SLS interfaces with a uniformly formed overcut will take more time to complete the filtration process when compared to those without, if the same volume of Bentonite is present at both.
6. The post-stoppage peak friction increase can be up to 14 kPa, which is similar to the shear strength of the consolidated lubricants tested using the shear box apparatus presented in Chapter 5. In these cases the Bentonite at the interface has filtered to form a cake in contact with the test piece, and/or contact is occurring between the TP and a sand/Bentonite mix.
7. Tests containing overcuts had significantly smaller peak frictions of < 5 kPa after 60 h stopped. Evidence of unfiltered (or 'wet') Bentonite was found at the TP side of the SLS interface. Even a small thickness of lubricant in the original condition was found to

reduce the friction significantly.

These findings will be used in Chapter 8, alongside the findings of Chapters 4 and 5, to inform the empirical model developed for predicting interface friction changes during stoppages. Further to this, the findings will be used to predict conditions at the SLS interface during pipe-jacking and develop strategies to reduce friction during tunnelling.

8 | Results discussion and soil-lubricant-structure interface friction model development

8.1 Introduction

The main objectives of this DPhil are to improve the understanding of the mechanics of the SLS interface around pipe-jacked tunnel drives in the field and, in turn, improve methods of predicting friction during tunnelling. In this chapter the results from field studies (Chapter 4), elemental laboratory investigations (Chapter 5), and scale SLS interface apparatus testing (Chapter 7) completed during this research are discussed and the data are used to inform a new conceptual model of the SLS interface, from which an empirical model to predict the SLS interface friction is derived. Additionally, methods for mitigating friction increases during tunnelling are proposed based on the research findings, to guide future industry practice.

8.2 Results discussion

The industry case histories and instrumented tunnel drives studied as part of this research have demonstrated that current industry practice is effective at reducing SLS interface friction during tunnelling through various ground types. Maximum interface frictions of 2 kPa were measured during construction of tunnels through gravelly soils, whilst steady state frictions of under 0.5 kPa were recorded in rock and soft clay conditions. These magnitudes are significantly less than those reported less than a decade ago, for example 8 kPa in similar ground conditions by Reilly (2014). This reduction is attributed to improved lubrication practice by tunnelling contractors, who now place greater emphasis on ensuring pipe-jacks are well lubricated during installation.

Because of these small steady state frictions, the uncontrolled increase in interface friction during stoppages is now more significant. Increases of up to 7 kPa have been measured during

this research, which represent a significant increase in the required thrust to advance the pipe-jack after a stoppage. Although monitoring has shown that these peaks may only be transient, the peak behaviour increases the risk of pipe or shaft damage and necessitates the inclusion of additional, costly, interjack stations within the tunnel.

The two instrumented pipe sections deployed during this research have shown that these friction forces are generated predominantly in the regions of the tunnel pipe in contact with the tunnel bore (e.g. the crown in buoyant pipes), both during tunnelling and after stoppages. This has shown that the friction increases measured during stoppages are driven primarily by the increase in friction where the tunnel pipe is in contact with the lubricant – soil interface, not between the pipe and lubricant itself. This has also been observed in the experimental testing, where the increases in friction after a stoppage were negligible if unfiltered lubricant remained present at the SLS interface but increased by up to 14 kPa where the interface was in contact with the soil.

Analysis of 12 additional industry case histories has demonstrated that the rate of friction increase during stoppages is dependent on the ground condition, despite best industry practice being following in all cases. Tunnel drives in gravel were found to have higher steady state friction but slower friction increases during stoppages when compared to those in stable bore conditions (i.e. rock or clay). The data for the drives in gravel were also more varied, with some stoppages resulting in significantly larger friction increases than others. In contrast, the data from tunnelling through clay were more uniform, with less variation about the mean trend. This finding is important for the design of tunnelling works, as it means that the predictions for tunnel drives through clay are likely to be more reliable, and hence a smaller degree of conservatism is required in design.

The results of the monitored tunnel drives also revealed shortcomings of current lubrication practice. During the Castlerigg tunnel drive (D1) overcut pressures in excess of 1 MPa were

recorded at the instrumented pipe location, whilst at Putney (D2) overcut pressures were more modest, with a maximum of under 150 kPa, both of which decreased linearly with log-time during stoppages. The pressures measured during D1 were far in excess of those required, considering the stable bore conditions in the mudstone being tunnelled through. Consolidation shear box testing has shown that the higher pressure will have generated a higher shear strength, lower water content, filter cake as shear strength of the cake was shown to increase by 0.15 kPa per 1 kPa of applied pressure. During the drive, this would have resulted in larger friction increases during stoppages as the pipe adhered to the filter cake, when compared to an overcut maintained at more modest pressure.

The SLS interface experiments demonstrated that lubrication of the SLS interface at injection pressures equal to the normal stress at the interface is effective. Providing that a boundary layer is formed (either through the generation of an overcut or through sufficient lubricant injection), the friction between the tunnel pipe and soil was reduced to near zero, such that they were not detectable amongst noise in the data caused by small friction variations. These magnitudes are smaller than those measured in the field (0.5 kPa to 2 kPa) and confirm that a sector of the tunnel is generating frictions in excess of these magnitudes, confirming the IP resultant force location measurements. The testing also demonstrated that the formation of the boundary layer was less effective for SLS interfaces without an overcut present, as these resulted in larger interface friction variations during shearing.

The presence of the overcut also ensured more even lubricant distribution across the width of the interface during testing. The shear stress measured by the test piece local stress sensors (in line with the lubricant ports) and the global shear stress (averaged over the whole interface) were similar during the overcut tests. In contrast, for the no overcut tests, the overall friction was an order of magnitude greater than the local sensor measurements. During the no overcut tests, a central band of each test piece was observed to be covered with primarily Bentonite

lubricant, with the regions either side covered by a mixed layer of sand and Bentonite.

This finding is crucial for field practice, as it demonstrates that the initial lubricant injection (behind the TBM) is essential in ensuring effective lubrication around the tunnel pipe. Considering the large circumferential spacing of the 3 lubricant delivery ports in field tunnels (typically up to 3.1 m), if the lubrication is insufficient during overcut formation and soil is in contact with the tunnel pipe wall, additional lubricant injection will not effectively reform the boundary layer and reduce friction, as demonstrated by the persistently higher actuation forces measured during the tests without an overcut during formation.

It was also found that the filter cakes formed during tests with overcuts had a lower permittivity than those formed without overcuts. This reduced the filtration rate of the water out of the lubricant and into the soil during the tests and, coupled with the additional volume of Bentonite within the overcut, resulted in the filtration of the Bentonite at the interface being incomplete after the 60 h test stoppages at the tested normal stresses of up to 50 kPa. As filtration was incomplete, a band of unfiltered lubricant remained at the lubricant - pipe side of the interface, which sheared at low stress after the stoppage. For the tests without overcuts, the filtration process completed during the stoppages and the interface shearing occurred against the filtered Bentonite, which had significantly higher shear strengths of up to 14 kPa.

Considering the filter cake strengths measured using the consolidation shear box of between 13 kPa and 47 kPa, and without the presence of further lubrication, testing has shown that the interface shear stress remains high during tests where filtration has completed after a stoppage, with peak friction increase of over 13 kPa and residual friction of up to 9.4 kPa after 60 h stoppages. As the peak stress corresponded to the predicted shear strength of the filter cake at the 50 kPa normal stress applied at the interface during the test, the interface friction coefficients were up to 1. Residual interface stresses decreased to typically 50% of the peak value although these did increase at larger shear strains without subsequent lubricant injection. The

presence of an overcut resulted in no significant residual stress increases during the testing, although smaller global peaks of up to 2.5 kPa were observed after 60 h stoppages tests at higher normal stress (50 kPa), suggesting that the filtration process was near completion in the chamber. These findings were similar to the field study data, which showed that once the drive had advanced one lubrication pipe spacing (12 m to 20 m) the interface friction typically returned to the pre-stoppage levels.

8.3 SLS interface model

8.3.1 Form of model

To maximise the impact of this research on industry practice a new conceptual model of the SLS interface during tunnelling has been developed. This is required as current understanding is based primarily on the work of the PJA research program described in Section 2.6, which was conducted before automated lubrication systems were in use; Praetorius and Schößer (2017), which covered automated lubrication techniques at the time of publication; or engineering judgement on the part on tunnelling practitioners, evolved from accumulated previous site experience. These methods do not capture the mechanics of the SLS interface identified during this research and their implications for interface friction.

The model of the SLS interface proposed is formed of 2D 'slices' which are extrapolated along relevant sections of the tunnel length to calculate the interface friction of the whole tunnel. This simple approach has been adopted to capture the key processes affecting SLS interface friction and allow accurate empirical predictions, without a large number of numerical or site derived inputs, as these can be poorly defined. Figure 8.1 provides a schematic of typical 'slices' and the different SLS interface conditions within a tunnel with a stable bore. Three conditions at the SLS interface are considered in the model: lubricant - pipe contact (LP), filter cake - pipe contact (FP), and (in the absence of a filter cake) soil - pipe contact (SP). If the tunnel bore is unstable, for example during drives in gravel, the SP contact type is used around the

whole tunnel exterior, as a consistent external filter cake will not form at the SLS interface.

8.3.2 Interface friction calculation

In stable overcut conditions, the interface friction stress of the LP sector is equal to the yield stress of the lubricant (τ_0), which can be determined using the viscometer apparatus in the field, or interpolated from the results in Section 5.2 of this research. The frictional force (T_L) on this sector of the pipe can then be calculated as:

$$T_L = \tau_0.\Phi_L.\frac{D_O}{2} \tag{8.1}$$

where Φ_L is equal to the angle of the pipe circumference in contact with the fresh lubricant only and D_O is the outside diameter of the pipe.

To determine Φ_L, the other sector of the pipe must be considered. The contact angle between the soil and pipe (Φ_S) is calculated by treating the tunnel pipe and bore as concentric elastic cylinders of different diameters, using Equation 2.10 - adapted from Young et al. (1976). To complete this calculation, the elastic modulus of the soil surrounding the tunnel (E_s) and the pipe wall elastic modulus (E_p) must be known, as well as the effective pipe weight ($N\prime$; Equation 2.9). The contact width is then calculated using Equation 2.10, and the sector angle Φ_S can be determined.

For the SP contact condition in granular soils, the total friction force (T_S) is calculated as:

$$T_S = \overline{n}'.\mu.\Phi_S.\frac{D_O}{2} \tag{8.2}$$

where $\overline{n}'$ is the average normal contact stress between the tunnel pipe and tunnel bore and μ is the interface friction angle. In cohesive soils T_S is calculated as:

$$T_S = S_u.\alpha.\Phi_S.\frac{D_O}{2} \tag{8.3}$$

where S_u is the soil undrained shear strength and α is the adhesion coefficient. In both conditions, Φ_L is then calculated as the remaining sector of the pipe circumference (i.e. $2\pi = \Phi_S + \Phi_L$).

In unstable bore conditions, it is assumed that the whole pipe circumference is in contact

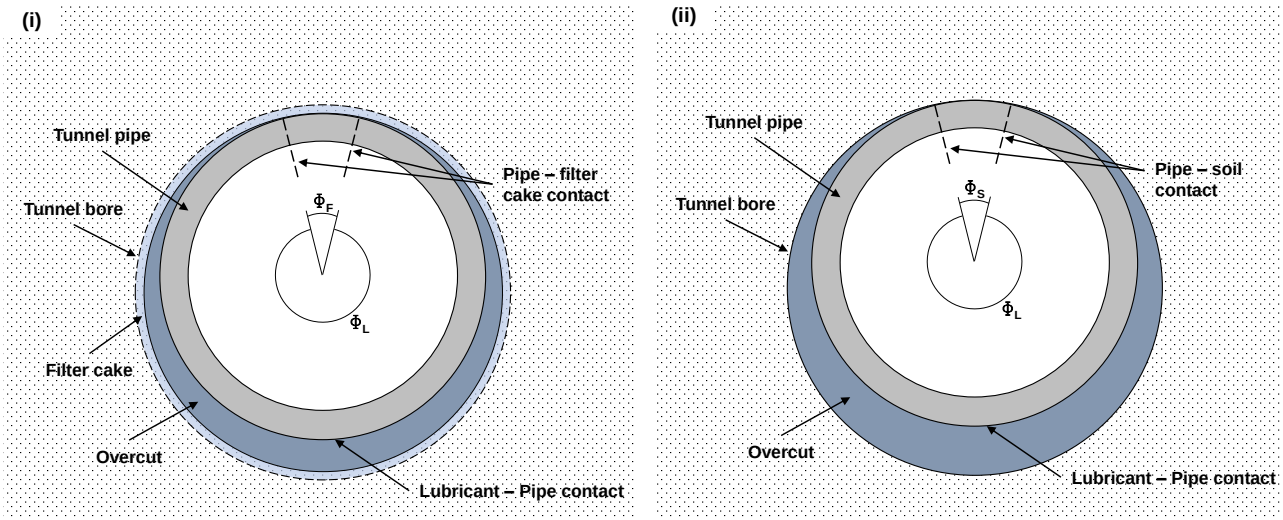


Figure 8.1: Schematic drawings showing the proposed model slices under stable bore conditions with: (i) Pipe - filter cake contact and (ii) pipe soil contact. The filter cake - pipe, lubricant - pipe, and soil - pipe contact angles are also labelled as: Φ_F, Φ_L, and Φ_S, respectively.

with the soil (such that $\Phi_S = 2\pi$). In this case, the vertical effective stress in the soil acting on the pipe $\sigma'_{v,c}$ is calculated using the Terzaghi trapdoor model (Equation 2.4) and reduced by the overcut pressure (P_a), such that T_S is calculated as:

$$T_S = (\sigma'_v - P_a).\mu.\pi.D_O \tag{8.4}$$

If the tunnel bore is stable and a filter cake forms at the SLS interface the pipe will be in contact with the filter cake (i.e. the SF condition). Young et al. (1976) can still be used to calculate the contact angle (Φ_F) and friction (T_F) can then be calculated, similarly to Equation 8.3, as:

$$T_F = \tau_c.\alpha.\Phi_F.\frac{D_O}{2} \tag{8.5}$$

where τ_c is the maximum shear strength of the filter cake, and α is the adhesion coefficient between the filter cake and the tunnel pipe.

To predict τ_c, as measurements directly from tunnel overcuts are not currently available, the consolidation shear box testing findings can be used. The consolidation shear box testing completed during this research demonstrated that τ_c can be predicted using the WC alone, if it is possible to take samples of the filter cake from within the tunnel bore. Alternatively,

the relationships identified in Section 5.3 can be used to predict τ_c using the mean value of P_a during the drive and the original mix properties. Whilst the interface friction coefficients α and μ can be predicted using previous literature (such as Staheli et al. (2006) and Namli and Guler (2017)), direct measurement using shear box testing of the lubricant - soil interface and/or back-calculation from previous tunnel data in similar ground are perceived to be a more accurate method of calculation until a library of previous case histories is compiled. Additionally, if τ_c exceeds S_u of the soil, the smaller of the two values should be used when calculating interface shear capacity.

Once these parameters are determined, the mean interface friction for each slice (p) can be calculated for the stable bore SP condition in granular soil as:

$$p = \tau_0.(1 - \frac{\Phi_S}{2\pi}) + \overline{n}'.\mu.\frac{\Phi_S}{2\pi} \tag{8.6}$$

or for cohesive soils as:

$$p = \tau_0.(1 - \frac{\Phi_S}{2\pi}) + S_u.\alpha.\frac{\Phi_S}{2\pi} \tag{8.7}$$

Similarly, for the FP condition Equation 8.8 is used.

$$p = \tau_0.(1 - \frac{\Phi_F}{2\pi}) + \tau_c.\alpha.\frac{\Phi_F}{2\pi} \tag{8.8}$$

Finally, for unstable bore conditions, p is calculated using Equation 8.9 as examples of unstable bore conditions in well lubricated tunnel drives through cohesive soils were not found in the literature.

$$p = (\sigma'_v - P_a).\mu \tag{8.9}$$

In drives which pass through different ground conditions, or have sections such as curves which may increase interface friction, multiple slices can be defined to explain the tunnel behaviour. The interface friction coefficients can be applied to these different sectors if a suitable comparison is available, or a the same interface friction can be applied to all sections if the ground conditions are similar. The total interface friction force is then calculated for the drive

as:

$$F = \sum_{n=1}^{n} p_n.\pi.D_O.x_n \tag{8.10}$$

where n is the number of slices defined, p_n is the average friction of each slice, and x_n is the distance the slice applies for, such that $L = \sum_{n=1}^{n} x_n$.

These equations can also be used to account for different lubricants which will not form a filter cake at the SLS interface, such as polymers. With these lubricants the soil-pipe (SP) contact condition can be assumed with either a stable or unstable bore. The interface friction coefficient μ will be constant throughout tunnelling and stoppages, as the properties of the polymer lubricants are not dependant on t_s. Instead, the reduction in P_a measured during stoppages will result in increased friction through Equation 8.4.

8.3.3 Stoppage induced variations

During stoppages in stable bore conditions, experimental testing has shown that the properties τ_c, α and μ remain constant at the soil-pipe side of the SLS interface until the filtration process nears completion (i.e. at $t_s < t_{90}$). During this period, the increase in SLS interface friction is due to the sector lengths Φ_S or Φ_F increasing and Φ_L reducing. The rate of this transfer in area will vary due to numerous factors, such as: the elastic relaxation of the ground around the pipe (as P_a reduces), the rate of build-up of the filter cake around the pipe, filter cake thickness, the permittivity of the filter cake, ground permeability, lubricant mix properties, and the P_a both before and during the stoppage. Due to the complexities of these interactions, an empirical equation is proposed to account for these effects to allow fitting to previous tunnel drive data. To predict the change in Φ_S after a stoppage time t_s the following equation is proposed:

$$\Phi_{S,t} = \Phi_S + \frac{t_s}{t_{ref}}.(d_S + c_S.ln(\frac{t_s}{t_{ref}})) \tag{8.11}$$

where t_{ref} is a reference stoppage time (taken as 1 hour) and c_S and d_S are empirical factors which are back-calculated using historical drive data.

Similarly, for the FP condition, Φ_F after a time t_s can be predicted as:

$$\Phi_{F,t} = \Phi_F + \frac{t_s}{t_{ref}}.(d_F + c_F.ln(\frac{t_s}{t_{ref}})) \tag{8.12}$$

where c_F and d_F are empirical factors back-calculated using previous tunnel drive data.

Equations 8.11 and 8.12 are valid between $0 < \Phi_{S,t} \leq 2\pi$ and $0 < \Phi_{F,t} \leq 2\pi$, respectively. Once $\Phi_{S,t}$ or $\Phi_{F,t} = 2\pi$ (and therefore $\Phi_L = 0$) additional increases in interface friction are controlled by μ or α increasing due to the filtration of the lubricant at the pipe - lubricant boundary, for contact with granular soils and cohesive soils or the filter cake respectively. During experimental testing without the presence of an overcut, the peak interface stress was shown to be equal to the predicted τ_c of the filter cake, such that the interface friction coefficient ($\mu_{F,peak}$) was equal to one. Without the addition of further lubrication, the residual stress upon shearing was in the range $0.35 \leq \mu_{F,cs} \leq 0.5$. Although the laboratory testing did not consider a clay interface directly, α is expected to exhibit the same behaviour as μ due to the presence of Bentonite at the interface in both cases. It is also of note that the lower permeability of the ground in cohesive soils will influence the filtration rate of the lubricant, increasing t_{90}.

During stoppages in unstable bore conditions, $\Phi_S = 2\pi$ during tunnelling and the increase in friction measured during stoppages is due to the reduction in P_a. Field monitoring has shown that P_a follows a log-linear relationship with t_s during stoppages, such that the pressure after a stoppage can be calculated as:

$$P_{a,t} = P_a - \frac{t_s}{t_{ref}}.(d_p + c_p.ln(\frac{t_s}{t_{ref}})) \tag{8.13}$$

where $P_{a,t}$ is the pressure after a stoppage of duration t_s and is valid for the range $P_{a,t} \geq 0$, P_a is the overcut pressure at the onset of the stoppage in this case, and c_p and d_p are empirical factors which are back-calculated using previous tunnel drive data.

8.3.4 Model application procedure

To use the proposed model to predict SLS interface conditions during tunnelling, a simple procedure has been developed to identify if stable or unstable bore conditions are present and

calculate changes in interface conditions during stoppages. It consists of the following 7 steps:

1. **Calculate the contact widths assuming stable bore conditions.**

   For the given tunnel dimensions and ground conditions use Equation 2.9 to calculate the normal force (per linear metre) between the tunnel pipe and bore in the 2D slice, then Equation 2.10 to calculate the contact width between the tunnel pipe and bore. From these this value is then used to calculate Φ_S or Φ_F simple trigonometry and hence Φ_L.

2. **Back-calculate the interface friction coefficient α or μ.**

   Depending on the ground type (cohesive or linear) and anticipated presence of an external filter cake ($D_{10} < 1$ mm), use Equations 8.6, 8.7 or 8.8, to calculate μ or α using mean interface friction values from existing tunnel drive data and the sector angles in step (1). Mean values are used as the model is intended to predict the average conditions along the tunnel drive, not the best case conditions which using the friction minima would produce. If the calculated coefficient is > 1 then either the bore is unstable or there is a large additional source of friction apparent in the data used for fitting (e.g. a significant obstruction). In the case of unstable bore conditions, the interface coefficients should be recalculated through step (5) of this procedure. If another friction source is believed to be present (and the friction effect cannot be quantified through the addition of another 'slice' representing the SLS conditions at the obstruction), this analysis will not accurately predict the friction of the remaining tunnel drive.

3. **In stable bore conditions:**

   Back-calculate stoppage parameters c and d.

   Once the steady state conditions are established in step (2), the changes in either Φ_S or Φ_F during stoppages can be determined using Equation 8.11 or 8.12, respectively. To achieve this, Equations 8.11 or 8.12 should be fitted to stoppage data from previous tunnel drives in similar ground conditions and the fitting coefficients c_S and d_S or c_F and d_F

calculated, respectively.

This analysis will also yield the time to $\Phi_{S,t} = \Phi_{F,t} = 2\pi$ and therefore the time at which μ or α increase rapidly to 1.

4. **In stable bore conditions:**

   Predict future stoppage interface friction.

   Once the c and d parameters are determined, the interface friction after a stoppage of length t_s can be predicted by inputting $\Phi_{S,t}$ or $\Phi_{F,t}$ (calculated using Equation 8.11 or Equation 8.12) back into Equations 8.6 or 8.8, respectively. To give the predicted interface friction of that slice.

   If the SLS interface friction force is required, or multiple slices have been defined to analyse the tunnel alignment, then each can be multiplied by the relevant tunnel length and interface area to yield the total force through Equation 8.10.

5. **In unstable bore conditions:**

   Recalculate Φ_S and μ.

   If the analysis in step (2) shows that the bore conditions are unstable, Equation 8.9 should be used to back calculate μ assuming the full pipe circumference is in contact with the soil at the interface.

6. **In unstable bore conditions:**

   Back-calculate stoppage parameters c_p and d_p.

   The change in overcut pressure during stoppages is then fitted to previous tunnel data using Equation 8.13 and the coefficients c_p and d_p are calculated. This will also yield the time taken for the overcut pressure P_a to dissipate to zero, after which the vertical effective soil stress will be acting at the SLS interface.

7. **In unstable bore conditions:**

   Predict future stoppage interface friction.

The coefficients c_p and d_p can then be used to predict future friction changes during stoppages by using Equation 8.13 to calculate the change in P_a and inputting this into Equation 8.9.

Finally, the stress predicted by Equation 8.9 for each slice can be summed using Equation 8.10 to yield the total interface friction on the tunnel.

8.3.5 Model and procedure validation

To validate the proposed model and interface friction prediction procedure, the method has been used to explain the behaviour of the field tunnel drives discussed in Chapter 4 of this research. The four drive groups were believed to contain both stable and unstable bore conditions and used both Bentonite and polymer lubricants, and as such provided a broad base of conditions to validate the model against.

To apply the model the required input parameters were compiled for each of the four drive groups. These are shown in Table 8.1. Due to a lack of information (or only anecdotal information) being available for some of the drives, some variables are interpreted based on available literature or the findings of this research. Most notably, direct measurements of P_a were not undertaken during the tunnel drives without instrumented pipe sections. Additionally, where drives are in a group (i.e. Hull ($D3$ - $D7$) and Dublin ($D8$ - $D14$) mean average parameters are taken as the model was used to predict the average conditions for the group.

Table 8.1: Additional input parameters for the interface friction model validation.

Parameter	Symbol	Unit	C'rigg	Putney	Hull	Dublin
Drive number(s)		-	$D1$	$D2$	$D3$ - $D7$	$D8$ - $D14$
TBM head diameter	D_{TBM}	m	2.856	3.030	1.540	1.926
Soil stiffness	E_s	MPa	31[1]	35[4]	7.5[6]	20[8]
Soil Poisson's ratio	ν_s	-	0.18[1]	0.2[5]	0.2[6]	0.2
Filter cake shear strength	τ_c	kPa	47[2]	N/A	13[7]	13[7]
Lubricant shear strength	τ_0	Pa	400	400	400	400
Pipe Young's modulus	E_p	GPa	37	37	37	37
Pipe Poisson's ratio	ν_p	-	0.2	0.2	0.2	0.2
Effective pipe weight	N'	kN/m	13.1	1.77	2.13	3.18
SLS interface friction[3]	p	kPa	0.6	1.7	0.4	1.15

[1] Taken as "North Head Siltstone Member", Reeves (2002).
[2] Predicted using $P_a = 250$ kPa and Figure 5.19.
[3] Mean steady state friction during tunnelling.
[4] Taken as "river terrace deposits" from Arup - Atkins Joint Venture (2016).
[5] Taken as "river terrace deposits" from Underground professional services LTD. (2017).
[6] Properties of Clay from Highways England (2021).
[7] Predicted using an assumed $P_a = 50$ kPa and Figure 5.19.
[8] Taken as "river terrace deposits", Arup - Atkins Joint Venture (2016).

Additional parameters were also defined for the Dublin group of tunnel drives ($D8$ - $D14$), as feedback form site suggested unstable tunnel bore conditions were experienced. As the group consisted of seven tunnel drives, mean values were calculated using McNamara (2010), comprising: cover depth ($H = 6$ m), overburden density ($\gamma = 20$ kN/m^3), overburden effective cohesion ($c' = 0$ kPa), and overburden friction angle ($\phi = 32\ ^o$). The average P_a during tunnelling is also required but was not routinely measured during the tunnel drives. Anecdotal evidence provided by the site team indicated the stress was ≈ 50 kPa, as the operatives were trying to avoid 'fracking out' of the slurry to ground level during the drives.

The analysis procedure predicted the unstable bore conditions within the Dublin group of drives with an initial μ estimate of 1.4, based on a stable bore contact angle $\Phi_S = 9.4\ ^o$. Once the unstable bore condition analysis was completed (steps (5) to (7) of Section 8.3.4), μ was predicted to be 0.034 which is within the ranges quoted for well lubricated drives in previous literature, e.g. Namli and Guler (2017).

Similarly, during the Putney drive (D2) the combination of the alignment having a gravel

overburden and the use of a polymer based lubricant resulted predicted unstable bore conditions, with an initial estimate of $\mu > 1$. The additional parameters required for the unstable analysis (H = 5 m, γ = 22 kN/m^3, c' = 0 kPa, and ϕ = 35 ^{o}; Arup - Atkins Joint Venture (2016)) were input into the model, alongside the average P_a of 27 kPa above hydrostatic pressure, which was calculated from the IP data. This analysis yielded μ = 0.14, which was again within the range of previous literature and higher than the Dublin group, which was believed to be due to the polymer lubricant usage.

The change in τ during stoppages on the drive was then used to back-calculate the change in P_a using Equation 8.9 and 8.13) with the calculated μ. This analysis yielded c_p = -388, d_p = 2923, and predicted a reduction in P_a of 3 kPa after t_s = 1 h. This is in good agreement with data measured using the IP (Figure 4.20), which showed reduction in P_a of between 2 kPa $\leq \Delta P_a \leq$ 6 kPa after t_s = 1 h during the drive.

For the Castlerigg tunnel drive ($D1$), the model predicted α = 0.13 and Φ_F = 12 ^{o} under steady state conditions. This is similar to shear box test results published in the literature. Due to the number of stoppages on the drive, the model has been used to predict up to t_s = 100 h, after which Φ_{SF} increased to 55 ^{o}. This shows that complete filtration of the lubricant did not occur during the stoppages and friction would therefore continue to increase at longer stoppage durations. This is reflected in the tunnel drive data, as the rate of friction increase during the longest stoppages had not decreased to zero.

Finally, for the Hull group of drives, the analysis output $\alpha \approx 0$ for the stable bore conditions, over a contact area of 14 ^{o}, which was larger than previous drives due to the low modulus of the clay. α was near zero for the drive, as the τ was similar to τ_0 of the lubricant used. This was due to the low permeability of the clay being tunnelled through preventing a filter cake from forming at the SLS interface, such that the lubricant in the bore remained in the fresh state, reducing friction by forming a film on the clay surface and reducing the effective pipe weight.

Additionally, the soft clay being tunnelled through during these drives had an S_u in the range 8 kPa $\leq S_u \leq$ 30 kPa (Highways England (2021)), such that the strength of the clay surrounding the tunnel was similar to the anticipated strength of any filter cake formed. It is also of note that either P could have been an underestimation during the drives, or R could have been an overestimation (due to slightly incorrect setup of the tunnelling equipment). Either of these errors would influence the calculated τ for the drive, reducing its magnitude. Regardless of this uncertainty, the results demonstrate that the lubrication was particularly effective in these ground conditions.

The model predicted a plateauing of interface friction after $t_s = 30$ h, which would have not been accounted for in previous literature. At this time, the model yielded $\Phi_S = 170\ ^o$, showing that the buoyant pipe was in contact with nearly the top half of the tunnel bore. The lower half of the pipe was still predicted to be in contact with the tunnel lubricant (the LP condition), due to the low permeability of the clay restricting the filtration of the lubricant further. As no measurements of P_a were taken during the drives, it was not possible to identify if the filtration process was still ongoing in the lower half of the tunnel, as this model output would predict, or if the pipe was floating in a stable bore with $P_a = u$.

These analyses of the four groups of tunnel drives have demonstrated that the proposed conceptual model and application procedure is sufficient to predict the different tunnel interface behaviours in granular and cohesive soils, as well as for stable and unstable bore conditions. It has been shown to account for plateaus in interface friction during stoppages, caused by physical mechanisms at the SLS interface around the tunnel pipes during stoppages - something previous empirical models were not sufficiently detailed to provide. Additional field data is required to refine the model further, in order build a database of accurate μ, α values in different ground types, as well as the fitting coefficients c and d.

8.4 Friction increase mitigation methods

The findings discussed in this chapter have identified the mechanisms by which interface friction increases during tunnelling. Using the model developed it is noted that, if the tunnel overcut was re-pressurised after a stoppage, or the lubrication system was left engaged (at a lower rate) during a stoppage, this should lead to reduced friction when tunnelling recommences. Lubrication should be maintained from the ports anticipated to be in contact with the tunnel bore to avoid an uneven lubricant pressure distribution around the tunnel pipe.

During stoppages the pipe will embed into the filter cake due (initially) to the buoyancy force of the pipe in the overcut, or through abrasion removing the filter cake during shearing. Once this occurs, the overcut pressure experienced by the pipe is P_a where the pipe extrados is in contact with the overcut, but reduces closer to u where it is embedded into the filter cake, as depicted schematically in Figure 8.2. The reduction in pressure where the pipe is in contact with the filter cake is due to the low permittivity filter cake causing a hydraulic gradient across its thickness, as measured during the Permeameter testing conducted within this research. The pressure difference (between P_a and u) around the pipe extrados causes a resultant force on the pipe, acting towards the filter cake - pipe contact area, further increasing friction. By injecting lubricant at the anticipated point of pipe - filter cake contact, a fresh layer of Bentonite and filter cake will form and the overcut pressure will be uniform around the tunnel pipe, eliminating the additional resultant force. It will also have the effect of providing a layer of fresh lubricant for the pipe to shear against.

Anecdotal evidence from field tunnel drives has alluded to this phenomenon, with operatives reporting reduced friction after venting overcut lubricant into the tunnel. But, as no overcut pressure measurements have previously been taken, it has not been possible to quantify this effect. The effect was also not apparent during the Castlerigg tunnel drive ($D1$), although this was possibly due to the failure of the contact stress sensors after only a short duration or the

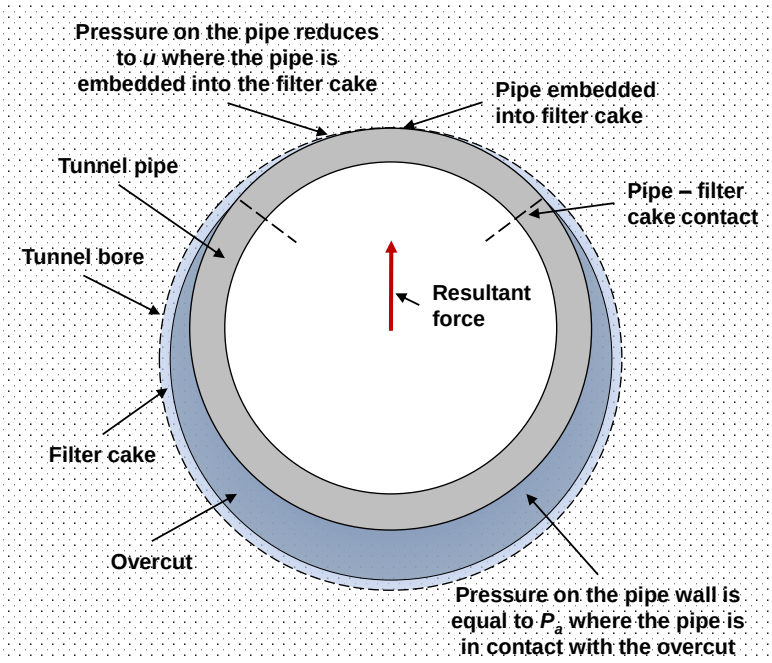


Figure 8.2: A schematic showing the differential pressure around a tunnel pipe and the resultant force caused by the pipe wall embedding into the filter cake when the overcut pressure (P_a) is greater than the surrounding pore pressure (u).

low permeability of the mudstone being tunnelling through.

Further to this, the implementation of a pressure-controlled lubrication system instead of the time or volume controlled systems currently used would reduce friction from over-pressurising the overcut. This research has shown that the current methods of lubricant injection can result in overcut pressures significantly higher than those required to maintain bore stability in low permeability grounds. The higher overcut pressure promotes faster lubricant filtration and generates high shear strength filter cakes (as increasing the chance of frack outs of the lubricant from the tunnel bore). If the lubricant pressure in the overcut was maintained at the overcut stability pressure (plus a safety margin to ensure overcut instability did not occur) then interface frictions, and smaller increases in friction during stoppages, would be decreased, due to the lower shear strength filter cake formed.

8.5 Summary

In this chapter the findings of the elemental lubricant testing and SLS interface apparatus tests have been used to explain the observed field behaviour and develop a more detailed understanding of how the SLS interface behaves during shearing and stoppages. Contact between

either the filter cake or the soil and the pipe has been shown to dominate the SLS behaviour, due to the lower relative yield strength of the lubricants. It has then been shown that the properties of the fresh lubricant and filter cake remain largely constant during stoppages, and the increase in friction observed is caused by either: an increasing sector of the pipe extrados adhering to the tunnel bore (in stable bore conditions), or the overcut pressure reducing (in unstable conditions).

Using these findings, a new conceptual model of the SLS interface has been developed and an empirical model derived from it to predict interface friction. This model comprises of a number of 'slices' (which define the interface conditions over a portion of the tunnel) extrapolated along the tunnel length to determine the overall friction. The proposed model uses properties of the lubricant which can be determined on site and ground parameters from site investigations to predict the interface friction during tunnelling. The model can also be used to predict when stable bore conditions have not been achieved, for example during tunnel drives in gravel. In these cases, the model can be adapted to account for the additional frictional stresses caused by the soil - pipe contact. The model has been shown to explain the behaviours of the four tunnel drive groups examined in this research, and output reasonable predictions of interface friction coefficients and changes in overcut pressure.

Finally, mitigation methods have been proposed to reduce the friction increase during stoppages. These centre around two concepts: firstly, to break the bond between the filter cake and tunnel pipe by physically injecting fresh lubricant into the interface, and secondly, optimising the pressure control of the overcut lubricant - so that over pressurisation does not occur.

9 | Conclusions

9.1 Introduction

This research has explored the mechanics of the soil-lubricant-structure (SLS) interface around pipe-jacked tunnels during construction to gain insight into the mechanisms which control interface friction. This has been achieved using a combination of elemental testing of lubricants, field monitoring of tunnel drives during construction, back analysis of historical tunnel drives, and laboratory testing using a bespoke plane strain SLS interface apparatus. The improved understanding developed has then been used to develop a new conceptual model for the SLS interface during pipe jacking, from which an empirical model for predicting frictional changes has been derived. Using these findings mitigation measures have been proposed which will reduce the influence of stoppages on SLS interface friction. This chapter summarises these findings and their implications for design and practice, as well as making suggestions for areas of future research.

9.2 Key contributions

Identification of SLS conditions during tunnel drives

The overcut pressures measured during field tunnel drives have shown that lubricant injections over 20 m from the pressure sensor locations can be detected, demonstrating that the SLS interface was continuously lubricated along the tunnel drives in all ground conditions. The sensors measured significant variations in overcut pressure, ranging from hydrostatic conditions to in excess of 1 MPa. The higher pressures were found to cause numerous problems for the tunnelling contractor (such as lubricant leaks into the tunnel and at shaft seals) and a need for better overcut pressure control was identified. Additionally, the high overcut pressures were thought to increase interface friction when the pipes embedded into the tunnel filter cake.

Changes in SLS interface friction were found to vary depending on the ground conditions,

despite the industry best practice lubrication employed by the contractor. Steady state SLS interface frictions were found to range between 0.5 kPa in soft clays and 2 kPa in gravel soils, less than results quoted in previous literature. During stoppages, increases of up to 7 kPa were recorded, which were also less than reported in previous literature. A logarithmic relationship was established between stoppage duration and friction increase which and a limit value was identified during longer stoppages. Tunnels through soft clays experienced larger short term increases in friction than than gravels due to their initial lower interface friction, but drives through gravel resulted in the largest overall increases. The significant increases in friction during stoppages showed the requirement for a deeper understanding of the interface changes during these periods, which has been developed during this research.

During stoppages, the overcut pressure was observed to decrease towards hydrostatic pressure linearly with the log of the time stopped. Similarly, the rate of friction increase during a stoppage was found to vary linearly with log-time. This provides evidence that the friction at the SLS interface during stoppages and overcut pressure changes were influenced by the same mechanisms (i.e. filtration of the lubricant through the filter cake).

Data from a monitored rock tunnel drive showed that the SLS interface friction reduced during each tunnel advance, such that the force required at the end of a 3 m pipe advance was, on average, 10% lower than at the start. The reduction was attributed to the continued lubrication during the advances reducing the SLS interface friction. As the pipe was buoyant in the lubricated overcut, the resultant frictional force on the pipe was found to be within the top half of the pipe for 75% of the advanced distance, including after stoppages. This highlighted that friction at the SLS interface in stable bore conditions was dominated by the relatively small surface area of the pipe wall in contact with the lubricant filter cake and/or tunnel bore wall.

Tunnelling lubricant behaviour

Testing of two common tunnelling Bentonite lubricants (Tunnel Gel and Hydraul-ez) was conducted using industry standard apparatus (a filter press and viscometer) as well as a consolidation shear box and permeameter apparatus developed specifically for this research. The time taken to complete 90% of primary consolidation of singularly drained, 25 mm deep, Bentonite samples was found to vary between 52 hours and 320 hours depending on the Bentonite mixture and applied pressure. As stoppages in this range were recorded during field tunnel drives, the tests demonstrated that 90% consolidation of lubricants in the tunnel overcut is feasible during tunnel stoppages.

Once consolidated, the shear strength and water content of the lubricant samples were found to vary linearly with the applied stress. This relationship was much stronger than the relationship between other mix parameters and final shear strength, such that the water content of a sample alone was found to be a good predictor of the shear strength. The shear strengths of the consolidated lubricants were found to vary between 13 kPa and 48 kPa for applied pressures of 50 kPa to 250 kPa, which exceeded the increases in interface friction recorded during the field tunnel drives, proving that total consolidation of the overcut lubricant around tunnel pipes during stoppages is not the cause of friction increases during stoppages.

Permeameter testing showed that the behaviour of the lubricant-soil interaction was controlled by the permittivity of the soil-lubricant system. The formation of the filter cake at the soil-lubricant interface occurred when the permittivity of the soil-lubricant system decreased below that of the soil itself. Once the filter cake formed, the process of water being driven from the lubricant into the soil was found to be a filtration mechanism instead of consolidation, as the pore pressure distribution with depth within the lubricant sample remained constant away from the interface. This resulted in the Bentonite outside the filter cake remaining in the fresh state throughout testing.

SLS interface testing

Tests where Bentonite was injected into the interface between a simulated concrete jacking pipe and 14/25 Leighton Buzzard sand without an overcut showed that the lubricant did not distribute evenly across the SLS interface. The region in line with the lubricant port was well lubricated by the injection, with a boundary layer of Bentonite formed and the interface shear stresses being dictated by the properties of the lubricant alone. Away from the injection port location, the interface consisted of a sand - Bentonite mixture, which had a higher interface friction angle as the Bentonite travelled parallel to the interface and did not create the boundary layer.

The inclusion of an overcut allowed for a more even distribution of lubricant across the interface and an external filter cake to form at the soil - lubricant boundary. The filter cake resulted in a lower permittivity interface than the non-overcut tests, and hence lower filtration rates of lubricant. The lower filtration rate, coupled with the larger volume of Bentonite at the interface, resulted in a fresh layer of Bentonite being maintained at the lubricant-structure side of the interface after 60 h stoppages. This meant that little to no friction increase was recorded when shearing restarted, compared to peaks of up to 14 kPa for the non-overcut tests. Additionally, no residual change in shear stress occurred during shearing after stoppages with an overcut, whereas for non-overcut tests up to 2 kPa of addition friction was measured.

The testing therefore demonstrated that the increases in friction at the SLS interface during stoppages are caused by a change from the tunnel pipe being in contact with fresh Bentonite lubricant to filtered Bentonite lubricant, not from changes in the lubricant properties in the fresh state. The lower water content of the filtered Bentonite resulted in a higher yield stress, as determined by elemental lubricant testing, and adhesion between the tunnel pipe and clay deposited on the soil surface. It was observed that only a thin band of fresh Bentonite was required at the lubricant-structure interface to prevent the increase in friction.

A new conceptual model of the SLS interface and prediction of friction

A new conceptual model of the SLS interface around tunnels has been developed to encompass the findings of the field monitoring and laboratory testing. The model defines a series of 2D slices, which are divided into sectors experiencing different contact conditions: structure-lubricant, structure-filter cake, or structure-soil. The friction properties of these sectors can be defined in different ground conditions using either predictions from laboratory experimentation, samples collected from the field tunnel drives, or back-calculation using previous tunnel drive data. The model is able to predict whether a tunnel bore is stable or unstable in different ground conditions and calculate the interface frictions accordingly.

The model captures frictional behaviour in stable bore conditions primarily through changes to the relative lengths of the different sectors changing during a stoppage in line with the findings of the laboratory test program. It has been proposed that during a stoppage the sector of the pipe extrados in contact with the filter cake or soil increases due to the filtration of the lubricant from the overcut with time. In unstable ground conditions, changes in the overcut pressure, and hence the effective stress at the SLS interface, have been shown to predict the friction behaviour as the whole SLS interface is in contact with the surrounding soil.

The empirical model has been used to demonstrate the behaviours of tunnels in different ground types, for example the tunnel pipes floating into the top half of the tunnel bore during the Hull group of drives, or predicting the decrease in overcut pressures measured during the Putney tunnel drive. A procedure has been developed to apply the model to future tunnel drive parameters to predict the friction magnitudes during tunnelling.

9.3 Key recommendations for industry practice

Overcut pressure monitoring

To more effectively manage lubrication during tunnelling, the installation of overcut pressure monitoring is recommended. This can take the form of pressure sensors installed into the lubrication system within tunnel pipes and configured to display and log in the existing

control programs. Using this system, the overcut pressures should be maintained at a safe margin above the minimum overcut stability pressure, so as not to over-pressurise the overcut, which results higher interface frictions due to the build-up of lower water content (and hence higher yield stress) filter cakes. Minimising the overcut pressures will also minimise the effects of pressure differentials around the tunnel pipes when they are embedded in the filter cake and the increase in friction caused by the increased normal contact force.

Stoppage lubrication practice

During stoppages, where possible, contractors should run the tunnel lubrication system to maintain the overcut pressure at a safe margin above the required stability pressure. The lubrication rate will be significantly lower than during normal tunnelling operations, as only the volume of lubricant lost through filtration will need to be replaced to maintain the overcut pressure. Lubricant should be delivered to the sectors of the pipe where contact between the pipe and filter cake (or soil) are likely to occur, e.g. the pipe crown for buoyant pipes or outside of curves in the tunnel alignment. This will ensure that a fresh layer of Bentonite is maintained at the SLS interface, preventing adhesion between the high shear stress filter cake and tunnel pipe or embedment of the pipe into the filter cake. If it is not possible to run the lubrication system during a stoppage, the tunnel advance should not be restarted until the overcut pressure has been re-established at the desired magnitude.

9.4 Recommendations for future research

Areas for further study which may be useful are detailed below:

- Additional monitoring of field tunnel drives, in a variety of ground conditions, to further refine the proposed empirical model. The monitoring should focus on assessing the regions of pipe in contact with the unfiltered lubricant, filter cake, and surrounding soil, whilst allowing for samples of each to be taken during the tunnel drive. Data should also be gathered on the overcut pressure and volume of lubricant injected to generate reference

tables for the empirical parameters in different ground conditions. These data could also be utilised improve the understanding of the influence factors such as scour and filter cake thickness have on the SLS interface.

- Additional laboratory testing examining the behaviour of the SLS interface with larger soil particle sizes could be conducted. This could be used to ascertain the effectiveness of Bentonite at reducing friction through the effective stress reduction and friction coefficient reduction mechanisms. The influence of the larger particle sizes on internal filter cake formation should also be assessed, to inform predictions of the time taken for the lubricant to complete filtration under those conditions.
- The SLS interface apparatus developed for this research could be used to identify the behaviours of polymer based lubricants and their behaviour during tunnelling. The experimentation could also identify any time dependant behaviours of these lubricants under field conditions.
- The opportunity to change the lubricant mix supplied to different sections of longer tunnels could be explored. Once the overcut is formed, and the filter cake established, pumping a lubricant mix with a greater water content could reduce friction whilst maintaining overcut pressure and reducing the costs of the tunnelling contractor. The implications of this approach could be explored using scale testing and ultimately field tunnel drives.
- Machine learning methods of analysis could be applied to a larger set of industry tunnel drive data to better predict interface friction based on the empirical model devised as part of this research. Similarly, such methods could be employed to analyse additional data provided by overcut pressure monitoring systems when installed into future tunnel drives, to refine the pressure-friction relationship identified as part of this work.
- Finally, collaboration with industry could be undertaken to develop a pressure controlled lubricant distribution system, as opposed to the time or volume controlled systems cur-

rently in use. The system should ensure the tunnel overcut is maintained at a desired pressure throughout the tunnel drive, which could eliminate the over-lubricating of tunnel sections and associated higher frictional forces and additional costs.

9.5 Concluding remarks

As pipe-jacked tunnel drive lubrication effectiveness has improved, the uncontrolled increase in friction at the soil-lubricant-structure interface during periods of stoppages has become a limiting factor in the design of the tunnel drives. Mitigations, such as interjacks stations or the restricting the tunnel maximum length, are currently employed to manage the risk, however these measures increase the cost, embodied carbon, and duration of tunnelling projects. This research, through a combination of laboratory testing and field monitoring, has gained insight into the physical processes which occur at the SLS interface during tunnel construction and has identified the key causes of these friction increases during stoppages. To inform future tunnelling practice, a new conceptual model of the soil-lubricant structure interface has been developed and simple friction mitigation methods have been proposed for adoption by tunnelling practitioners.

Bibliography

Acikgoz, S., Fidler, P. R. A., Pascariello, M. N., Kechavarzi, C., Bilotta, E., DeJong, M. J., and Mair, R. J. (2022). A Fibre-optic Strain Measurement System to Monitor the Impact of Tunnelling on Nearby Heritage Masonry Buildings. *International Journal of Architectural Heritage*, 16(9):1347–1365.

Aggregate Industries (2022). "Aggregate Industries Leighton Buzzard" URL: https://www.aggregate.com/location-finder/aggregates/bedfordshire/leighton-buzzard/433.

Ahmad, H. M., Kamal, M. S., and Al-Harthi, M. A. (2018). Rheological and filtration properties of clay-polymer systems: Impact of polymer structure. *Applied Clay Science*, 160(July 2017):226–237.

Al-Maamori, H. M. S., El Naggar, M. H., Micic, S., and Lo, K. (2016). Influence of lubricant fluids on swelling behaviour of Queenston shale in southern Ontario. *Canadian Geotechnical Journal*, 53(7):1059–1080.

American Petroleum Institute (2003). Recommended Practice for Field Testing of Water-based Drilling Fluids. Technical report, Washington.

Arup - Atkins Joint Venture (2016). PUTEF DESIGN - Geotechnical Design Note. Technical report, Thames Tideway LTD., London.

Atkinson, J. H. and Potts, D. M. (1977). Stability of a shallow circular tunnel in cohesionless soil. *Géotechnique*, 27(2):203–215.

Bingham, E. C. (1916). An investigation of the laws of plastic flow. *Bulletin of the Bureau of Standards*, 13(2):309.

Borghi, F. X. (2006). *Soil conditioning for pipe-jacking and tunnelling*. Dphil thesis, University of Cambridge.

Brachman, R. W. I., Moore, I. D., and Rowe, R. K. (2001). The performance of a laboratory facility for evaluating the structural response of small-diameter buried pipes. *Canadian Geotechnical Journal*, 38(2):260–275.

British Standards Institution (1990). BS EN 1377-4:1990 Soils for civil engineering purposes - Part 4 - Compaction-related tests. Technical Report 1, British Standards Institution, London.

British Standards Institution (1995a). BS EN 640:1995 Reinforced concrete pressure pipes and distributed reinforcement concrete pressure pipes (non-cylinder type), including joints and fittings. Technical report, British Standards Institution, London.

British Standards Institution (1995b). BS EN 641:1995 Reinforced concrete pressure pipes, cylinder type, including joints and fittings. Technical report, British Standards Institution, London.

British Standards Institution (2003). BS EN ISO 14689-1:2003: Geotechnical investigation and testing. Identification and classification of rock - Part 1 - Identification and description.

British Standards Institution (2011). BS EN ISO 10414-2:2011 -Petroleum and natural gas industries — Field testing of drilling fluids — Part 2: Oil-based fluids. Technical report, International Standards Organisation, Geneva.

British Standards Institution (2012). BS EN ISO 22282-3:2012: Geotechnical investigation and testing. Geohydraulic testing - Part 3 - Water pressure tests in rock.

British Tunnelling Society (2010). *Specification for tunnelling*. Thomas Telford Ltd, London, third edition.

Calçada, L., Scheid, C., de Araújo, C., Waldmann, A., and Martins, A. (2011). Analysis of Dynamic and Static Filtration and Determination of Mud Cake Parameters. *Brazilian Journal of Petroleum and Gas*, 5(3):159–170.

Cebo Holland BV (2019). Cebo Holland. URL: https://cebo.com/en/.

Cetco Minerals Technologies (2019). Cetco Minerals Technologies URL: http://www.cetco.co.uk/.

Chen, T. (2020). Preventing Wall Slip in Rheology Experiments. *TA Instruments*.

Cheng, W. C., Ni, J. C., Arulrajah, A., and Huang, H. W. (2018). A simple approach for characterising tunnel bore conditions based upon pipe-jacking data. *Tunnelling and Underground Space Technology*, 71(October 2017):494–504.

Chesterton, D. (2019). *Monitoring Microtunneling Construction Processes*. PhD thesis, University of Oxford, Oxford.

Comité Français des Travaux sans Tranchée (2006). *Microtunneling and horizontal drilling: French national project "Microtunnels" : recommendations*. Wiley-ISTE, first edition.

Concrete Pipe Association of Australasia (2013). CPAA Design Manual: Jacking Design Guidelines. Technical report, Concrete Pipe Association of Australasia, Gordon.

Curran, B. G. and McCabe, B. A. (2011). Analysis of jacking force data for microtunnels in glacial till at Kilcock , Ireland. *Proceedings of the 15th European Conference on Soil Mechanics and Geotechnical Engineering*, 1(Figure 1):6.

Dean, A. and Goodwin, N. (2021). "Microtunneling: The next big thing" URL: https://www.stantec.com/en/ideas/content/blog/2021/microtunneling-the-next-big-thing.

Deng, Z., Liang, N., Liu, X., de la Fuente, A., Lin, P., and Peng, H. (2021). Analysis and application of friction calculation model for long-distance rock pipe jacking engineering. *Tunnelling and Underground Space Technology*, 115(April).

Deng, Z., Liu, X., Zhou, X., de la Fuente, A., Han, Y., Xiong, F., and Peng, H. (2022a). Field monitoring of mechanical parameters of deep-buried jacketed-pipes in rock: Guanjingkou water control project. *Tunnelling and Underground Space Technology*, 125(May 2021):104531.

Deng, Z., Liu, X., Zhou, X., Yang, Q., Chen, P., de la Fuente, A., Ren, L., Du, L., Han, Y., Xiong, F., and Yan, R. (2022b). Main engineering problems and countermeasures in ultra-long-distance rock pipe jacking project: Water pipeline case study in Chongqing. *Tunnelling and Underground Space Technology*, 123(November 2021):104420.

Dept. for Environment Food and Rural Affairs (2021). Statistical Digest of Rural England - Population. Technical report, DEFRA, London.

FBGS International (2022). FBGS International URL: https://fbgs.com/.

Fernandes, R. R., Turezo, G., Andrade, D. E., Franco, A. T., and Negrão, C. O. R. (2019). Are the rheological properties of water-based and synthetic drilling fluids obtained by the Fann 35A viscometer reliable? *Journal of Petroleum Science and Engineering*, 177(August 2018):872–879.

Halliburton (2021). Halliburton URL: https://www.halliburton.com/.

Hariprasad, C., Rajashekhar, M., and Umashankar, B. (2016). Preparation of Uniform Sand Specimens Using Stationary Pluviation and Vibratory Methods. *Geotechnical and Geological Engineering*, 34(6):1909–1922.

Health and Safety Executive, British Tunnelling Society, and Pipe Jacking Association (2006). Tunnelling and Pipejacking : Guidance for designers. Technical report, Pipe Jacking Ascociation, London.

Heinz, A., Stengele, R. H., and Plotze, M. (2004). Rheological Properties of Bentonite Suspensions Modified with Polymers. *Annual Transactions of the Nordic Rheology Society*, 12(1):221–226.

Herrenknecht AG (2019). Herrenknecht URL: https://www.herrenknecht.com/en/.

Highways England (2021). Geotechnical Design Report Appendix A4: Underpass, Mytongate Junction Bridge and Mytongate Pumping Station. Technical report, Highways England.

Inglethorpe, S. D. J., Morgan, D. J., Highley, D. E., and Bloodworth, A. J. (1993). *Technical Report WG9320: Industrial Minerals Laboratory Manual: Bentonite*. British Geological Survey, Mineralogy and Petrology Group, first edition.

International Tunnelling and Underground Space Association (2016). "Tunnel Market Survey 2016" URL: https://www.tunnel-online.info/en/.

Jamiolkowski, M., Ladd, C., Germaine, J., and Lancelotta, R. (2003). Evaluation of relative density and shear strength of sands from CPT and DMT. In *Soil behavior and soft ground construction*, pages 201–238, Cambridge, Massachusetts. American societry of Civil Engineers.

Jung, J., Park, N., and Lee, B. (2000). Simultaneous measurement of strain and temperature by use of a single fiber Bragg grating written in an erbium:ytterbium-doped fiber. *Applied Optics*, 39(7):1118.

Kendon, M., McCarthy, M., Jevrejeva, S., Matthews, A., Sparks, T., and Garforth, J. (2021). State of the UK Climate 2020. *International Journal of Climatology*, 41(S2):1–76.

Khazaei, S., Shimada, H., Kawai, T., Yotsumoto, J., and Matsui, K. (2006). Monitoring of over cutting area and lubrication distribution in a large slurry pipe jacking operation. *Geotechnical and Geological Engineering*, 24(3):735–755.

Knappett, J. and Craig, R. F. (2012). *Craig's Soil Mechanics*. CRC Press LLC, London, UNITED STATES, 8 edition.

Lam, C. (2011). *Properties and applications of polymer support fluids in geotechnical engineering*. Dphil thesis, University of Oxford.

Lam, C., Jefferis, S. A., and Martin, C. M. (2014). Effects of polymer and bentonite support fluids on concrete-sand interface shear strength. *Geotechnique*, 64(1):28–39.

Larsen, D. (1938). Determining the filtration characteristics of drilling muds. *J. Petrol. Eng*, pages 42–48.

Lehmann, G., Käsling, H., Cambier, A., Praetorius, S., and Thuro, K. (2022). Performance analysis of utility tunneling data: A case study of pipe jacking in hard rock in Brittany, France. *Tunnelling and Underground Space Technology*, 127(September 2021).

Li, M.-c., Wu, Q., Song, K., De Hoop, C. F., Lee, S., Qing, Y., and Wu, Y. (2016). Cellulose Nanocrystals and Polyanionic Cellulose as Additives in Bentonite Water-Based Drilling Fluids: Rheological Modeling and Filtration Mechanisms. *Industrial and Engineering Chemistry Research*, 55(1):133–143.

Lin, Y., Fang, Y., He, C., and Wang, W. (2021). Experimental study on degree of match between slurry and ground based on particle retention rate. *Tunnelling and Underground Space Technology*, 116(November 2020):104105.

Majumder, M., Gangopadhyay, T. K., Chakraborty, A. K., Dasgupta, K., and Bhattacharya, D. K. (2008). Fibre Bragg gratings in structural health monitoring-Present status and applications. *Sensors and Actuators, A: Physical*, 147(1):150–164.

Marshall, M. (1998). *Pipe Jacked Tunnelling: Jacking loads and ground movements*. Dphil thesis, University of Oxford.

Martin, C. M. (1994). *Physical and numerical modelling of offshore foundations under combined loads*. Dphil thesis, University of Oxford.

Mayall, R. (2019). *Monopile Response to Scour and Scour Protection*. Deng thesis, University of Oxford.

Mayall, R. O., McAdam, R. A., Whitehouse, R. J. S., Burd, H. J., Byrne, B. W., Heald, S. G., Sheil, B. B., and Slater, P. L. (2020). Flume Tank Testing of Offshore Wind Turbine Dynamics with Foundation Scour and Scour Protection. *Journal of Waterway, Port, Coastal, and Ocean Engineering*, 146(5):04020033.

McNamara, F. (2010). 779-01-08: Factual report on site investigation for the Blanchardstown Regional drainage scheme. Technical report, Dublin.

Milligan, G. W. E. and Norris, P. (1996). Site-based research in pipe jacking—objectives, procedures and a case history. *Tunnelling and Underground Space Technology*, 11(1):3–24.

Min, F., Zhu, W., and Han, X. (2013). Filter cake formation for slurry shield tunneling in highly permeable sand. *Tunnelling and Underground Space Technology*, 38:423–430.

Min, F., Zhu, W., Han, X., and Zhong, X.-C. (2010). The Effect of Clay content on filter-cake formation in highly permeable gravel. *Geoenvironmental engineering and geotechnics*, pages 210–215.

Mohammed, A. S. (2017). Effect of temperature on the rheological properties with shear stress limit of iron oxide nanoparticle modified bentonite drilling muds. *Egyptian Journal of Petroleum*, 26(3):791–802.

Mokhtar, M. R., Owens, K., Kwasny, J., Taylor, S. E., Basheer, P. A. M., Cleland, D., Bai, Y., Sonebi, M., Davis, G., Gupta, A., Hogg, I., Bell, B., Doherty, W., McKeague, S., Moore, D., Greeves, K., Sun, T., and Grattan, K. T. V. (2012). Fiber-optic strain sensor system with temperature compensation for arch bridge condition monitoring. *IEEE Sensors Journal*, 12(5):1470–1476.

Mostafa, B. A., Assaad, F. F., and Attia, M. (2007). Rheological and electrical properties of Egyptian bentonite as a drilling mud. *Journal of Applied Polymer Science*, 104(3):1496–1503.

Mudtech LTD (2022a). "MUDTECH - Sloop EC" URL: https://mudtech.co.uk/products/sloop-ec.aspx.

Mudtech LTD (2022b). "MUDTECH LTD" URL: https://mudtech.co.uk/products.aspx.

Namli, M. (2011). *Effect of bentonite slurry injection of pipe jacking forces*. Phd thesis, Bogazici University, Istanbul, Turkey.

Namli, M. and Guler, E. (2017). Effect of bentonite slurry pressure on interface friction of pipe jacking. *Journal of Pipeline Systems Engineering and Practice*, 10(1).

Namli, M. and Guler, E. (2019). Closure to "Effect of Bentonite Slurry Pressure on Interface Friction of Pipe Jacking". *Journal of Pipeline Systems Engineering and Practice*, 10(1):4.

Norris, P. (1992). *The Behaviour of Jacked Concrete Pipes during Site Installation*. Dphil thesis, University of Oxford, Oxford.

O'Dwyer, K. G., McCabe, B. A., and Sheil, B. B. (2019). Interpretation of pipe-jacking and lubrication records for drives in silty soil. *Underground Space*, pages 1–11.

OMEGA Engineering (2021). Omega Engineering URL: https://www.omega.co.uk/.

Pan, Y., Li, P., Zhen, L., and Li, X. (2021). Model test for the simultaneous injecting of super-large rectangular pipe jacking. *IOP Conference Series: Earth and Environmental Science*, 861(5).

Pellet-Beaucour, A. L. and Kastner, R. (2002). Experimental and analytical study of friction forces during microtunneling operations. *Tunnelling and Underground Space Technology*, 17(1):83–97.

Pellet-Beaucour, A. L., Kastner, R., Pellet-Beaucour, K., Pellet-Beaucour, A. L., Kastner, R., Pellet-Beaucour, K., Pellet-Beaucour, A. L., and Kastner, R. (2002). Experimental and analytical study of friction forces during microtunneling operations. *Tunnelling and Underground Space Technology*, 17(1):83–97.

Pipe Jacking Association (1995). Guide to best practice for the installation of pipe jacks and microtunnels. Technical report, Pipe Jacking Association, London.

Pipe Jacking Association (2022). The Pipe Jacking Association URL: http://pipejacking.org/.

Praetorius, S. and Schößer, B. (2017). *Bentonite Handbook: Lubrication for Pipe Jacking*. Wiley-VCH Verlag GmbH and Co. KGaA, Weinheim, Germany, first edition.

Psomas, S. (2001). Properties of Foam / Sand Mixtures for Tunnelling Applications. *University of Oxford*, page 147.

Reeves, H. (2002). *The effect of stress fractures on fluid flow in crystalline rocks, Cumbria, UK*. Phd thesis, Durham University.

Reilly, C. C. (2014). *The Influence of Lubricant Slurries on Skin Friction Resistance in Pipe jacking*. Phd, Trinity College Dublin.

Reilly, C. C. and Orr, T. L. L. (2017). Physical modelling of the effect of lubricants in pipe jacking. *Tunnelling and Underground Space Technology*, 63:44–53.

Reilly, C. C., Orr, T. L. L., and McCabe, B. A. (2012). Analysis of microtunnel jacking forces in alluvium and glacial till in Mullingar, Ireland. *Conference: Proceedings of World Tunnelling Conference*, 1(1).

Reilly, C. C., Orr, T. L. L., Namli, M., and Guler, E. (2019). Discussion of "Effect of Bentonite Slurry Pressure on Interface Friction of Pipe Jacking". *Journal of pipeline systems*, 10(1):1.

Richards, I. (2019). *Monopile foundations under cyclic lateral loading*. Dphil thesis, University of Oxford.

Ripley, K. J. (1989). *The performance of jacked pipes*. Phd thesis, University of Oxford.

Royston, R. (2018). *Investigation of Soil-Structure Interaction for Large Diameter Caissons*. Dphil thesis, University of Oxford.

Sanvitale, N., Zhao, B. D., Bowman, E. T., and O'Sullivan, C. (2021). Particle-scale observation of seepage flow in granular soils using PIV and CFD. *Geotechnique*.

Scott, R. H., Chikermane, S., Vidakovic, M., McKinley, B., Sun, T., Banerji, P., and Grattan, K. T. V. (2019). Development of low cost packaged fibre optic sensors for use in reinforced concrete structures. *Measurement: Journal of the International Measurement Confederation*, 135:617–624.

Sheil, B. B., Curran, B. G., and McCabe, B. A. (2016). Experiences of utility microtunnelling in Irish limestone, mudstone and sandstone rock. *Tunnelling and Underground Space Technology*, 51(January):326–337.

Shi, P., Liu, W., Pan, J., and Yu, C. (2018). Experimental and analytical study of jacking load during microtunneling Gongbei tunnel pipe roof. *Journal of Geotechnical and Geoenvironmental Engineering*, 144(1):1–8.

Shou, K., Yen, J., and Liu, M. (2010). On the frictional property of lubricants and its impact on jacking force and soil-pipe interaction of pipe-jacking. *Tunnelling and Underground Space Technology*, 25(4):469–477.

Shukla, S. K., Sivakugan, N., and Das, B. M. (2009). Methods for determination of the coefficient of consolidation and field observations of time rate of settlement - An overview. *International Journal of Geotechnical Engineering*, 3(1):89–108.

Sims, G. (2020). *Fluid Loss and Adsorption of Polymer Support Fluids Used in Deep Foundations*. Mphil thesis, University of Cambridge.

Simulia (2009). *ABAQUS/Standard User's Manual, Version 6.9*. Dassault systems Simula Corp, Providence, RI, USA.

Sisko, A. W. (1958). The Flow of Lubricating Greases. *Industrial and Engineering Chemistry*, 50(12):1789–1792.

Staheli, K. (2006). Jacking force prediction an interface friction approach based on pipe surface roughness. *School of Civil and Environmental Engineering*, PhD:385.

Staheli, K., Frost, D., and Iscimen, M. (2006). Studies of interface friction between jacking pipe materials and frictional soils and the impact on jacking forces. *NASTT North American No-Dig 2006*, 3(3):1–11.

Stein, D. (2005). *Trenchless technology for installation of cables and pipelines*. Stein und Partner, Bochum, forst edition.

Talesnick, M. L., Avraham, R., and Ringel, M. (2014). Measurement of contact soil pressure in physical modelling of soil-structure interaction. *International Journal of Physical Modelling in Geotechnics*, 14(1):3–12.

Taylor, D. (2021). "HS2 loses large amount of potentially highly polluting Bentonite" URL: https://www.theguardian.com/uk-news/2021/sep/10/hs2-potentially-highly-polluting-bentonite.

Taylor, D. W. (1948). *Fundamentals of soil mechanics*. J. Wiley, 1948, New York (State), first edition.

Templeman, J. O. (2023). *Novel measurement and modelling of soil-structure interaction for open caissons*. Dphil thesis, University of Oxford.

Terzaghi, K. (1943). *Theoretical Soil Mechanics*. John Wiley and Sons, Inc., Hoboken, NJ, USA, 1st edition.

Thames Water PLC (2021). "Thames Tideway Tunnel" URL: https://www.thameswater.co.uk/about-us/investing-in-our-region/thames-tideway-tunnel.

Tognon, A. R., Rowe, R. K., and Brachman, R. W. (1999). Evaluation of side wall friction for a buried pipe testing facility. *Geotextiles and Geomembranes*, 17(4):193–212.

Ulusay, R. (2014). *The ISRM suggested methods for rock characterization, testing and monitoring : 2007-2014*. Springer Cham, Cham, first edition.

Underground professional services LTD. (2017). Project Geotechnical Design Note. Technical report, London.

United Utilities LTD. (2021). "West Cumbria Water Supply Scheme" URL: https://www.unitedutilities.com/cumbria/our-plans/west-cumbria/.

Vaid, Y. P. and Negussey, D. (1984). Relative Density of Pluviated Sand Samples. *Soils and Foundations*, 24(2):101–105.

Verst, R., Blumenthal, A., Du, J., Konig, D., Pulsfort, M., and Wichtmann, T. (2022). Systematic laboratory and field study on the shear resistance of the soil-concrete interface of diaphragm walls and bored piles. In *DFI-EFFC International Conference on Deep Foundations and Ground Improvement: Smart Construction for the Future*, pages 156–167, Berlin.

VMT GMBH (2019). "VMT GMBH | Microtunelling" URL: https://www.vmt-gmbh.de/en/products/navigate-tunnelling/microtunnelling/.

Vryzas, Z., Kelessidis, V. C., Nalbantian, L., Zaspalis, V., Gerogiorgis, D. I., and Wubulikasimu, Y. (2017). Effect of temperature on the rheological properties of neat aqueous Wyoming sodium bentonite dispersions. *Applied Clay Science*, 136:26–36.

Wang, G., Du, H., and Guo, B. (2018). Determination of Viscosity and Wall Slip Behavior of a Polymer-Gel Used for Leakage Control from Couette Viscometry Data. *Journal of Energy Resources Technology, Transactions of the ASME*, 140(3).

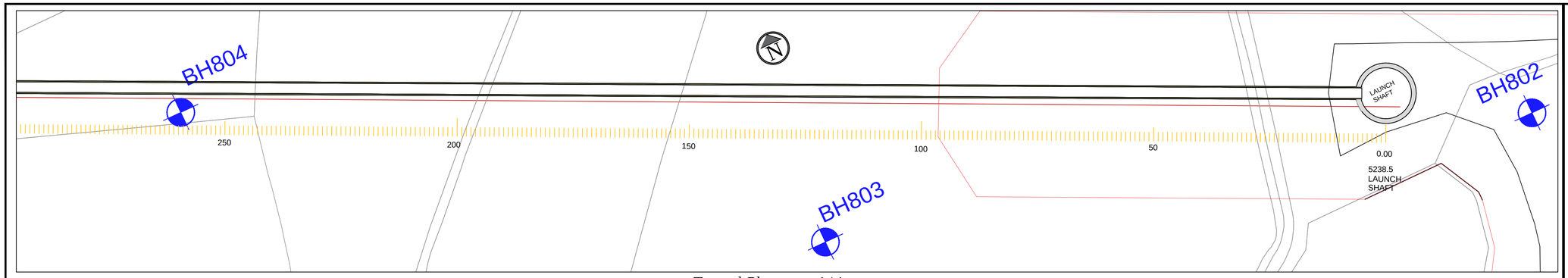
Xu, T. and Bezuijen, A. (2019). Bentonite slurry infiltration into sand: filter cake formation under various conditions. *Géotechnique*, 69(12):1–12.

Yonan, S. J. (1993). *Pipe jacking forces in sand*. PhD thesis, University of Loughborough.

Young, W. C., Budynas, R. G., and Sadegh, A. M. (1976). *Roark's Formulas for Stress and Strain, Fith Edition*. McGraw-Hill Education, New York, 8th ed. / edition.

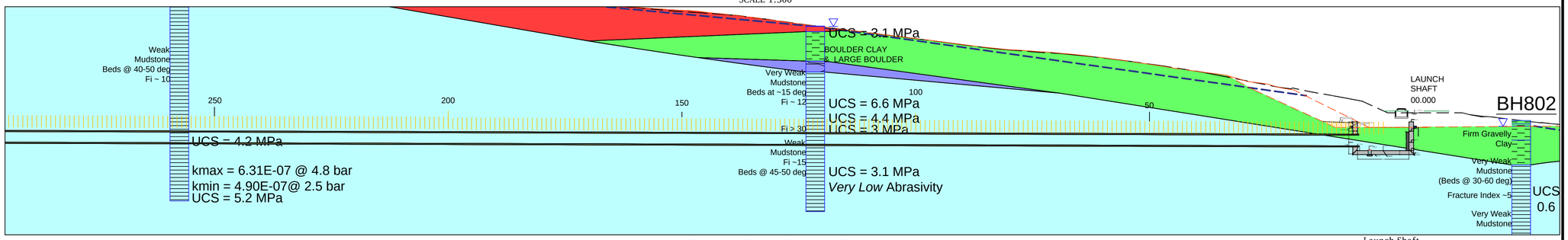
Zhong, Z., Li, C., Liu, X., Xiong, Y., Fan, Y., and Liang, N. (2021). Assessment of experimental friction parameters and contact property of pipe string for the estimation and verification of a solution for pipe stuck in the China's first rock pipe jacking. *Tunnelling and Underground Space Technology*, 107(June 2020).

Appendix A | Castlerigg tunnel drawings



Tunnel Plan part 1/4

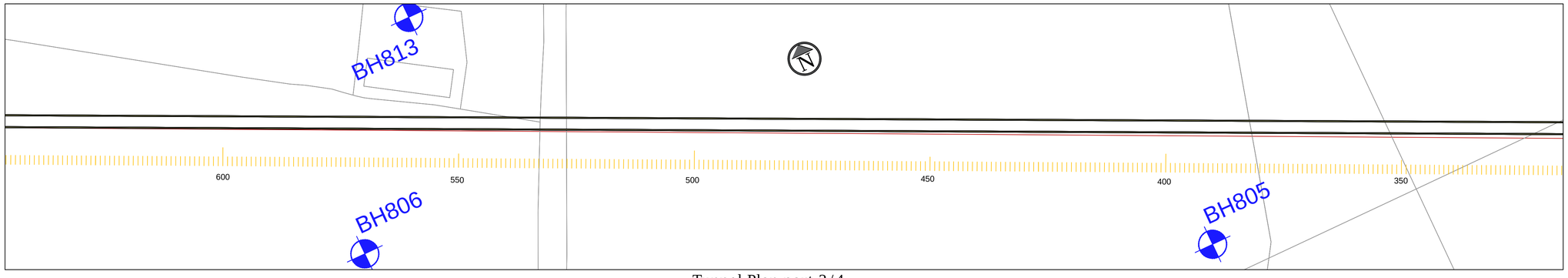
SCALE 1:500



Tunnel Cross Section Part 1/4

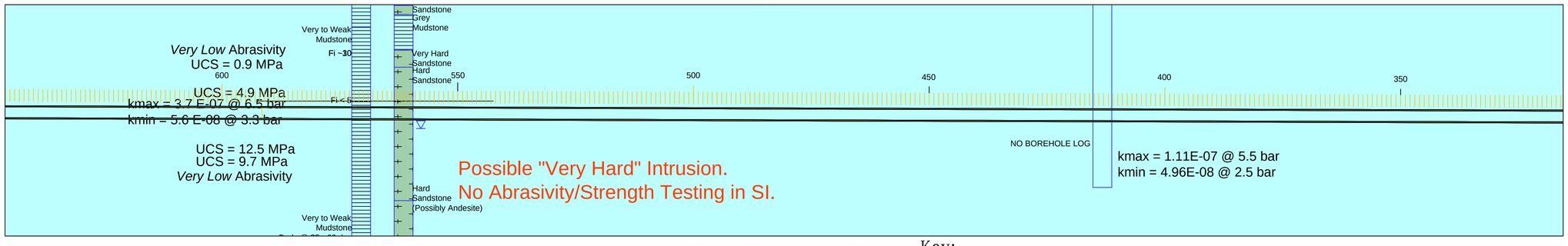
SCALE 1:500

Launch Shaft
Chainage = 5227m



Tunnel Plan part 2/4

SCALE 1:500



Tunnel Cross Section Part 2/4

SCALE 1:500

Interjack Locations:

CHAINAGE (m)	42	146	263	391	519	632	745	948	1061	1123
PIPE No	12	47	86	129	172	210	248	316	354	375
IJS No	1A	2A	3A	4A	5A	6A	7A	8A	9A	10A

2286 ID / 2750 OD Tunnel Pipe

ACELEROL MITTAL PILING HANDBOOK, 9TH EDITION (2016)

Density index, I_D (%)	Relative density	SPT blow count $(N_1)60$	Cone resistance q_c (MPa)	Angle of shearing resistance ϕ (°)
0 – 15	Very loose	0 – 3	<2.5	29 – 32
15 – 35	Loose	3 – 8	2.5 – 5.0	32 – 35
35 – 65	Medium dense	8 – 25	5.0 – 10.0	35 – 37
65 – 85	Dense	25 – 42	10.0 – 20.0	37 – 40
85 – 100	Very dense	42 – 58	> 20.0	40 – 42

Table 4.2. Typical correlations for quartz sands.

Key:

Clay
Mudstone
Sand
Boulder
Sandstone
Limestone
Concrete
Gravel
Water Level
Site Boundary
Existing GL
Proposed GL
Chainage

SAFETY HEALTH & ENVIRONMENTAL INFORMATION

CONSTRUCTION
Ci - WORKING IN CLOSE PROXIMITY TO LOCAL RESIDENTS
Cii - GROUND CONDITIONS DIFFERENT TO SURVEY

OPERATIONS
Oi - UNPROVEN OBSTRUCTIONS ALONG TUNNEL DRIVE

DISMANTLING/DEMOLITION
Di - REMOVING TBM FROM RECEPTION SHAFT

10m 0m 10m 20m 30m
Scale 1:500

NOTES

1. ALL DIMENSIONS IN MILLIMETERS AND ALL LEVELS IN METERS AOD UNLESS NOTED OTHERWISE.

2. CAISSONS ONLY TO BE SUNK ONCE A MINIMUM OF TWO POURS ARE COMPLETED.

3. SHAFTS TO BE BACKFILLED USING SELECTED EXCAVATED MATERIAL WITHIN SHAFTS (LARGE STONES REMOVED USING RIDDLING BUCKET) AND USE SHINGLE LOCALLY AROUND THE DUCTS. SHINGLE WILL ALSO ACCOMMODATE LOCAL SETTLEMENTS. BACKFILL SELECTED EXCAVATED MATERIAL IN 750mm LAYERS AND COMPACT MATERIAL USING A RAMEX ROLLER. MATERIAL WITHIN 750mm OF THE DUCTILE IRON PIPEWORK WILL BE 100mm DOWN STONE.

8. THE MAXIMUM EXPECTED JACKING FORCE IS 325 TONNES.

2. ENGINEER WILL MONITOR EXPOSED ROCK FOR STABILITY OF 2.3M BEING EXPOSED FOR ANY SOFT SPOTS. IF SOFT SPOTS IDENTIFIED THEN POUR HEIGHT OR EXCAVATION HEIGHT TO BE REDUCED TO 1.5m (1.3m OF EXPOSED ROCK)

3. VALUES MARKED CXX/XXX ARE CONE STANDARD PENETRATION VALUES - XX BLOWS / XXX EMBEDMENT

4. VALUES MARKED (USC) ARE UNIAXIAL COMPRESSIVE STRESS OF SAMPLES. 'PARA' MEANS IN LINE WITH THE LAYERS IN THE ROCK 'PERP' ACROSS THEM.

5. K VALUES ARE FROM IN-SITU PERMEABILITY TESTING. EITHER AN AVERAGE OR A MAXIMUM & MINIMUM AT DIFFERENT HEAD IS SHOWN.

6. LABELS OF ROCK STRENGTH ARE TO BS EN ISO 14689 - 1 : 2018

EN ISO 14689-1 : 2003 Rock Strength Terms	
Compressive Strength mpa	Term
<1.0	Extremely Weak
1 to 5	Very Weak
5 to 25	Weak
25 to 50	Medium Strong
50 to 100	Strong
100 to 250	Very Strong
> 250	Extremely Strong

7. QUALITATIVE CLAY STRENGTHS TO BS EN ISO 14688 - 2 : 2018

Undrained shear strength c_u (kPa)	Strength	Equivalent consistency
< 10	Extremely low	Very soft
10 – 20	Very low	Very soft
20 – 40	Low	Soft
40 – 75	Medium	Firm
75 – 150	High	Stiff
150 – 300	Very high	Very stiff
> 300	Extremely high	Hard

Table 4.4. Strength of fine soils

9. 'FI' STANDS FOR THE FRACTURE INDEX (THE NUMBER OF FRACTURES IN THE ROCK PER M).

CURRENT ISSUE INFORMATION

VERSION	AUTH	CHKD	REVD	REASON FOR ISSUE	DATE
P02	CD	DM	BP	For Information	26/07/18
S4				Issued for Construction Approval	
SUITABILITY CODE				SUITABILITY DESCRIPTION	

United Utilities
helping life flow smoothly

WARD & BURKE CONSTRUCTION LIMITED
FARRANS ROADBRIDGE

WCS - THIRLMERE LINK MAIN - RAW WATER AQUEDUCT

CIVIL

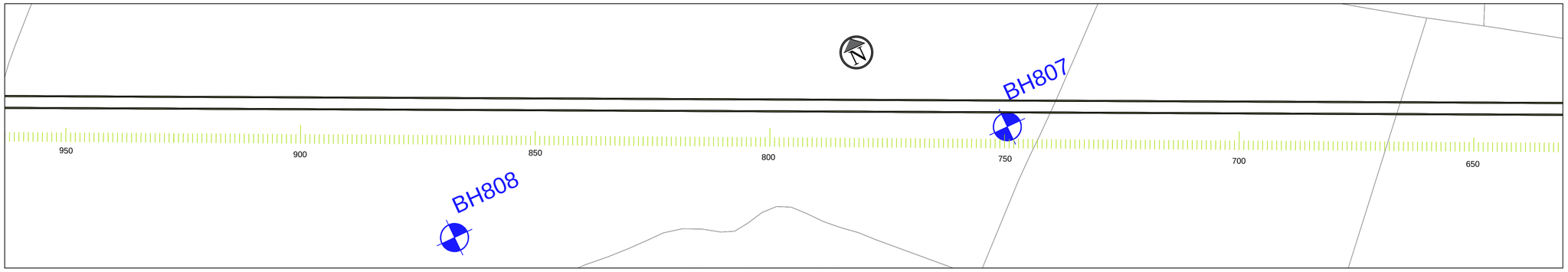
CASTLERIGG TUNNEL

GENERAL ARRANGEMENT

PART 1 AND 2

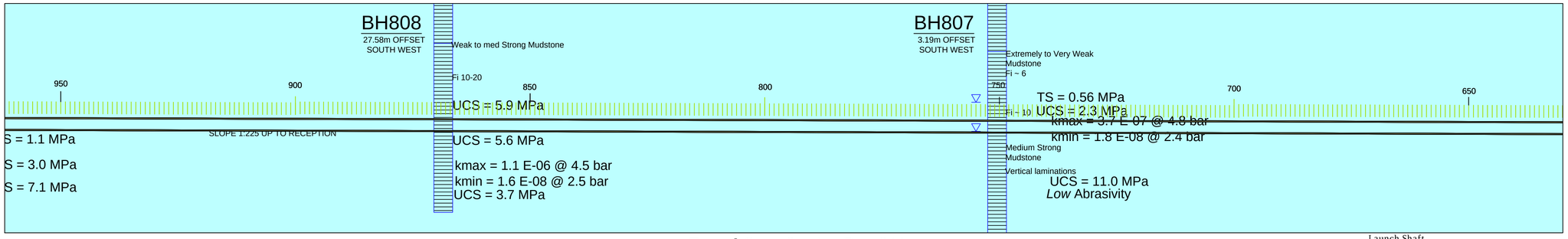
SCALE	SHEET SIZE
AS SHOWN	A1
DRAWING NUMBER	REVISION
80040112-50-WAB-00041-PL-DR-01-70300	P02

©The copyright of this document, which contains information of a proprietary nature, is vested in United Utilities Water Limited. The content of this document may not be used for purposes other than that for which it has been supplied and may not be reproduced, either wholly or in part, in any way whatsoever. It may not be used by, or its contents divulged to any other person whatsoever without the prior written permission of United Utilities Water Limited.
Copyright Acknowledgement: Use of Ordnance Survey map data sanctioned by the controller of H.M. Stationery Office. OS Licence Number 100019326. Crown copyright reserved. Unauthorised production infringes copyright



Tunnel Plan part 3/4

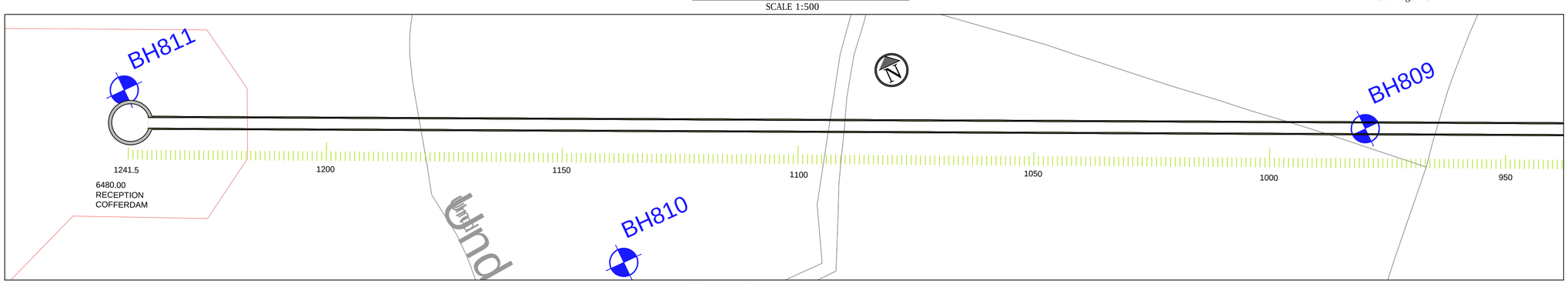
SCALE 1:500



Tunnel Cross Section Part 3/4

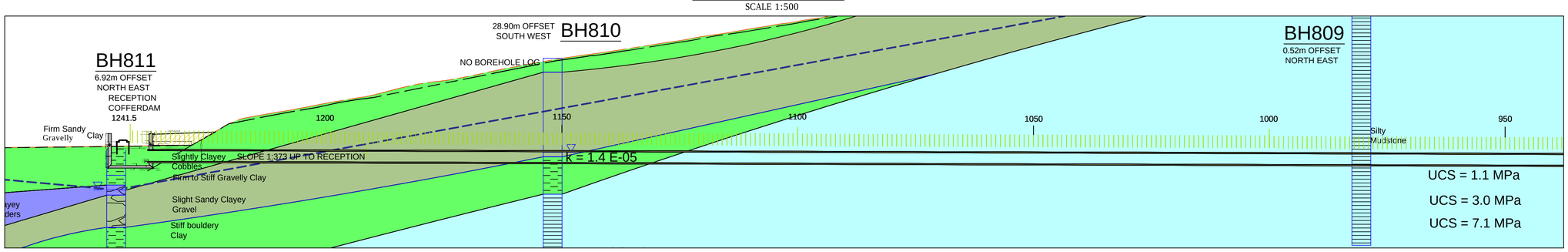
SCALE 1:500

Launch Shaft
Chainage = 5227m



Tunnel Plan part 4/4

SCALE 1:500



Tunnel Cross Section Part 4/4

SCALE 1:500

Key:

Clay
Mudstone
Sand
Boulder
Sandstone
Limestone
Concrete
Gravel
Water Level
Site Boundary
Existing GL
Proposed GL
Chainage

10m 0m 10m 20m 30m
Scale 1:500

Interjack Locations:

CHAINAGE (m)	42	146	263	391	519	632	745	948	1061	1123
PIPE No	12	47	86	129	172	210	248	316	354	375
IJS No	1A	2A	3A	4A	5A	6A	7A	8A	9A	10A

2286 ID / 2750 OD Tunnel Pipe

ACELEROL MITTAL PILING HANDBOOK, 9TH EDITION (2016)

Density index, I_D (%)	Relative density	SPT blow count (N_1) 60	Cone resistance q_c (MPa)	Angle of shearing resistance ϕ (°)
0 – 15	Very loose	0 – 3	<2.5	29 – 32
15 – 35	Loose	3 – 8	2.5 – 5.0	32 – 35
35 – 65	Medium dense	8 – 25	5.0 – 10.0	35 – 37
65 – 85	Dense	25 – 42	10.0 – 20.0	37 – 40
85 – 100	Very dense	42 – 58	> 20.0	40 – 42

Table 4.2. Typical correlations for quartz sands.

NOTES

1. ALL DIMENSIONS IN MILLIMETERS AND ALL LEVELS IN METERS AOD UNLESS NOTED OTHERWISE.

2. CAISSONS ONLY TO BE SUNK ONCE A MINIMUM OF TWO POURS ARE COMPLETED.

3. SHAFTS TO BE BACKFILLED USING SELECTED EXCAVATED MATERIAL WITHIN SHAFTS (LARGE STONES REMOVED USING RIDDLING BUCKET) AND USE SHINGLE LOCALLY AROUND THE DUCTS. SHINGLE WILL ALSO ACCOMMODATE LOCAL SETTLEMENTS. BACKFILL SELECTED EXCAVATED MATERIAL IN 750mm LAYERS AND COMPACT MATERIAL USING A RAMEX ROLLER. MATERIAL WITHIN 750mm OF THE DUCTILE IRON PIPEWORK WILL BE 100mm DOWN STONE.

8. THE MAXIMUM EXPECTED JACKING FORCE IS 325 TONNES.

2. ENGINEER WILL MONITOR EXPOSED ROCK FOR STABILITY OF 2.3M BEING EXPOSED FOR ANY SOFT SPOTS. IF SOFT SPOTS IDENTIFIED THEN POUR HEIGHT OR EXCAVATION HEIGHT TO BE REDUCED TO 1.5m (1.3m OF EXPOSED ROCK)

3. VALUES MARKED CXX/XXX ARE CONE STANDARD PENETRATION VALUES - XX BLOWS / XXX EMBEDMENT

4. VALUES MARKED (USC) ARE UNIAXIAL COMPRESSIVE STRESS OF SAMPLES. 'PARA' MEANS IN LINE WITH THE LAYERS IN THE ROCK 'PERP' ACROSS THEM.

5. K VALUES ARE FROM IN-SITU PERMEABILITY TESTING. EITHER AN AVERAGE OR A MAXIMUM & MINIMUM AT DIFFERENT HEAD IS SHOWN.

6. LABELS OF ROCK STRENGTH ARE TO BS EN ISO 14689 - 1 : 2018

EN ISO 14689-1 : 2003 Rock Strength Terms	
Compressive Strength mpa	Term
<1.0	Extremely Weak
1 to 5	Very Weak
5 to 25	Weak
25 to 50	Medium Strong
50 to 100	Strong
100 to 250	Very Strong
> 250	Extremely Strong

7. QUALITATIVE CLAY STRENGTHS TO BS EN ISO 14688 - 2 : 2018

Undrained shear strength c_u (kPa)	Strength	Equivalent consistency
< 10	Extremely low	Very soft
10 – 20	Very low	Very soft
20 – 40	Low	Soft
40 – 75	Medium	Firm
75 – 150	High	Stiff
150 – 300	Very high	Very stiff
> 300	Extremely high	Hard

Table 4.4 Strength of fine soils.

9. 'FI' STANDS FOR THE FRACTURE INDEX (THE NUMBER OF FRACTURES IN THE ROCK PER M).

CURRENT ISSUE INFORMATION

VERSION	AUTH	CHKD	REVD	REASON FOR ISSUE	DATE
P02	CD	DM	BP	For Information	26/07/18
S4				Issued for Construction Approval	
SUITABILITY CODE				SUITABILITY DESCRIPTION	

United Utilities
helping life flow smoothly

WARD & BURKE CONSTRUCTION LIMITED

FARRANS ROADBRIDGE

WCS - THIRLMERE LINK MAIN - RAW WATER AQUEDUCT

CIVIL

CASTLERIGG TUNNEL

GENERAL ARRANGEMENT

PART 3 AND 4

SCALE	SHEET SIZE
AS SHOWN	A1
DRAWING NUMBER	REVISION
80040112-50-WAB-00041-PL-DR-01-70301	P02

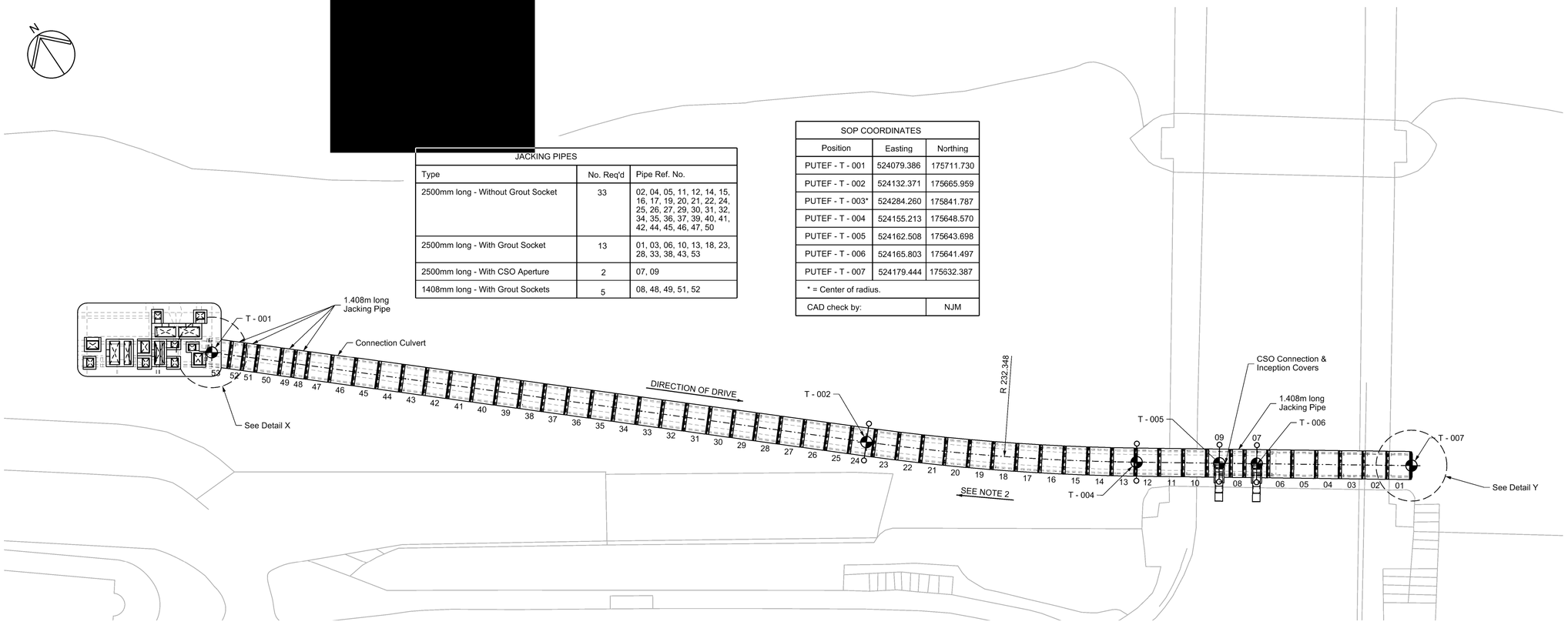
©The copyright of this document, which contains information of a proprietary nature, is vested in United Utilities Water Limited. The content of this document may not be used for purposes other than that for which it has been supplied and may not be reproduced, either wholly or in part, in any way whatsoever. It may not be used by, or its contents divulged to any other person whatsoever without the prior written permission of United Utilities Water Limited.
Copyright Acknowledgement: Use of Ordnance Survey map data sanctioned by the controller of H.M. Stationery Office. OS Licence Number 100019326. Crown copyright reserved. Unauthorised production infringes copyright

Appendix B | Putney tunnel drawings

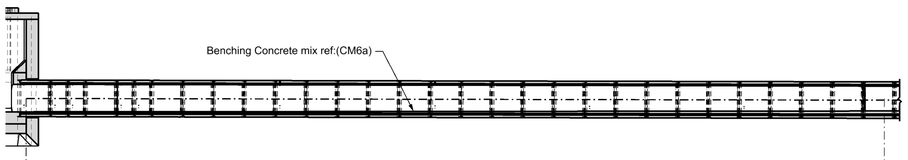
[redacted]

JACKING PIPES		
Type	No. Req'd	Pipe Ref. No.
2500mm long - Without Grout Socket	33	02, 04, 05, 11, 12, 14, 15, 16, 17, 19, 20, 21, 22, 24, 25, 26, 27, 29, 30, 31, 32, 34, 35, 36, 37, 39, 40, 41, 42, 44, 45, 46, 47, 50
2500mm long - With Grout Socket	13	01, 03, 06, 10, 13, 18, 23, 28, 33, 38, 43, 53
2500mm long - With CSO Aperture	2	07, 09
1408mm long - With Grout Sockets	5	08, 48, 49, 51, 52

SOP COORDINATES		
Position	Easting	Northing
PUTEF - T - 001	524079.386	175711.730
PUTEF - T - 002	524132.371	175665.959
PUTEF - T - 003*	524284.260	175841.787
PUTEF - T - 004	524155.213	175648.570
PUTEF - T - 005	524162.508	175643.698
PUTEF - T - 006	524165.803	175641.497
PUTEF - T - 007	524179.444	175632.387
* = Center of radius.		
CAD check by:		NJM

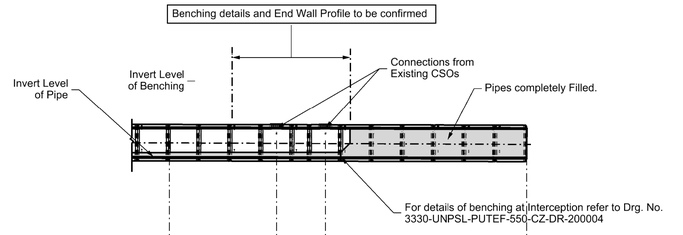


1 Plan
SCALE 1:250

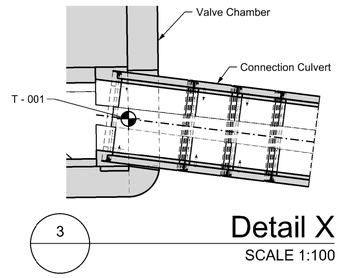


Invert of pipes in this length to be primed Immediately prior to casting benching with FOSROC Nitrobond SBR slurry coat brushed into clean roughened surface(See Note 6).

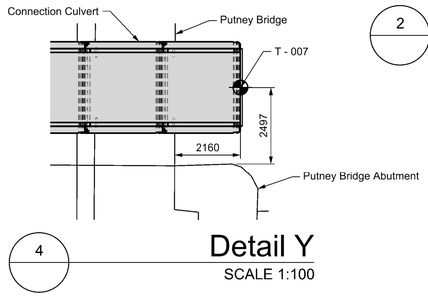
Benching details and End Wall Profile to be confirmed



Chaninage (m)	00.00	70.017	98.743	107.491	111.451	127.881
Benching Invert Level	96.977	97.047	97.076	97.084	97.088	N/A
Pipe Invert Level	96.926	96.786	96.729	96.711	96.703	96.670
Benching Gradient	1:1000	1:1000	1:1000			
Pipe Gradient	1:500	1:500	1:500			
Horizontal Alignment	Straight	Radius	Straight			



3 Detail X
SCALE 1:100



4 Detail Y
SCALE 1:100

2 Long Section
SCALE 1:250

Notes

1. All dimensions are in metres unless noted otherwise.
2. Welding of joints to commence from reception pit towards Valve Chamber.
3. All Jacking Pipes 2.5m Long unless noted otherwise.
4. This drawing is to be read in conjunction with the following:-

   3330-UNPSL-PUTEF-550-CZ-DR-200001
   - Connection Culvert Geological Section
   3330-UNPSL-PUTEF-550-CZ-DR-200006
   - CSO Interception General Arrangement
5. For concrete specification refer to 3120-BMBJV-CONTR-106-ZZ-OL-000001
6. Invert of all pipes to be roughened to ensure good bond with benching concrete. To Be Confirmed
7. Maximum permitted (unfactored) jacking force allowing for a total joint deflection of 1.1 degrees = 250 tonnes.

[redacted]

BMB ISSUED FOR CONSTRUCTION
Identical to Revision P03

Keyplan:



Mapping reproduced by permission of Ordnance Survey on behalf of HMSO. © Crown Copyright and Database right 2017. All rights reserved. Ordnance Survey licence number 100056637

Coordinates are to Ordnance Survey Datum OSGB36. All levels are in metres and relate to the tunnel datum which is 100 metres below Ordnance Datum Newlyn.

Safety, Health and Environmental Information

Notes below are additional to hazards/risks normally associated with this type of work:

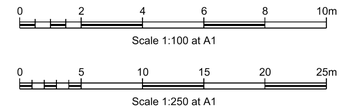
Construction
- Ci Tidal groundwater pressure to be monitored to allow TBM to balance face pressure.
- Cii Measures to be in place to deal with unexpected obstructions to TBM advance should they be encountered.
- Ciii Measure to be in place to ensure confinement of face slurry and prevent escape to river.
- Civ Tidal working during TBM removal and installation of Interception Culvert pieces. Isolation of Connection Culvert from flooding from river to be maintained.
- Cv Method to be developed to push TBM off end of lead pipe upon completion of drive while maintaining isolation of Connection Culvert from river flooding.
- Cvi Temporary stability of Interception Culvert units when being lifted and installed into aperture in existing bridge abutment.
- Cvii Welding. Provide adequate ventilation and fire ignition protection measures for site welding of the stainless steel Interception Culvert pieces.
- Cviii Temporary stability of Interception Covers while being slid into position and before being fixed in place.
- Cix Working in front of existing CSO discharge subject to sewage discharges during or after heavy rainfall events.

Operation
Oi.n/a

Maintenance
- Mi Utilise remotely operated CCTV for inspections
- Mii When entering Connection Culvert, a secondary means of egress is to be provided via a light-weight extension ladder from the Culvert invert up into one of the existing CSO channels and then out via the existing access manholes.
- Miii Inspection and maintenance of Interception Covers is to be done between tides.
- Miv Due to the form of structure, the design concept for watertightness and the known ground conditions, there is no risk of contaminated ground water entering the works

Dismantling/Demolition (Future)
Di.n/a

These notes are based on the use of experienced and competent contractors carrying out the work using an approved safe method of working.



Rev	Date	Issue history
P01	2018-06-07	Gate 4 Alternative Design
P02	2018-11-19	Gate 5 Alternative Design
P03	2018-11-30	Gate 5 Alternative Design
C01	2018-12-03	Authorised for BMB by Rajiv.Gupta

Description of change - Line 1
Description of change - Line 2
Description of change - Line 3
Description of change for current revision

Authorised for BMB by Rajiv.Gupta

Checker: MMUS
Approver: SPSO

C01

Approved as Gate 5 Complete A5

Location
Putney Embankment Foreshore
London Borough of Wandsworth

Document Information
UnPS - Tunnels, Shafts & Temporary Works
Connection Culvert General Arrangement & Setting Out

2018-12-03
3330-UNPSL-PUTEF-550-CZ-DR-200019
Official

Tideway

PDF Created: 03/12/2018 16:50:43 Valid only at time of creation

© Copyright Bazalgette Tunnel Limited 2015